ABSTRACT

Title of Dissertation: ATOMIC LAYER DEPOSITION OF LEAD ZIRCONATE-TITANATE AND OTHER LEAD-BASED PEROVSKITES

Nicholas Anthony Strnad
Doctor of Philosophy, 2019

Dissertation directed by: Professor Raymond J. Phaneuf
Department of Materials Science and Engineering

Dr. Ronald G. Polcawich
U.S. Army Research Laboratory, Adelphi, MD

Lead-based perovskites, especially lead zirconate-titanate ($PbZr_xTi_{1-x}O_3$, or PZT), have been of great technological interest since they were discovered in the early 1950s to exhibit large electronic polarization. Atomic layer deposition (ALD) is a thin-film growth technique capable of uniformly coating high aspect-ratio structures due to the self-limited nature of the precursor chemisorption steps in the deposition sequence. In this thesis, a suite of related processes to grow lead-based perovskites by ALD are presented. First, a new process to grow ferroelectric lead titanate ($PbTiO_3$, or PTO) by ALD using lead bis(3-N,N-dimethyl-2-methyl-2-propanoxide) [$Pb(DMAMP)_2$] and

tetrakis dimethylamino titanium [TDMAT] as the lead and titanium cation precursors, respectively, is discussed. A 360-nm thick PTO film grown by ALD displayed a maximum polarization of 48 $\mu C/cm^2$ and remanent polarization of ± 30 $\mu C/cm^2$. Second, a new process (similar to the ALD PTO process) to grow PZT by ALD is demonstrated by partial substitution of TDMAT with either tetrakis dimethylamino zirconium or zirconium tert-butoxide. The 200 nm-thick ALD PZT films exhibited a maximum polarization of 50 $\mu C/cm^2$ and zero-field dielectric constant of 545 with leakage current density < 0.7 $\mu A/cm^2$. Third, a new ALD process for antiferroelectric lead hafnate ($PbHfO_3$, or PHO) is presented along with electrical characterization showing a field-induced antiferroelectric to ferroelectric phase transition with applications for capacitive energy storage. Finally, ALD lead hafnate-titanate ($PbHf_xTi_{1-x}O_3$, or PHT), considered to be an isomorph of PZT, is demonstrated by combining the process for PTO and PHO. The thin-film PHT grown by ALD is shown to have electronic properties that rival PZT grown at compositions near the morphotropic phase boundary (MPB). The processes for both ALD PZT and PHT are shown to yield films with promising properties for microelectromechanical systems (MEMS) actuators and may help to dramatically increase the areal work density of such devices.

ATOMIC LAYER DEPOSITION OF LEAD ZIRCONATE-TITANATE AND OTHER LEAD-BASED PEROVSKITES

by

Nicholas Anthony Strnad

Dissertation submitted to the Faculty of the Graduate School of the
University of Maryland, College Park, in partial fulfillment
of the requirements for the degree of
Doctor of Philosophy
2019

Advisory Committee:
Professor Raymond J. Phaneuf, Chair
Dr. Ronald G. Polcawich
Professor Ichiro Takeuchi
Professor Lourdes G. Salamanca-Riba
Professor Raymond A. Adomaitis

Dedication

Dedicated to Eliza Hawk

Acknowledgements

I would like to acknowledge my parents, Tony and Virginia Strnad. Their sacrifices and encouragement provided the foundation for my personal and professional successes in life. Special thanks to my girlfriend, Rebecca Hawk, for supporting me and providing flexibility at home which enabled me to dedicate the long-hours necessary to complete this thesis.

Growing up in public school, I had many teachers that made a positive impact on me. However, several teachers stand out as truly exceptional, including (but not limited to): Steve Nikirk, Denise Frye, Chuck Grover, Jon Evans, Alan Lescalleet, Lou Eskuchen and Scott Strait.

I would like to thank James (Jim) Mulcahy of the cleanroom staff who trained me as a green equipment engineer and was (and continues to be) a great colleague for 7+ years. Jim enabled a significant portion of the research contained in this thesis by shouldering the burden of equipment maintenance and training when I needed to focus other tasks. Thanks to the rest of the cleanroom staff: Madhu Roy, Brant Hempel, Robert Burke, Nelson Mark, Joyce Bell-Sampson, Wendell Windsor (emeritus), Ida Holley (emeritus), and Brittany Poetzsch (emeritus) for timely service and much-needed friendship over the years.

Thanks to William Benard (cleanroom manager, emeritus) for taking a chance on hiring me as a new materials engineering graduate, and for providing technical expertise and (much needed) mentorship early in my career. Thanks to Paul Sunal (cleanroom manager) for continuing to provide institutional support for atomic layer deposition and for personally advocating for my career advancement.

This work would not be possible without Noel O'Toole and Bruce Rayner of the Kurt J. Lesker Company, Inc. Noel provided many hours of technical training to myself and our staff, including rare wisdom from his years of working at Intel. Noel also personally rescued us from many (self-inflicted) maintenance conundrums. Bruce also provided hours of training and technical expertise, including serving as a Co-PI on much of the early work and mentoring me as a nascent ALD scientist.

Thanks to my advisor Raymond Phaneuf who taught me kinetics as a materials undergraduate and welcomed me into his group as a graduate student. Thanks for always making time for me when I needed it and teaching me something new (and often critically important) each time I visited your office.

Thanks to my co-advisor Ronald Polcawich who adopted me into the wide world of PZT as I was deciding a research direction for my thesis and career. Ron was instrumental in acquiring the initial infrastructure funding for ALD and in developing the program dedicated to ALD PZT. He also makes the best venison-BBQ.

Thanks to Brendan Hanrahan who aided with the inception of lead hafnate and with pyroelectric measurements of lead hafnate-titanate. Brendan was also in the trenches (so to speak) with me, helping out with ferroelectric measurements before it was clear that ALD could yield good properties. Thanks to Jeff Pulskamp who, as my team lead, continues to support my research as we drive toward device applications. Also thanks to Robert Benoit, Brian Power, Joel Martin, Ryan Rudy, and my other teammates for selflessly lending a hand, especially when it was not convenient.

Last but certainly not least, special thanks to Daniel Potrepka who carefully read multiple thesis drafts (and papers, abstracts, presentations, posters…), put up with my

stubbornness, and served as a de-facto advisor to me for the last several years. It has been a pleasure working with you and getting to know you.

Table of Contents

List of Tables

List of Figures

Chapter 1: Introduction, Motivation, and ALD Literature Review

Introduction

Atomic layer deposition (ALD) is a thin-film deposition technique whereby films are grown by a sequence of self-limited surface chemical reactions. A typical deposition utilizes two or more gas-phase co-reactants, or precursors, which serve as the source material for the film. One typically cited example is the ALD Al_2O_3 process that utilizes trimethylaluminum (TMA) and H_2O as the aluminum and oxygen precursors, respectively.[1] The precursor dose and purge sequence is graphically depicted in Fig. 1.1, shown below. Each precursor dose step is followed by a gas purge, or process chamber evacuation step. The purpose is to purge surface reaction byproducts and excess precursor from the process chamber before introduction of the co-precursor. The example depicted in Fig. 1.1 proceeds in alphabetical order of the blocks. One important requirement of ALD is that the growth surface is returned to the original state after one complete ALD cycle. For the example presented in Fig. 1.1, the hydroxylated growth surface depicted in block A is regenerated upon completion of the final step shown in block D.

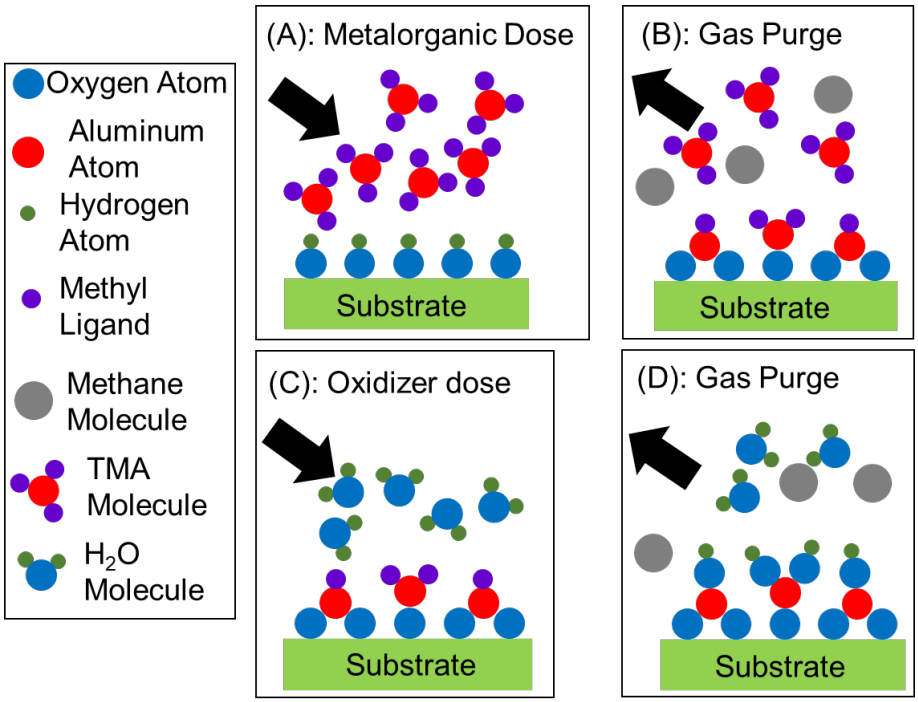

Figure 1.1: Dose sequence of an ALD Al_2O_3 process.

The primary benefit of ALD compared to other thin-film deposition techniques such as sputtering, sol-gel, pulsed-laser deposition (PLD), or metal-organic chemical vapor deposition (MOCVD) is the ability to uniformly coat high aspect-ratio substrates. Conformal Al_2O_3 grown by ALD has been previously demonstrated on ultrahigh-aspect-ratio anodic aluminum oxide nanopores with a depth-to-diameter ratio of > 500:1.[2]

Lead zirconate-titanate ($PbZr_xTi_{1-x}O_3$ or PZT) is a lead-containing ceramic perovskite that is a solid-solution of lead zirconate ($PbZrO_3$ or PZO) and lead titanate ($PbTiO_3$ or PTO).[3] Lead hafnate-titanate ($PbHf_xTi_{1-x}O_3$ or PHT) is also a lead-containing ceramic perovskite with properties similar to PZT. PHT, similarly, is a solid solution of lead hafnate ($PbHfO_3$ or PHO) and PTO. All five of the Pb-based perovskites referenced here (PTO, PZO, PZT, PHO, PHT) are technologically relevant materials. PTO, a

tetragonal perovskite, is typically investigated as an end-member for PZT, though it has been demonstrated on its own to have promising properties for ferroelectric random-access memory (FRAM).[4] PZO and PHO are both orthorhombic perovskites at room temperature and may be considered to be structurally isomorphic.[5,6] Both PZO and PHO exhibit an electric-field induced antiferroelectric to ferroelectric phase transition that has been shown to promote dielectric energy storage.[7] The properties of both PZT and PHT depend strongly on the relative concentration of the 4^+ cations. The most desired composition of PZT and PHT occurs at the morphotropic phase boundary (MPB) at which the unit cell adopts a monoclinic structure. The MPB occurs at $PbZr_{0.52}Ti_{0.48}O_3$ for PZT, and $PbHf_{0.50}Ti_{0.50}O_3$ for PHT.[8,9] Both PZT and PHT exhibit maximum values of dielectric constant and piezoelectric properties at compositions near the MPB.[10] PZT in particular has numerous technological applications that are covered in detail in Chapter 2. For the purposes of the work covered in this thesis, the primary focus is the application of PZT towards piezoelectric actuators.

Motivation for ALD of PZT

Thin-film PZT deposition techniques are dominated by traditionally "2-D deposition" techniques such as sputtering, sol-gel, PLD, and MOCVD. 2D deposition processes put limitations on the micro-machining device space, narrowly enabling planar electrode/PZT stacks with out-of-plane actuation. A typical PZT actuator film stack cross-section is drawn in Fig. 1.2, while a cross-section of a micro-machined horizontal actuator is drawn in Fig. 1.3.

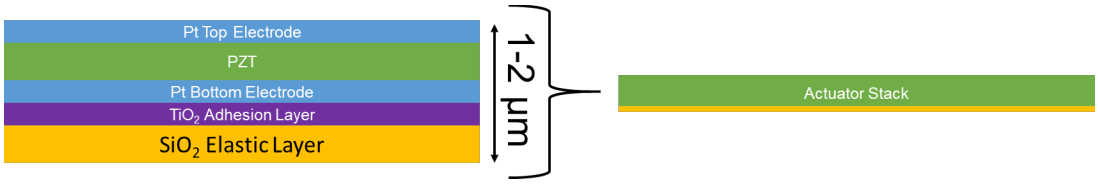

Figure 1.2: Typical MEMS horizontal actuator film stack (cross-section).

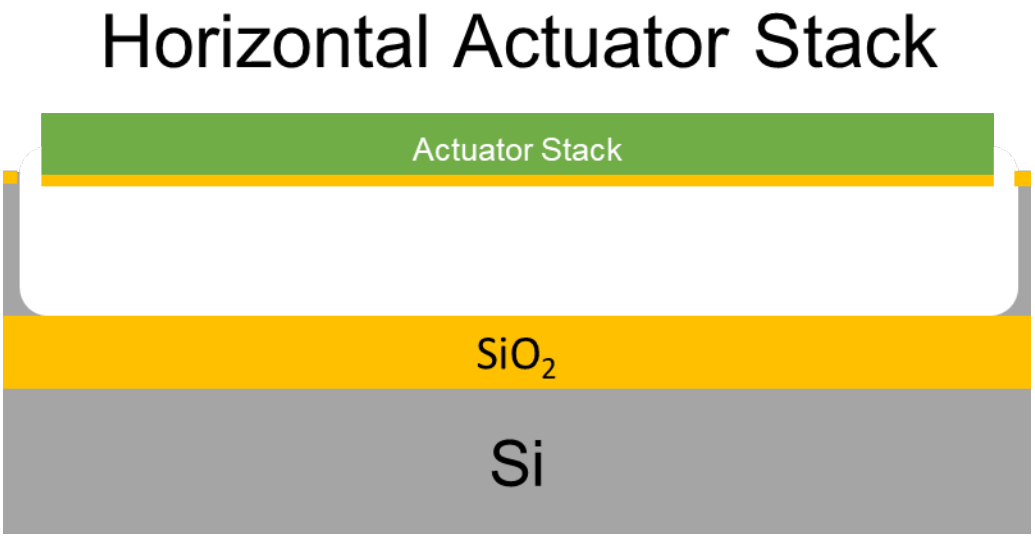

Figure 1.3: Horizontal actuator film stack integrated on a silicon-on-insulator substrate (cross-section).

To date, ALD is the only industry-proven technique to deposit conformal thin films onto devices with extreme aspect ratios and arbitrary topographies. The areal density of devices, and thus the force or displacement per unit area could be greatly increased with vertically stacked, high aspect-ratio actuators utilizing in-plane movement.[11] A drawing illustrating the work-area-improvement of vertical actuators over horizontal actuators is shown below in Fig. 1.4.

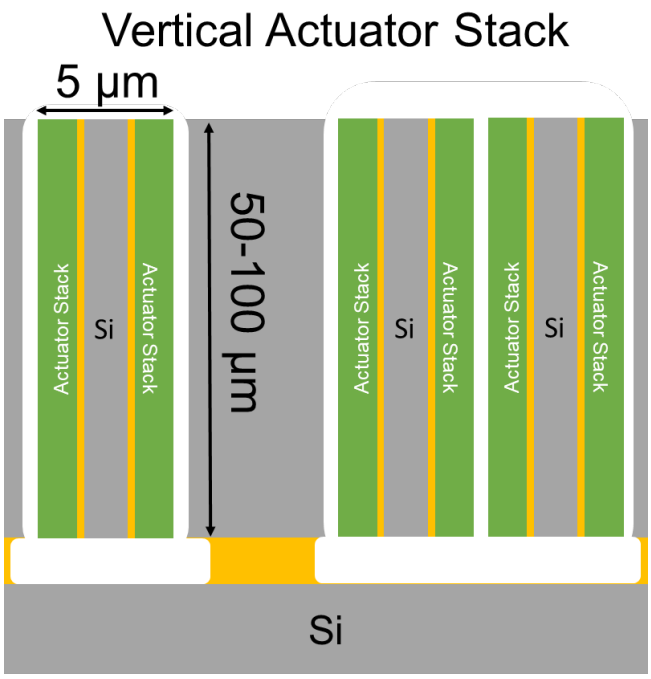

Figure 1.4: Concept vertical MEMS vertical actuator stack with film layers grown by ALD (cross-section).

Equation 1.1, shown below, is a simple equation detailing the work-area improvement of vertical actuators over horizontal actuators as a function of depth and pitch.

$$A_w = \frac{2D}{P} \qquad \text{Equation 1.1}$$

Where A_w is the areal work density ratio relative to horizontal actuators, D is the trench depth, and P is the trench pitch. A 2x increase in the planar work area (A_w=2) can be achieved for trench structures 100 µm-deep, 20 µm-wide, with a 100 µm pitch. An example of such a structure fabricated in this thesis project is shown below in Fig. 1.5 which is coated with as-grown ALD PZT using a new process that is described in Chapter 6. The structure depicted in Fig. 1.5 was micro-machined from a Si-substrate using the Bosch deep-silicon etch process. The insets (each is a different magnification) clearly show that ALD was able to coat deep into the trench including the sidewalls.

The PZT thickness slightly varied as a function of the coating depth. The reasons behind the difference in thickness are explored in detail in Chapter 6. Nonetheless, Fig. 1.5 serves as a demonstration of the capability of ALD PZT to coat high aspect-ratio structures suitable for vertical, 3D-MEMS actuators.

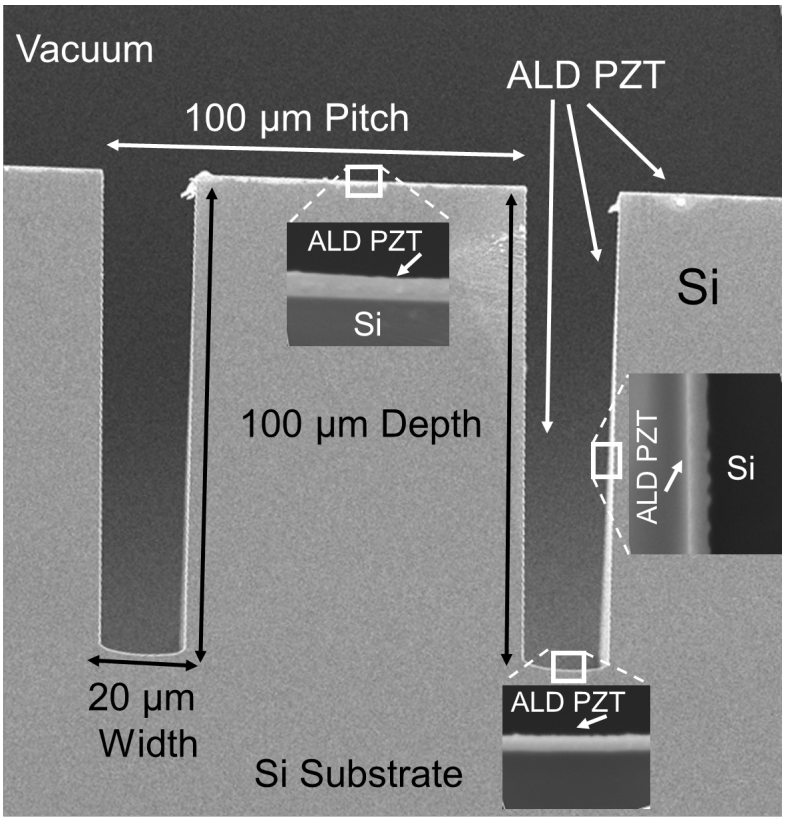

Figure 1.5: SEM image of micro-machined trench structure with 3x increase in areal work density. The insets are zoomed-in sections of the PZT film, and each are at different magnifications.

It will be shown in Chapters 5 and 6 that high-quality electrical properties are obtainable from PTO and PZT grown by ALD. However, it is not yet clear if ALD PZT can yield piezoelectric coefficients equivalent to world-class sol-gel or sputtered PZT. Luckily, possible degradation in the e_{31} piezoelectric coefficient can be overcome by the increased areal work density of vertical actuators. The piezoelectric coefficients are described in detail in Chapter 2, but for quick reference, the displacement of the tip of

a PZT cantilever actuator is proportional to the e_{31} piezoelectric coefficient times the voltage. Figure 1.6 shows the break-even point for vertically actuated ALD PZT with e_{31} ranging from -5 to -20 C/m^2 as a function of depth over pitch. Even ALD PZT with e_{31} of only -5 C/m^2 may generate as much force or displacement at depth/pitch = 2 as a horizontal actuator with an e_{31} of -20 C/m^2 (which is approximately the value obtained for high-quality PZT deposited by other techniques[12]).

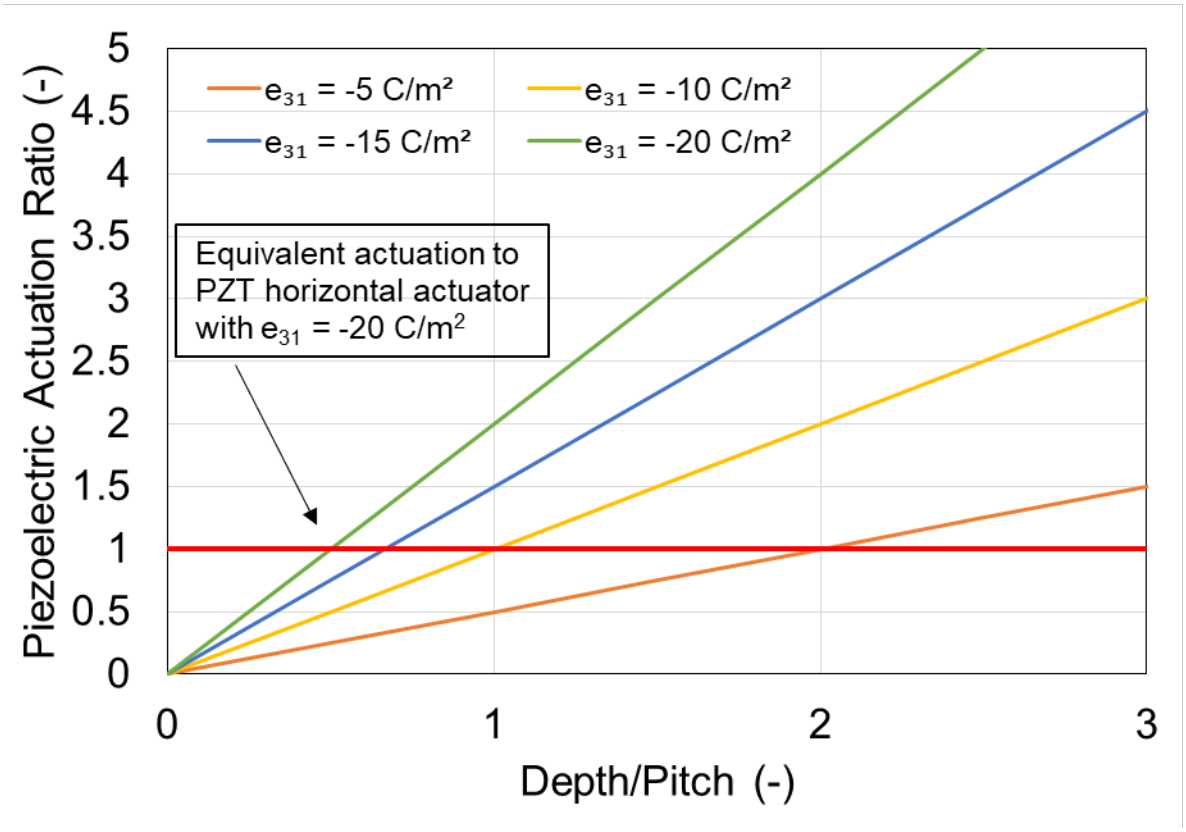

Figure 1.6: Calculated piezoelectric actuation ratio as a function of depth/pitch for theoretical values of the piezoelectric e_{31} coefficient (calculated using Equation 1.1)

Robust ALD processes have already been developed for typical films employed for MEMS actuators, including SiO_2,[13,14] TiO_2,[15,16] and Pt.[17,18] Despite many prior attempts to grow PZT by ALD, to date no process has been demonstrated capable of delivering high aspect-ratio films with electrical properties suitable for PiezoMEMS. In addition,

there are no reports of either PHT or PHO grown by ALD to-date, nor are there reports of PHO thin-films grown by any deposition technique.

The remainder of this thesis is organized as follows. The rest of this chapter is a literature review of all prior attempts to grow PTO, PZO, and PZT by ALD and includes a down-selection of suitable precursors. Chapter 2 contains the details regarding the perovskite structure, the MPB, the phenomenology of piezoelectricity, a brief review of actuation mechanisms for microelectromechanical systems (MEMS), as well as a review of other PZT deposition techniques. Chapter 3 describes the ALD platform and subsystems implemented in the growth of ALD of Pb-based perovskites, and provides an overview of the primary characterization techniques used throughout the results sections (Chapters 5-8) of this thesis. Chapter 4 contains the experimental details regarding the ALD processes and device fabrication. Chapters 5-7 present the growth and characterization of new ALD processes for PTO (Chapter 5), PZT (Chapter 6), PHO (Chapter 7), and PHT (also Chapter 7). Chapter 8 contains a summary of the electrical properties obtained for the various Pb-based perovskites investigated in Chapters 5-7 and compares the results to relevant literature examples. Chapter 8 also contains preliminary results for ALD PZT (grown with a different precursor than the film in Chapter 6), ALD growth models for each of the successfully-deposited films, and presents a list of future work.

Prior Work: ALD $PbTiO_3$, $PbZrO_3$, and $PbZr_xTi_{1-x}O_3$

This section primarily contains a literature review of lead-based perovskites deposited by ALD. It is followed by a brief discussion section and concludes with a summary of

the precursors selected for this work. A binary oxide process is defined here as one complete ALD dose-sequence that forms either PbO_x, TiO_x, or ZrO_x. In each of the reports referenced below regarding ALD lead-based perovskites (such as PTO, PZO, and PZT), the films are grown using sequences of binary oxide processes which form a "super-cycle". The order of, and the relative number of each binary oxide process in the super-cycle determines the cation ratio and growth rate of the deposited film. The growth rate and cation incorporation is rarely a linear function of the binary oxide processes. In the discussion of the following reports, the term "ALD" is used casually and is not intended to imply any judgement regarding the ideality or non-ideality of the relevant growth conditions. A discussion regarding "ideal" ALD growth conditions is reserved for the section labelled "Discussion".

ALD $PbTiO_3$

The first demonstration of PTO grown by ALD was reported by Harjuoja et al. in which tetraphenyl lead ($PbPh_4$) and titanium tetraisopropoxide (TTIP) were used as the lead and titanium cation precursors, respectively.[19] The films were grown on (100) single-crystal Si carried out at a substrate temperature of 250 °C and 300 °C using O_3 as the oxidizer for the $PbPh_4$ and H_2O as the oxidizer for the TTIP. Following a post deposition anneal at temperatures ranging from 600-900 °C with a 10 minute hold in N_2 or O_2 atmospheres, the films crystallized primarily into the perovskite phase which was confirmed by X-ray diffraction (XRD). This study by Harjuoja was innovative as the first demonstration of ALD-grown PTO.[19] However, the films were not grown on a bottom electrode and no electrical measurements were performed. The growth rate of

the process (growth per-cycle, or GPC) was also just 0.25 Å per cycle, which is quite low, and relative number of $PbPh_4$ precursor pulses per TTIP precursor pulse was quite high at 10 $PbPh_4$ pulses per TTIP pulse at 250 °C and 28 $PbPh_4$ pulses per TTIP pulse at 250 °C. In addition, detailed precursor dose uptake curves were not given for the reported ALD PTO process. However the uptake characteristics for the binary PbO ALD process using $PbPh_4$ were discussed elsewhere.[20]

A separate study by Watanabe[21] utilized $Pb(C_{12}H_{21}O_2)_2$ [$Pb(TMOD)_2$] and $Ti(OC_3H_7)_2(C_{11}H_{19}O_2)_2$ [$Ti(O\textit{i}\text{-}Pr)_2(TMHD)_2$] as the lead and titanium cation precursors, respectively. The common name for the TMHD ligand is referenced at least three different ways in the literature reports. It is noted here that "TMHD", "DPM", and "thd" all refer to the same (2,2,6,6,tetramethyl-3,5-deptanedione) β-diketonate ligand and will be henceforth referenced only as "TMHD". The cation precursors were dissolved in ethylcyclohexane (ECH) and dosed into the reactor using a vaporaizer that was held at 200 °C. The titanium precursor $Ti(OC_5H_{11})_2(C_{10}H_{17}O_2)_2$ [$Ti(O\textit{t}\text{-}Am)_2(IBPM)_2$] was also evaluated but was ruled out for subsequent Pb-Ti-O super-cycles because $Ti(O\textit{i}\text{-}Pr)_2(TMHD)_2$ had a higher dose-saturated growth rate and a lower activation energy for chemisorption. The GPC of the mixed Pb-Ti-O supercycle was reported to be 1 Å/cycle at 300 °C with the $Ti(O\textit{i}\text{-}Pr)_2(TMHD)_2$ and $Pb(TMOD)_2$ cation precursors, with H_2O used as the oxidizer. Although both the $Ti(O\textit{i}\text{-}Pr)_2(TMHD)_2$ and $Pb(TMOD)_2$ displayed self-limited growth with respect to precursor dose at 300 °C for the TiO_x and PbO_x binary oxide ALD processes, respectively, the PbO_x growth increased in a linear fashion with respect to $Pb(TMOD)_2$ dose for the combined PbO_x-TiO_x super-cycle. The interpretation was that the process contained a CVD-like growth

component. Although the proper Pb:Ti cation ratio of 1:1 was demonstrated, the films were not annealed and the presence of perovskite $PbTiO_3$ was not demonstrated. No electrical characterization was performed on the Pb-Ti-O films.

Another demonstration of ALD PTO was reported by Hwang et al. in which lead bis(3-N,N-dimethyl-2-methyl-2-propanoxide) [$Pb(DMAMP)_2$] and titanium tert-butoxide [$Ti(O\textit{t}\text{-}Bu)_4$] were used as the lead and titanium cation precursors, respectively, and H_2O was used as the oxidizer for both precursors.[4] The films were grown at substrate temperature of 200 °C on $Ir/IrO_2/SiO_2$ coated Si. The growth rate for stoichiometric PTO grown with a Pb:Ti half cycle ratio of 3:4 was 0.64 Å per cycle. The films crystallized into the perovskite phase with a preferred (001)/(100) orientation following rapid thermal anneal (RTA) at 500-600 °C with a 30 minute hold in an O_2 atmosphere. Hwang presents the first ALD PTO growth on a suitable bottom electrode (Ir coated Si), the first ALD PTO electrical characterization, and the first reported use of $Pb(DMAMP)_2$ a suitable lead precursor.[4] Metal-insulator-metal (MIM) capacitors were fabricated from the ALD PTO samples using Pt as the top electrode. Polarization hysteresis loops were obtained whereby the crystallized PTO films displayed a maximum dielectric constant of 280 with a remnant polarization (P_r) of 11.2 $\mu C/cm^2$. Precursor dose uptake curves were reported, indicating that the precursor did saturate with increasing dose, and that the ALD process window was 190-280 °C. While the reported electrical results are promising, no leakage current measurements were reported, and the plotted polarization/voltage hysteresis loops did not appear to saturate at high fields which may be an indicator of high leakage current. Leakage current is an important extrinsic property of PTO and affects its technological viability.

Watanabe et al. demonstrated an ALD PTO process using $Pb(C_{11}H_{19}O_2)_2$ [$Pb(TMHD)_2$] and $Ti(O\textit{i}\text{-}Pr)_2(TMHD)$ dissolved in ECH as the lead and titanium precursors, respectively, and H_2O was used as the oxidizer.[22] The films were grown at 240 °C on Pt-coated Si substrates and crystallized into randomly oriented perovskite crystallites following a two-step RTA. The first step included RTA at 400 °C with a 30 minute hold in O_2, while the second step included RTA between 500 °C and 600 °C with a 10 minute hold in O_2. Stoichiometric PTO was achieved using a Pb:Ti half cycle ratio of 4:1, though the thickness per cycle wasn't reported. The study by Watanabe represents the first demonstrated coating of a micro machined hole (1.3 μm in diameter and 0.5 μm deep) using an ALD PTO process.[22] The relative Pb:Ti cation ratio varied for different regions of the hole geometry: 54:46 at the top of the step, 55:45 at the top corner, 58:42 at the sidewall, 54:46 at the bottom corner, and 53:47 at the bottom of the hole. The relative thickness difference between the top and bottom of the hole was not directly reported. Although the ALD PTO films were grown on a suitable lower electrode (Pt), electrical characterization was not performed. Finally, growth rate of the PTO did not saturate with increasing $Pb(TMHD)_2$, indicating a CVD-like growth component.

Lee et al. evaluated the growth behavior of ALD PTO films grown using $Pb(DMAMP)_2$ and TTIP as the lead and Ti cation precursors, respectively, and using a combination of H_2O and O_3 as oxidizers.[23] The ALD PTO films were grown on Si and Ru substrates at 200 °C. The purpose of the study was to show that the growth rate of binary PbO_x could be increased by alternating H_2O and O_3 oxidizers, instead of using a single oxidizer. The GPC of the PTO was shown to be the largest when H_2O was used as the

lead oxidizer and O_3 was used as the Ti oxidizer. There is no report of using H_2O and O_3 in the same ALD half-cycle. No attempt was made to crystallize the films, and thus no electrical characterization was performed.

Finally, Sbrockey et al. grew PTO by ALD using tetraethyl-lead [$Pb(Et)_4$] and tetrakis dimethylamino titanium (TDMAT) as the lead and titanium precursors, respectively.[24] $Pb(Et)_4$ was oxidized by O_3, while TDMAT was oxidized by H_2O or O_3. Stoichiometric PTO was grown at a substrate temperature of 250 °C on a Pt coated Si substrate. The films were crystallized following RTA at 600 °C with a one minute hold in O_2. MIM capacitors were fabricated using a Pt top electrode which displayed a P_r of 13.5 $\mu C/cm^2$ and a maximum polarization (P_{max}) above 20 $\mu C/cm^2$ at 800 kV/cm. Trenches 5 µm wide by 20 µm deep were micro machined and coated with ALD PTO, though there was approximately a 30% thickness difference between the thickness of the film outside the trench and the film inside the trench. A 15:1 Pb:Ti half-cycle ratio was required to achieve near stoichiometric PTO. Surprisingly, the growth rate of the PTO films was not reported. The authors claim that the film thickness was independent of precursor dose above a certain threshold, however quantitative evidence wasn't presented. The study by Sbrockey is the first to use $Pb(Et)_4$ as a lead precursor for PTO. However, the reported ferroelectric figures of merit for the annealed ALD PTO are not as good as, nor is the characterization as thorough as, that reported by Hwang.[4] The study by Sbrockey did not include capacitance/voltage measurements, and neither Sbrockey nor Hwang published leakage current measurements. A summary of prior attempts to grow PTO by ALD is presented below in Table 1.1.

Table 1.1: Summary of ALD PTO Growth Conditions, Post-Treatment and Properties

Ref.	Lead Precursor (Oxidizer)	Titanium Precursor (Oxidizer)	Growth Temp.	Anneal	Resulting Structure: Ferroelectric Figures of Merit
Harjuoja[19]	$PbPh_4$ (O_3)	TTIP (H_2O)	250 °C, 300 °C	600-900 °C with a 10 minute hold in N_2 or O_2	Perovskite PTO: N/A
Watanabe[21]	$Pb(TMOD)_2$ (H_2O)	$Ti(O\textit{i}\text{-}Pr)_2(TMHD)_2$ (H_2O)	240 °C, 300 °C	N/A	N/A
Hwang[4]	$Pb(DMAMP)_2$ (H_2O)	$Ti(O\textit{t}\text{-}Bu)_4$ (H_2O)	200 °C	RTA at 500 °C to 600 °C, 30 minute hold in O_2	(001)/(100) Oriented Perovskite PTO on Ir: P_r=11.2 μC/cm^2 P_{max}=40 μC/cm^2 (Approx.) ε_r=280
Watanabe[22]	$Pb(TMHD)_2$ (H_2O)	$Ti(O\textit{i}\text{-}Pr)_2(TMHD)_2$ (H_2O)	240 °C	RTA at 400 °C, 30 minute hold in O_2, then 500 °C – 600 °C, 10 minute hold in O_2	Perovskite PTO: N/A
Lee[23]	$Pb(DMAMP)_2$ (H_2O or O_3)	TTIP (H_2O or O_3)	200 °C	N/A	Near-Stoichiometric amorphous PTO: N/A
Sbrockey[24]	$Pb(Et)_4$ (O_3)	TDMAT (H_2O or O_3)	250 °C	RTA at 600 °C, one minute hold in O_2	Perovskite PTO: P_r= 13.5 μC/cm^2 P_{max}= 20 μC/cm^2 at 800 kV/cm

ALD $PbZrO_3$

PZO deposited by ALD has been reported by Harjuoja et al. using $PbPh_4$ and zirconium 2,2,6,6-tetramethyl-3,5-hepatadionato [$Zr(TMHD)_4$] as the lead and zirconium precursors, respectively, with ozone used as the oxidizer for both cation precursors.[25] The growths were performed at 275 °C and 300 °C, and near stoichiometric ALD PZO

films that were grown on single crystal $SrTiO_3$ (100) substrates crystallized into the perovskite phase following annealing at 600 °C with a 10 minute hold in O_2. A Pb:Zr half cycle ratio of 7:2 yielded stoichiometric PZO at 275 °C and a growth rate of 0.12 Å per cycle. The study by Harjuoja is the first and only reported growth of PZO by ALD, however the films weren't grown on a suitable lower electrode, and the films weren't electrically characterized.[25] While the reported film growth was quite linear as a function of the number of deposited cycles, precursor uptake curves to quantitatively test whether the growth rate saturates with increasing dose were not reported. The growth conditions for the PZO grown by Harjuoja are summarized below in Table 1.2.

Table 1.2: Summary of ALD PZO Growth Conditions, Post-Treatment and Properties

Ref.	Lead Precursor (Oxidizer)	Titanium Precursor (Oxidizer)	Zirconium Precursor (Oxidizer)	Growth Temp.	Anneal	Resulting Structure: Ferroelectric Figures of Merit
Harjuoja[25]	$PbPh_4$ (O_3)	N/A	$Zr(TMHD)_4$ (O_3)	275 °C, 300 °C	600 °C with a 10 minute hold in O_2	Perovskite PZO: N/A

ALD $PbZr_xTi_{1-x}O_3$

PZT deposited by ALD was reported by Watanabe et al. using $Pb(TMHD)_2$, $Ti(Oi\text{-}Pr)_2(TMHD)_2$ or TTIP, and tetrakis(dipivaloylmethanato) zirconium [$Zr(TMHD)_4$] as the lead, titanium, and zirconium cation precursors, respectively.[26] H_2O was used to oxidize each of the cation precursors and the substrate was held at 240 °C for the ALD growths. The first combination of precursors investigated was $Pb(TMHD)_2$, Ti(O*i*-

$Pr)_2(TMHD)_2$, and $Zr(TMHD)_4$. Although the reported molar cation ratios suggest that Pb-excess PZT was deposited, neither the growth rate of the Pb half cycle nor the Ti half cycle saturated with increased precursor dose, indicating a CVD-like component to the growth. The second combination of precursors investigated was $Pb(TMHD)_2$, TTIP, and $Zr(TMHD)_4$. The substitution of TTIP for $Ti(Oi\text{-}Pr)_2(TMHD)_2$ led to saturation of the lead and zirconium precursors, but the growth rate of the titanium half cycle did not saturate with increasing TTIP dose, again indicating CVD-like growth behavior. Additionally, the zirconium content could not be increased above x=0.2 for $PbZr_xTi_{1-x}O_3$ (which is well short of the MPB with x=0.52). Despite the complex interrelationship between precursor dose and half-cycle growth rate, perovskite PZT was obtained after a two-step anneal consisting of a 400 °C RTA with 30 minute hold, followed by a 700 °C RTA with a 10 minute hold in O_2 when the PZT was grown on a Pt coated Si substrate. ALD PZT was uniformly deposited on hole structures 200 nm wide and 300 nm deep. Ferroelectric polarization-voltage curves were not reported, however, piezoelectric force microscopy (PFM) showed clear evidence of piezoelectricity in the annealed samples.

In a related study, Watanabe again reported ALD PZT using $Pb(TMHD)_2$ and TTIP as the lead titanium and cation precursors but with tetrakis(diisobutyrylmethanato) zirconium [$Zr(DIBM)_4$] substituted for $Zr(TMHD)_4$ as the zirconium precursor.[27] H_2O was again used as the oxidant for all cation precursors, and the substrate temperature was held at 240 °C for all depositions. Although the zirconium precursor substitution enabled PZT compositions near the MPB, neither the growth rate of the lead nor the titanium half-cycles saturated with increasing dose, again implying a CVD-like growth

component. PZT films grown at compositions near the MPB on a platinum bottom electrode and annealed using the same two-step RTA process used in the previous study,[26] crystallized into randomly oriented perovskite grains. MIM capacitors were fabricated using 70 nm thick PZT and circular top platinum electrodes for polarization-voltage measurements which showed $2P_r$ = 24 μC/cm^2, $2E_c$=20 kV/cm, and P_{max}= (approximately) 50 μC/cm^2. Neither electrical leakage current nor capacitance-voltage measurements were reported. STEM cross-section images indicated that the films did not form a homogeneous amorphous film. In contrast, PbO segregated into crystallized nuclei embedded within an amorphous Ti-Zr matrix. ALD PZT was grown on Ir-coated micro machined holes, approximately 250 nm wide and 300 nm deep. STEM cross-sectional images were presented of the annealed PZT deposited on the hole structure, and showed that delamination occurred at the bottom of the hole, and that the film contained nanometer-sized pores.

Zhang et al. deposited PZT by ALD using $Pb(TMHD)_2$, $Ti(O\textit{i}\text{-}Pr)_2(TMHD)_2$, and zirconium tetrachloride [$ZrCl_4$] as the lead, titanium, and zirconium cation precursors, respectively.[28] The substrate temperature was held at 250 °C, and H_2O was used as the oxidant for all cation precursors. Perovskite PZT was shown to have crystallized with no preferred orientation following a 950 °C anneal in N_2 with a 3 minute hold when grown on Al_2O_3-coated 4H-SiC substrates. The cation composition was estimated to be $PbZr_{0.44}Ti_{0.56}O_3$ based on the XRD peak index, though the stoichiometry was not directly measured. The precursor-dose saturation characteristics weren't reported, nor was the film cation composition quantified. Polarization-voltage hysteresis loops were reported for metal-oxide-semiconductor (MOS) capacitors where P_r was reported to be

4.3 $\mu C/cm^2$ and P_{max} was 8.5 $\mu C/cm^2$ for PZT films 14 nm thick. Although the ferroelectric figures of merit are not as large as those previously reported by Watanabe,[27] the films were far thinner (14 nm compared to 70 nm), and the applied voltage was divided between the 14 nm PZT, 10 nm Al_2O_3, and 4H-SiC depletion layer. Therefore, equivalent figures of merit were not expected, given the limitations of the device structure. Electrical leakage currents were reported to be 4.6 x 10^{-7} A/cm^2 at 0.1 MV/cm and 5.5 x 10^{-6} A/cm^2 at 8 MV/cm. PFM measurements showed clear evidence of piezoresponse and retention.

Choi et al.[29] utilized an ALD PZT process similar to Zhang[28] but substituted $Zr(TMHD)_4$ for $ZrCl_4$, which is the same combination of precursors used by Watanabe.[26] The ALD PZT was grown at a substrate temperature of 250 °C on Si(100) or Al_2O_3 coated 4H-SiC. PZT grown on either Si(100) or 4H-SiC crystallized into the perovskite phase after a 600 °C anneal in a PbO atmosphere (evaporated from a crucible). MOS capacitors were fabricated in similar manner to Zhang[28] for films with a thickness of 15 nm. The new PZT film displayed similar ferroelectric figures of merit, with P_r=1.1 $\mu C/cm^2$, P_{max}=8.5$\mu C/cm^2$, and E_c=0.32 MV/cm, but leakage current measurements weren't reported. Similar to the Zhang study, PFM showed that the films had a switchable piezoelectric response. Detailed in-situ FTIR measurements were used to quantify the number of incubation cycles required to nucleate oxide growth for each component of the PZT supercycle. Precursor dose uptake curves were not reported, though the authors note that thermal decomposition of the precursors was not observed, evidenced by the presence of the C-$C(CH_3)_3$ vibration mode at 750, 870, and

1100 cm^{-1} for each cation precursor, and the CH_3 vibration mode at 1025 cm^{-1} for Ti(Oi-Pr)$_2$(TMHD)$_2$.

Finally, Sbrockey et al. attempted to grow ALD PZT using Pb(Et)$_4$, TDMAT and tetrakis ethylmethylamino zirconium [TEMAZ] as the lead, titanium, and zirconium precursors, respectively with O_3 or H_2O used as the oxidizers.[24] Although Pb(Et)$_4$ and TDMAT were shown to yield perovskite PTO with ferroelectric properties as reported earlier in this chapter, the introduction of TEMAZ as the zirconium cation source dramatically suppressed the lead incorporation. The composition of ALD PZT grown with varying Pb:Zr:Ti half-cycle ratios was shown to be between 33% and 54% lead deficient. Nonetheless, lead deficient ALD PZT with the composition $Pb_{0.78}Zr_{0.40}Ti_{0.60}O_3$ was grown on micro machined trenches 5 μm wide by 20 μm deep. The ALD PZT thickness on the top surface was approximately 40% thicker than the film grown on the sidewall and bottom of the trench. Precursor dose uptake curves were not presented for the ALD PZT, but the authors note that the film thickness was invariant with dose for planar samples. Since the PZT was significantly lead deficient, it did not crystallize into the perovskite phase upon annealing. Thus, no electrical measurements were performed. Table 1.3 shown below summarizes the process conditions and figures of merit for each of the previous attempts to grow PZT by ALD.

Table 1.3: Summary of ALD PZT Growth Conditions, Post-Treatment and Properties

Ref.	Lead Precursor (Oxidizer)	Titanium Precursor (Oxidizer)	Zirconium Precursor (Oxidizer)	Growth Temp.	Anneal	Resulting Structure: Ferroelectric Figures of Merit
Watanabe[26]	$Pb(TMHD)_2$ (H_2O)	$Ti(Oi\text{-}Pr)_2(TMHD)_2$ (H_2O) Or TTIP (H_2O)	$Zr(TMHD)_4$ (H_2O)	240 °C	RTA at 400 °C, 30 minute hold in O_2, then 700 °C, 10 minute hold in O_2	Perovskite $PbZr_{0.2}Ti_{0.8}O_3$ (max Zr cation %): N/A
Watanabe[27]	$Pb(TMHD)_2$ (H_2O)	TTIP (H_2O)	$Zr(DIBM)_4$ (H_2O)	240 °C	RTA at 400 °C, 30 minute hold in O_2, then 700 °C, 10 minute hold in O_2	Perovskite PZT near the MPB: $2P_r$ = 24 μC/cm^2, $2E_c$=20 kV/cm, P_{max}=50 μC/cm^2 (Approx.)
Zhang[28]	$Pb(TMHD)_2$ (H_2O)	$Ti(Oi\text{-}Pr)_2(TMHD)_2$ (H_2O)	$ZrCl_4$ (H_2O)	250 °C	950 °C in N_2, 3 minute hold	Perovskite PZT with unknown composition: P_r = 4.3 μC/cm^2, P_{max} = 8.5 μC/cm^2
Choi[29]	$Pb(TMHD)_2$ (H_2O)	$Ti(Oi\text{-}Pr)_2(TMHD)_2$ (H_2O)	$Zr(TMHD)_4$ (H_2O)	250 °C	600 °C anneal under PbO ambient	Perovskite PZT near the MPB: P_r=1.1 μC/cm^2, P_{max}=8.5μC/cm^2, E_c=0.32 MV/cm
Sbrockey[24]	$Pb(Et)_4$ (O_3)	TDMAT (H_2O or O_3)	TEMAZ (H_2O or O_3)	250 °C	N/A	Pb Deficient amorphous $Pb_{0.78}Zr_{0.40}Ti_{0.60}O_3$: N/A

Discussion

ALD Process Evaluation

Most of the works cited in the above literature review of ALD PTO, PZO, and PZT either did not contain detailed precursor dose uptake-curves or contained detailed

uptake-curves which indicated a CVD-like component to the growth. It is important to clarify what is meant when a process is described as "ALD" and what growth conditions are expected in reality. An ideal ALD process consists of layer-by-layer growth of a target material that is achieved by alternating pulses of precursors that display self-limited chemisorption. For an ideal ALD process, the film growth rate is completely independent of the overall dose (total precursor volume) and dose time (Langmuir exposure) within a certain temperature window, referred to as the "ALD Window". Experimentally, even a theoretically ideal ALD process is strongly influenced by conditions such as the starting substrate surface, precursor purge times, pumping speed, purge gas chemistry and purity, chamber material and design, selection and number of vacuum seals, and precursor impurities. Therefore, the ideal ALD process will deviate from ideality if precise control is not exerted over the aforementioned variables. From a practical standpoint, it is not possible to control all of the aforementioned variables simultaneously to the ideal level of precision. Therefore, it is better to think of ALD-like processes as a spectrum spanning ideal ALD and pulsed-CVD (p-CVD). For ALD, the film thickness is determined only by the number of cycles. For p-CVD, the film thickness is a function of the precursor dose. Three subcategories of p-CVD may be defined as follows: dose-limited p-CVD, decomposition-limited p-CVD, and parasitic p-CVD. For dose-limited p-CVD, thermal decomposition of precursors occurs instantly at the surface and the growth rate is limited only by the dose volume. For decomposition-limited p-CVD, thermal decomposition occurs slowly and the growth rate is a function of dose time. For parasitic p-CVD, inadequate purge time leads to some percentage of growth rate

(thickness per unit time) to be a result of coexistence of two or more precursors in the reaction chamber simultaneously, and the growth rate is a function of the concentration of the rate-limiting species.

For devices that demand high aspect ratio ALD coatings, dose limited p-CVD is not acceptable because uniform deposition would require a uniform precursor exposure on all surfaces at all times, which is impractical if not impossible. Thermal decomposition also often leads to impurities in the as-grown film which are undesirable. Decomposition-limited p-CVD and parasitic p-CVD may be acceptable depending on the severity of the problem and the demands of the end device. For a given ALD film grown under a specified set of parameters, the relevant question to ask is what percentage of the film growth results from ALD-like processes versus the percentage resulting from CVD-like processes. For the case of decomposition-limited p-CVD, if the decomposition is slow or doesn't lead to additional chemisorption (i.e. the process remains self-limited), only a small percentage of the film would be attributed to p-CVD and would likely satisfy demanding device requirements. For parasitic p-CVD, if the amount of residual precursor is also small, only a small increase in the film growth would result. Asking whether or not a process could be considered ideal ALD, ideal ALD with a p-CVD component, or pure p-CVD is important from an academic standpoint, but generally less relevant from an engineering standpoint. When engineering real devices, what matters is whether or not the specified process deposits a film with adequate properties to achieve the desired performance metrics at a practical and affordable cost.

ALD Precursor Selection

The preceding literature review revealed that there are far more reports of ALD PTO and PZT, compared to just one for ALD PZO. In the single report of ALD PZO, no electrical properties were reported. The general approach presented here towards ALD PZT is to first develop an ALD PTO process, and then substitute a suitable zirconium precursor in place of the titanium precursor in varying ratios. The choice of lead precursor presents the largest challenge because there are far fewer commercially available lead precursors than there are titanium and zirconium precursors. Lead oxide is a complicated materials system in part because there are many stable phases between PbO and PbO_2 with varying cation oxidation states. Therefore, the lead precursor should be selected first, followed by a selection of compatible titanium and zirconium precursors. The following subsections present an overview of selected precursors, but are not meant to be comprehensive. Instead, only the most relevant precursors are presented for evaluation.

Selection of the Lead Precursor

The reports summarized in the literature review of ALD PTO, PZO, and PZT point to four lead precursors that were successfully used to grow a lead-based perovskite. Those precursors include: $PbPh_4$, $Pb(DMAMP)_2$, $Pb(TMHD)_2$, and $Pb(Et)_4$. Of those four, precursor dose uptake-curves were only reported for two: $Pb(DMAMP)_2$ and $Pb(TMHD)_2$.

For $Pb(DMAMP)_2$, the ALD window for binary PbO_x was reported to be between 200 °C and 280 °C.[4] Uptake curves were provided for $Pb(DMAMP)_2$ binary PbO_x process

that showed saturating growth behavior. Surprisingly, the specific temperature of the substrate during the uptake curve measurements wasn't reported, but it can be assumed to be 200 °C because that was the temperature used for subsequent ALD PTO growth. No uptake curves were provided for the mixed oxides, for example $Pb(DMAMP)_2$ on a TiO_x surface, or $Ti(O\textit{t}\text{-}Bu)_4$ on a PbO_x surface, so the chemisorption kinetics of the PTO process itself is currently unreported. Nonetheless, the ferroelectric properties of the resulting PTO films were quite encouraging, indicating that $Pb(DMAMP)_2$ is a viable choice for the lead precursor.

Precursor-dose uptake curves were also provided for $Pb(TMHD)_2$, but the growth rate did not saturate in combination with $Ti(Oi\text{-}Pr)_2(TMHD)_2$ and $Zr(TMHD)_4$.[26] A conflicting report by Choi presents in-situ FTIR evidence (but no uptake curves) that suggests the $Pb(TMHD)_2$ precursor is stable at a deposition temperature of 250 °C in combination with the same $Ti(O\textit{i}\text{-}Pr)_2(TMHD)_2$ and $Zr(TMHD)_4$ precursoors.[29] Simply stated, the results of Watanabe[26] and Choi[29] are in direct conflict. Since the precursor dose characterization of Watanabe appears to be more comprehensive, $Pb(TMHD)_2$ is tentatively ruled out due to CVD-like behavior, although the conflict needs to be resolved to avoid future confusion.

Both $PbPh_4$ and $Pb(Et)_4$ required an excessive number of sequential PbO cycles to yield stoichiometric PTO (12-28 cycles for $PbPh_4$,[19] 15 cycles for $Pb(Et)_4$[24]). Precursor dose uptake curves were not provided for either precursor for the mixed oxide processes, so no judgement can be made as to whether either precursor is ideal. No electrical characterization was attempted on ALD PTO or PZO films grown using $PbPh_4$, and the ferroelectric properties obtained using $Pb(Et)_4$ were lower than those reported using

$Pb(TMHD)_2$ or $Pb(DMAMP)_2$. Finally, stoichiometric PZT was not obtained from either $PbPh_4$ or $Pb(Et)_4$. Therefore, these precursors are ruled out for ALD PZT.

For the ALD PZT presented in this work, $Pb(DMAMP)_2$ was selected as the lead precursor due to the availability of published dose uptake curves and due to the quality ferroelectric figures of merit reported for PTO. $Pb(TMHD)_2$ may be considered as a viable alternative only if the conflicting literature can be resolved.

Selection of the Titanium Precursor

Given $Pb(DMAMP)_2$ as the selected lead precursor, a compatible titanium precursor must also be selected. It is difficult to predict the complex growth mode that occurs when mixing two binary oxides together to form a ternary oxide. It cannot be assumed that the ternary oxide process for PZT will behave as ideal ALD even if a temperature is selected that falls within the ALD window of each binary oxide. Nonetheless, selecting a titanium precursor with an overlapping ALD window is a good place to start. It is not necessary to limit the selection of the titanium precursor to those previously investigated, but they should be considered in context.

$Pb(DMAMP)_2$ has not been used to grow PZT, but has been used to grow PTO. Of the two reports of ALD PTO using $Pb(DMAMP)_2$, Hwang[4] and Lee[23] reportedly used $Ti(O\textit{t}\text{-}Bu)_4$ and TTIP as titanium cation precursors, respectively. Hwang reported the ALD window of the $Pb(DMAMP)_2$ has been reported to be 200 °C – 280 °C.[4] CVD-like growth is reported to occur above 200 °C for $Ti(O\textit{t}\text{-}Bu)_4$ and TTIP.[4,30] Therefore, 200 °C was used by Hwang and Lee, since it is the only temperature that overlaps both

the lead and titanium precursors' ALD growth regime. Having a narrow-range compatible temperatures leaves a slim margin-of-error and is not ideal, since higher temperatures typically lead to faster precursor saturation. Additionally, an ALD window of just a single temperature for PTO strictly limits the number of permissible zirconium precursors to those that can be grown at low (200 °C) temperatures. While Ti(O*t*-Bu)$_4$ and TTIP should be considered viable titanium precursors, a better candidate likely exists that is highly reactive and more thermally stable.

TDMAT is an alkylamide precursor with a reported ALD window of 50 – 260 °C,[31] which provides a wide overlap with the ALD window of Pb(DMAMP)$_2$. TDMAT has also been reported to have good ozone sensitivity, a high deposition rate, and little decomposition inside a heated ampoule.[32] TDMAT has already been used to grow ALD PTO with Pb(Et)$_4$ at 250 °C.[24] Therefore, TDMAT is a viable titanium precursor for ALD PZT.

Ti(O*i*-Pr)$_2$(TMHD)$_2$ was used to grow ALD PZT with Pb(TMHD)$_2$ used as the lead precursor. However, at a substrate temperature of 240 °C, the growth per cycle did not saturate with increasing Ti(O*i*-Pr)$_2$(TMHD)$_2$ dose.[26] It is possible that the non-saturation occurred only for the mixed PZT oxide, and it is also possible that substitution of a different lead precursor would mitigate the problem. However, since the isopropoxide ligand is known to show CVD-like behavior above 200 °C,[4,30] it is not clear whether Ti(O*i*-Pr)$_2$(TMHD)$_2$ is a viable titanium precursor. Choi reported saturating growth behavior of the Ti(O*i*-Pr)$_2$(TMHD)$_2$ precursor and a GPC of 2.8 Å/cycle, which is 10x larger than the GPC reported by Watanabe.[21] This is the second direct conflict between the Choi paper[29] and other literature, though the conflict arises

with the same first author (Watanabe refs [21] and [26]). Since the literature regarding the $Ti(O\textit{i}\text{-}Pr)_2(TMHD)_2$ precursor is apparently controversial and the saturation behavior was questionable to begin-with, it was removed from consideration.

Several other titanium precursor chemistries were considered. Halides were ruled out due to concerns over fluorine or chlorine residual contamination. The commercial precursor Star-Ti™ was initially tested up to a 250 °C substrate temperature but required impractically large doses for the style of reactor used in the current study. Star-Ti™ is probably a viable alternative to TDMAT, but TDMAT is preferred due to its having a higher reactivity, provided the substrate temperature is kept low enough to prevent thermal decomposition.

TDMAT is the first choice for titanium precursor to be paired with $Pb(DMAMP)_2$ as the lead precursor. Star-Ti™ is a viable alternative if ALD PTO and PZT cannot be achieved with TDMAT. Many other titanium chemistries exist that may be compatible with the $Pb(DMAMP)_2$, and those chemistries may be considered if both of the precursors selected here fail to produce ALD PZT.

Selection of the Zirconium Precursor

Four zirconium precursors have been previously used to grow ALD PZO or PZT, including: $Zr(TMHD)_4$, TEMAZ, and $Zr(DIBM)_4$, and $ZrCl_4$. The zirconium precursor should have a portion of its ALD temperature window overlap with both $Pb(DMAMP)_2$ and TDMAT. For the maximum possible process flexibility, it is ideal if the overlap is as wide as possible. $ZrCl_4$ was immediately ruled out for this study due to concerns over chlorine contamination, though it has been previously used to grow ALD PZT by Zhang.[28]

$Zr(TMHD)_4$ was used by Harjuoja[25] as the zirconium precursor to grow PZO with $PbPh_4$ as the lead precursor at 275 °C-300 °C and by Choi[29] to grow PZT with $Pb(TMHD)_2$ and $Ti(O\textit{i}\text{-}Pr)_2(TMHD)_2$ as the lead and titanium precursors, respectively, at 250 °C. Although precursor dose uptake curves were not reported in either study, $Zr(TMHD)_4$ may be considered a viable zirconium precursor for ALD PZT. There are a few notable drawbacks to using $Zr(TMHD)_4$. First, the temperature required for vaporization was reported to be 190 °C by Choi,[29] but Harjuoja reported it to be 130 °C.[25] 130 °C is a reasonable ALD ampoule temperature typical of many well-known processes. 190 °C is problematic because it is beyond the upper temperature limit of most standard ALD valves. The discrepancy between the two studies is likely due to either source or chamber design. Second, the ALD window (reported as the atomic layer epitaxy window, but with the same meaning) was reported by Putkonen et al. to be 375 °C-400 °C,[33] which is much lower than the substrate temperatures of the previous reports. $Zr(TMHD)_4$ was used by Watanabe as the zirconium precursor with $Pb(TMHD)_2$ as the lead precursor and $Ti(O\textit{i}\text{-}Pr)_2(TMHD)_2$ or TTIP as the titanium precursor at 240 °C substrate temperature.[26] The ALD PZT process using TTIP, $Zr(TMHD)_4$, and $Pb(TMHD)_2$ could not achieve compositions near the MPB because the zirconium content could not be increased above x=0.2 for $PbZr_xTi_{1-x}O_3$. It was later reported that the inability to incorporate zirconium was due to the low vaporization rate of $Zr(TMHD)_4$, and not due to fundamental chemical kinetic factors.[34] Nonetheless, given the conflicting information, $Zr(TMHD)_4$ was ruled out for the present study in favor of better alternatives.

$Zr(DIBM)_4$ was used to grow near MPB PZT with $Pb(DPM)_2$ as the lead precursor and TTIP as the titanium precursor at 240 °C.[27] However, for substitution of $Zr(DIBM)_4$ in place of $Zr(TMHD)_4$, the growth rate of the lead and titanium half-cycles did not saturate with increasing dose. It is unclear whether $Zr(DIBM)_4$ would have a similar effect if combined with $Pb(DMAMP)_2$ and TDMAT. In addition, the $Zr(DIBM)_4$ was vaporized at 200 °C which is not an ideal temperature for the current reactor configuration. Therefore, $Zr(DIBM)_4$ was ruled out for the current study.

TEMAZ was used together with $Pb(Et)_4$ and TDMAT at 250 °C, but unfortunately the introduction of TEMAZ caused a drastic reduction in the lead incorporation, and thus "stoichiometric" PZT was not achieved.[24] The maximum ALD temperature for TEMAZ is reported to be 300 °C, with the lower limit below 200 °C.[35] A similar alkylamide, tetrakis dimethylamino zirconium (TDMAZ), has a reported maximum temperature limit of 250 °C and a lower limit below 200 °C.[33] Thus, the ALD windows of both TEMAZ and TDMAZ widely overlap the ALD windows of TDMAT and $Pb(DMAMP)_2$. TEMAZ would be slightly preferred to TDMAZ, having a slightly wider ALD temperature window overlap and being liquid at room temperature (compared to TDMAZ which is a solid), except that it has been proven to suppress Pb incorporation when used with $Pb(Et)_4$, as previously mentioned. It is unclear if the TEMAZ would cause the same effect with $Pb(DMAMP)_2$ substituted as the lead precursor, so TEMAZ is still considered a viable zirconium precursor for PZT. The use of TDMAZ as the zirconium precursor hasn't been reported for Pb-based ferroelectrics, but it is still considered viable for ALD PZT within the stated temperature range.

Zirconium tert-butoxide [Zr(O*t*-Bu)$_4$] is a common ALD precursor used to grow ZrO_2 when oxidized by H_2O, N_2O or O_2.[35] Zr(O*t*-Bu)$_4$ is liquid at room temperature and has an ALD window of 150 °C to 250 °C.[36] Thus, Zr(O*t*-Bu)$_4$ widely overlaps the ALD window of both TDMAT and Pb(DMAMP)$_2$. Although it is an untested chemistry for incorporation into lead-based perovskites, Zr(OtBu)$_4$ is a viable precursor for evaluation in the present study.

In summary, of the previously reviewed zirconium precursors, three are viable options. The viable zirconium precursors are: TDMAZ, TEMAZ, and Zr(O*t*-Bu)$_4$. Neither TDMAZ nor Zr(O*t*-Bu)$_4$ have been tested for incorporation into lead-based perovskites and should be investigated thoroughly. TEMAZ is less preferred since it has previously suppressed lead incorporation, but may be used as a backup if neither TDMAZ nor Zr(O*t*-Bu)$_4$ provide stoichiometric PZT near the MPB. Thus, two sets of cation precursors warrant further investigation: Pb(DMAMP)$_2$, TDMAT, and TDMAZ, along with Pb(DMAMP)$_2$, TDMAT, and Zr(O*t*-Bu)$_4$.

Desired Substrate Temperature

The substrate temperature must be kept in a region that overlaps the ALD window of all three selected cation precursors. Conveniently, the overlap occurs between 200 °C-250 °C for both sets of precursors considered here. Since hotter temperatures increase the reactivity of the precursors and decrease the required purge time, 250 °C is a reasonable starting temperature, and matches the growth temperature of several other attempts at ALD PZT. If thermal decomposition occurs, the temperature may be lowered to 200 °C.

Motivation for Additional Research Towards ALD PZT

It is clear that any ALD process should be optimized around the necessary properties of the film, with the final device architecture in mind. The goal of the present work is to develop ALD PZT for suitable 3D MEMS. Of the previous reports of ALD PTO, PZO, and PZT summarized in this chapter, only three (Harjuoja,[25] Choi,[29] and Sbrockey[24]) mention MEMS as a secondary motivation, with FRAM serving as the typical primary motivation. As mentioned in Chapter 1, the typical minimum thickness for PZT in MEMS layers is 250 nm, however, no electrical characterization has been reported for either ALD PTO, PZO, or PZT thicker than 78 nm.[4] PFM measurements have been previously performed on ALD PZT films to indicate the presence of piezoelectricity,[29] but that is not an accepted method for determining the viability of piezoelectric films for MEMS. To evaluate ALD PZT films for the purpose of MEMS, the piezoelectric coefficients should be measured on released devices, and those measurements are lacking in the current literature. Prior attempts to grow PZT by ALD have not yet yielded an ideal process with robust ferroelectric or piezoelectric characterization. Therefore, there is a clear need for further process development towards ALD PZT for MEMS.

Summary

Two sets of precursors have been identified for evaluation, each using $Pb(DMAMP)_2$ as the lead precursor and TDMAT as the titanium precursor. The zirconium precursor was selected to be either TDMAZ or $Zr(O\textit{t}\text{-}Bu)_4$. The initial substrate temperature was chosen to be 250 °C, which is at the top end of the overlapping temperature windows of the sets of precursors. H_2O and O_3/O_2 are available as oxidizers and will be

evaluated. O_2 plasma is also available but will not be evaluated because it is not suitable for coating of high aspect ratio structures.

References

[1] Ott AW, Klaus JW, Johnson JM, George SM. Al3O3 thin film growth on Si(100) using binary reaction sequence chemistry. *Thin Solid Films.* 1997;292:135-144.
[2] Elam JW, Routkevitch D, Mardilovich P, George SM. Conformal Coating of Ultrahigh-Aspect-Ratio Nanopores of Anodic Alumina by Atomic Layer Deposition. *Chem Mater.* 2003;15:3507:3517.
[3] Jaffe B, Roth RS, Marzullo S. Piezoelectric Properties of Lead Zirconate- Lead Titanate Solid Solution Ceramics. *J Appl Phys.* 1954;25:809-810.
[4] Hwang GW, Lee HJ, Lee K, et al. Atomic Layer Deposition and Electrical Properties of $PbTiO_3$ Thin Films Using Metallorganic Precursors and H_20. *J Electrochem Soc.* 2007;154:G69-G76.
[5] Tan X, Ma C, Frederick J, et al. The Antiferroelectric – Ferroelectric Phase Transition in Lead-Containing and Lead-Free Perovskite Ceramics. *J Am Ceram Soc.* 2011;94:4091-4107.
[6] Wei J, Yang T, Want H. Excellent Energy Storage and Charge-discharge Performances in PbHfO3 Antiferroelecctric Ceramics. J Eur Ceram Soc. 2019;39:624-630.
[7] Nguyem MD, Rijnders G, Electric field-induced phase transition and energy storage performance of highly-textured PbZrO3 antiferroelectric films with a depositions temperature dependence. *J Eur Ceram Soc.* 2018;38:4953-4961.

[8] Noheda B, Cox DE, Shirane G, et al. A monoclinic ferroelectric phase in the $Pb(Zr_{1-x}Ti_x)O_3$ solid solution. *Appl Phys Lett.* 1999;74:2059-2061.
[9] Frantti J, Fujioka Y, Eriksson S, et al. Neutron Powder Diffraction Study of $Pb(Hf_xTi_{1-x})O_3$ Ceramics ($0.10 \leq x \leq 0.50$). *Inorg Chem.* 2005;44:9267-9278.
[10] Jaffe B, Roth SR, Marzullo S, Properties of Piezoelectric Ceramics in the Solid-Solution Series Lead Titanate-Lead Zirconate-Lead Oxide: Tin Oxide and Lead Titanate-Lead Hafnate. *J Res Natl Bur Stand.* 1955; 55:239-254.
[11] Pulskamp JS, Polcawich RG.Three dimensional piezoelectric MEMS, US8966993 B2. 2012
[12] Oldham KR, Pulskamp JS, Polcawich RG, et al. Thin-Film PZT Actuators With Extended Stroke. *J Microelectromech S.* 2008;17:890-899.
[13] Gasser W, Uchida Y, Matsumura M. Quasi-monolayer deposition of silicon dioxide. *Thin Solid Films.* 1994;250:213-218.
[14] Lee J-H, Kim U-J, Han C-H, et al. Investigation of Silicon Oxide Thin Films Prepared by Atomic Layer Deposition Using SiH_2Cl_2 and O_3 as the Precursors. *Jpn J Appl Phys.* 2004;43:L328-L330.
[15] Lakomaa EL, Haukka S, Suntola T. Atomic layer growth of TiO_2 on silica. *Appl Surf Sci.* 1992;60/61:742-748.
[16] Kim SK, Hoffmann-Eifert S, Reiners M, et al. Relation Between Enhancement in Growth and Thickness-Dependent Crystallization in ALD TiO2 Thin Films. *J Electrochem Soc.* 2011;158:D6-D9.
[17] Aaltonen T, Ritala M, Sajavaara T, et al. Atomic Layer Deposition of Platinum Thin Films. *Chem Mater.* 2003;15:1924-1928.
[18] Potrepka DM, Sanchez LM, Polcawich RG, et al. Atomic layer deposition of Pt growth template for orienting $PbZr_xTi_{1-x}O_3$ thin films. *J Vac Sci Technol A*. 2012;30:01A129.
[19] Harjuoja J, Kosola A, Putkonen M, et al. Atomic layer deposition and post-deposition annealing of $PbTiO_3$ thin films. *Thin Solid Films.* 2006;496:346-352.
[20] Harjuoja J, Putkonen M, Niinisto L. Exploiting volatile lead compounds as precursors for the atomic layer deposition of lead dioxide thin films. *Thin Solid Films.* 2006:497:77-82.

[21] Watanabe T, Hoffmann-Eifert S, Hwang CS, et al. Liquid-Injection Atomic Layer Deposition of TiO_x and Pb-Ti-O Films. *J Electrochem Soc.* 2006:153:F199-F204.
[22] Watanabe T, Hoffman-Eifert S, Mi S, et al. Growth of ternary PbTiOx films in a combination of binary oxide atomic layer depositions. *J Appl Phys.* 2007;101:014114.
[23] Lee HJ, Park MH, Min Y-S, et al. Unusual Growth Behavior of Atomic Layer Deposition $PbTiO_3$ Thin Films Using Water and Ozone as Oxygen Sources and Their Combination. *J Phys Chem C.* 2010;114:12736-12741.
[24] Sbrockey NM, Tompa GS, Lavelle R, et al. Atomic layer deposition of $PbTiO_3$ and $PbZr_xTi_{1-x}O_3$ films using metal alkyl and alkylamide precursors. *J Vac Sci Technol A.* 2018;36:031509.
[25] Harjuoja J, Vayrynen S, Putkonen M, et al. Atomic layer deposition of $PbZrO_3$ thin films. *Appl Surf Sci.* 2007;253:5228-5232.
[26] Watanabe T, Hoffman-Eifert S, Peter F, et al. Liquid Injection ALD of $Pb(Zr,Ti)O_x$ Thin Films by a combination of Self-Regulating Component Oxide Processes. *J Electrochem Soc.* 2007:154:G262-G269.
[27] Watanabe T, Hoffman-Eifert S, Hwang CS, et al. Growth Behavior of Atomic-Layer-Deposited Pb(Zr,Ti)Ox Thin Films on Planar Substrate and Three-Dimensional Hole Structures. *J Electrochem Soc.* 2008:155:D715-D722.
[28] Zhang F, Perng Y-C, Choi JH, Wu T, et al. Atomic layer deposition of Pb(Zr, Ti)Ox on 4H-SiC for metal-ferroelectric-insulator-semiconductor diodes. *J Appl Phys.* 2011;109:124109.
[29] Choi JH, Zhang F, Perng Y-C, et al. Tailoring the composition of lead zirconate titanate by atomic layer deposition. *J Vac Sci Technol B.* 2013;31:012207.
[30] Strnad NA, Johs B, Phaneuf RJ, et al. Investigation of Bare Silicon and Sputtered Platinum Surface Effects on ALD Growth of TiO_x and ZrO_x by In-Situ Ellipsometry. *Presented at the 15th international conference on atomic layer deposition*; 2015; Portland, OR.
[31] Xie Q, Musschoot J, Deduytsche D, et al. Growth Kinetics and Crystallization behavior of TiO_2 Films Prepared by Plasma Enhanced Atomic Layer Deposition. *J Electrochem Soc.* 2008;155:H688-H692.

[32] Hendrix BC, Cameron TM, Hunks W, et al. Precursor Screening for TiO_2 ALD for Semiconductor Applications. *Presented at the 14th international conference on atomic layer deposition*; 2014; Kyoto, Japan.
[33] Putkonen M, Niinisto L. Zirconia thin films by atomic layer epitaxy. A comparative study on the use of novel precursors with ozone. *J Mater Chem.* 2001;11:3141-3147.
[34] Hwang CS. Atomic Layer Deposition for Semiconductors. Chapter 6 FeRAM, page 163. New York, NY: Springer Science+Business Media:2014
[35] Hausmann DM, Kim E, Becker J, et al. Atomic Layer Deposition of Hafnium and Zirconium Oxides Using Metal Amide Precursors. *Chem Mater.* 2002:14:4350-4358.
[36] Joeng D, Lee J, Kim J. Effects of Various Oxidizers on the ZrO2 Thin Films Deposited by Atomic Layer Deposition. *Integr Ferroelectr.* 2004:67:41-48.

Chapter 2: Introduction to MEMS, Piezoelectricity, and PZT

MEMS

Microelectromechanical systems (MEMS) have come to dominate several areas of technology where size, weight, power, and cost (SWAP-C) are critical. While complementary metal-oxide-semiconductor (CMOS) devices have dominated integrated circuit (IC) technology, MEMS typically exist in a different product space where structural movement is required at the micron scale. Historically the IC industry has been the driver of innovations in micro and nano-fabrication, simultaneously pushing both an increase in overall silicon substrate size and decrease in overall feature size.

While there does not seem to be unanimous agreement on the inception of the term "MEMS" one often cited document is a proposal to the Defense Advanced Research Project Agency (DARPA) titled, "Micro Electro-Mechanical Systems (MEMS)" from The Center for Engineering Design at the University of Utah, Salt Lake City on July 15, 1986 which was co-authored by Stephen C. Jacobsen and John E. Wood.[1] It is more important to note that the concept of MEMS has been pondered since at least the mid-twentieth century, with one notable early milestone being the discovery of the piezoresistance effect in cubic semiconductors, namely germanium and silicon in 1953 by C. S. Smith[2] which would be exploited for commercial applications including strain gauges,[3] inertial sensors,[4] and pressure sensors,[5] to name a few. These and other MEMS greatly benefitted from advances in IC micromachining, enabling consistently

shrinking devices through the end of the twentieth-century[6] and beyond. State-of-the-art lithography techniques have enabled the fabrication of MEMS devices on the nanometer-scale, facilitating the otherwise named nanoelectromechanical systems (NEMS).

PiezoMEMS

Piezoelectric MEMS (PiezoMEMS) exist as a subset of MEMS whereby transduction and actuation are achieved by the piezoelectric effect rather than driven by electrostatic,[7] magnetic,[8,9] or thermal actuation.[10,11] Devices such as transducers,[12,13] gyroscopes,[14,15] actuators,[16,17] resonators,[18,19] and speakers[20,21] can be fabricated as piezoMEMS using conventional cleanroom processing techniques including deposition, etching, and lithography.

Lead Zirconate Titanate (PZT) Based PiezoMEMS

Lead zirconate-titanate, or $PbZr_xTi_{1-x}O_3$ (PZT) is in particular an attractive material for use in piezo-MEMS due to its ferroelectricity and large piezoelectric coefficients. To date PZT has been integrated into several commercial MEMS products including industrial inkjet printheads from Xaar[22] and Fujifilm Dimatix[23] product lines, inkjet printheads for consumer electronics such as Epson PrecisionCore,[24] Panasonic EWTTS9P series MEMS gyro sensors,[25] and USound MEMS speakers and headphones.[26]

ARL PZT PiezoMEMS

Other PZT based PiezoMEMS technology has been extensively developed for commercial and military applications by the United States Army Research Laboratory (ARL). ARL has developed a mature sol-gel deposition process for PZT,[27-30] and has leveraged that process to fabricate MEMS devices for radio-frequency (RF) and micro-scale robotics. Some of those devices include actuators for robotic mobility,[31,32] angular rate sensors mimicking a fly's haltere,[33] travelling wave ultrasonic motors,[34] switches,[35] mechanical logic,[36] resonators,[37] and RF filters.[38]

Piezoelectricity

Piezoelectricity is a property of certain materials that exhibit strong electromechanical coupling and can be divided into two sub-categories: the direct piezoelectric effect and the converse piezoelectric effect. The direct piezoelectric effect is defined as the charge displacement or field generated with applied stress or strain, while the converse piezoelectric effect is defined as stress or strain resulting from an applied electric field or charge displacement.

Not all crystals are piezoelectric. Whether or not a crystal is piezoelectric depends on its point group symmetry. Piezoelectric crystals must be non-centrosymmetric because piezoelectricity is a polar effect. Twenty of the 32 point groups are piezoelectric, and the symmetry of each piezo-class determines the form of the piezoelectric coefficient matrix.[39] Ten of the 20 piezoelectric point groups contain a unique polar axis which causes them to also be pyroelectric.[39] Pyroelectricity is the phenomenon whereby a uniform change in temperature causes a charge displacement. Pyroelectric crystals may

also (but do not necessarily) exhibit ferroelectricity, which is described by the presence of a spontaneous, reversible, electronic polarization in absence of an applied electric field.

The piezoelectric coefficients relate the observed or applied stress, strain, displacement, and electric field by the piezoelectric constitutive relations, which are shown in Table 2.1. The piezoelectric e, d, g, and h coefficients take the form of a 3x6 matrix when expressed in Voigt notation. One example piezoelectric matrix for the e coefficient for the triclinic polar point group (point group class 1) is shown below in Table 2.2. For that point group, none of the coefficients are equivalent, and none are equal to zero. The e coefficient matrix for tetragonal PZT (point group class 4*mm*) is shown below in Table 2.3. For tetragonal PZT, all of the coefficients are equal to zero except for e_{31}, e_{32}, e_{33}, e_{24}, and e_{15}. However, since $e_{31} = e_{32}$, and $e_{24} = e_{15}$, there are only three independent coefficients. Tables 2.1, 2.2, and 2.3 were adapted from Ballato.[39]

Table 2.1: Piezoelectric linear constitutive relations

Linear Constitutive Relations		
Direct Piezoelectric Effect	**Converse Piezoelectric Effect**	**Piezoelectric Coefficients**
$D = eS + \varepsilon^S E$	$T = c^E S - e'E$	$e = \left(\frac{\partial D}{\partial S}\right)^E = -\left(\frac{\partial T}{\partial E}\right)^S$
$D = dT + \varepsilon^T E$	$S = s^E T + d'E$	$d = \left(\frac{\partial D}{\partial T}\right)^E = \left(\frac{\partial S}{\partial E}\right)^T$
$E = -gT + \beta^T D$	$S = s^D T + g'D$	$g = \left(\frac{\partial E}{\partial T}\right)^D = \left(\frac{\partial S}{\partial D}\right)^T$
$E = -hS + \beta^S D$	$T = c^D S - h'D$	$h = -\left(\frac{\partial E}{\partial S}\right)^D = \left(\frac{\partial T}{\partial D}\right)^S$

Table 2.2: Piezoelectric *e* coefficient matrix (Class 1 Crystal)

Longitudinal Stress or Strain	Shear Stress or Strain

E-Field or Displacement	X-axis	Y-axis	Z-axis	YZ or ZY	XZ or XY	XY or YX
X-axis	e_{11}	e_{12}	e_{13}	e_{14}	e_{15}	e_{16}
Y-axis	e_{21}	e_{22}	e_{23}	e_{24}	e_{25}	e_{26}
Z-axis	e_{31}	e_{32}	e_{33}	e_{34}	e_{35}	e_{36}

Table 2.3: Piezoelectric *e* coefficient matrix (Class 4*mm* Crystal)

	Longitudinal Stress or Strain			Shear Stress or Strain		
E-Field or Displacement	X-axis	Y-axis	Z-axis	YZ or ZY	XZ or XY	XY or YX
X-axis	0	0	0	0	e_{15}	0
Y-axis	0	0	0	e_{15}	0	0
Z-axis	e_{31}	e_{31}	e_{33}	0	0	0

In the Table 2.1 above, the linear constitutive relations are expressed in compressed matrix form. The terms used in the relations are defined below in Table 2.4. Superscripts denote which state variable is held constant, and the prime symbol denotes a matrix transpose. The indices are dropped for simplicity, and Table 2.4 denotes the form of each variable. Each of the piezoelectric coefficients are related by multiplicative identities and vary only in the associated pairing of independent and dependent variables. The piezoelectric *e* and *d* coefficients are far more commonly used than the g and h coefficients because it is experimentally far easier to maintain a constant electric field than to maintain a constant electronic displacement. The linear constitutive relations are valid for either adiabatic or isothermal conditions, and may be used to quantify the piezoelectric effects.

Table 2.4: Definition of terms.

Label	**Definition**	**Form**	**Units**
D	Electronic Displacement	Rank One Tensor	C/m^2
S	Strain	Six-dimensional Vector	m/m
E	Electric Field	Rank One Tensor	V/m
T	Stress	Six-dimensional Vector	N/m^2
ε	Dielectric Permittivity	3x3 Matrix	F/m
β	Dielectric Impermeability	3x3 Matrix	m/F

s	Elastic Compliance Coefficient	6x6 Matrix	m^2/N
c	Elastic Stiffness Coefficient	6x6 Matrix	N/m^2
α	Thermal Expansion Coefficient	Six-Dimensional Vector	1/K
e	Piezoelectric Stress Coefficient	3x6 Matrix	C/m^2
d	Piezoelectric Strain Coefficient	3x6 Matrix	m/V
g	Piezoelectric Voltage Coefficient	3x6 Matrix	m^2/C
h	Piezoelectric h Coefficient	3x6 Matrix	V/m

Thin film piezoelectric materials experience boundary conditions imposed by the substrate and behave differently than the ideal single-crystal case described above. For thin films, the piezoelectric is free to move in the out-of-plane direction (the "3" direction), but is clamped in-plane (directions "1" and "2"). Therefore, the out-of-plane stress is zero, while the in-plane stresses are assumed to be equal for symmetrical structures. The in-plane strains can be described by the following (from Muralt[40]):

$$S_1 = s_{11}^E T_1 + s_{12}^E T_2 + d_{31} E_3 \qquad \text{Equation 2.1}$$

$$S_2 = s_{12}^E T_1 + s_{11}^E T_2 + d_{31} E_3 \qquad \text{Equation 2.2}$$

Thus, the average in-plane stresses are given by the sum of Eqns. 2.1 and 2.2:

$$\frac{(T_1+T_2)}{2} = \frac{S_1+S_2-2d_{31}E_3}{2\left(s_{11}^E+s_{12}^E\right)} \qquad \text{Equation 2.3}$$

Assuming the film is perfectly clamped (in-plane strains = 0), and that the in-plane stresses are equivalent yields the following expression:

$$T_1 = T_2 = \frac{-d_{31}E_3}{\left(s_{11}^E+s_{12}^E\right)} = -e_{31,f}E_3 \qquad \text{Equation 2.4}$$

Where $e_{31,f}$ is the effective piezoelectric coefficient for perfect clamping of a thin film and may be defined as follows:

$$e_{31,f} = \frac{d_{31}}{\left(s_{11}^E+s_{12}^E\right)} = e_{31} + \frac{s_{13}^E e_{33}}{\left(s_{11}^E+s_{12}^E\right)} \qquad \text{Equation 2.5}$$

Ferroelectricity

Ferroelectricity may be considered a subset of pyroelectricity (which in turn is a subset of piezoelectricity), and is defined by the presence of a stable, but reversible polarization even at zero applied electric field.[41] The phenomenon of ferroelectricity is marked by the presence of ferroelectric (FE) domains, which are regions within the material that share the same polarization direction.[41] The ferroelectric domains are separated by walls that move in response to an applied electric field. Upon the application of an electric field, some domains, those whose polarizations nearly align with the applied field, grow at the expense of the other domains. The domain wall movement is achieved by shifting the lattice atoms, which results in dielectric loss. Once switched, the domains remain in place until a field sufficient to move the domains walls is applied. The field required to switch the polarization direction is known as the coercive field (E_c). The alignment of the ferroelectric domains results in a polarization, known as the remanent polarization (P_r), at zero applied field. $P_{max+/-}$ refers to the maximum polarization magnitude in the + or – bias directions, respectively. The result of these effects is polarization hysteresis, which can be observed by sweeping an applied field between $\pm E_c$ and measuring the resulting polarization (see Fig. 2.1 below with labelled figures of merit). Ferroelectric crystals typically exhibit a large relative permittivity (ε_r) that is a function of the applied electric field and the polarization state.[41]

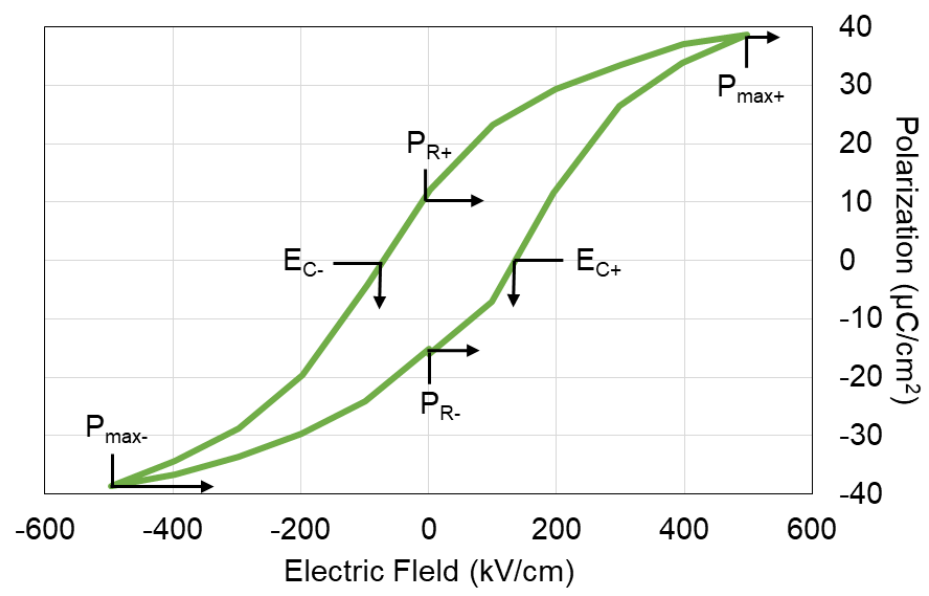

Figure 2.1: Example polarization hysteresis of a ferroelectric material (metal-insulator-metal capacitor structure) with labelled figures of merit.

AntiFerroelectricity

Antiferroelectricity is a related phenomenon to ferroelectricity, except that the spontaneous dipoles align anti-parallel, and thus cancel out leaving no remanent polarization ($P_r = 0$ in the ideal case).[42] Some antiferroelectric (AFE) crystals such as PZO and PHO undergo an electric-field induced ferroelectric phase transition.[42] The polarization/electric-field loops of antiferroelectric crystals are characterized by different figures of merit than their ferroelectric counterparts. E_F defines the minimum field required to induce the AFE-FE phase transition. E_A defines the FE-AFE phase transition occurs once the voltage magnitude is lowered. The polarization exhibits hysteresis because energy loss is associated with the phase transition. See Fig. 2.2

below for an example hysteresis loop of an antiferroelectric material that exhibits a field-induced AFE-FE phase transition with labelled figures of merit.

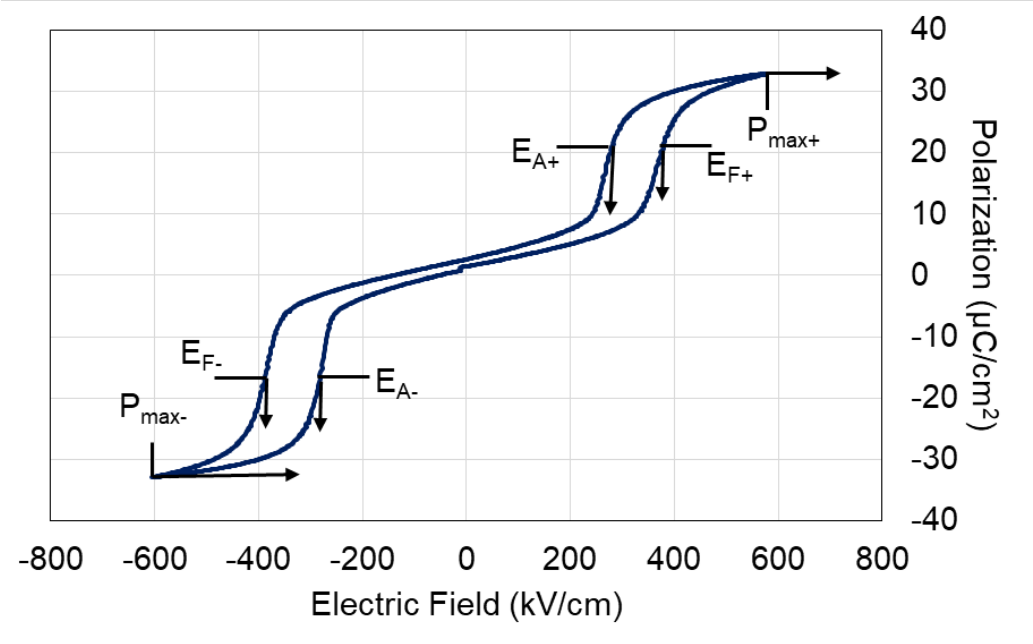

Figure 2.2: Polarization/electric-field loop of antiferroeelctric material that exhibits a field-induced ferroelectric phase transition with labelled figures of merit.

Loss Tangent (Tan δ)

The dielectric loss tangent (dissipation factor, or Tan δ) for a capacitor is a measure of the resistive versus the capacitive properties of the dielectric medium. A real capacitor may be modeled as a series containing an ideal capacitor and a resistor (equivalent series resistance, or ESR). The dielectric function (ε) contains real and imaginary parts and is given as follows (following a similar treatment from Reference [43]):

$$\varepsilon = \varepsilon' + i\varepsilon'' \qquad \text{Equation 2.6}$$

Where ε' and ε'' are the real and imaginary parts of the dielectric function, respectively. The ESR is given by

$$ESR = \frac{\sigma}{\varepsilon' \omega^2 C} \qquad \text{Equation 2.7}$$

where σ is the conductivity, ω is the angular frequency of the signal, and C is the lossless capacitance. The capacitive reactance (χ_c) is given by

$$\chi_c = \frac{1}{2\pi f C} = \frac{1}{\omega C} \qquad \text{Equation 2.8}$$

where f is the signal frequency. By definition, δ is the angle formed between the impedance vector of the capacitor (the vector connecting the origin and ESR [x-coordinate] and negative reactance [y coordinate]) and the negative reactance (y) axis. Tan δ can then be written as follows:

$$\tan\delta = Dissipation\ Factor = \frac{ESR}{|\chi_c|} = \frac{\sigma}{\varepsilon' \omega} \qquad \text{Equation 2.9}$$

PZT

PZT in particular is an attractive material for use in piezo-MEMS due to its large piezoelectric coefficients. PZT is a ceramic with the perovskite structure whose unit cell is depicted like Fig. 2.3 seen below using a "hard sphere" model.[44] The crystallographic axes and angles are labelled on the left side of Fig. 2.3. PZT may be considered a solid solution of $PbTiO_3$ (PTO) and $PbZrO_3$ (PZO), and may adopt either a tetragonal, rhombohedral, monoclinic, or cubic unit cell depending on the relative mol % PTO and the crystal temperature.[44]

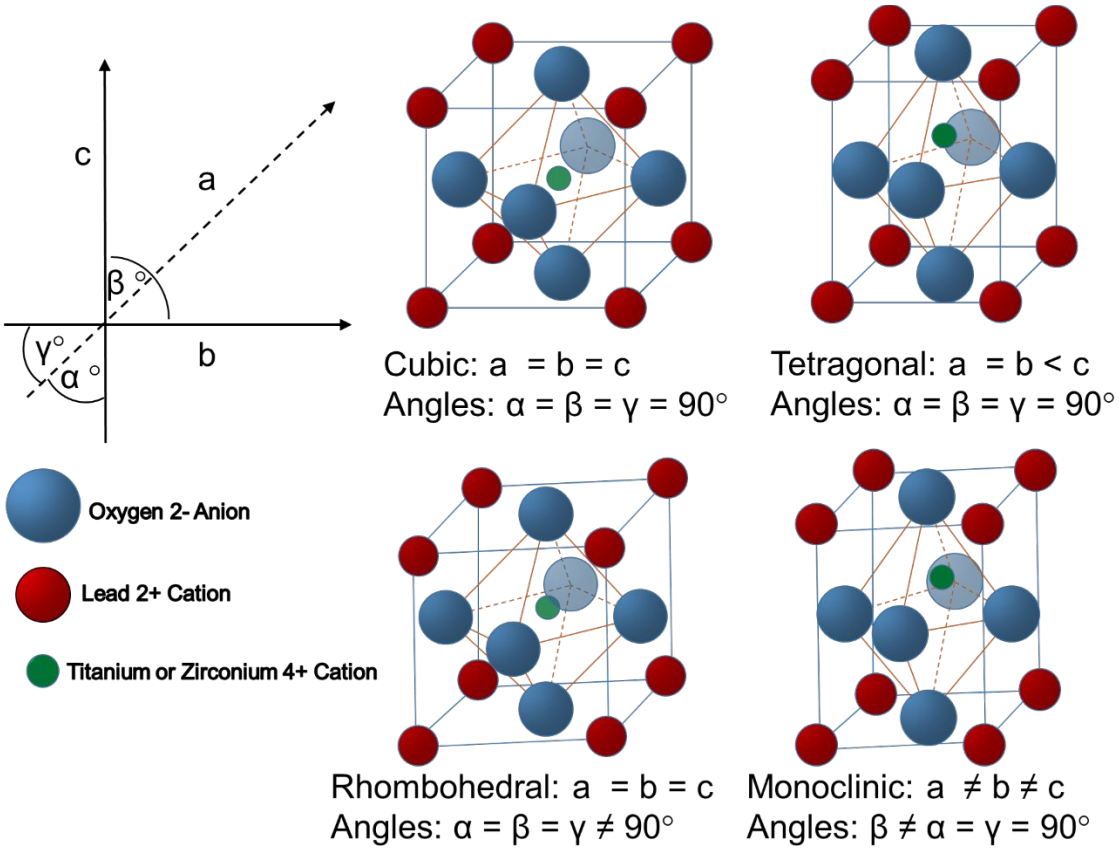

Figure 2.3: Perovskite structure unit cell in cubic and tetragonal arrangements.

As depicted in Fig. 2.3, the lead cations occupy the corners of the unit cell (red spheres), while the oxygen anions occupy the face centers (blue spheres) forming a central octahedron. The central cation (green sphere) can be either Ti^{+4} in the case of PTO, Zr^{+4} in the case of PZO, or alternating between Ti and Zr for PZT. Like PZT, PTO and PZO are also ceramics with the perovskite structure with the central green cation representing all titanium or all zirconium atoms, respectively. The phase diagram of PZT, modeled after Jaffe[41] is shown below in Fig. 2.4. At PTO-rich compositions, PZT adopts a tetragonal structure which is depicted in Fig. 2.3. For the tetragonal structure (Fig. 2.3) each of the axes are normal to one another. The unit cell lengths “a” and “b” are shown to be equal for the tetragonal structure, and the crystalline anisotropy arises

from cell length "c" with is longer than "a" and "b". In the tetragonal ferroelectric phase, the net charge results from the central cation which is displaced from its cube-center position. PZO-rich compositions of PZT adopt a rhombohedral structure at room temperature (Fig. 2.4). The rhombohedral structure is shown in Fig 2.3. Each of the cell lengths and axis angles for the rhombohedral structures are equivalent, but the axis angles slightly off-normal.

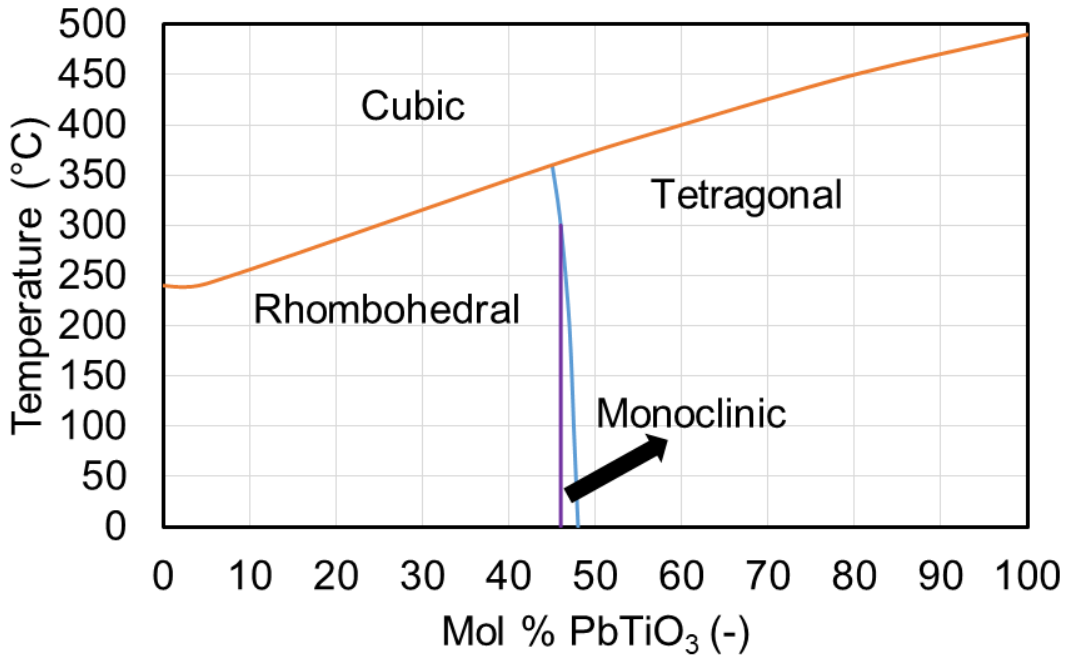

Figure 2.4: Phase diagram of PZT, modeled after Jaffe.[44]

As mentioned above, a temperature driven transform, which occurs at the Curie temperature is a technologically important property of ferroelectrics and piezoelectrics. The Curie temperature is defined as the temperature below which a ferroelectric crystal exhibits spontaneous polarization and above which the crystal loses its spontaneous polarization and becomes paraelectric.[45] The Curie temperature of pure PTO lies at 490 °C[46] while pure PZO lies at 230 °C.[47] The Curie temperature for PZT lies between 230

°C and 490 °C and varies depending on the Zr:Ti composition. When heated above the Curie temperature (depicted as the orange line, Fig. 2.4), PZT phase transitions into a cubic crystal structure that no longer retains a net polarization in the absence of an applied electric field. The cubic structure is isotropic as depicted in Fig. 2.3. For the cubic structure, all axes are equal length and the axes angles are all 90°.

Morphotropic Phase Boundary

The morphotropic phase boundary (MPB) in PZT has been studied for decades, and it is the basis for a significant portion of the interest in PZT as a technologically relevant electronic material. It is defined by Noheda et al. as, "the steep boundary where two neighboring phases in the phase diagram are degenerate, and is often observed in real systems as a finite region of coexistence."[48] PZT is a solid solution of PTO and PZO, and the MPB lies between the titanium-rich tetragonal phase and the zirconium-rich rhombohedral phase PZT centered at the composition 52 mol% PZO / 48 mol% PTO.[44] At compositions near the MPB, PZT exhibits its largest dielectric constants and piezoelectric coefficients. Near the MPB (x=0.52 for $PbZr_xTi_{1-x}O_3$) the Curie temperature is 360 °C,[49] as depicted in Fig. 2.4. The reasons for the unusually good properties have been shown to be the existence of narrow monoclinic phase (which is by definition of lower symmetry) between the tetragonal and rhombohedral phases of PZT, as shown in Fig. 2.4.[48,50] Furthering the technological importance of the MPB in PZT is the fact that the PZO/PTO mole fraction is relatively invariant with respect to temperature (see Fig. 2.4), meaning that the properties are largely preserved over a relatively wide operating temperature range.

Extrinsic Versus Intrinsic Properties

The properties of thin-film PZT are often determined by the process conditions of the films themselves and are not necessarily representative of intrinsic limitations of PZT. Intrinsic properties can be defined as the physical and chemical attributes of a given materials system that are independent of the processing method. Process-dependent attributes such as microstructure, chemical defects, inhomogeneity, and density are defined as extrinsic properties. It is therefore important to differentiate between the various existing methods of depositing PZT and to evaluate the benefits and limitations of each one.

Sol-gel

Solution-gelation (sol-gel) is a process method whereby dense films can be processed through a sequence of: liquid precursor mixture, application to a substrate (typically spun-on), heated solvent evaporation, calcination to remove organics, and crystallization via rapid thermal anneal or tube furnace anneal. A sol-gel process for PZT was originally developed by Budd et al.[51] in 1985, whereby lead acetate, titanium tetra-isopropoxide and zirconium tetra-isopropoxide were used as precursors in a methoxyethanol solvent.[52] One of the primary benefits of PZT deposited by sol-gel is that a vacuum system is not required for deposition, thereby greatly reducing the cost and complexity of the technique. Thick-films up to and in excess of 3-μm in thickness may be deposited by repetitive sequences of deposition and annealing. However, since the sol-gel PZT layers are applied and annealed sequentially, thicker films may crack

due to repeated thermal cycling of the under-layers. In addition, the odds of deleterious particle deposition increases with increasing number of deposition/crystallization steps. This is a particularly bad problem for sol-gel films that are spun-on because sufficiently large particles can cause shadowing defects that extend well beyond the contaminated particle surface. Other benefits of sol-gel synthesis of PZT are that the Zr/Ti ratio is determined by the initial mixture of the solution, and excess lead can be easily added to compensate for evaporation and diffusion during crystallization. Sol-gel PZT has been commercially implemented by Xaar for their 1201 GS2p5 PZT printhead.[53] Several companies produce commercial, high-throughput sol-gel deposition tools, including SUSS MicroTec, YOUTEC, solarsemi, Primaxx, and Mitsubishi Materials.[54]

Thick-film PZT Ceramic Particle Sintering (Screen Printing, Sol-gel Spinning)

Thick film PZT (> 10 μm) can be deposited onto a substrate by screen printing via mixing PZT particles into a paste (or ink) with glass powder and an organic binder. Maas et al[55] describe a screen printing process whereby powdered PZT particles approximately 6 μm in size are combined with boro-silicate glass powder and ESL 400,[56] which is a Texanol[57] based organic vehicle. Thick film PZT may also be deposited by mixing ceramic PZT particles into a traditional PZT sol-gel solution.[58] Once printed or spun-on, the films are sintered at temperatures often higher than 900 °C for full densification.[59] The densified films however retain a porous structure which adds complexity to subsequent micromachining processes. Specifically, the porous nature of the PZT causes inconsistency in wet-etch processes.[60] The porous thick-film PZT often shows degraded polarization characteristics compared to non-porous thin-

film PZT.[59] The addition of a sintering aid into the paste has been shown to greatly improve the film density even at firing temperatures lower than 900 °C.[61] Wu et al[62] have shown that 90% dense (relative to bulk) thick films may be deposited by a composite sol-gel method consisting of PZT particle addition to traditional PZT sol with a 6:1 solution-to-powder mass ratio, and vacuum infiltration of pure PZT sol into the as-deposited thick films to reduce the porosity. In that work, the films were deposited layer-by-layer in the following manner: spin-on of composite solution onto platinum-coated silicon substrates, two-step pyrolysis in air at 200 °C for 2 min then 400 °C for 2 min, RTA at 750 °C for 1 min, and vacuum infiltration of PZT solution into porous matrix. The deposition steps were repeated until 15 µm thick films were deposited. This method showed improvements to film density, polarization, dielectric constant, and $e_{31, f}$ with higher solution mass ratios (range tested was 0.5:1 to 6:1), however the thickness deposited per spin step decreased with higher solution mass ratios, with 2-µm deposited per spin step with composite mass ratio of 1:1, but only 0.5-µm per spin with a solution composite mass ratio of 6:1. In summary, past work demonstrates the possibility that very thick PZT, with thickness up to at least 15-µm may be deposited using thick-film ceramic particle sintering with excellent electrical properties and density equal to 90% of bulk PZT. It also demonstrated that the improvements to density and electrical properties come at the cost of a 4x lower deposition rate per spin coating, and that for now the thick-film PZT density is still significantly less than thin-film PZT density. Commercially, Meggitt A/S produces a line of thick-film (up-to and exceeding 20 µm) screen printed PZT under the Ferroperm™ product line.[63]

Pulsed-laser deposition

Pulsed laser deposition (PLD) is a technique whereby a high-powered laser is pulsed and rastered over a target which causes vaporization of material at the target surface producing a flux toward a substrate inside a vacuum chamber. The substrate, target, or both may be rotated and translated to generate a uniform coating. High-quality PZT and doped variants have been successfully deposited by PLD in a lab setting[64-67] but historically commercialization of PLD-based PZT has not occurred due to challenges in uniformly coating large area substrates with sufficiently high throughput. For PLD films, deposition is limited to line-of-site, and due to shadowing it is not possible to deposit conformal coatings into dense trench structures. However, PLD is an attractive technique in general because of the flexibility in depositing a wide variety of complex epitaxial films, notably perovskite oxides with essentially arbitrary composition.

Recently there has been more interest in PZT deposited by PLD due to implementation of combination in-situ/ex-situ laser annealing, which has been shown to effectively reduce the processing temperature of polycrystalline PZT to below 400 °C, and produce good electrical properties.[68,69] The reduction in overall thermal budget is desirable for PZT integration into heat sensitive MEMS architectures, or possibly back end-of-line (BEOL) integration of MEMS directly into ICs with moderately small node sizes.[70] Despite possible technological benefits of PLD, the primary limitation for commercial integration has been limited throughput. Recently, Solmates B.V.[71] (The Netherlands) has begun addressing PLD throughput with the development of a commercial platform capable of coating substrates up to 200-mm in diameter.[72]

Metal-organic chemical vapor deposition

PZT is also commonly deposited by metal-organic chemical vapor deposition (MOCVD) and has been commercialized by Texas Instruments for ferroelectric random access memory (FRAM).[73-75] PZT is useful for FRAM applications for several reasons. The remnant polarization in absence of an applied electric field for PZT is quite high compared to other ferroelectrics, especially at thicknesses less than 100-nm when deposited using a well-optimized MOCVD process such as that described by Aggarwal et al.[75] The magnitude of the remnant polarization effectively determines the precision with which the data bits within the FRAM can be read. More specifically, the greater the magnitude of the remnant polarization, the larger the charge difference between "0" and "1" FRAM bits when read by the sense amp.[76] It is desirable to keep the PZT ferroelectric film relatively thin to allow low switching voltages especially for embedded ferroelectric memory applications. However, scaling of the PZT thickness to below 40-50 nanometers using MOCVD is limited due to high leakage current, which is attributed to the high surface roughness on the order of the film thickness.[74,77] The MOCVD process for PZT is highlighted here for several reasons. First, FRAM is an important commercial use of PZT which utilizes the ferroelectric properties of PZT, not the piezoelectric. FRAM is a commercial non-MEMS application of PZT. Generally, the benefits of PZT deposited by MOCVD include fast deposition rates, on the order of 15 nm/minute,[75] precise control of stoichiometry based on the relative chemical precursor flow rates, self-correcting lead concentration within a relatively wide process window,[75] perovskite phase purity, and in-situ crystallization at 650 °C substrate temperature which eliminates the need for a post-deposition anneal.

Sputtering

Sputtering is a physical vapor deposition technique whereby a plasma is generated near the surface of a target material. The generated ions bombard the target due to an applied electronic bias, thereby ejecting the target material in the direction of a substrate. Silicon Sensing Systems Limited utilizes sputtered thin-film PZT to produce commercial MEMS gyroscopes, while Fujifilm utilizes sputtered thin-film PZT to produce industrial inkjet printheads.[78,79] For PZT sputtering, the stoichiometry of the sputtered film is determined by a combination of the starting sputter target stoichiometry, the relative sputter yield of the elements within the target, and lead-loss due to both evaporation of PbO_x at the film surface and diffusion of lead into the lower electrode. Therefore, PZT sputter targets must be fabricated with a lead-excess to prevent the formation of lead-poor interfaces.[80] The lead-excess cannot be too large, otherwise deleterious lead oxide phases will form within the deposited film.[80] The target must be fabricated carefully, as non-uniformities in the target may be transferred to the deposited film. The stoichiometry of the target must also be selected carefully in order to maximize the usable lifetime.

The main benefits of sputtered PZT films are the high deposition rates that are comparable to MOCVD,[81,82] relatively low surface roughness compared to MOCVD,[80,82] negligible carbon contamination, and the relatively easy process integration of sputtered PZT with the other films within a typical planar electrode stack. Specifically, the bottom and top electrodes, typically Pt, Ir, or IrO_x, are often deposited by sputtering, so the integration of a sputter process for the ferroelectric layer is quite convenient, especially when clustered together on the same commercial system.[81,82]

The limitations of sputtered PZT include possible increased thermal budget due to necessary post-deposition crystallization anneal (for "cold chuck" sputter processes), difficulty in controlling the uniformity in the lead cation concentration throughout the thickness of the deposited films, as well as the expense and variability in sourcing large diameter, sintered PZT targets.

References

[1] Jacobsen SC, Wood JE. Micro Electro-Mechanical Systems (MEMS). Presented at The Center for Engineering Design; July 15, 1986; University of Utah, Salt Lake City, UT.

[2] Smith CS. Piezoresistance Effect in Germanium and Silicon. *Phys Rev.* 1954;94:42-49.

[3] Sanchez JC. Semiconductor Strain Gauge. U.S. Patent 3084300. 1963.

[4] Yadzi N, Ayazi F, Najafi K. Micromachined Intertial Sensors. *Proceedings of the IEEE*. 1998;86:1640-1659.

[5] Mastrangleo CH, Muller RS. Fabrication and performance of a fully integrated μ-pirani pressure gauge with digitial readout. *Presented at 6th Int. Conf. on Solid-State Sensors and Actuators (Transducers '91)*; 1991; San Francisco CA. Technical Digest. 245-248.

[6] Eaton WP, Smith JH. Micromachined pressure sensors: review and recent developments. *Smart Mater Struct.* 1997;6:530-539.

[7] Legtenberg R, Groeneveld AW, Elwenspoek M. Comb-drive actuators for large displacements. *J Micromech Microeng.* 1996;**6**:320-329.

[8] Ahn CH, Allen MG. A Fully Integrated Surface Micromachined Magnetic Microactuator with a Multilevel Meander Magnetic Core. *J Microelectromech S.* 1993;2:15-22.

[9] Wright JA, Tai YC, Chang SC. A Large-Force, Fully-Integrated MEMS Magnetic Actuator. *Presented at 1997 Int. Conf. on Solid-State Sensors and Actuators (Transducers '97)*; 1997; Chicago IL. Technical Digest. 793-796.

[10] Huang QA, Lee NKS. Analysis and design of polysilicon thermal flexure actuator. *J Micromech Microeng.* 1999;9:64-70.
[11] Comtois JH, Bright VM. Applications for surface-micromachined polysilicon thermal actuators and arrays. *Sens Actuators, A.* 1997;58:19-25.
[12] Lee WS, Lee SS. Piezoelectric microphone built on circular diaphragm. *Sens Actuators, A.* 2008;144:367-373
[13] Mina IG, Kim H, Kim I, et al. High Frequency Piezoelectric MEMS Ultrasound Transducers. *IEEE Trans on Ultrason Ferroelectr Freq Control.* 2007;54:2422-2430.
[14] Jose KA, Suh WD, Xavier PB, et al. Surface acoustic wave MEMS gyroscope. *Wave Motion.* 2002;36:367-381.
[15] Nemirovsky Y, Nemirovsky A, Muralt P, et al. Design of a novel thin-film piezoelectric accelerometer. *Sens Actuators, A.* 1996;56:239-249.
[16] Harris NR, Hill M, Torah R, et al. A multilayer thick-film PZT actuator for MEMS applications. *Sens Actuators, A.* 2006;132:311-316.
[17] Chakraborty I, Tang WC, Bame DP, et al. MEMS micro-valve for space applications. *Sens Actuators.* 2000;83:188-193**.**
[18] Pulskamp JS, Bedair SS, Polcawich RG, et al. Electrode-Shaping for the Excitation and Detection of Permitted Arbitrary Modes in Arbitrary Geometries in Piezoelectric Resonators. *IEEE Trans on Ultrason Ferroelectr Freq Control.* 2012;59:1043-1060
[19] Piazza G, Stephanou PJ, Pisano AP. Piezoelectric Aluminum Nitride Vibrating Contour-Mode MEMS Resonators. *J Microelectromech S.* 2006;15:1406-1418
[20] Yi SH, Kim ES. Piezoelectric Microspeaker with Compressive Nitride Diaphragm. *The fifteenth IEEE International Conference on Micro Electro Mechanical Systems*; 2002.
[21] Kim HJ, Koo K, Lee SQ, et al. High Performance Piezoelectric Microspeakers and Thin Speaker Array System. *ETRI J.* 2009;31:680-687.
[22] [Internet] [Cited 2019 Feb 11] Available from: http://www.xaar.com/en/products/xaar-printheads/
[23] [Internet] [Cited 2019 Feb 11] Available from: http://www.fujifilmusa.com/shared/bin/PDS00015%20(3).pdf

[24] [Internet] [Cited 2019 Feb 11] Available from: https://global.epson.com/innovation/core_technology/pdf/precisioncore.pdf
[25] [Internet] [Cited 2019 Feb 11] Available from: https://industrial.panasonic.com/cdbs/www-data/pdf/ARC0000/ARC0000CE13.pdf
[26] [Internet] [Cited 2019 Feb 11] Available from: microsound piezo-MEMS earphone/headphone startup http://www.usound.com/technology.html#microsound
[27] Trolier-Mckinstry S. Improved Thin Film Piezoelectrics for Actuator Applications. U.S. Army Research Laboratory Sensors and Electron Devices Directorate *Technical Report. 2008.*
[28] Sanchez LM, Polcawich RG. Optimization of PbTiO3 Seed Layers for PZT MEMS Actuators. U.S. Army Research Laboratory Sensors and Electron Devices Directorate *Technical Report.* 2008.
[29] Sanchez LM, Potrepka DM, Fox GR, et al. Improving PZT Thin Film Texture Through Pt Metallization and Seed Layers. *MRS Proceedings.* 2011.
[30] Sanchez LM, Grobicki AD, Smith GL, et al. Texture Control in lead Zirconate Titanate Multilayer Thin Films. *IEEE Trans on Ultrason Ferroelectr Freq Control.* 2014;61:654-661
[31] Oldham KR, Pulskamp JS, Polcawich RG. Thin-Film Piezoelectric Actuators for Bio-Inspired Micro-Robotic Applications. *Integr Ferroelectr.* 2007;95:54-65.
[32] Oldham KR, Pulskamp JS, Polcawich RG, et al. Thin-Film PZT Actuators With Extended Stroke. *J Microelectromech S.* 2008;17:890-899.
[33] Smith GL, Bedair SS, Schuster BE, et al. Biologically inspired, haltere, angular-rate sensors for micro-autonomous systems. *Proceedings of SPIE 8373 Micro- and Nanotechnology Sensors, Systems, and Applications IV;* May 3, 2012; Baltimore, MD.
[34] Smith GL, Rudy RQ, Polcawich RG, et al. Integrated Thin Film Piezoelectric Traveling Wave Ultrasonic Motor. *Sens Actuators.* 2012;188:305-311.
[35] Polcawich RG. Design, fabrication, test and evaluation of RF MEMS series switches using lead zirconate titanate (PZT) thin film actuators. PhD Dissertation*; The Pennsylvania State University*; 2007.

[36] Proie RM, Polcawich RG, Pulskamp JS, et al. Development of a PZT MEMS Switch Architecture for Low-Power Digital Applications. *J Microelectromech S.* 2011;20:1032-1042.
[37] Pulskamp JS, Bedair SS, Polcawich RG, et al. Ferroelectric PZT RF MEMS Resonators. *2011 Joint Conference of the IEEE International Frequency Control and the European Frequency and Time Forum (FCS)*; May 2-5, 2011; San Francisco, CA.
[38] Pulskamp JS, Judy DC, Polcawich RG, et al. Monolithically Integrated Piezomems SP2T Switch and Contour-Mode Filters. *International Conference on Micro Electro Mechanical Systems;* Jan 25-29, 2009; Sorrento, Italy.
[39] Ballato A. Piezoelectricity: Old Effect, New Thrusts. *IEEE Trans on Ultrason Ferroelectr Freq Control* 1995;42:916-926.
[40] Muralt P, Kholkin A, Kohli M, et al. Piezoelectric actuation of PZT thin-film diaphragms at static and resonant conditions. *Sens Actuators, A.* 1996;53:398-404.
[41] Scott JF, Paz de Araujo CA. Ferroelectric Memories. *Science.* 1989;246:1400-1405.
[42] Jaffe B. Antiferroelecric Ceramics with Field-Enforced Transitions: A New Nonlinear Circuit Element*. *Proc IRE*. 1961;1264-1267.
[43] Lynch AC. Relationship between permittivity and loss tangent. Proc IEEE. 1971;118:244-246.
[44] Jaffe B, Cook WR, Jaffe H. Piezoelectric Ceramics. London, UK: London Academic Publishing:1971:136.
[45] Kasap SO. Principles of Electronic Materials and Devices. 3rded. New York, NY: PUBLISHER;2006:648.
[46] Jaffe B, Cook WR, Jaffe H. Piezoelectric Ceramics. London, UK: London Academic Publishing:1971:117.
[47] B Jaffe B, Cook WR, Jaffe H. Piezoelectric Ceramics. London, UK: London Academic Publishing:1971:125.
[48] Noheda B, Cox DE, Shirane G, et al. A monoclinic ferroelectric phase in the $Pb(Zr_{1-x}Ti_x)O_3$ solid solution. *Appl Phys Lett.* 1999;74:2059-2061.
[49] B Jaffe B, Cook WR, Jaffe H. Chapter 7 in Piezoelectric Ceramics. London, UK: London Academic Publishing:1971.

[50] Noheda B. “Structure and high-piezoelectricity in lead oxide solid solutions”, *Curr Opin Solid St M.* 2002;6:27-34.
[51] Budd KD, et al. Sol-gel Processing of PbTiO3, PbZrO3, PZT, and PLZT Thin Films. *Br Ceram Proc.* 1985;36:107-121.
[52] Dey SK, Budd KD, Payne DA. Thin Film Ferroelectrics of PZT by Sol-Gel Procesing. *IEEE Trans on Ultrason Ferroelectr Freq Control.* 1988;35:80-81
[53] [Internet] [Cited 2019 Feb 10] Available from: https://www.prnewswire.com/news-releases/complete-teardown-report-of-xaars-1201-gs2p5-pzt-printhead-overview-physical-analysis-manufacturing-process-cost-analysis--price-analysis-300744632.html
[54] YOLE development. [Internet] [Cited 2019 Feb 10] Available from: http://www.yole.fr/iso_upload/Samples/Yole_thin_film_PZT_applications_sample.pdf
[55] Maas R, Koch M, Harris NR, et al. Thick-film printing of PZT onto silicon. *Mater Lett.* 1997;31:109-112.
[56] [Internet] [Cited 2019 Feb 12] Available from: http://electroscience.com/400
[57] [Internet] [Cited 2019 Feb 12] Available from: http://www.innovationlab.eastman.com/materials/eastman-texanol
[58] Barrow DA, Petroff TE, Sayer M. Thick ceramic coatings using a sol gel based ceramic-ceramic 0-3 composite. *Surf Coat Technol.* 1995;76-77:113-118.
[59] Jeon Y, Chung J, No K. Fabrication of PZT Thick Films on Silicon Substrates for Piezoelectric Actuator. *J Electroceram.* 2000;4:195-199.
[60] Beeby SP, Blackburn A, White NM. Processing of PZT piezoelectric thick films on silicon for microelectromechanical systems. *J Micromech Microeng*. 1999;9:218-229.
[61] Corker DL, Whatmore RW, Ringgaard E, et al. Liquid-phase sintering of PZT ceramics. *J Euro Ceram Soc.* 2000;20:2039-2045
[62] Wu D, Zhou Q, Kirk K, et al. Dielectric and Piezoelectric Properties of PZT Composite Thick Films with Variable Solution to Powder Ratios. *J Am Ceram Soc.* 2009;92:1276-1279.

[63] [Internet] Meggitt A/S. TF2100 all-round hard PZT. [Cited 2019 Feb 12] Available from: https://www.meggittferroperm.com/wp-content/uploads/2017/10/201708_MSSDK_TF2100_Datasheet-TF2100-1.pdf
[64] Tseng TF, Liu KS, Lin I-N, et al. Growth Behavior of pulsed-laser-deposited PLZTO thin films. *J Ceram Proc.* 1997;43:2857-2864.
[65] Verardi P, Dinescu M, Craciun F. Pulsed laser deposition and characterization of PZT thin films. *Appl Surf Sci.* 2000;154-155:514-518.
[66] Verardi P, Craciun F, Mirenghi L, et al. An XPS and XRD study of physical and chemical homogeneity of $Pb(Zr,Ti)O_3$ thin films obtained by pulsed laser deposition. *Appl Surf Sci.* 1999;138-139:552-556.
[67] Pham MTN, Boukamp BA, Bouwmeester HJM, et al. Microstructural and electrical properties of nanocomposite PZT/Pt thin films made by pulsed laser deposition. *Ceram Int.* 2004;30:1499-1503.
[68] Rajashekhar A, Fox A, Bharadwaja SSN, et al. In situ laser annealing during growth of $Pb(Zr_{0.52}Ti_{0.48})O_3$ thin films. *Appl Phys Lett.* 2013;103:032908.
[69] Rajashekhar A, Zhang HR, Srowthi B, et al. Microstructure Evolution of In Situ Pulsed-Laser Crystallized Pb(ZrTi)O3 Thin Films. *J Am Ceram Soc.* 2016;99:43-50.
[70] Fedder GK, Howe RT, Liu T-J K, et al. Technologies for Cofabricating MEMS and Electronics. *Proc IEEE.* 2008;96:306-322
[71] [Internet] [Cited 2019 Feb 12] Available from: https://www.solmates.nl/40/publications.html
[72] Blank DHA, Dekkers M, Rijnders G. Pulsed laser deposition in Twente: from research tool towards industrial deposition. *J Phys D: Appl Phys.* 2014;47:034006.
[73] Summerfelt SR, Moise TS, Xing G, et al. Demonstration of scaled ($\geq$0.12 μm^2) $Pb(Zr,Ti)O_3$ capacitors on W plugs with Al interconnect. *Appl Phys Lett.* 2001;79:4004-4006.
[74] Gilbert SR, Hunter S, Ritchey D, et al. Preparation of $Pb(Zr,Ti)O_3$ thin films by metalorganic chemical vapor deposition for low voltage ferroelectric memory. *J Appl Phys.* 2003;93:1713-1717.

[75] Aggarwal S, Udayakumar KR, Rodriguez JA. Stoichiometry and phase purity of Pb(Zr, Ti)O_3 thin films deposited by metal organic chemical vapor deposition *J Appl Phys.* 2006;100:064103.
[76] Kumar VC, Underdahl B. *Texas Instruments Fram MCUs for Dummies.* Hoboken, New Jersey. John Wiley and Sons, Inc. 2012.
[77] Bilodeau SM, Johnston ST, Russell MW, et al. Voltage scaling of ferroelectric thin films deposited by CVD. *Integr Ferroelectr.* 1999;26:119-135.
[78] [Internet] Silicon Sensing PZT Piezoelectric Sputtering Service. [Cited 2019 Mar 12] Available from: https://www.siliconsensing.com/services/foundry-services/pzt
[79] [Internet] Fugifilm Dimatix Industrial Inkjet Printheads. [Cited 2019 Mar 12] Available from: https://www.fujifilmusa.com/products/industrial_inkjet_printheads/print-products/printheads/index.html
[80] Chu F, Fox GR, Davenport T, et al. The Control of Pb Loss for PZT Based FRAM. *Integr Ferroelectr.* 2002;48:161-169.
[81] Suu K, Tani N, Chu F, et al. Process stability of ferroelectric PLZT thin film sputtering for FRAM ® production. *Integr Ferroelectr*. 1999;26:9-19.
[82] Chu F, Hickert G, Hadnagy TD, et al. Ferroelectric properties of PLZT thin films prepared using ULVAC ZX-1000 sputtering system. *Integr Ferroelectr.* 1999;26:47-55.

Chapter 3: Instrumentation

Introduction

The following chapter is intended to provide details regarding the ALD platform used in this study, as well as the key measurement and characterization techniques referenced in Chapters 5-8. The externally-charged ALD source and ozone source subsystems referenced here (Figs. 3.2 and 3.4) were co-developed between the author of this thesis and engineers from the Kurt J. Lesker Company, Inc. Rutherford backscattering measurements were performed by EAG Laboratories (formerly Evans Analytical Group).

ALD Platform

A commercial Kurt J. Lesker Company, Inc. (Jefferson Hills, PA, USA) ALD 150-LX platform with a six wafer load-lock cassette and automatic wafer handling was used to deposit each ALD film referenced in this work. The 150-LX contains four independent reactant input lines and a central out-of-plane plasma gas input. A heated chuck with substrate lift pins is located in the center of the process chamber and can handle circular samples up to 150-mm diameter. The substrate lift pins are raised and lowered to facilitate automated transfer. See Fig. 3.1 below for a geometric representation of a top down view of the process chamber with associated plasma source and cation precursor locations.

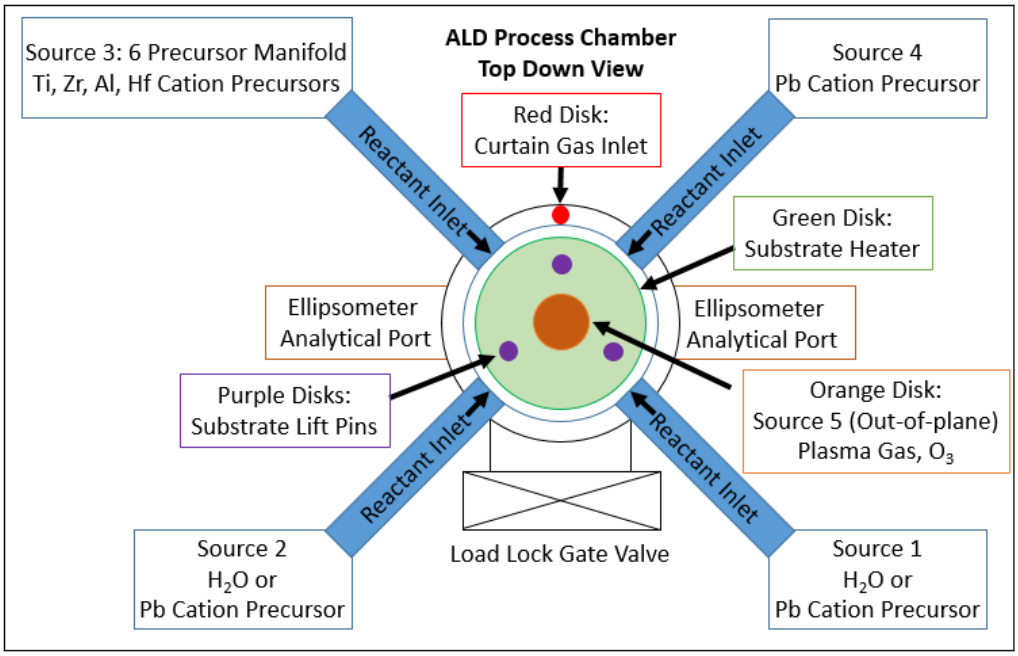

Figure 3.1: ALD process chamber drawing in a top-down view. The green disk in the center of the chamber represents the heated chuck capable of handling circular samples up to 150 mm diameter. In the retracted position (down) the substrate lift pins are flush with the surface of the substrate heater.

Sources 1 and 2 are in the vapor-draw style and consist of a normally closed three-way ALD dosing valve with an upstream two-way carrier gas isolation ALD valve. The ALD dosing valves were typically pulsed between 0.2 to 2 seconds for precursor delivery while inert gas was constantly flown through them to ensure sufficient purging between cycles. H_2O was pulsed only from sources 1 and 2 to prevent ALD reactions from occurring within the reactant inlet lines. Varying lead cation precursors were alternately mounted to sources 1 or 2 depending on the materials system tested and the location of the H_2O source.

Titanium, zirconium, aluminum, and hafnium cation precursors share source 3, which contains a heated 6-way precursor manifold. The precursor manifold consists of 6

normally-closed three-way ALD dosing valves connected in parallel and housed within a heated oven. Each ALD dosing valve was typically pulsed between 0.25 to 1 second during precursor delivery. Similar to sources 1 and 2, inert gas was constantly flown through source 3 to ensure sufficient purging between cycles. Typically, 45 sccm of argon was sufficient to purge the lines within 5-10 seconds, depending on the precursor. Source 4 is in a flow-through style and consists of three normally-closed ALD valves connected in series including a 3-way ALD dosing valve (ALD-out), an upstream 2-way ALD valve (bypass) and further upstream 3-way ALD valve (ALD-in). Source 4 was typically operated using a single-stem source mounted to only the ALD-out side with the bypass held open to enable constant inert gas purging of the valves. The source 4 ALD dosing valve was typically pulsed multiple times in series at 0.25 seconds per pulse to obtain a saturating dose.

Source 4 can be operated in a flow-through configuration if a two stem ampoule is mounted to the ALD-in and ALD-out side. Inert gas is redirected through the ampoule itself when the bypass is closed and both the ALD-in and ALD-out valves are open. The flow-through increases the overall dose compared to the vapor-draw style configuration. Source 4 may also be used to charge an ampoule with inert gas prior to pulsing. However, charging may introduce residuals into the chamber and affects the overall flow inside the chamber during the process. To circumvent the issue, plumbing was added to enable ampoule charging externally, thus not disrupting the overall ALD process. A schematic of the externally charged source is shown below in Fig. 3.2, and was implemented on sources 2, 3, and 4.

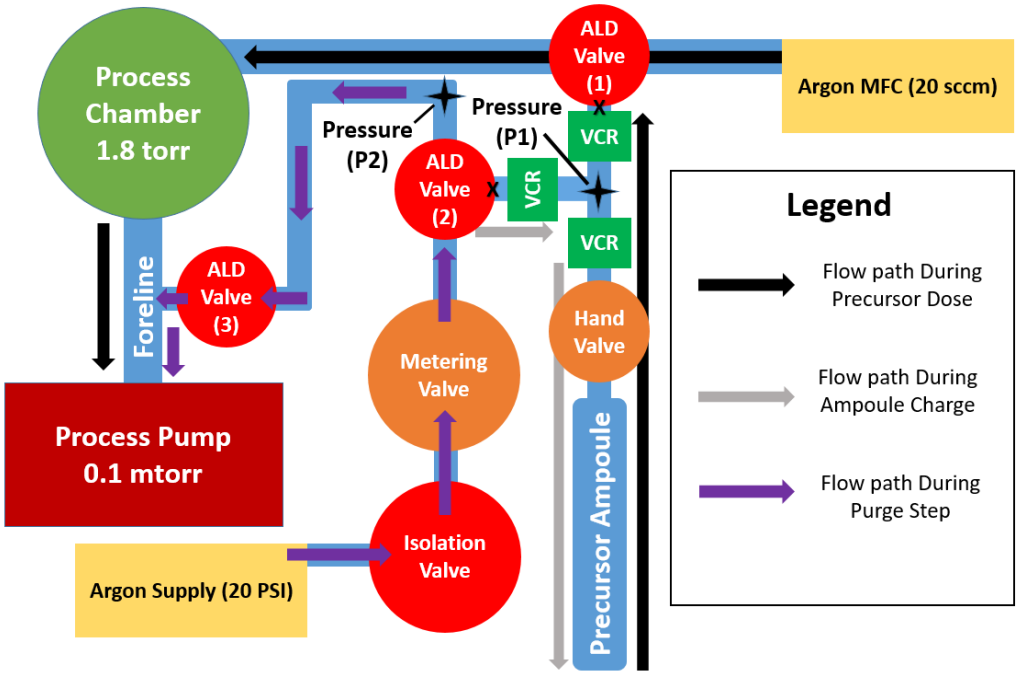

Figure 3.2: Block diagram of externally-charged ALD source

A description of a normal precursor dose process using the externally-charged source follows. The ampoule starts in the charged state, because the final step of the preceding cycle is the external ampoule charge. The charged precursor ampoule is pulsed into the process chamber by the actuation of ALD valve (1), which is pulsed between 0.25 and 1 second(s). ALD valve (1) is normally closed, with the "X" denoting the ALD valve open/close port. ALD valve (1) always flows the argon carrier gas (20 sccm from the MFC. Multiple (or longer) ALD valve (1) pulses may be necessary to fully evacuate the ampoule. During the precursor pulse, the pressure P1 > 1.8 torr > 0.1 mTorr, and the gas flow follows the black arrows into the process chamber. The pressure P1 is influenced by the amount of time ALD valve (2) is open during the charge and the setting of the metering valve. P1 should be optimized around the process but generally should not exceed 2.1 Torr to avoid deleterious chamber deposition.

Once the precursor dose step is over and ALD valve (1) is closed, the ampoule is recharged immediately by the simultaneous opening of ALD valve 2 and closing of ALD valve (3). During the charge step, the gas flow follows the gray arrow. ALD valve (3) (which is normally open) is closed to prevent precursor back-streaming into the charge line. Additionally, the pressure P2 continuously builds, which easily enables control of P1 by the timing of the charge. The charge step for the processes referenced in this work typically lasted between 1-2 seconds. The purging of the process chamber is not significantly affected by the ampoule charge step, except that the chamber base pressure is momentarily reduced due to the closure of ALD valve (3). Once the charge is complete and ALD valve (2) is closed and ALD valve (3) is opened, the flow resumes along the purple arrows, continuously purging the charge line until the next charge step. Because the charge line is continuously purged, any residual precursor is safely evacuated. The continuous purge also permits connecting of several of these sources in series, which is convenient. In this work, the lead source is typically pulsed from two alternating sources. Since the chemical is identical, the lead sources are charged back-to-back. For cases where different chemicals are present in the charged ampoules, it is best to wait at least 20 seconds between charging to ensure adequate purging.

The ampoule charge source increases the dose of solid and liquid precursors. Although liquid precursors may be heated to achieve adequate vapor pressure, it may be desirable to charge them instead near room temperature to prevent thermal decomposition. For many solid precursors, achieving adequate vapor pressure may not be possible if the thermal decomposition temperature is sufficiently low. In that case, the ampoule charge source is highly desirable.

The exterior of Source 5 is shown below in Fig. 3.3, and consists of a quartz plasma tube with a water-cooled copper induction coil surrounded by a Faraday cage. Reactant gases such as O_2 (plasma gas) and O_3 are fed through the source 5 inlet upstream of the o-ring sealed plasma tube. During normal operation source 5 is purged with argon gas to prevent back-streaming of precursors into the plasma tube. The films described in this work were deposited using H_2O as the oxidizing co-reactant, so the details of the plasma and ozone sources are not critical.

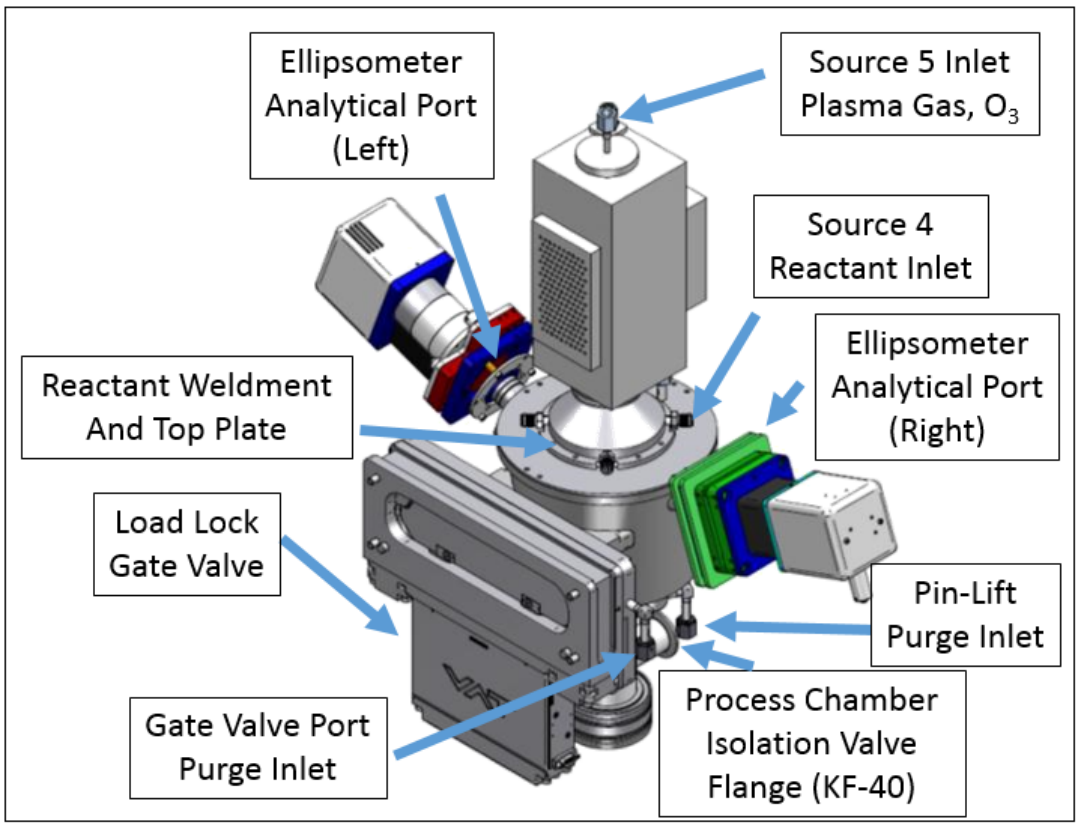

Figure 3.3: CAD drawing of process chamber exterior reproduced with permission of the Kurt J. Lesker Company. The process chamber exterior is shown in an off-angle view. Sample hardware is shown mounted to the ellipsometer analytical ports for example purposes.

The manifold ALD valves, single-source ALD valves, oven ALD valves, and all reactant lines were typically held at 150˚ C to prevent condensation. Each source was individually purged with between 20 to 50 sccm of high purity argon from dedicated mass flow controllers (MFCs). The chamber walls were purged with additional argon using a single gas inlet, dispersion ring, and showerhead around the edge of the chamber to prevent deposition buildup. The ellipsometer analytical ports, load lock gate valve port, pin-lift, and plasma adapter ring (not shown in figure) received additional argon purges to prevent trapping of reactant gases between half-cycles. The plasma adapter ring is eclipsed by the plasma source in Fig. 3.3 and is located between the bottom of the plasma source and the top of the reactant weldment. The total argon purge flow through the system was typically 1.1 SLPM. Shutters were not used on the ellipsometer analytical ports or the ICP tube because the purge flow prevents deleterious coating under normal operation.

The ozone source design is shown below as a block diagram in Fig. 3.4. Under normal operation the oxygen MFC flows 200 sccm through the Nano Ozone Generator constantly and follows the black arrows. The ozone generator is held constant at 20 PSI by the back-pressure regulator, which is adjusted manually. The pressure is monitored by the first in-line capacitance manometer (capman) which provides feedback for an interlock script that automatically shuts off the generator if the pressure drops below 15 PSI. The ozone/oxygen mixture charges a 1 liter reservoir that is monitored by the second in-line capman and contained by two normally-closed ALD valves, (4) and (5). The ozone concentration sensor (Teledyne Instruments Model 452) was used in initial tests to calibrate the ozone concentration, but for this work was turned off during

operation because the UV radiation used by the sensor to measure the ozone concentration also decomposed some of the ozone entering the process chamber. The preliminary tests using the ozone concentration sensor suggested 200 sccm of O_2 yielded an ozone concentration of 10 mol%. 200 sccm O_2 was used as the flow rate for all ALD depositions described in this work. During the oxidation step of the present ALD processes, ALD Valve (4) is opened between 5-10 seconds to empty the contents of the reservoir into the chamber. Once ALD valve (4) is closed, the reservoir is able to recharge until the next oxidation step. The 1 liter reservoir typically reached a pressure of approximately 100 Torr prior to the ozone pulse, which led to a spike in the chamber pressure to just above 10 Torr, which decayed at a rate depending on the pump speed. The chamber typically pumped back down to a base pressure of 1.8 Torr after about 10 seconds, but 20 seconds was used as the purge time for added tolerance. The ozone source is automatically shut down after each deposition and the reservoir is evacuated through ALD valve (5). The ozone is converted to O_2 using a platinum catalyst and evacuated through the rough pump for the load lock (Ebara EV-A03).

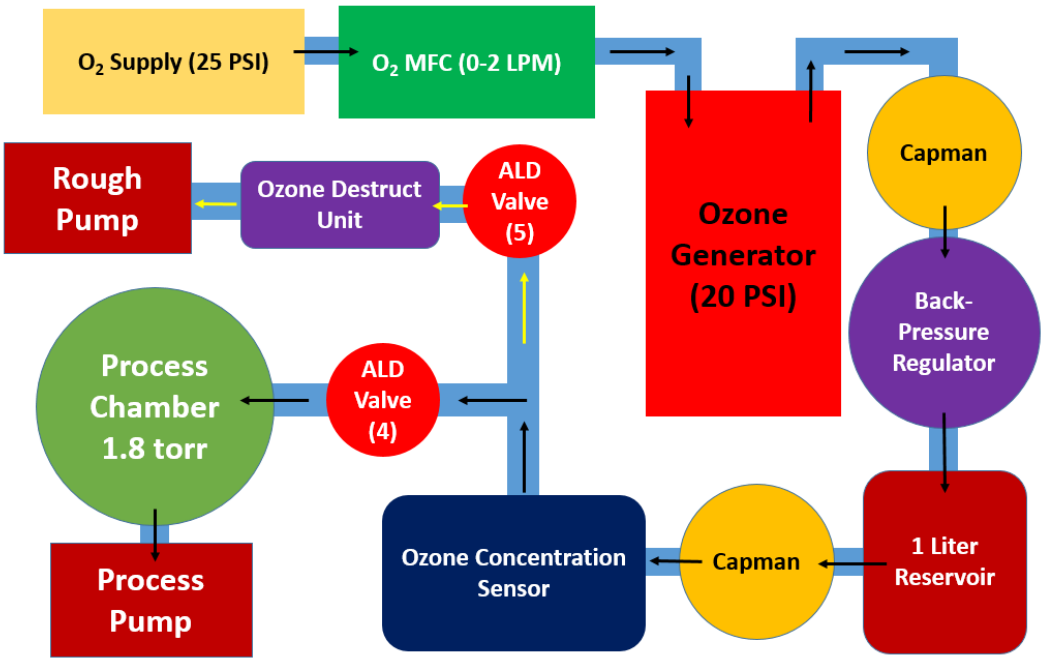

Figure 3.4: Block diagram of the custom ozone source

High purity argon was supplied by boil-off from a cryogenic liquid dewar with starting purity of 99.999 atomic % and filtered through a SAES Getters (Lainate, Italy) Microtorr® MC-190 purifier before reaching the principle cleanroom argon distribution line. The argon was filtered again at the tool using an identical purifier. Stainless steel tubing was used for all inert and process gases.

Ellipsometry

Background and Experimental

Fundamentally, ellipsometry is a technique whereby a sample is exposed to incident light with a known polarization which is reflected into a different polarization state and measured by a detector. The difference between the polarization states of the incident and reflected beams is used to calculate the optical properties of the sample. The

polarization state of light may be defined by the Stokes vector, with elements defined as follows: (from Chipman[1])

$$S_i = \begin{bmatrix} S_1 \\ S_2 \\ S_3 \\ S_4 \end{bmatrix} = \begin{bmatrix} P_H + P_V \\ P_H - P_V \\ P_{45} - P_{135} \\ P_R - P_L \end{bmatrix} \qquad \text{Equation 3.1}$$

where S_1, S_2, S_3, S_4 are the Stokes vector elements, with $i = (1,2.3,4)$. The subscripts of P refer to the light flux through the following ideal polarizers: horizontal linear polarizer (H), vertical linear polarizer (V), 45° linear polarizer (45), 135° linear polarizer (135), right circular polarizer (R), and left circular polarizer (L). The elements of the Stokes vector may be used to calculate the overall degree of polarization, the degree of linear polarization, and the degree of circular polarization. The ellipticity, orientation of major axis (azimuth), and eccentricity of the polarization ellipse traced by the electric field vector as a function of time (hence ellipsometry) may also be calculated from the Stokes vector elements. The details of the above calculations may be found elsewhere.[1]

Upon reflection, transmission, or scattering, the polarization of the incident light (thus the Stokes vector) is transformed from S_i into S_i' by the following relation: (from Chipman[1])

$$S_i' = MS_i \qquad \text{Equation 3.2}$$

where M is the 4 x 4 Mueller matrix which is a function of the wavelength of light, and the propagation direction (which is the measurement angle, for the purposes of this work). The Mueller matrix is a complete characterization of the polarization properties of a sample. It is clear from Eqn. 3.2 that if the Mueller matrix is known for a given wavelength and propagation direction (detector angle), and the Stokes vector of the

incident light is known, the Stokes vector of the reflected beam may be calculated using simple matrix multiplication.

The Stokes vectors can be decomposed into two components: p-polarized light within the plane of the propagation vectors of incidence (E_p), and s-polarized light normal to the plane of incidence (E_s). For light reflected off of the surface of a sample, both the incident and reflected light lie within the same plane, which is defined as the plane of incidence. The change in polarization state can be characterized by the ratio (ρ) of the sample's reflectivity of p-polarized light (R_p) to the sample's reflectivity of s-polarized light (R_s), and can be represented in terms of the ellipsometric angles Ψ and Δ as follows: (from Johs[2])

$$\rho = \frac{E_p'/E_p}{E_s'/E_s} = \frac{R_p}{R_s} = \tan\Psi\, e^{i\Delta} \qquad \text{Equation 3.3}$$

which is the Fundamental Equation of Ellipsometry. In the second term of Eqn. 3.3, the prime denotes the component of the reflected beam, while no prime denotes the incident beam. Ψ and Δ are the quantities measured directly by ellipsometry, and are a function of wavelength and the angle of incidence between the reflected beam and the sample. The thickness and index of the films of interest are therefore not directly measured by the instrument. Instead, the measured Ψ and Δ must be modeled optically, and solutions must be systematically guessed until there is a minimum disagreement between the modeled and measured parameters. Therefore, the thickness and index are measured indirectly, and are only accurate if the specified model is a physical representation of the film(s).

The raw data provided by ellipsometry are a Ψ and Δ angle at each specified wavelength at a particular specified incidence angle. Often, a sample will contain many more unknowns than can be solved directly, such as several films of unknown thickness and unknown optical consonants. For an ellipsometer that measures a wavelengths, the number of unique data points is $2a$, therefore the number of unique film parameters that can be measured directly is $2a$. For most thin film samples, neither the thickness, roughness, nor optical constants (real n or imaginary k) are precisely known, which leaves (at least) $2a + 2$ unknown variables (if the angle is known) and only $2a$ data points. For those under-determined solutions, parametrized dispersion models are employed to reduce the number of unknowns. For the simple case of optically transparent homogeneous films ($k = 0$), the first two terms of Cauchy's dispersion formula[3] are sufficient to describe the optical constants:

$$n(\lambda) = A + \frac{B}{\lambda^2} \qquad \text{Equation 3.4}$$

where A and B are the Cauchy coefficients that describe the real index of refraction (n) as a function of wavelength (λ). Thus, the number of variables required to describe the unknown film reduce from $2a + 2$ to just four. In this case, an ellipsometer with $a \geq 2$ can provide a unique solution for the thickness, roughness, and n, since we assumed $k = 0$ when we picked the Cauchy model. Complex equations may be used to model semi-transparent and opaque films using the same general methodology.

Ellipsometer measurements are typically performed on substrates with multiple films of varying optical properties and thicknesses. In those cases, parameterized models are essential as there may be multiple unknowns in multiple layers of the sample. To generate a solution, modelling software is typically used to fit the unknown variables

to the raw data. It is often useful to pair ellipsometry with other techniques that can provide thickness and roughness measurements, because they reduce the number of unknown variables on a complicated sample. Details related to the film models used in this work are presented at the end of this section.

In-situ ellipsometery measurements were taken with a Film Sense™ (Lincoln, NE, USA) FS-1 multi-wavelength ellipsometer. The FS-1 supplies light using four different visible LED sources centered at 465 nm, 525 nm, 580 nm, and 635 nm directed through a linear polarizer. The reflected light is split using a beam splitter (now two beams) and refracted through Wollaston prisms (now four beams) and transduced using four linear photodetectors. The Film Sense™ FS-1 operates generally as a Division of Amplitude Polarimeter (DOAP) in which the Stokes vectors for the beam entering the detector are calculated using the following equations (adapted from Azzam[4,5]):

$$\vartheta_k = FS_i \qquad \text{Equation 3.5}$$

$$S_i = F^{-1}\vartheta_k \qquad \text{Equation 3.6}$$

where S_i is the Stokes vector of the reflected beam (note that the prime notation is dropped here for convenience), and ϑ_k are the signal vectors from the linear photodetectors, where $k = (1,2,3,4)$. F is the 4 x 4 instrument matrix which is determined by an initial calibration whereby polarized light in four different known states whose stokes vectors are linearly independent are reflected off of a known sample and are collected by the detector. The signal vectors of the calibration measurements, ϑ_k, may be combined into a single matrix, Y, where:

$$Y = (\vartheta_{k1}, \vartheta_{k2}, \vartheta_{k3}, \vartheta_{k4}) \qquad \text{Equation 3.7}$$

The corresponding Stokes vectors may also be combined into a signal 4 x 4 matrix X, where:

$$X = (S_{i1}, S_{i2}, S_{i3}, S_{i4}) \qquad \text{Equation 3.8}$$

Equation 3.5 then becomes:

$$Y = FX \qquad \text{Equation 3.9}$$

Rearranging Equation 3.9 yields:

$$F = YX^{-1} \qquad \text{Equation 3.10}$$

The matrix elements of F are a function of the sensitivities of the linear photodetectors, the reflection and transmission matrices of the beam splitter, and the azimuth settings of the Wollaston prisms, though they may be empirically determined using the above method.

In practical terms, Eqn. 3.10 shows that in order to calibrate the instrument matrix, the Stokes equations of the light entering the detector must be known. For the FS-1, this is accomplished by initially polarizing the light into a known state, and measuring light reflected off of a substrate whose optical properties are known. The calibration procedure is fast since the FS-1 calibrates all four wavelengths simultaneously. Conveniently, the instrument matrix only needs to be calibrated once.

For a sample measurement, the Stokes vector S_i is related to the ellipsometeric angles by the following relations, when the incident beam is linearly polarized (Adapted from Lodewijks[6]):

$$S_1 = \sin^2 \Psi + \sin^2 \Psi = 1 \qquad \text{Equation 3.11}$$

$$S_2 = -\cos 2\Psi \qquad \text{Equation 3.12}$$

$$S_3 = \sin 2\Psi \cos \Delta \qquad \text{Equation 3.13}$$

$$S_4 = \sin 2\Psi \sin \Delta \qquad \text{Equation 3.14}$$

Equation 3.11 indicates that the Stokes vector must be normalized such that $S_1 = 1$ before the ellipsometric angles may be calculated. Once normalized, the ellipsometric angles are readily calculated from Eqns. 3.12-3.14.

The FS-1 was mounted and aligned at an incidence angle of nominally 70˚ from the source/detector to the sample. The source and detector were periodically aligned and calibrated taking into account window effects using a 150-mm silicon wafer with native oxide thickness of nominally 14 Å. The wafer alignment was individually recorded before each deposition ensuring accurate measurements. Dynamic measurements were performed throughout each ALD growth in increments of 50-ms to 1000-ms.

Ex-situ measurements were performed with a J.A. Woollam Company, Inc. (Lincoln, NE, USA) M-2000® spectroscopic ellipsometer with an automated-angle adjusting base and a 200mm diameter R-theta stage for full wafer mapping. The M-2000® is a fixed polarizer rotating compensator-rotating analyzer (FPRC-RA) configuration-type ellipsometer.[7,8] A FLS-300 Xe Arc Light Source with a M2000-F Detector and Lamp Power Supply Module provided the light output spectrum. The beam collimation optics, fixed polarizer, and rotating compensator are housed within the FLS-300 Xe Arc Light Source. The Output Unit contains a rotating polarizer and transmits the spectroscopic measurement signal to the detector through a fiber optic cable. The detector uses a spectrometer to diffract the signal into 474 discrete wavelengths between 246.3 nm and 989.7 nm and a CCD array as the transducer.

The CCD array provides a measured signal versus time for each ellipsometer measurement at each wavelength in the detector array. The ellipsometric angles Ψ and

Δ are calculated for each wavelength differently than the FS-1. Whereas the FS-1 directly measures the Stokes vector of the light reflected off of the surface of the sample and compares it to the initial polarization state to determine the ellipsometric angles, the M-2000® fits the voltage versus time of the reflected beam to the following equation for an elliptically polarized beam (From J.A. Woollam Co. Inc.[7]):

$$V(t) = DC + a\cos(2\omega t) + b\sin(2\omega t) \qquad \text{Equation 3.15}$$

where $V(t)$ is the voltage generated versus time, DC is the background signal, ω is the angular frequency of the rotating analyzer, t is time, and a and b are the Fourier transform coefficients that are fit to the input signal. DC is measured before each ellipsometry measurement, and ω is controlled by the hardware.

The Fourier transform coefficients can be normalized if they are divided by the DC offset and can be represented in terms of the ellipsometric angles Ψ and Δ as follows (From J.A. Woollam Co. Inc.[7]):

$$\alpha = \frac{a}{DC} = \frac{\tan^2(\Psi) - \tan^2(P)}{\tan^2(\Psi) + \tan^2(P)} \qquad \text{Equation 3.16}$$

$$\beta = \frac{b}{DC} = \frac{2\tan(\Psi)\cos(\Delta)\tan(P)}{\tan^2(\Psi) + \tan^2(P)} \qquad \text{Equation 3.17}$$

where α and β are the normalized Fourier coefficients and P is the polarizer azimuthal angle relative to the plane of incidence of the incident and reflected beams, which is a known equipment parameter. Equations 3.16 and 3.17 can thus be used to solve for Ψ and Δ, which are in turn used to infer the optical properties of the measured sample. In practice, the precision of the calculated Ψ and Δ is improved the longer the data are collected at constant ω.

All samples measured in the ex-situ mode were mounted horizontally and aligned using a four-quadrant laser alignment detector. Measurements were typically performed at 65˚ incidence between the sample and the source/detector. Data was typically averaged over 100 revolutions of the analyzer (100 Revs./Meas.) at a measurement time of approximately 70 ms per revolution.[9]

Model Parameters for Pb-Based Perovskites (Present Work)

Each of the films presented in this work, including $PbTiO_3$, $PbZr_xTi_{1-x}O_3$, $PbHfO_3$ and $PbHf_xTi_{1-x}O_3$ were measured by ex-situ spectroscopic ellipsometry and analyzed using the same parametrized optical model. The model primarily consists of a Tauc-Lorentz (TL) optical function which was first derived by Jellison.[10] Using the TL model, the imaginary ($\epsilon_{2,TL}$) and real (ϵ_1) parts of the dielectric function at energy E are described as follows:

$$\epsilon_{2,TL} = \left[\frac{AE_0C(E-E_g)^2}{(E^2-E_0^2)+C^2E^2}\frac{1}{E}\right] \qquad \text{Equation 3.18}$$

$$\epsilon_1 = \epsilon_{1,\infty} + \frac{2}{\pi}P\int_{E_g}^{\infty}\frac{\xi\epsilon_2(\xi)}{\xi^2-E^2}d\xi \qquad \text{Equation 3.19}$$

where the potential fit parameters are E_g (the Tauc-Gap energy), A (units-energy), E_0 (units-energy), C (units-energy), and $\epsilon_{1,\infty}$ (the real part of the dielectric function as E approaches infinity). In the present work, E_g, A, E_0, and C were held constant for all films at 1.2938 eV, 7.0322 eV, 5.3351 eV, and 0.039697 eV, respectively. The variable $\epsilon_{1,\infty}$ was left as a fit parameter with a starting value of 1.6494. P is the Cauchy principle part of the integral, and ξ is a variable with units of energy but is not a fit parameter. An ultra-violet pole was added to the TL model to simulate an oscillator at a wavelength

below the measured range that affects the real part of the dielectric function. With the additional pole, Eqn. 3.19 is transformed into the following:

$$\epsilon_1 = \epsilon_{1,\infty} + \frac{A_p}{E_p^2 - E^2} + \frac{2}{\pi} P \int_{E_g}^{\infty} \frac{\xi \epsilon_2(\xi)}{\xi^2 - E^2} d\xi \qquad \text{Equation 3.20}$$

where A_p is the pole amplitude (units-energy^2) and E_p is the center of the pole energy (units-energy). Both A_p and E_p were left as fit parameters with starting values of 0 eV^2 and 7 eV, respectively. The dielectric functions were converted into the optical constants at each wavelength by the following relations (From J.A. Woollam Co. Inc.[7]):

$$n = \sqrt{\frac{\left[\varepsilon_1 + \sqrt{\left(\varepsilon_1^1 + \varepsilon_2^2\right)}\right]}{2}} \qquad \text{Equation 3.21}$$

$$k = \sqrt{\frac{\left[-\varepsilon_1 + \sqrt{\left(\varepsilon_1^1 + \varepsilon_2^2\right)}\right]}{2}} \qquad \text{Equation 3.22}$$

Several additional fit parameters were added to the film model including the thickness of the ALD film, roughness of the ALD film, and intermix-layer thickness. The substrate used for the optical model was 100 nm-thick Pt, which fully attenuated the light signal. The intermix model was added between the Pb-based film and the Pt-substrate to simulate interface growth effects that may lead to slightly different film properties. In this work, the interface thickness always fit as zero-nm unless otherwise specified. To avoid interactions from the bandgap of the crystallized perovskites, all ex-situ models were performed in the wavelength range of 500-1000 nm. Both the annealed and unannealed films fit well to the modified TL model, with values of the mean squared error (MSE) typically below 10.0 (calculated by WVASE32). The final model contained 6 unknowns compared to hundreds of measured Ψ and Δ values, therefore the film properties were quite over-determined. After the films were

characterized using ex-situ ellipsometry, the optical constants were extracted and fed into an n and k model for in-situ analysis using the FS-1 multi-wavelength ellipsometer.

X-ray Diffraction

The following section consists of a brief introduction to the general principles of X-ray diffraction, followed by the experimental conditions of the X-ray scans performed in this work. The principles presented in this section were adapted from Kittel,[11] but the exact treatment is slightly different.

The fundamental principle of X-ray diffraction is related to the elastic scattering of X-rays between crystal planes of a sample material which will interfere either constructively or destructively depending on the inter-planar spacing and the wavelength of the incident X-ray. The energy (E) of an X-ray is proportional to the frequency (ν) are related by Planck's Law,

$$E = h\nu \qquad \text{Equation 3.23}$$

where h is the Planck constant. The frequency is related to the wavelength (λ) by the following relation:

$$\nu = \frac{c}{\lambda} \qquad \text{Equation 3.24}$$

where c is the speed of light in vacuum. After combining Eqns. 3.23 and 3.24, solving for λ gives:

$$\lambda = \frac{hc}{E} \qquad \text{Equation 3.25}$$

For a given X-ray wavelength (λ), it is possible to predict what pairs of inter-planar spacing (d) and incident angles (θ) will produce constructive interference using Bragg's law:

$$2d \sin\theta = n\lambda \qquad \text{Equation 3.26}$$

where n is any positive integer. It is convenient to solve Bragg's law in terms of d and θ because in practice (for commercial X-ray diffraction equipment), λ is always known for a given X-ray source:

$$d = \frac{n\lambda}{2\sin\theta} \qquad \text{Equation 3.27}$$

$$\theta = \sin^{-1}\frac{n\lambda}{2d} \qquad \text{Equation 3.28}$$

Thus, if the inter-planar spacing (d) is known, one can predict which incident angles (θ) *could* produce constructive interference at different values of n. If a diffraction peak is observed at θ, one may calculate the inter-planar spacing d if n is determined by other means. A simple 2-D schematic of Bragg's law is shown below in Fig. 3.5.

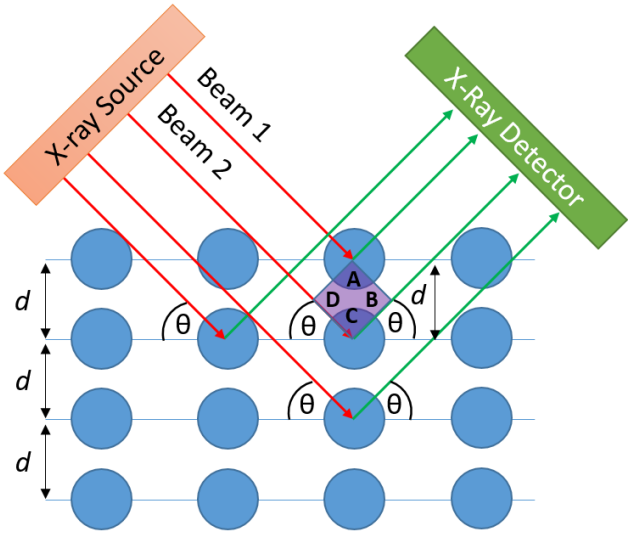

Figure 3.5: 2D Graphical representation of Bragg's law.

Figure 3.5 shows a coherent, collimated beam of X-rays originating from an X-ray source which are elastically scattered from atoms residing in a cubic lattice. The flux is measured by a detector. Beams 1 and 2 are labelled. The corners of the purple diamond are labelled A, B, C, and D in clockwise fashion. Point A intersects the top row of atoms and Beam 1. Point C intersects the second row of atoms and beam 2. Segment AD is normal to the incoming beams, while section AB is normal to the scattered beams. The scattered X-rays will stay in phase if they travel a distance that differs by some integer multiple of the wavelength. Therefore, when

$$Length\ of\ Segments\ DC + CB = n\lambda \qquad \text{Equation 3.29}$$

beams 1 and 2 remain in phase. Since the angles formed by both AD and DC, and AB and CB are 90°, it follows that,

$$Length\ of\ DC = Length\ of\ CB \qquad \text{Equation 3.30}$$

and,

$$Length\ of\ Segment\ CB = d \sin\theta \qquad \text{Equation 3.31}$$

Substitution of equations M8 and M9 into equation M7 reduces to Bragg's law.

The majority of the X-ray diffraction scans presented in this work were performed on a Rigaku MiniFlex benchtop X-ray diffractometer using a copper anode and the θ-2θ configuration. The samples were measured with identical measurement parameters. The X-ray tube was held at 40 kV and 15 mA. Each scan was performed within a measurement range of $10° \leq 2\theta \leq 70°$ and took approximately 3.5 minutes to complete. The scan speed was 20°/min at a 0.02° step increment, and the tool was equipped with a D/tex Ultra silicon strip detector.

The copper X-ray source emits X-rays at different energies. The Table 3.1 below characterizes the emission spectra of the highest intensity copper radiation at 40 kV. (from Deutsch[12])

Table 3.1: Copper Emission Spectra

Emission Spectrum Line	**Energy (eV)**	**Wavelength (λ, nm)**	**Intensity (Relative to $K\alpha_1$ for $K\alpha$ and $K\beta_{1,3}$, for $K\beta$)**
$K\alpha_{11}$	8047.84	0.15406	0.94
$K\alpha_{22}$	8045.29	0.15411	0.01
$K\alpha_{22}$	8028.02	0.15444	0.34
$K\alpha_{22}$	8026.56	0.15447	0.11
$K\beta_1$	8905.49	0.13922	0.74
$K\beta_3$	8903.10	0.13926	0.35
$K\beta'$	8897.12	0.13935	0.07
$K\beta_1''$	8908.49	0.13918	0.18
$K\beta_2''$	8911.15	0.13913	0.04

The $K\alpha$ emission spectra are higher in intensity than $K\beta$, and are thus preferred due to the improved signal. The $K\beta$ X-rays are often filtered out by a nickel filter, at the cost of reduced $K\alpha$ flux, but $K\beta$ reflections can remain from strong peaks. The X-ray beam used for the scans performed in this work utilized a thin nickel foil filter, so the platinum $K\beta$ peak is reduced but still present, and is labelled in the relevant charts.

Rutherford Backscattering

The following is a brief overview of the operating principles of Rutherford backscattering (RBS), which is the primary technique used to determine the elemental composition of the ALD films grown in this work. The basics of the analysis and certain

experimental conditions are detailed here, however only the elemental compositions determined by the RBS analysis are contained in the results section of this work.

The experimental setup for the RBS measurements performed in this study chiefly consists of a vacuum chamber, a particle accelerator, a sample holder, and two detectors. The particle accelerator accelerates a beam of charged alpha particles (He^{2+} nuclei) towards a sample (in this case a thin film on a silicon wafer) oriented normal to the beam. The angle of the sample relative to the beam is shifted only slightly from the normal to avoid ion channeling effects. The energy of the He^{2+} ions is 2.275 MeV. The two detectors, labelled the normal detector and grazing detector, were oriented at 20° and 80° relative to the incident beam vector, respectively (which correspond to backscattering angles of 160° and 100°). The detectors are divided into channels that separate the backscattered ions by their energies. Each channel records the number of incident ions at the given energy. The resulting data is expressed as peaks or plateaus over the range of measured energies with features characteristic of the elements sensed by the bombarding alpha particles. As will be described in detail below, for a given incident He^{2+} ion energy and scattering angle, each element will scatter a He^{2+} ion with a characteristic scattered energy that can be measured to identify the element. The concentration of that particular element can be determined by the flux of the scattered He^{2+} ions at the characteristic energy level (which is represented by a peak or plateau).

The Rutherford formula describes differential cross section, σ, which is a function of atomic number of the incident alpha particle (Z_1), the atomic number of target (or sample) particle (Z_2), the energy of the incident alpha particle E_0 (in this case 2.275 MeV), and scattering angle θ: (from Chu[13])

$$\sigma = \frac{Z_1 Z_2 e^2}{E_0 \sin^4(\theta/2)} \qquad \text{Equation 3.32}$$

where e is the charge of one electron. The total (ideal) area (A) underneath a given Z_2 peak is given by the following: (from Chu[13])

$$A = Q\Omega\sigma N t \qquad \text{Equation 3.33}$$

where Q is the total integrated charge of the alpha particles, which was typically set to 40.0 micro-Coulombs for the analyses presented in this work. Ω is the detector solid angle which is a function of the distance between the detector and sample, σ is defined by Eqn 3.32, N is number of atoms per unit volume, and t is the thickness of the sample (or film). It follows from Eqns. 3.32 and 3.33 that:

$$A = cZ_2 N t \qquad \text{Equation 3.34}$$

where c is a constant defined by fixed values of the experimental parameters Z_1, E_0, θ, Q, and Ω. At this point, if we measure the total flux at a specific scattering angle (for a chemically homogeneous sample), we can calculate either Z_2, N, or t, if we knew the other two variables, without knowledge of the energy of the scattered alpha particle. However, much of the power of RBS is derived from the fact that the detector separates the ion flux energies into separate channels. Based on energy and momentum conservation arguments in Chu[13] and Perriere[14]:

$$E_1 = K_M E_0 \qquad \text{Equation 3.35}$$

$$K_M = \left(\frac{m_1 \cos\theta + \sqrt{m_2^2 - m_1^2 (\sin\theta)^2}}{m_1 + m_2} \right)^2 \qquad \text{Equation 3.36}$$

where E_1 is the energy of the scattered alpha particle under ideal conditions, E_0 is the energy of the incident alpha particle, K_M is the kinematic factor (Eqn. 3.36) and m_1 and

m_2 are the masses of the incident alpha particle and target particle, respectively. For a given E_0 and scattering angle θ, the target particle of mass m_2 will produce a flux peak at a characteristic energy, E_1. Simply put, the peak position (along the measured scattered particle energy, *E*) informs which particle is doing the scattering, and the area under the peak determines the product of the atom density, N, and thickness, t. The values of either *N* or *t* may be calculated if the other is known by other characterization methods.

The samples measured in this work are multi-layered films, each with different thicknesses, compositions, and densities. In order to quantify the elemental composition of unknown films, the measured particle flux between $E + \mathrm{d}E$ vs E spectra are fit to a model which assumes either the thickness or the density of the films in the stack. The ideal spectra containing i species may be defined as follows, with $N(E)\mathrm{d}E$ defined as the number of alpha particles detected between E and $E + \mathrm{d}E$: (from Perriere[14])

$$N(E)\mathrm{d}E = \sum_i \; C_i(x_i)\mathrm{d}x_i \frac{\mathrm{d}\sigma_i}{\mathrm{d}\Omega}[E(x_i)]n\Omega \qquad \text{Equation 3.37}$$

Where $C_i(x_i)$ is the concentration of species i at depth x_i, n is the number of incident alpha particles, and $E(x_i)$ is the energy of the scattered alpha particle at depth x_i. The quantity $\frac{\mathrm{d}\sigma_i}{\mathrm{d}\Omega}$ may be defined as the scattering cross section, which is shown in Eqn. 3.37 to be a function of scattered particle energy at depth x_i. A measured spectrum may be fit to Eqn. 3.37 to solve for unknown concentrations. The fit is far more reliable if the thickness and/or density of the films in the sample film stack are known to at least moderate precision.

In reality, the peaks themselves can undergo broadening as a result of stopping forces (namely electrons) in the target medium. Thus, there is a difference, ΔE, between the theoretically derived peak position E_1, and the actual detected energy, which is given by: (from Perriere[14])

$$\Delta E = X\left[K_M \varepsilon(E_{in}) + \left({}^{1}/_{\cos\theta}\right)\varepsilon(E_{out})\right] \qquad \text{Equation 3.38}$$

Where X is the penetration depth of the alpha particle, $\varepsilon(E_{in})$ is the stopping cross section of the incoming path, $\varepsilon(E_{out})$ is the stopping cross section of the outgoing path, E_{in} is the average energy of an incoming alpha particle, and E_{out} is the average energy of an outgoing alpha particle.

In summary, RBS is a powerful technique used to quantify elemental concentrations and thicknesses of thin film samples. RBS data presents as an integrated particle flux or charge versus measured particle energy at a particular scattering angle, which is defined by the experimental parameters. Peaks are present in the RBS data that are characteristic to a particular element. Equation 3.34 presents the theoretical flux produced by a particular element for a specific set of experimental parameters, and is a function of the density and thickness of the element. Equation 3.35 may be used to identify an unknown element in a measured sample by the energy of the particles at a measured peak. For multi-element and multi-layered films, Eqn. 3.37 may be used to calculate the unknown concentration of elements as a function of depth, however, fitting software is typically implemented to produce the analysis.

References

[1] Chipman RA. Handbook of Optics, Vol. II (Devices, Measurements and Properties). 2nded. New York, NY: McGraw Hill, Inc.:1994;22.

[2] [Internet] [Cited 2019 Jan 19] Johs B. http://www.film-sense.com/technology/ellipsometry/
[3] Cauchy MAL. Me'moire sur la Dispersion de la Lumie`re. Calve, Prague. 1836
[4] Azzam RMA. Division-of-amplitude photopolarimeter based on conical diffraction from a metallic grating. *Appl Opt.* 1992;31.
[5] Azzam RMA. Division-of-Amplitude Photopolarimeter (DOAP) for the simultaneous measurement of All Four Stokes Parameters of Light. *Opt Acta.* 1982;29:685-689.
[6] [Internet] [Cited 2019 March 4] Lodewijks K. http://www.kristoflodewijks.be/research/theoretical-background/6-spectroscopic-ellipsometry/
[7] J.A. Woollam Co., Inc. Guide to Using WVASE® Spectroscopic Ellipsometry Data Acquisition and Analysis Software. Version 3.690.: 2008
[8] Garcia-Caudrel E, De Martino A, Gaston JP, et al. Application of Spectroscopic Ellipsometry and Mueller Ellipsometry to Optical Characterization. *Appl Spectrosc.* 2013;67.
[9] J.A. Woollam Co., Inc. M-2000F Spectroscopic Ellipsometer Hardware Manual. Version M2FHB200RT: 2001.
[10] Jellison GE, Modine FA. Parametrization of the optical functions of amorphous materials in the interband region. Appl Phys Lett. 1996;69:371-373.
[11] Kittel C. Introduction to Solid State Physics. 8thed. John Wiley and Sons, Inc.: 2005
[12] Deutsch M, Holzer G, Hartwig J, et al. Kα and Kβ x-ray emission spectra of copper. *Phys Rev A.* Vol.:1995;51.
[13] Chu WK, Mayer JW, Nicolet MA, et al. Principles and Applications of Ion Beam Techniques for the Analysis of Solids and Thin Films. *Thin Solid Films.* 1973;17:1-41.
[14] Perriere J. Rutherford backscattering spectrometry. *Vacuum.* 1987;37:429-432.

Chapter 4: Fabrication

Introduction

The following chapter discusses the fabrication techniques used to produce the samples presented in Chapters 5-8. First, a brief overview of the fabrication facility itself is discussed, followed by a detailed description of the ALD processes. The sample preparation, including the lower electrode fabrication and micromachining steps, are then detailed schematically in sequence with several images of real devices.

Fabrication Facility

Samples were prepared in the Specialty Electronic Materials and Sensors Cleanroom (SEMASC) within the United States Army Research Laboratory (Adelphi, Maryland, USA). The SEMASC contains 10,000 ft^2 Class 100 and 5,000 ft^2 Class 10 cleanroom space. The ALD platform, wet benches, evaporators, and etch tools referenced below were located in the class 100 space, while the CLC 200 sputter platform and tube furnaces were located in the class 10 space. All electrical measurements were performed in the class 10 space. The cleanroom was arranged in a "cleanroom-chase" configuration with laminar air-flow separating the clean and gray spaces.

ALD Processes

The ALD processes for ternary and quaternary oxides described in this work consisted of alternating binary oxide processes (defined in Chapter 1 as the ALD processes for

PbO_x, TiO_x, ZrO_x and HfO_x) which were combined to form a super-cycle which was repeated to achieve the desired film thicknesses. The details related to the super-cycles used are discussed in the relevant results sections (chapters 5, 6, 7 and 8), however the binary oxide process details are discussed in this chapter. For consistency, the process parameters for the binary oxides remained constant for all of the PTO, PZO, PZT, PHO, and PHT depositions.

ALD PbO_x

Lead oxide, or PbO_x was grown by ALD using $Pb(DMAMP)_2$ (98% purity) procured from Strem Chemicals, Inc. contained within a 50 mL stainless steel ampoule. The ampoule was heated to maintain a temperature gradient between the shut-off valve and the chemical at the bottom of the ampoule. The temperature of the shut-off valve was controlled and held at constant 125 ± 2 °C. The temperature at the bottom of the ampoule was not controlled directly but typically measured 88 ± 2 °C. The precision of the temperature of the shut-off valve was prioritized over that of the ampoule in order to prevent condensation of the solid precursor. The uncertainty in the ampoule temperature mainly resulted from changes in the cleanroom temperature that varied somewhat day-to-day. No temperature change was observed as a result of the gas charging. The vapor pressure of the $Pb(DMAMP)_2$ was not large enough to produce a pressure pulse in the process chamber at 88 °C, so the ampoule was charged with Ar after each cycle using the method described in Chapter 3. To improve the thickness uniformity and to maximize precursor economy, $Pb(DMAMP)_2$ was mounted on two

sources, 180° apart (shown schematically in chapter 3). The sequence of the PbO_x sub-cycle is shown below in Fig. 4.1.

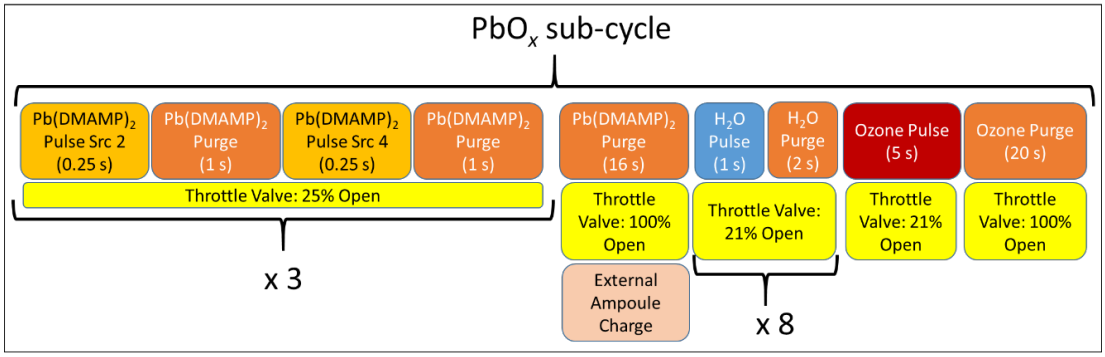

Figure 4.1: Schematic of binary PbO_x sub-cycle

At first, the throttle valve was set to 25% open to increase the precursor residence time in the chamber. Then, $Pb(DMAMP)_2$ doses were alternated from sources 2 and 4 (3x each) to fully deplete the Ar charge. Following the $Pb(DMAMP)_2$ doses, the throttle valve was opened to 100% to help to evacuate the chamber. During the purge step, the $Pb(DMAMP)_2$ ampoules were recharged with Ar. Following a 16-s final $Pb(DMAMP)_2$ purge, the throttle valve was set to 21% open to increase further the residence time during the oxidation step. The film was then oxidized using 8 consecutive 1-s H_2O (demineralized) pulses followed by a 5-s ozone dose. The throttle valve was fully opened after the ozone dose to allow for complete evacuation during the 20-s purge.

ALD TiO_x

The binary TiO_x ALD process was based on the alkyl-amide precursor TDMAT. TDMAT PURATREM (99.99% purity) was procured from Strem Chemicals, Inc and housed within a custom chemical ampoule manufactured by Precision Fabricators, LLC. The custom ampoule had a 350-cc working volume with a single-stem

pneumatically actuated shutoff valve and ½'' VCR fill port. The ampoule was held constant at 90 °C to provide sufficient vapor pressure. The TiO_x sub-cycle is shown schematically below in Fig. 4.2.

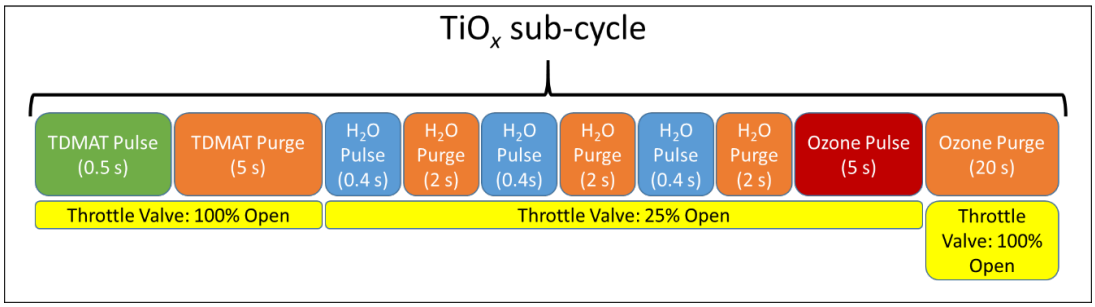

Figure 4.2: Schematic of binary TiO_x sub-cycle

The TDMAT was first pulsed for 0.5-s with the throttle valve 100% open. The reactor pressure with the throttle valve at 100% open was approximately 1.8 Torr. The TDMAT was then purged for 5-s under inert Ar gas flow. In previous experiments, a 5-s purge time was shown to deliver the best thickness uniformity for the binary TiO_x oxide process. Once the throttle valve was set to 25% open, three consecutive 0.4-s demineralized H_2O pulses were used to oxidize the film followed by a 5-s ozone pulse. The H_2O pulses caused pressure spikes in the process chamber approximately 200 mTorr above the base pressure, which was approximately 4.5 Torr at the 25% open throttle valve set position. The throttle valve was then opened to 100% for the final 20-s purge.

ALD ZrO_x

The binary ZrO_x sub-cycle is nearly identical to the TiO_x sub-cycle, with TDMAZ substituted for TDMAT. The TDMAZ was contained in an identical ampoule as the TDMAT, but the TDMAZ was heated to 80 °C, which provided sufficient vapor

pressure. The TDMAZ purge time was set to 10-s instead of 5-s because 10- s yielded better non-uniformity for the binary ZrO_x ALD process. The process is shown schematically below in Fig. 4.3.

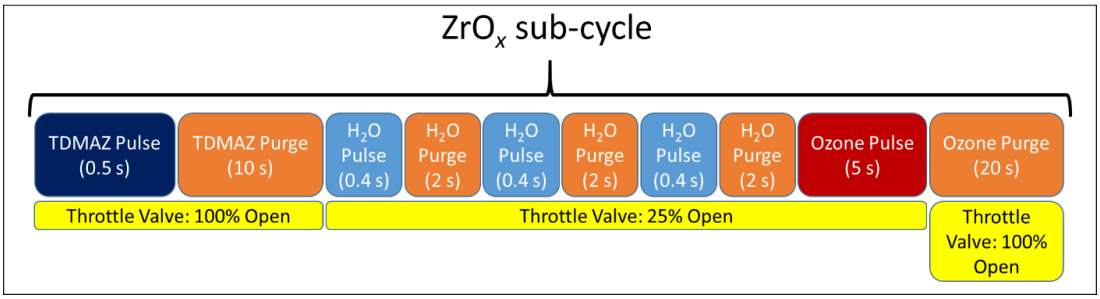

Figure 4.3: Schematic of binary ZrO_x sub-cycle

ALD HfO_x

The binary HfO_x ALD sub-cycle follows the same pattern as the TiO_x and ZrO_x binary sub-cycles, with TDMAH substituted as the Hf precursor. The TDMAH ampoule was heated to 82 °C. Other than the precursor, the only difference between the HfO_x and ZrO_x processes is that the TDMAH dose was set to 0.25-s versus 0.5-s because a 0.25-s dose was shown to provide a sufficiently saturating dose for ALD HfO_x. A schematic is shown below in Fig. 4.4.

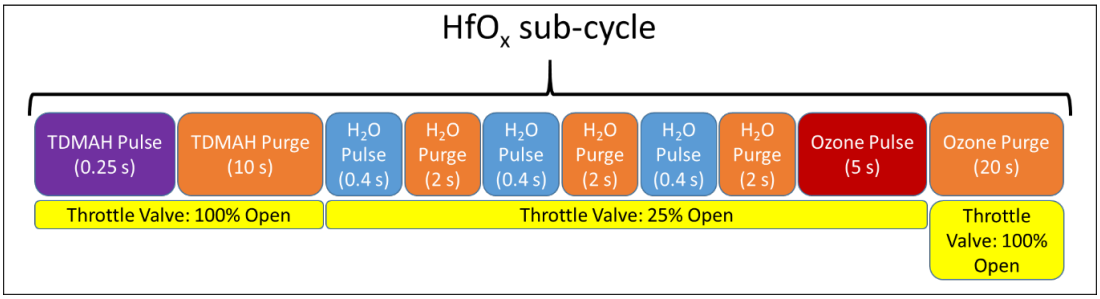

Figure 4.4: Schematic of binary HfO_x sub-cycle

Ternary Super-cycles

Ternary oxide super-cycles consisted of combinations of binary oxide cycles in varied ratios. The ratio of the binary oxide cycles influenced the elemental composition and growth rate of the as-grown films. A schematic of the PTO super-cycle is shown below in Figure 4.5.

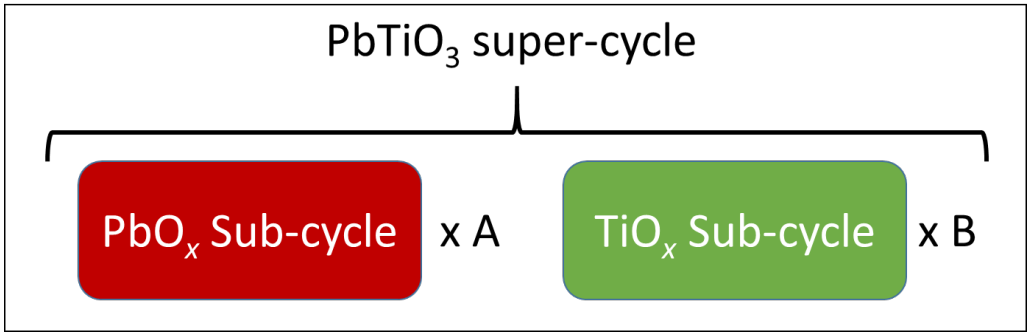

Figure 4.5: Schematic of $PbTiO_3$ super-cycle

To vary the Pb/Ti cation composition, the variable *A* was varied from 1 to 5 while the variable *B* was varied from 1 to 2. The range of *A* is wider than *B* because the PbO_x incorporated at a lower growth rate than the TiO_x. Therefore, more cycles of PbO_x than TiO_x were required to obtain the ideal $PbTiO_3$ composition. The ternary super-cycles for PZO and PHO follow the same pattern, and are shown below in Figs. 4.6 and 4.7, respectively.

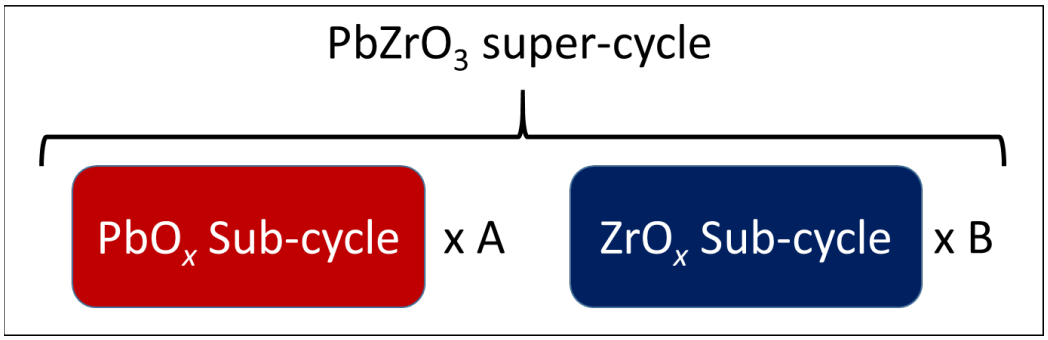

Figure 4.6: Schematic of $PbZrO_3$ super-cycle

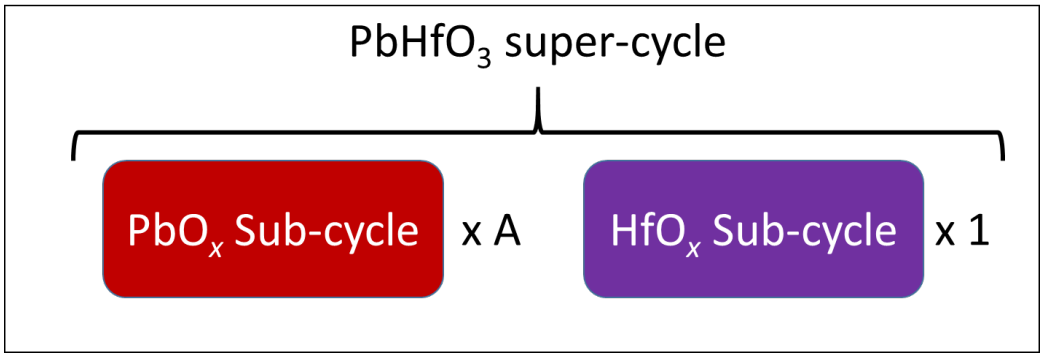

Figure 4.7: Schematic of $PbHfO_3$ super-cycle

For the PZO super-cycle the variable *A* was only varied between 5 and 6, while the variable *B* was varied between 1 and 4. The variable *B* was varied over a wider range compared to the PTO and PHO processes because of difficulties incorporating Zr into the PbO_x films. It should be noted that the PZO super-cycle did not appear to yield stoichiometric $PbZrO_3$, and the Zr incorporation into subsequent PZT was limited to about 5 atomic % (this phenomenon is detailed in Chapter 6). Alternatively, the PHO super-cycle yielded slightly Pb-rich PHO (discussed in Chapter 7) when the variable *A* was set to 4. For the PHO super-cycle, the "A" variable was varied between 3 and 4 to adjust the level of Pb-excess, while the "B" variable was left at 1 (which is reflected in Fig. 4.7).

Quaternary Super-cycles

Several different super-cycle strategies were implemented for PZT in order to investigate the limited Zr incorporation thoroughly. The super-cycle labelled "primary" in Fig. 4.8 was used for the majority of the PZT film growths and is simply a combination of PTO and PZO super-cycles.

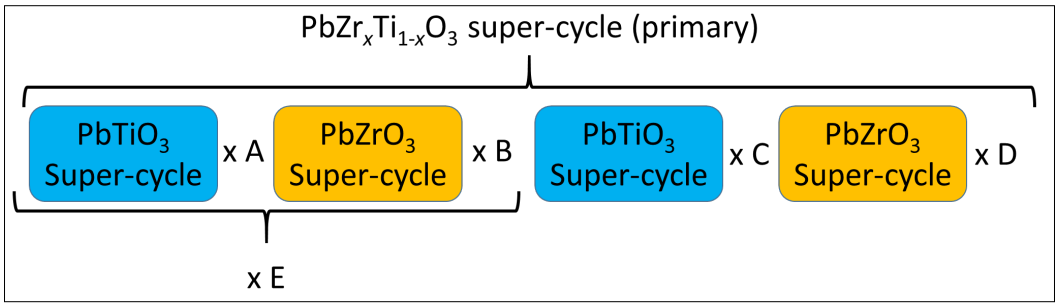

Figure 4.8: Schematic of the primary $PbZr_xTi_{1-x}O_3$ super-cycle

The PTO and PZO were alternated in order to maximize mixing for the various PTO:PZO super-cycles ratios. For the case of a 9:1 PTO:PZO ratio, the variables *A*, *B*, and *E* were set to zero, while *C* and *D* were set to nine and one, respectively. For a PTO:PZO ratio of 15:5, the variable *A* was set to three, *B* was set to one, and *E* was set to five, while *C* and *D* were both set to zero. The specific super-cycle ratio and dose order is specified in the relevant results section in Chapter 6.

Since Zr content was hard to incorporate into the ALD PZT, several alternative super-cycles labelled 1-3 (Figs. 4.9, 4.10, and 4.11, respectively) were investigated.

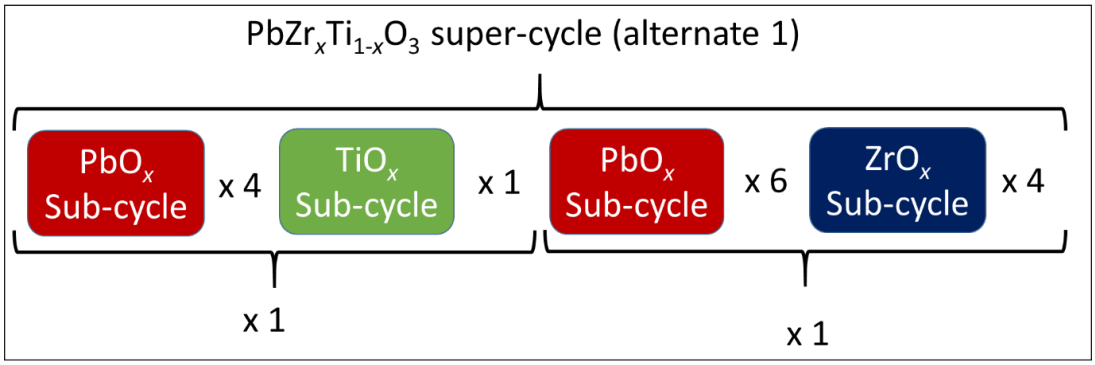

Figure 4.9: Schematic of the first alternate $PbZr_xTi_{1-x}O_3$ super-cycle

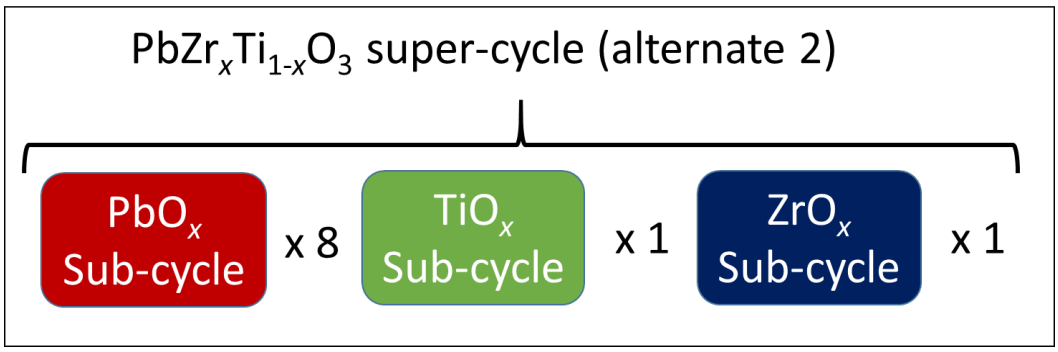

Figure 4.10: Schematic of the second alternate $PbZr_xTi_{1-x}O_3$ super-cycle

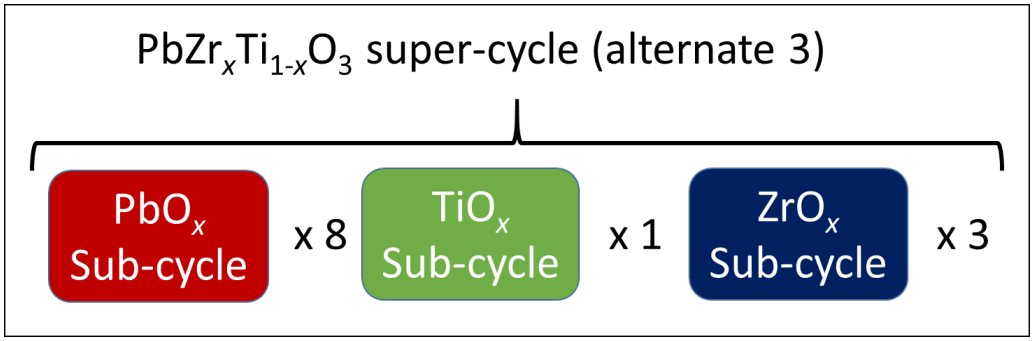

Figure 4.11: Schematic of the third alternate $PbZr_xTi_{1-x}O_3$ super-cycle

Since Hf incorporated easily into the ALD PHT (unlike Zr incorporation into ALD PZT), only a single super-cycle dose strategy was successful in synthesizing PHT with sufficient Hf content (Fig. 4.12).

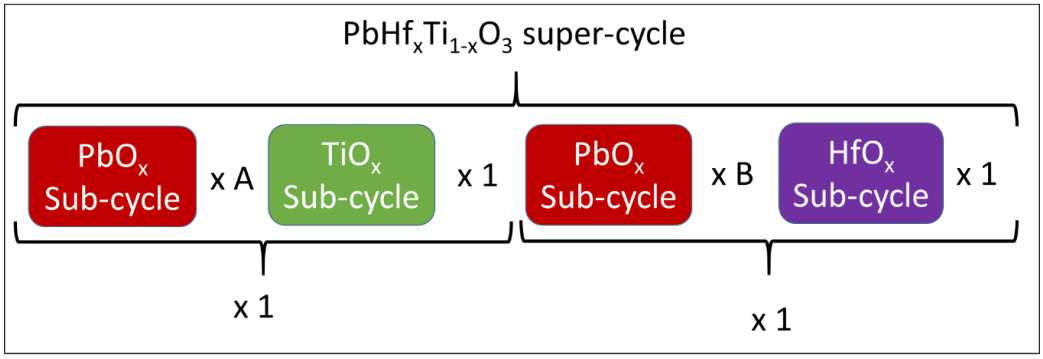

Figure 4.12: Schematic of the primary $PbHf_xTi_{1-x}O_3$ super-cycle

Sample Fabrication

Bottom Electrode

In this work {111}-textured Pt is used as the growth surface for all films processed for electrical characterization. {111}-textured Pt has proven to be a suitable lower electrode capable of reproducibly templating the growth of manufacturing-quality ferroelectric films.[1] Ultimately a $Pt/TiO_2/SiO_2/Si$ electrode film stack is required to ensure the optimum {111} Pt bottom electrode texture, adequate PZT film adhesion, chemical resistance to interfacial reactions and oxidation at high (700˚ C) process temperatures, and limited diffusion of titanium through the bottom electrode.[2] The following is a summary of the process sequence used in this work to fabricate the bottom electrode, which is modeled after Fox et al.[1] Although the $Pt/TiO_2/SiO_2/Si$ electrode film-stack is not grown by ALD, it is important to note that each layer in the film-stack could be substituted with suitably tuned ALD films albeit with poorer overall {111} Pt texture.

Low-resistivity (100)-oriented prime 150 mm wafers with 5000 Å +/- 5% thermal oxide were procured from Addison Engineering, Inc. or alternatively, pristine wafers were prepared by tube furnace oxidation (Tystar® Titan 3800) whereby 5000 Å of wet thermal oxide was grown at 1100 C for 38 min and 40 s. See Fig. 4.13a below for a graphical representation of the film stack cross section.

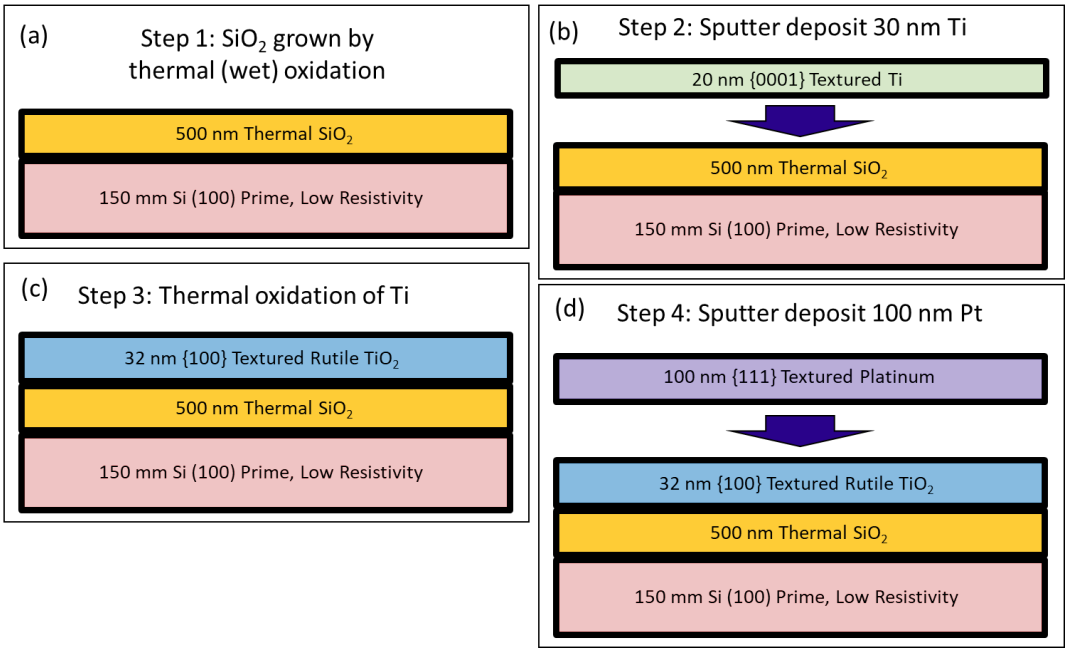

Figure 4.13: Graphical representation of the a) SiO_2 growth step, b) Ti sputter deposition step, c) TiO_2 thermal oxidation step, and d) Pt sputter deposition step.

The purposes of the SiO_2 film are to provide an elastic layer for subsequent MEMS structures and to electrically isolate the lower electrode from the underlying Si. Different films including ALD-grown Al_2O_x or other insulating oxides could be substituted for the silicon dioxide layer depending on the application.

Titanium metal was sputtered onto the silicon dioxide film in a commercial cassette-to-cassette handled Unaxis (Evatec) Clusterline 200 sputter tool using a purpose-built module at 40 °C. The titanium target (99.99% purity) was 260 mm in diameter, and the substrate was held fixed at 50 mm from the target. The nominal titanium thickness was 30 nm and is oriented with a {0001} hexagonal structure. The titanium deposition was monitored using a four-point probe where the target sheet resistance was 60 ohm/sq. The sputtering chamber undergoes a 30 s gas stabilization before plasma ignition. The critical processing parameters are summarized below in Table 4.1, while further details may be found in Fox et al.[1] Figure 4.13b includes a graphical representation of the film-stack after the titanium deposition.

Table 4.1: Process conditions for Ti sputter deposition

Process Parameter	Value
Chuck Gas Flow (Ar, sccm)	5.0
Chuck Gas Pressure (mbar)	8.0
Chuck Temperature (°C)	40
Chamber Pressure (mbar)	$5x10^{-3}$
Process Time (s)	35
DC Generator Power (w)	500
Chamber gas flow (Ar, sccm)	30

The titanium films were then oxidized in the Tystar® Titan 3800 furnace in a dedicated metals oxidation quartz tube. TiO_2 thickness was 32 nm and crystallized in the rutile phase with primarily {100} orientation. The TiO_2 thickness was measured by spectroscopic ellipsometry, and the Ti sputtering time was adjusted on subsequent runs if the oxide thickness deviated from 32 nm. The oxidized film stack containing TiO_2 is shown in Figure 4.13c.

Platinum was then sputtered onto the TiO_2 film in the Unaxis (Evatec) Clusterline 200 using a different purpose-built module with DC magnetron sputtering at 500 ˚C substrate temperature. The Pt target was 99.99% pure and 260 mm in diameter. Prior to substrate loading but before sputtering, the Pt-chamber underwent a 30 s gas stabilization. The critical process parameters are summarized below in Table 4.2. The substrate was held at a fixed 50 mm distance from the target, and the nominal sputtered platinum thickness was 100 nm. Platinum is a common lower electrode material used for PTO and PZT growth by sol-gel.[3] Platinum is also a commonly grown ALD metal, which is convenient for transitioning to 3D structures. Pt grown by ALD that was densified by RTA at 500 ˚C has been previously shown to be a suitable bottom electrode for PZT.[4] For the purposes of process evaluation, {111} oriented sputtered Pt films are used as the starting ALD growth surface. Note that the sputtered Pt did not

require RTA densification. A schematic of the film stack following Pt-sputtering is in Fig. 4.13d. Typically one or more cassettes of wafers were processed at a time and stored (often for months) until needed for PZT (or other perovskite) deposition.

Table 4.2: Process conditions for bottom platinum sputter deposition

Process Parameter	**Value**
Chuck Gas Flow (Ar, sccm)	5.0
Chuck Gas Pressure (mbar)	8.0
Chuck Temperature (°C)	500
Chamber Pressure (mbar)	$5x10^{-3}$
Process Time (s)	67
DC Generator Power (w)	500
Chamber gas flow (Ar, sccm)	50

ALD Film Processing

For the ALD films grown in this study, the number of cycles was selected so that 100 nm of film was deposited at a time. For simplicity, a schematic of ALD PZT is shown in Fig. 4.14. A similar schematic could describe ALD PTO, PZO, PZT, PHO, or PHT. Fig. 4.14, shown below, also details the film stack following RTA.

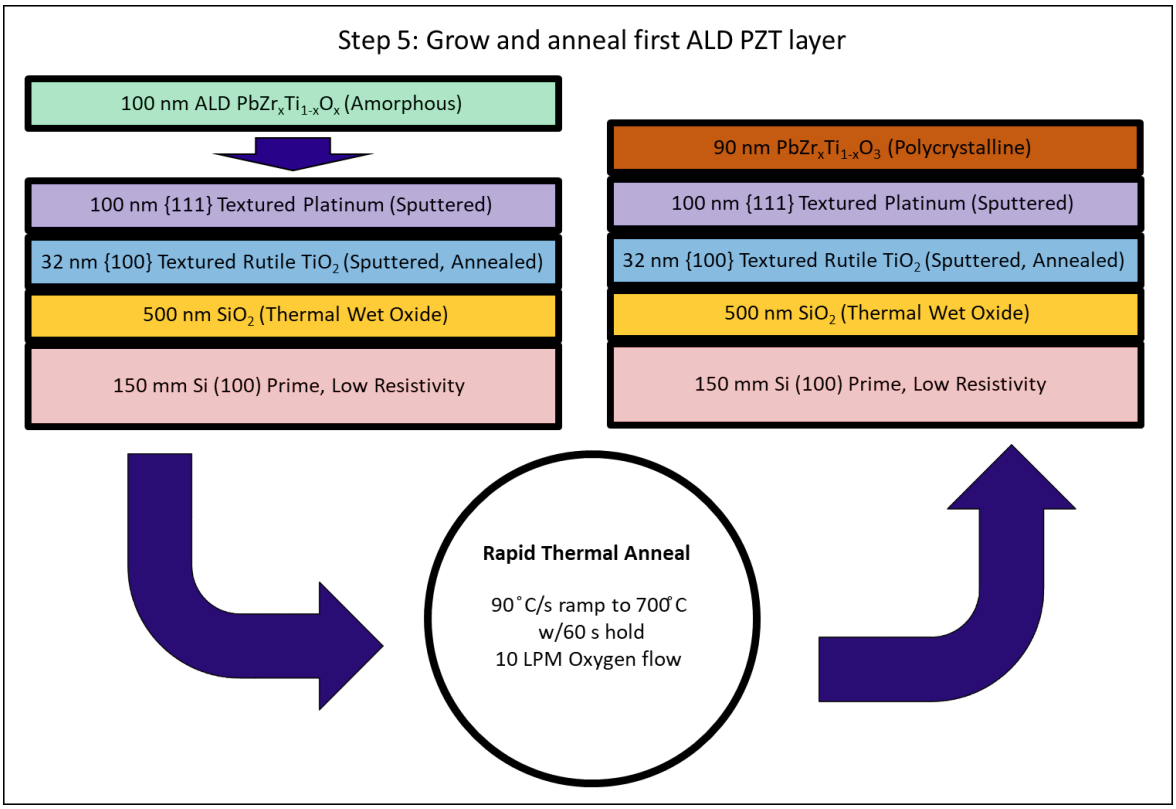

Figure 4.14: Graphical representation of the ALD and RTA step.

The ALD PZT film thickness was measured before and after annealing by both in-situ and ex-situ ellipsometry (see characterization subsection in this chapter). Following RTA, the films typically roughened and shrank by about 10% due to densification. Most of the films processed for electrical characterization received an additional ALD coating and anneal. Those steps are shown below in Fig. 4.15. The ALD and RTA steps were repeated as many times as necessary to grow the desired film thickness.

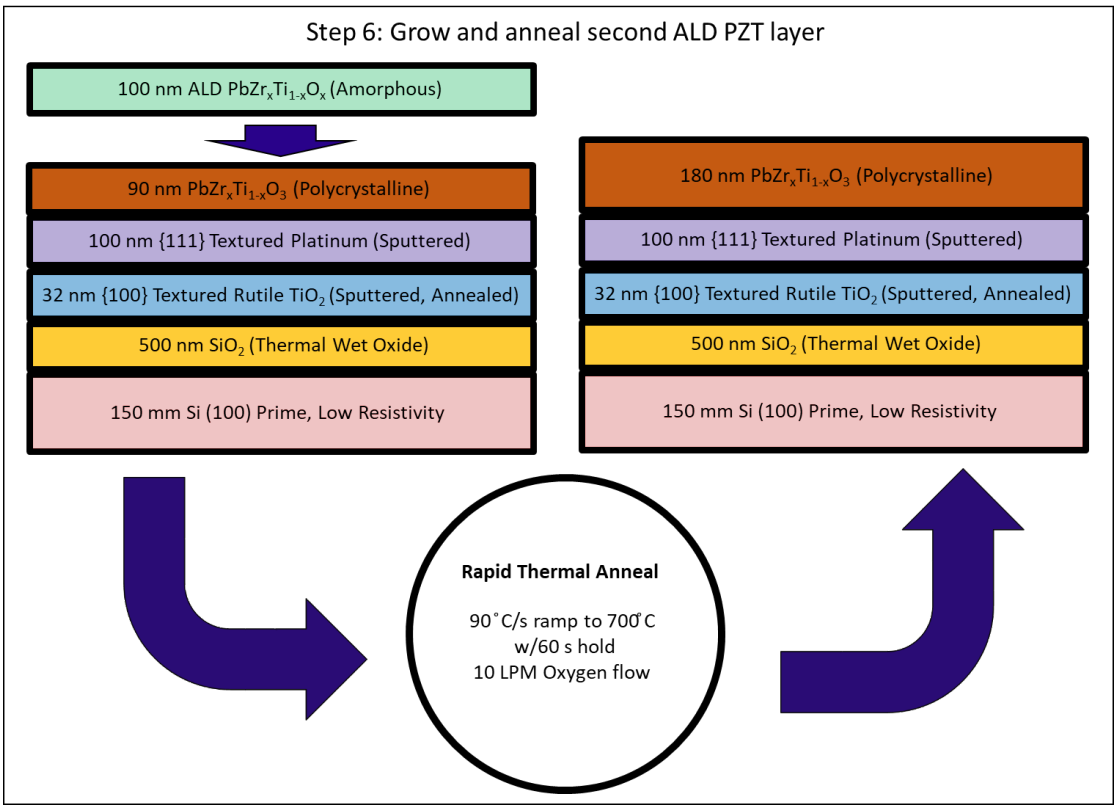

Figure 4.15: Graphical representation of the second ALD and RTA step.

Capacitor Fabrication

After the final PZT crystallization step, the top electrode was sputtered at 500 ˚C in the same Pt-chamber as the bottom electrode. A similar recipe to that used for the bottom electrode was used for the top electrode, but the time was cut approximately in half to reduce the deposited thickness to about 50 nm. A graphical representation is shown below in figure 4.16. Key process conditions are shown below in Table 4.3.

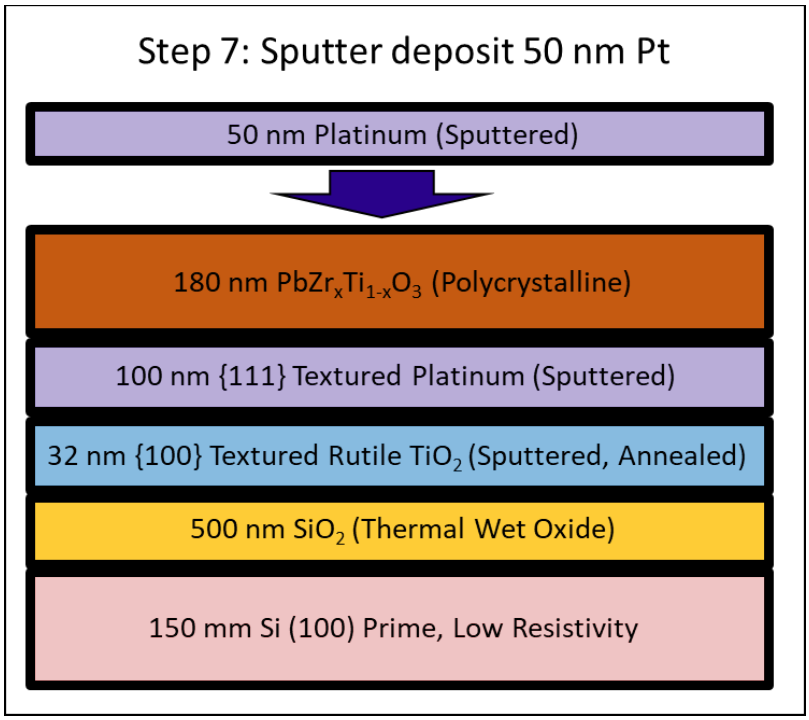

Figure 4.16: Graphical representation of the second ALD and RTA step.

Table 4.3: Process conditions for top platinum sputter deposition

Process Parameter	**Value**
Chuck Gas Flow (Ar, sccm)	5
Chuck Gas Pressure (mbar)	8
Chuck Temperature (°C)	500
Chamber Pressure (mbar)	$5x10^{-3}$
Process Time (s)	33
DC Generator Power (w)	500
Chamber gas flow (Ar, sccm)	50

After sputter deposition, the films were coated with 2-µm of AZ 5214 photoresist, followed by a 2-mm edge-bead removal in an EVG cassette-loaded track-coater. The film cross-section is graphically represented below in figure 4.17.

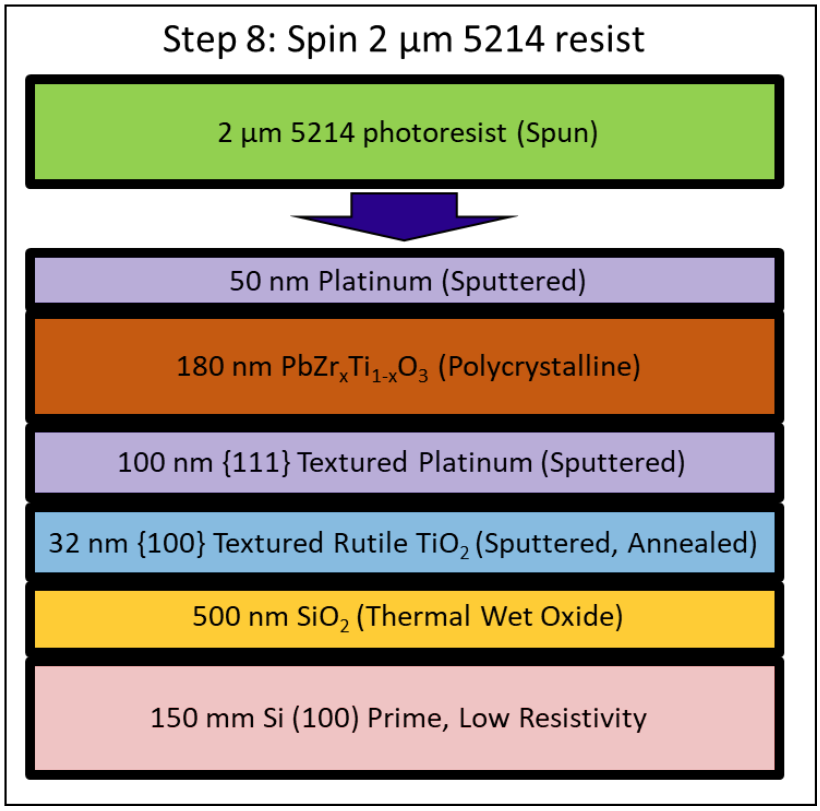

Figure 4.17: Graphical representation of 5214 resist spin step.

Bis(trimethylsilyl)amine [hexamethyldisilazane, or HMDS] was used as an adhesion promoter. Vapor-phase HMDS was exposed to the substrate (heated to 140 °C on a hotplate inside an oven) for 45 seconds, following a 30.0 second thermal equilibrium step. Upon unloading, the substrate was allowed to cool for 45.0 seconds before the resist coat step. 15 ml of AZ 5214 resist was evenly dispensed over a period of 15 seconds. After a 1 second delay, the wafer was spun at 500 RPM (250 RPM/s acceleration) for 5 seconds, before the final 2000 RPM spin (5000 RPM/s acceleration) for 40 seconds. The back of the wafer was then rinsed for 10 seconds before deceleration. Following the resist coating, the resist was baked at 110 °C for 1 minute and 15 seconds with the exhaust on, followed by 45 seconds with the exhaust off.

An edge bead removal program was used to remove the outermost 2 mm of resist. The edge bead solvent was a mixture containing 70% isopropanol and 30% acetone. The substrate was spun at 650 RPM (5000 RPM/s acceleration) during which time the IPA/acetone mixture was dispensed for 30 seconds. The substrate was then accelerated to 1000 RPM (5000 RPM/s acceleration) and rinsed on the backside for 10 seconds prior to deceleration.

The photoresist was patterned using a top electrode mask set, which typically contained arrays of patterns for capacitors and cantilevers for ferroelectric and piezoelectric measurements, respectively. The details of device dimensions are contained within the relevant results sections in subsequent chapters. . Low-vacuum contact alignment was used with a 20 μm spacing. Following 8-s exposure at constant 9.0 mW/cm^2 intensity on the SUSS-Microtech MA-6 aligner, the resist was developed using AZ 300 MIF TMAH-based developer in the EVG track coater, which left a positive image. The wafers were developed in a developer module in which the substrate was exposed to 12 seconds of developer (which is sprayed from a nozzle) without spinning. Following a 32 second delay, the wafers were spun slowly at 50 RPM (acceleration 50 RPM/s) to remove excess liquid. The substrate was then exposed to an additional 12 seconds of developer while spinning (still at 50 RPM) before decelerating to 0 RPM (5000 RPM/s deceleration) and then held for 32 seconds. DI water was then dispensed from the developer arm for 40 seconds to rinse-off the developer. The substrate was then spun up to 300 RPM (100 RPM/s acceleration) for a 10 second rinse. The substrate was finally spun up to 2000 RPM (5000 RPM/s acceleration) for 40 seconds to clear remaining liquid before deceleration. Upon unloading from the track tool, the wafers

were rinsed with deionized water by hand on the front and back to clear residual developer further. A representation of the newly developed resist is shown below in Fig. 4.18. The developed films are plasma-etched in a PVA Tepla platform using a 5-min descum program with parameters described in the Table 4.4.

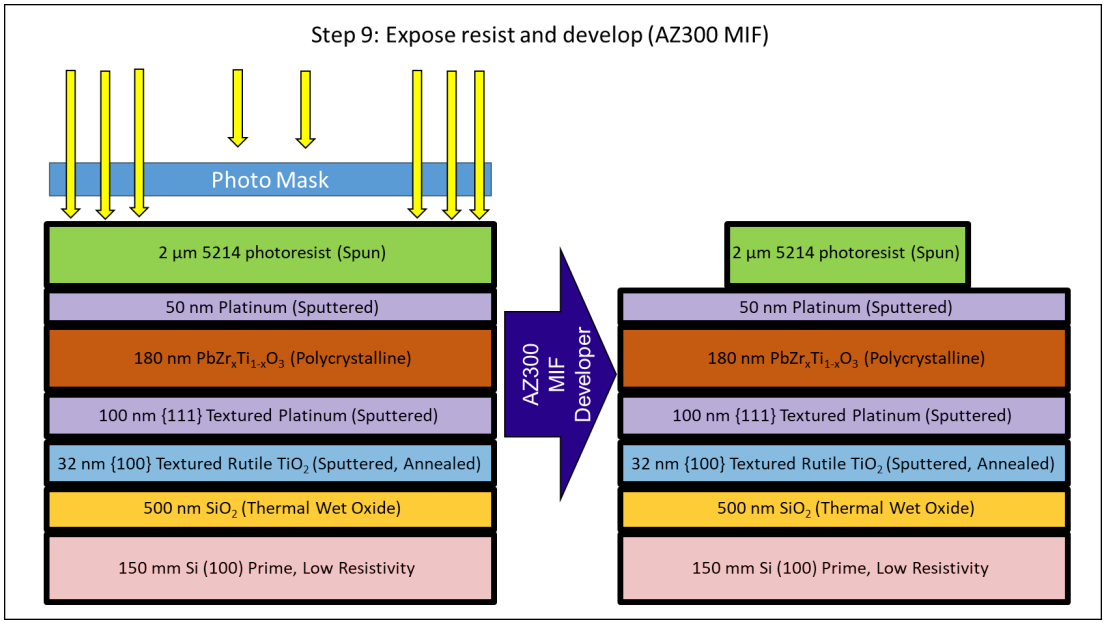

Figure 4.18: Graphical representation of 5214 resist spin step.

Table 4.4: Process conditions for 5-min descum program

Process Parameter	**Value**
Chamber O_2 Flow (sccm)	5
RF Power (W, 13.56 mHz)	200
Chamber Pressure (mtorr)	525
Etch Time (min)	5

To prepare the resist for the ion mill etch, the film is UV-stabilized using an Axcelis UV-stabilization platform using the recipe detailed in Table 4.5.

Table 4.5: Recipe for UV stabilization

Step	Temp (°C)	Time (sec)	Lamp	Time (sec)
1	110	50	Off	12
2	150	20	Flash	1
3	150	10	Off	15
4	170	20	Flash	2
5	170	10	Off	15
6	200	20	Low	5
7	200	10	High	90

The films were ion milled on a 4-Wave platform using a dual angle etch recipe. A Hiden mass spectrometer was used as an endpoint detector for the first angle etch step (95°). The ion mill was performed until the Pt signal reached a minimum and typically took about 3-min. The second etch angle step (140°) was used to clear debris from the sidewalls and was performed for 70 seconds. The samples were continuously spun and rotated to ensure uniform etch depth. The primary process parameters are shown below in table 4.6. A graphical representation of the film-stack with etched Pt is shown below in figure 4.19.

Table 4.6: Process conditions for Ion Mill

Process Parameter	Value (95°)	Value (140°)
Hollow Cathode Gas Flow (Ar, sccm)	13.9	13.9
Source Gas Flow (Ar, sccm)	20.85	20.85
Hollow Cathode Keeper Current (A)	1.5	1.5
Hollow Cathode Emission Current (A)	0.5	0.5
Source Beam Voltage (V)	400	400
Source Beam Current (mA)	400	400
Source Acceleration Voltage (V)	150	150
Etch Angle (°)	95	140
Process Time (s)	Endpoint	70

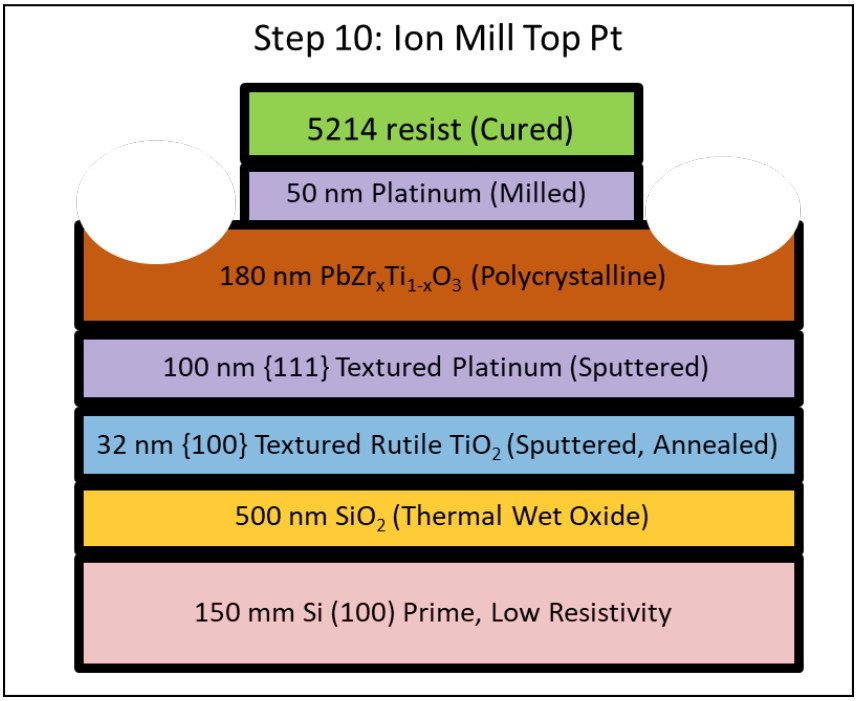

Figure 4.19: Graphical representation of 5214 resist spin step.

The ion mill typically etches somewhat into the PZT layer, which is represented schematically by the etch pits in Figs. 4.19 and 4.20. Following the ion mill step, the resist is stripped in a plasma ash tool (PVA Tepla) with the following parameters summarized in Table 4.7. A graphical representation of the wafer cross section following the resist strip is shown below in Fig. 4.20.

Table 4.7: Process conditions for 45-min resist strip program

Process Parameter	**Value**
Chamber O_2 Flow (sccm)	500
RF Power (W, 13.56 mHz)	400
Chamber Pressure (mtorr)	1000
Etch Time (min)	45

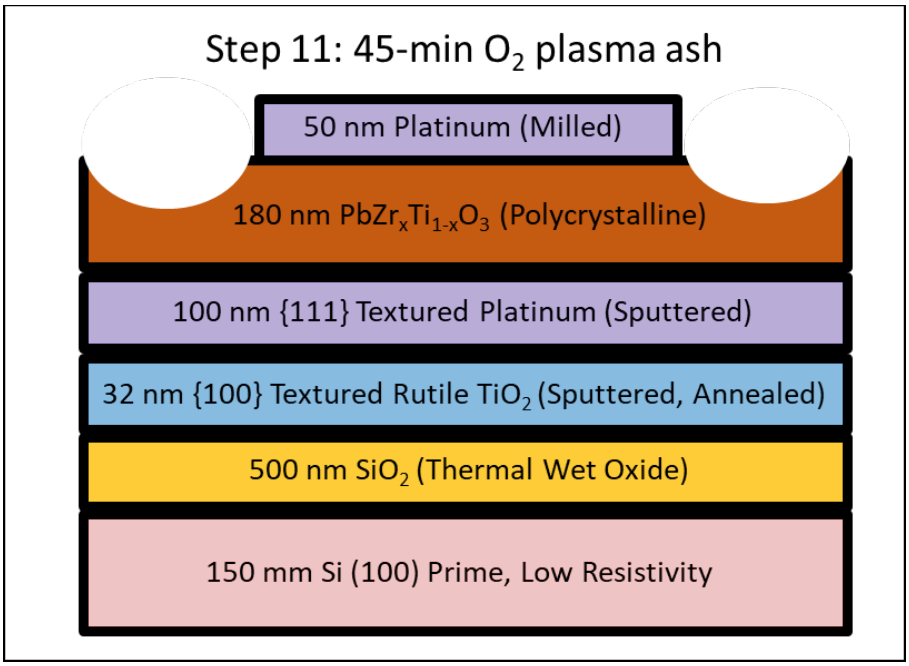

Figure 4.20: Graphical representation of O_2 plasma ash step.

At this point, the bottom electrode was accessed one of two ways. For films thinner than 500 nm, the remaining PZT was simply scratched through to expose the dense bottom Pt. Probes easily made contact with the scratched area, and it was this technique that was used for the majority of the metal-insulator-metal (MIM) capacitor testing. The other way was to wet etch a section of the PZT. The PZT etch solution contained 240 mL H2O, 120 mL HCl, and 1 mL HF. For the bottom electrode exposure via PZT wet-etch, AZ 5214 resist was applied again, and a small section of the wafer (where top Pt was previously etched) was patterned using UV light, typically from a microscope objective lens. Once the resist was developed with the AZ 300 MIF developer, as before, the PZT was immersed in the BOE until the bottom Pt was visible. A top-down microscope image of the micromachined Pt top electrodes is shown below in Fig. 4.21. The image has a yellow tint because the blue wavelengths were filtered out. The arrayed circular top Pt electrodes are clearly labelled, and the area is labelled

(lithographically) to the left of the array. The larger electrodes with area = 4.92×10^{-4} cm^2 were used for the majority of the electrical measurements in this thesis. The PZT appears as the orange film.

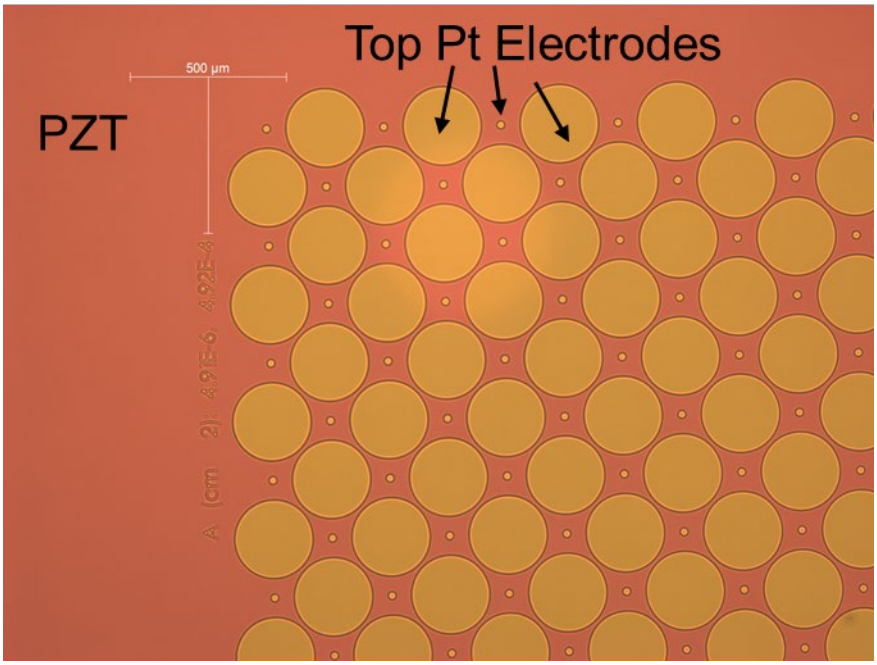

Figure 4.21: Microscope image of processed capacitor top electrodes

Cantilever Fabrication

The next mask was applied to mill through the Pt bottom electrode. Some of the PZT previously milled is preserved to separate the top and bottom electrical contacts, which is represented in Fig. 4.22 below by a small amount of resist in direct contact with the PZT. Since the bottom electrode etch step was also a mill step, the AZ 5214 was spun, exposed, developed, plasma etched (descum) and UV-cured as previously described in steps 8-9, but with a different mask.

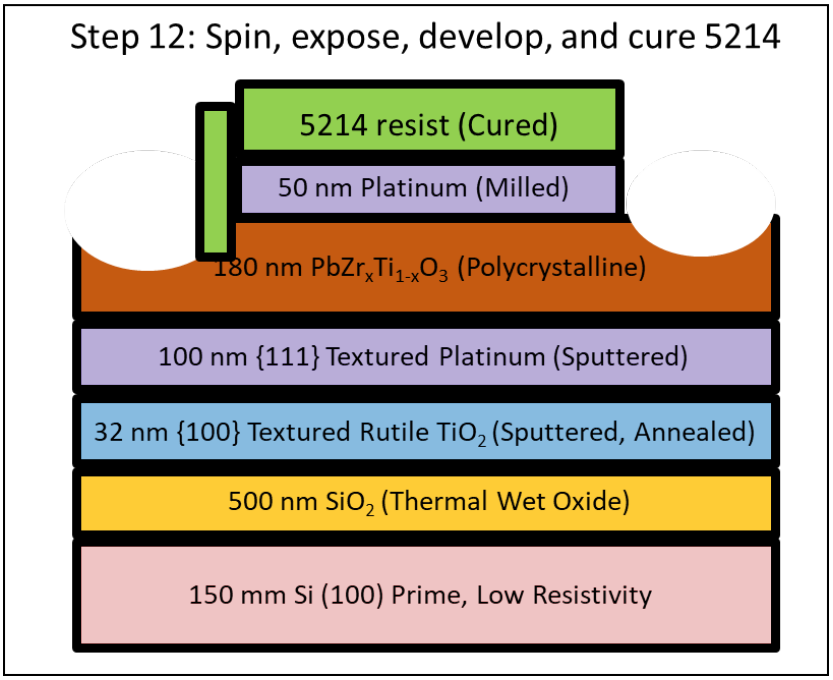

Figure 4.22: Graphical representation of the developed and cured resist

The PZT was milled using the same ion mill recipe detailed in Table 4.6. Though the 95° etch step was still monitored by endpoint, it took much longer to mill through both the PZT and the bottom Pt, and the monitor conditions slightly changed. Both the Pb and Pt signals were monitored. As the PZT was etched, the Pb signal decreased. Once the bottom Pt began to etch, the Pb signal reached a minimum background value. Once the Pt was etched through, the Pt signal returned to the background value, at which point the 95° ion mill was stopped and the 140° ion mill began. Figure 4.23 shown below is a graphical representation of the bottom platinum etch step with a slight over-etch into the underlying TiO_2.

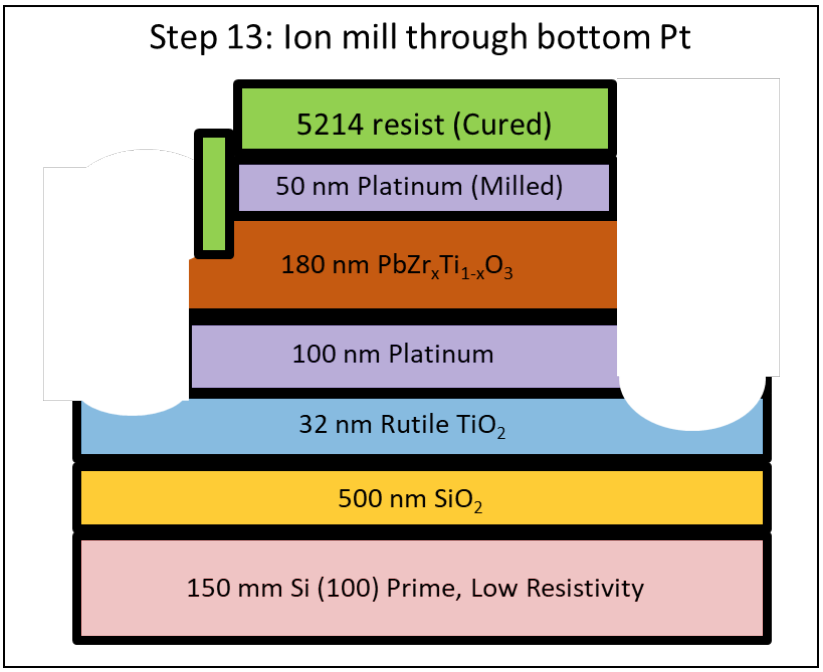

Figure 4.23: Graphical representation of the ion mill through the bottom Pt step

The UV-cured resist was then removed using the same resist strip recipe detailed in Table 4.7, with the sample cross-section shown below in Fig. 4.24.

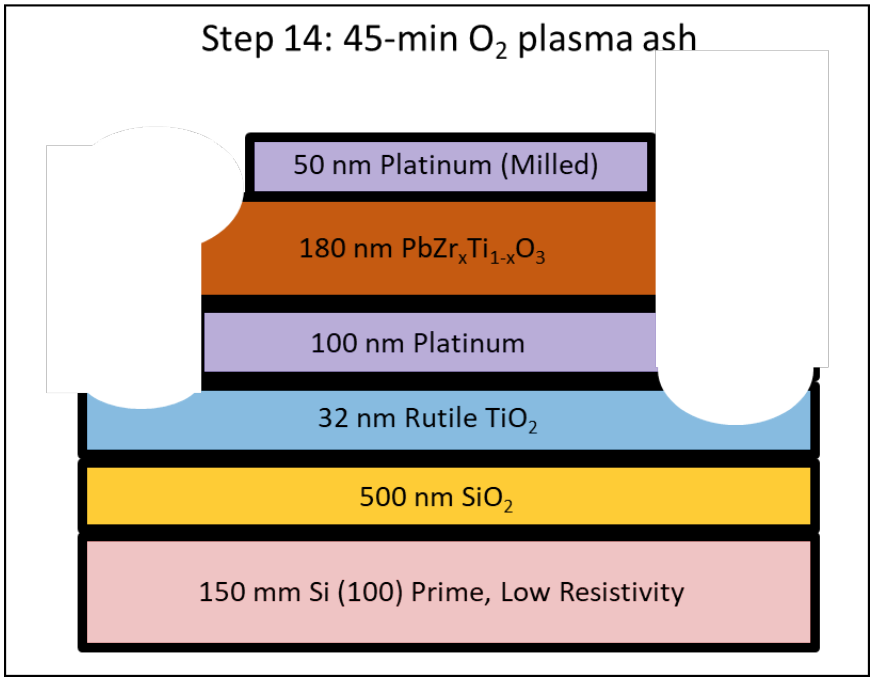

Figure 4.24: Graphical representation of the ion mill through the bottom Pt step

AZ 5214 resist was then applied using the same coat recipe as detailed in step 8, but a negative image process was used to expose and develop the pattern. The resist-coated substrate was exposed for 5.5 s at constant 9.0 mW/cm^2 intensity in the SUSS-Microtech MA-6 aligner. The substrate was then baked for 30 s at 120 °C in the EVG track-coater before an 11 s flood exposure at the same constant intensity. The resist was then developed in the EVG using the same program detailed in step 8. Following development, portions of the bottom electrode sidewall and top electrode surface were left bare. A graphical representation of the negative image is shown Fig. 4.25 below.

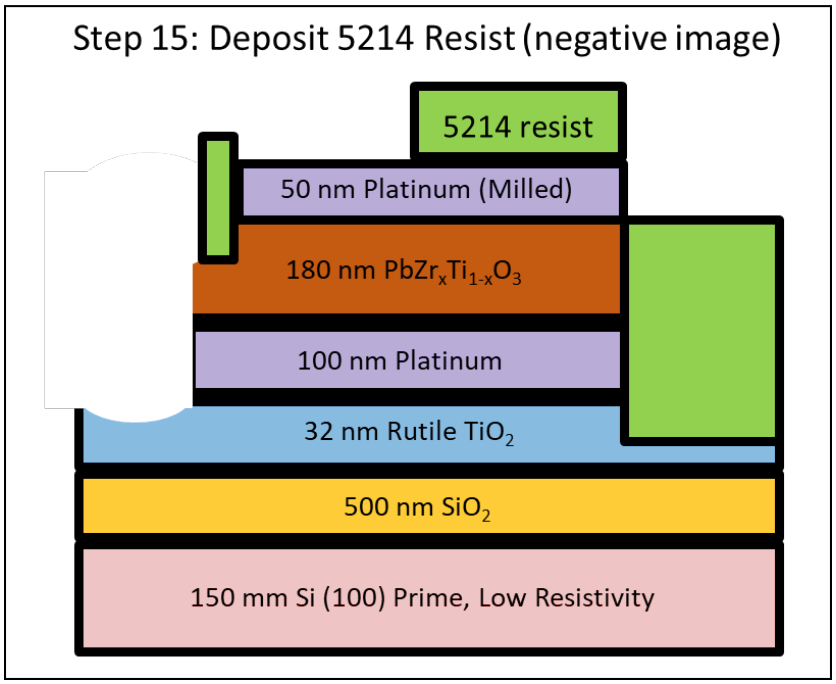

Figure 4.25: Graphical representation of 5214 deposition and development (negative image)

A metal stack containing 20 nm Cr, 20 nm Pt, and topped with 730 nm Au was then evaporated onto the substrates for liftoff. The metal stack was evaporated using an Evatec BAK batch-processing electron-beam deposition system. The source materials were Cr pellets (99.95% purity) housed in a Mo crucible, Pt pellets (99.99% purity) evaporated directly from the water-cooled Cu hearth, and Au pellets (99.999% purity)

evaporated from a Mo crucible. The Evatec BAK system was pumped to high-vacuum using a cryo-pump, and evaporations were performed at pressures below 2.0×10^{-6} mbar. The deposited thickness was monitored in-situ using a quartz crystal monitor.

The wafer was then subject to a liftoff step whereby the majority of the evaporated film was removed. The wafer was first immersed in acetone for two hours and agitated slightly so that the film came off in a single large piece. The piece was removed using tweezers and the dish containing the wafer and the acetone was placed in an ultrasonic bath for 60 s. The dish and wafer were then removed from the bath and the wafer rinsed with methanol, with the remaining acetone poured into a waste containment bottle. Once the wafer was thoroughly rinsed with methanol it was rinsed with isopropanol, with the remaining methanol poured into waste containment. Finally, the wafer was rinsed with deionized water and thoroughly agitated to remove any excess metal flakes remaining in the bath. The wafer was then dried and oxygen etched in the PVA Tepla platform using the resist strip program defined in Table 4.7, with the process time lowered from 45-min to 5-min. The substrate, now with well-defined and accessible electrodes is shown below in Fig. 4.26.

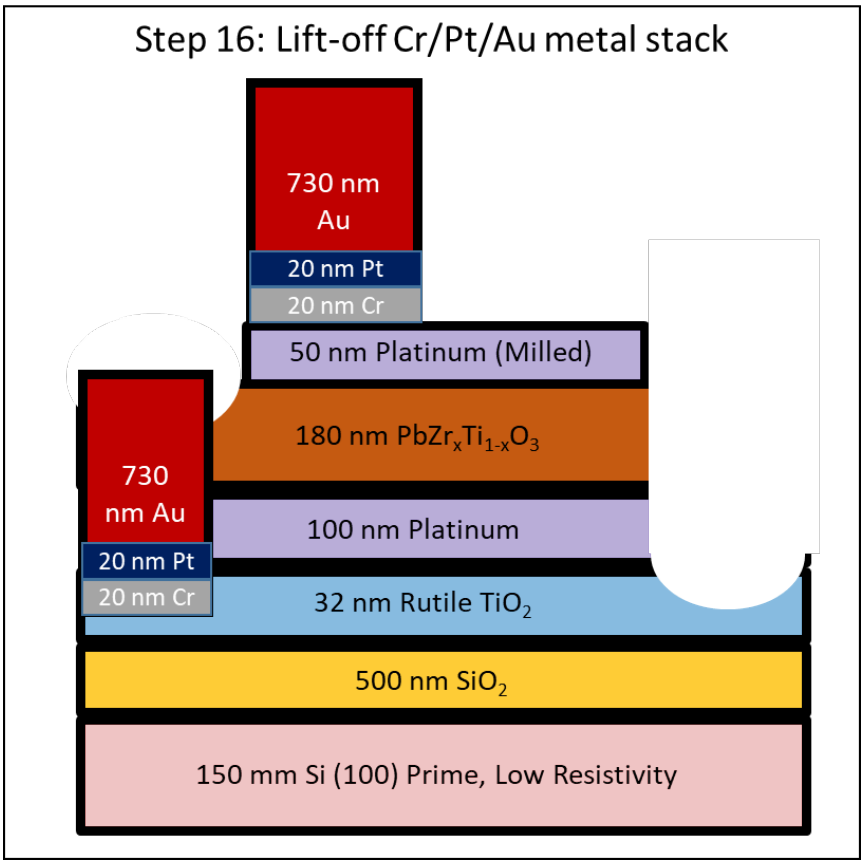

Figure 4.26: Graphical representation of evaporated Cr/Pt/Au liftoff

AZ 5214 was then deposited, exposed, and developed using the process detailed in step 8 to pattern a positive image. A representation is shown below in Fig. 4.27, which shows a portion of the TiO_2 film exposed for the subsequent reactive ion etch (RIE).

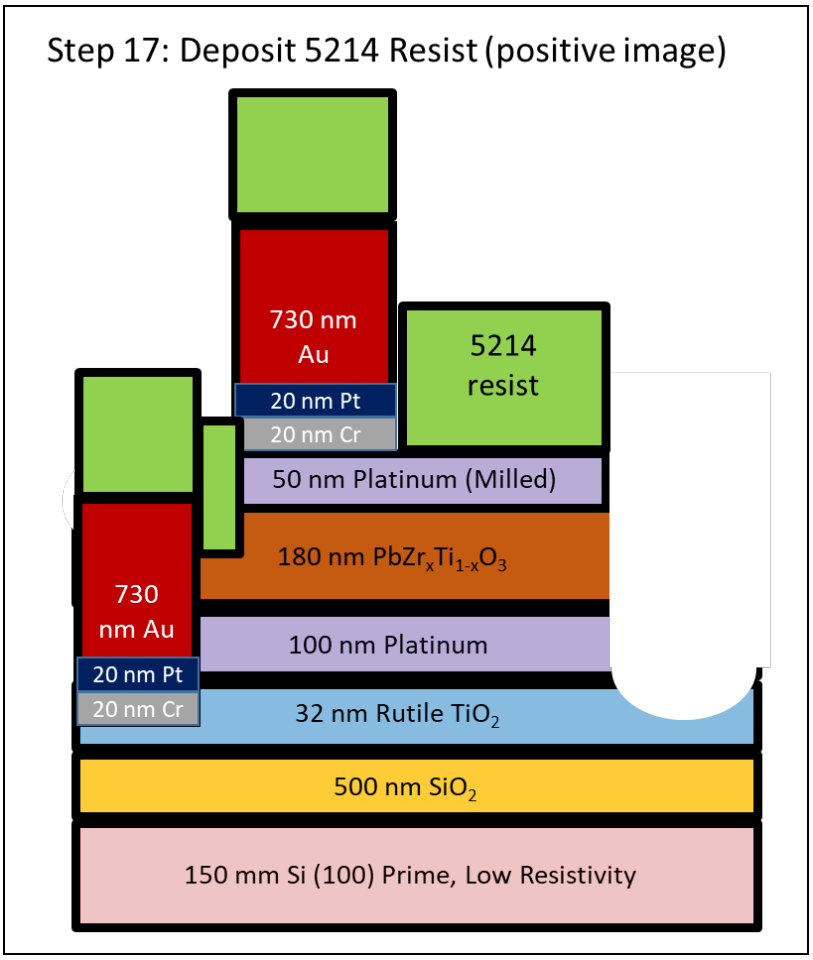

Figure 4.27: Graphical representation of 5214 reactive oxide etch mask

The remaining TiO_2 and SiO_2 were then reactive ion etched (RIE) using an Oxford Plasmalab ICP etch platform with cryogenically cooled chuck. The critical etch parameters are summarized in Table 4.8, and a graphical representation may be seen below in Fig. 4.28. The samples were slightly over-etched into the underlying silicon to ensure complete removal of SiO_2.

Table 4.8: Process conditions for oxide RIE etch

Process Parameter	Value
Chuck RF Power (W, 13.56 mHz)	100
Chuck DC Bias (V)	278
ICP RF Power (W, 13.56 mHz)	1500
Chamber Pressure (mtorr)	10
Ar Flow Rate (sccm)	10
CHF_3 Flow Rate	10
Chuck Temp (°C)	20
He Backing Pressure (Torr)	10
He Backing Flow Rate (sccm)	5
Etch Time (min)	7

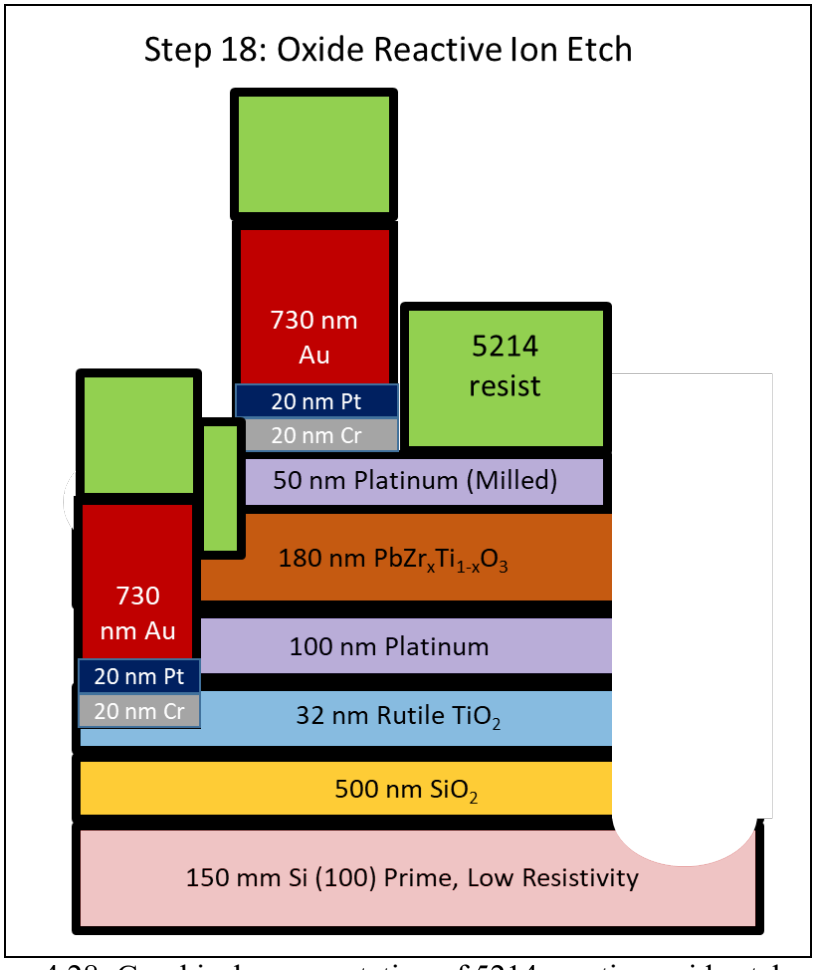

Figure 4.28: Graphical representation of 5214 reactive oxide etch mask

Following the oxide RIE etch, the remaining resist was stripped using the same procedure outlined in Table 4.7. A cross section of the substrate is shown below in Fig.

4.29. A top-down microscope image of the pre-released cantilever structures are shown below in Fig. 4.30. The green-film is the exposed PZT. The brown film is the exposed Si layer. The bottom electrode is Au-coated Pt and is shown making side-contact to the bottom Pt-layer, as depicted in Fig. 4.29.

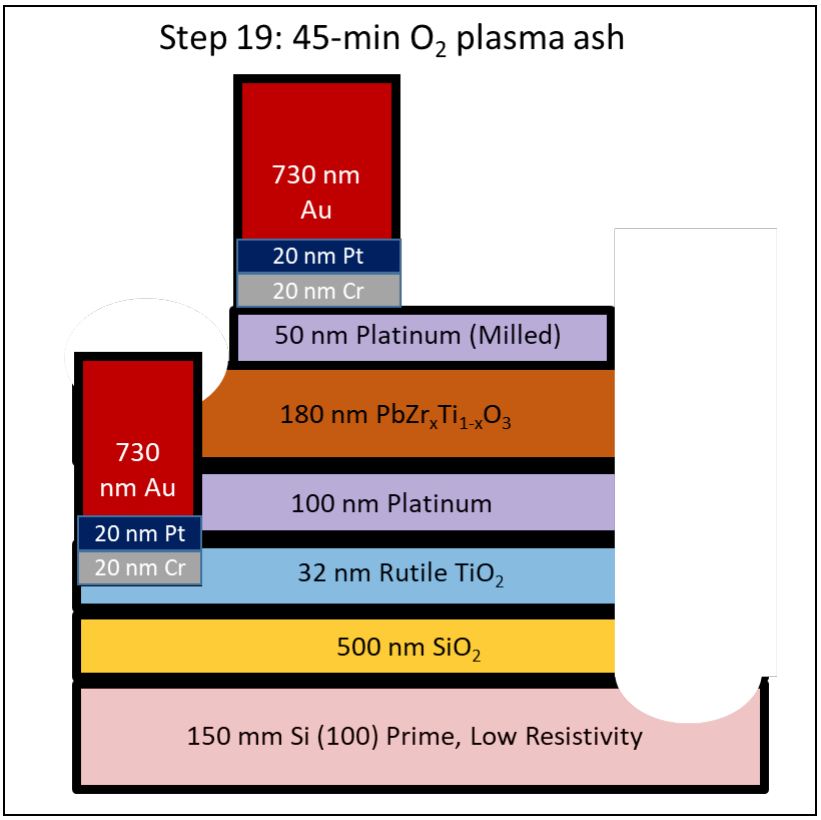

Figure 4.29: Graphical representation of O_2 plasma ash after the RIE etch

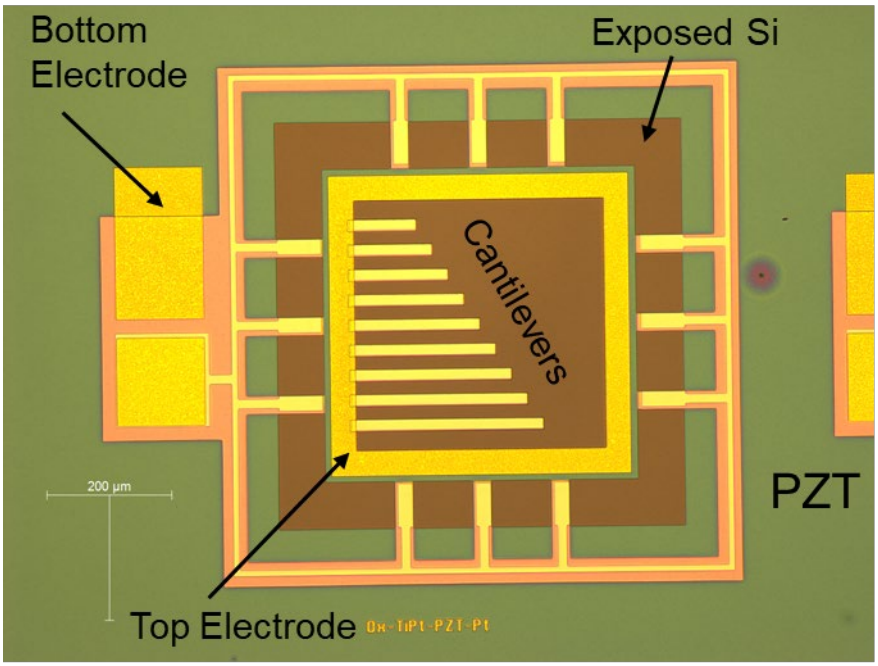

Figure 4.30: Microscope image of a micromachined cantilever array (pre-released structures)

The cantilever structures were released using a Xactix Inc. XeF_2 etch platform. The sublimated XeF_2 gas is highly selective to silicon, and because it is isotropic the XeF_2 allows large undercut. The normal etch recipe consists of four parameters: number of cycles, etch time (20 s), XeF_2 pressure (2.0 Torr), and N_2 pressure (20.0 Torr). At the start of one cycle, the expansion chamber isolation valve was opened, and both the XeF_2 and N_2 were fed simultaneously into the vacuum process chamber. The expansion chambers were pre-charged with each respective gas until the set pressure was reached which ensured an identical XeF_2 and N_2 charge for each cycle. After 20 s, the XeF_2 and N_2 were evacuated by a vacuum pump until the chamber reached base pressure. Once the chamber reached base pressure, the process was repeated. The wafers were inspected periodically to calibrate the number of etch cycles required for cantilever

release. 180 cycles were typically required to fully release the cantilevers. A schematic of the released structure is shown below in Fig. 4.31.

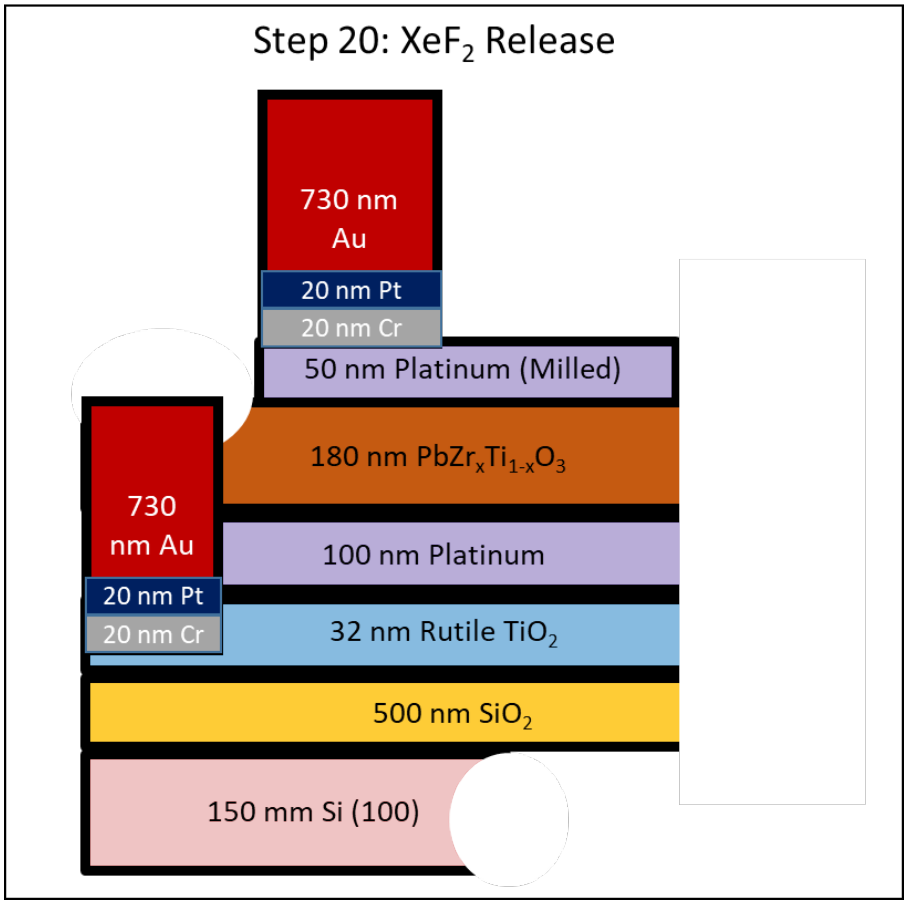

Figure 4.31: Graphical representation of XeF_2 release step

The final release cantilever structure is shown below in Fig. 4.32 with labels for the cantilever, along with the top and bottom electrodes.

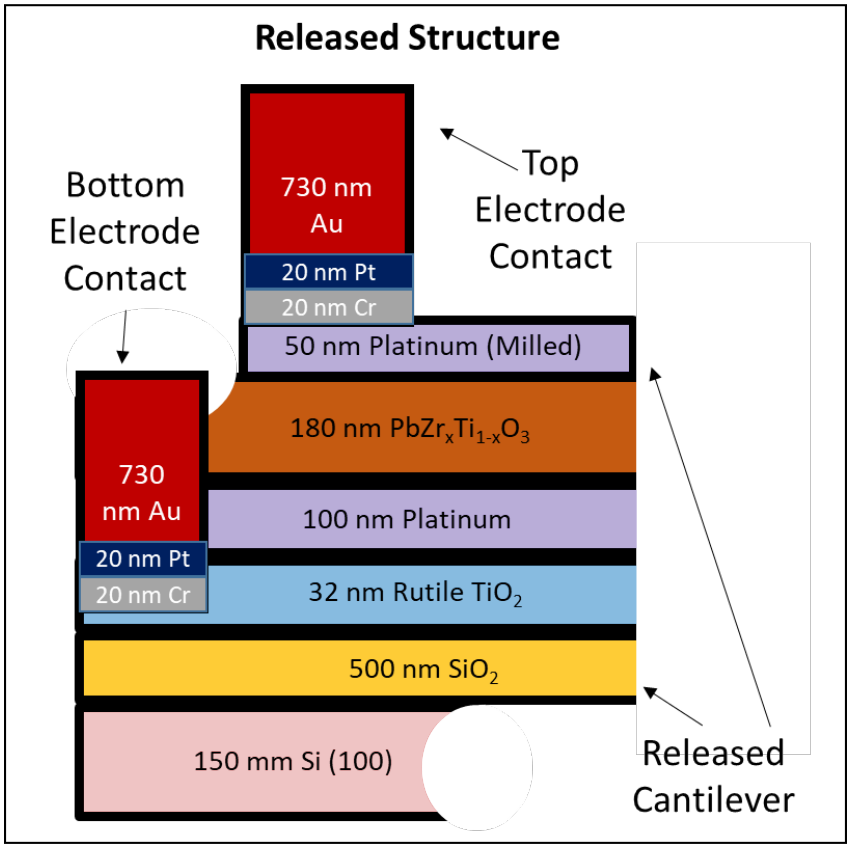

Figure 4.32: Graphical representation of final released cantilever structure

References

[1] Fox GR, Potrepka DM, Polcawich RG. Dependence of {111}-textured Pt electrode properties on TiO_2 seed layers formed by thermal oxidation. *J Mater Sci - Mater Electron.* 2018;29:412-426.

[2] Muralt P. PZT Thin Films for Microsensors and Actuators: Where Do We Stand?. *IEEE Trans Ultrason Ferroelectr Freq Control.* 2000;47:903-915.

[3] Sanchez LM, Potrepka DM, Fox GR, et al. Improving PZT Thin Film Texture Through Pt Metallization and Seed Layers. *MRS Proceedings.* 2011;*1299*.

[4] Potrepka DM, et al. Atomic layer deposition of Pt growth template for orienting $PbZr_xTi_{1-x}O_3$ thin films. *J Vac Sci Technol A*. 2012;30:01A129.

Chapter 5: ALD $PbTiO_3$

Introduction

The following chapter expands upon the previous research published in Reference 1. Lead titanate with a chemical composition near $PbTiO_3$ is shown in this chapter to be grown by an indirect ALD process that consists of the initial deposition, followed by crystallization via rapid thermal anneal. Electrical testing of micromachined capacitors indicated that the crystallized ALD PTO films were ferroelectric.

Chemical Composition

The chemical composition of the ALD PTO was explored for a range of binary PbO_x:TiO_x cycle ratios. Although evidence will be presented that indicates the PbO_x stoichiometry is very near PbO, and that the TiO_x stoichiometry is very near TiO_2, the subscript x is used for simplicity. In all cases, the ALD PTO was grown on the Pt bottom electrode stack described in Chapter 4. Each of the films received the same 1401 ALD cycles (note: this is the overall number of cycles, not the number of super-cycles), although final thicknesses varied due to differences in growth-per-cycle (GPC) which will be discussed later. Since the overall number of cycles remained unchanged, increasing the number of TiO_x cycles lowered the number of PbO_x cycles, and vice-versa. The Pb/Ti cation ratio was determined by RBS (described in Chapter 3) and the data is presented below in Fig. 5.1.

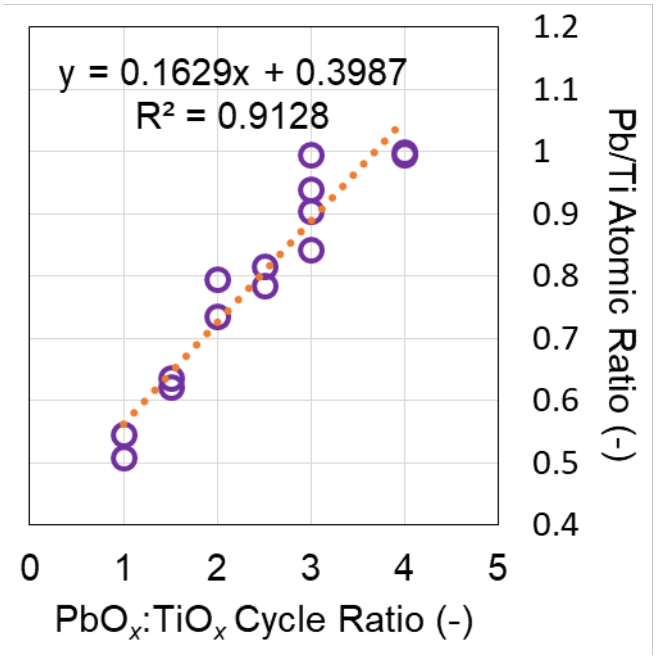

Figure 5.1: Composition variation of ALD PTO with varied PbO_x:TiO_x Cycle Ratios

The composition data fit to a line with an R^2 value of 0.9128. Multiple data points are plotted for each PbO_x:TiO_x cycle ratio which correspond to piece parts that were cleaved from a single wafer. The spread in the data is partly due to the uncertainty in the overall cation composition obtained from the RBS measurement. The uncertainty of the overall cation % was reported to be ± 0.3% for Pb and ± 1.0% for Ti. When computing the Pb/Ti atomic ratio, those uncertainties represent a spread of approximately 0.06, which very nearly covers each of the PbO_x:TiO_x data sets except 3:1. Most of the piece parts were cleaved from the center of their respective wafers, but for 3:1, the piece parts came from various sections. The spread therefore likely represents a composition gradient which is a result of slight non-optimization of the process parameters which were later addressed. Nonetheless, a nearly 1:1 Pb:Ti cation composition was shown for PbO_x;TiO_x ratio of 4:1.

RBS was performed on both pre and post-annealed samples grown with a 4:1 PbO_x:TiO_x cycle ratio. The elemental composition is tabulated below in Table 5.1. The uncertainty related to the oxygen atomic percentage was reported to be ± 4%. The chemical composition of both the annealed and unannealed samples fell within the margin of error of the ideal composition of $PbTiO_3$, where the Pb:Ti:O ratio is 1:1:3. It appears there may have been a slight lead loss during the anneal, along with a small increase in oxidation. However, since the sample size is so small and no other techniques were used to verify the chemical composition of the samples, this is left as a tentative observation to be explored with a more thorough design of experiments. Regardless, the RBS data implies that the films were deposited as-grown with very nearly the correct amount of oxygen for perovskite PTO, and little if any Pb-loss as a result of the anneal.

Table 5.1: Chemical composition of ALD PTO films grown with a 4:1 PbO_x:TiO_x cycle ratio.

PbO_x: TiO_x Ratio	Anneal	Pb %	Ti %	O %
4:1	No	19 (±0.3)	19 (±1.0)	62 (±4.0)
4:1	700 °C, 1-min hold	18.6 (±0.3)	18.7 (±1.0)	62.7 (±4.0)

Growth Per Cycle

Ex-Situ Thickness Measurements

The GPC varied for each of the tested PbO_x:TiO_x cycle ratios. The final thickness of each sample was measured by spectroscopic ellipsometry using a parametrized Tauc-Lorentz model with a UV pole which incorporated wavelengths in the range of 500-1000 nm (above the bandgap of PTO). The details related to the fit parameters are discussed in Chapter 4. The final thickness was then divided by the number of cycles to determine the linear GPC. For the purposes of this generalized calculation, the roughness was ignored because it typically fell in the range of only 1-2% of the final thickness and was consistent sample-to-sample. For the as-deposited films, the roughness (modeled by the ellipsometer) typically measured 1-2 nm. The GPC is plotted versus the PbO_x;TiO_x cycle ratio below in Fig. 5.2 and is shown below; the dependence is essentially linear with R^2 value of 0.927.

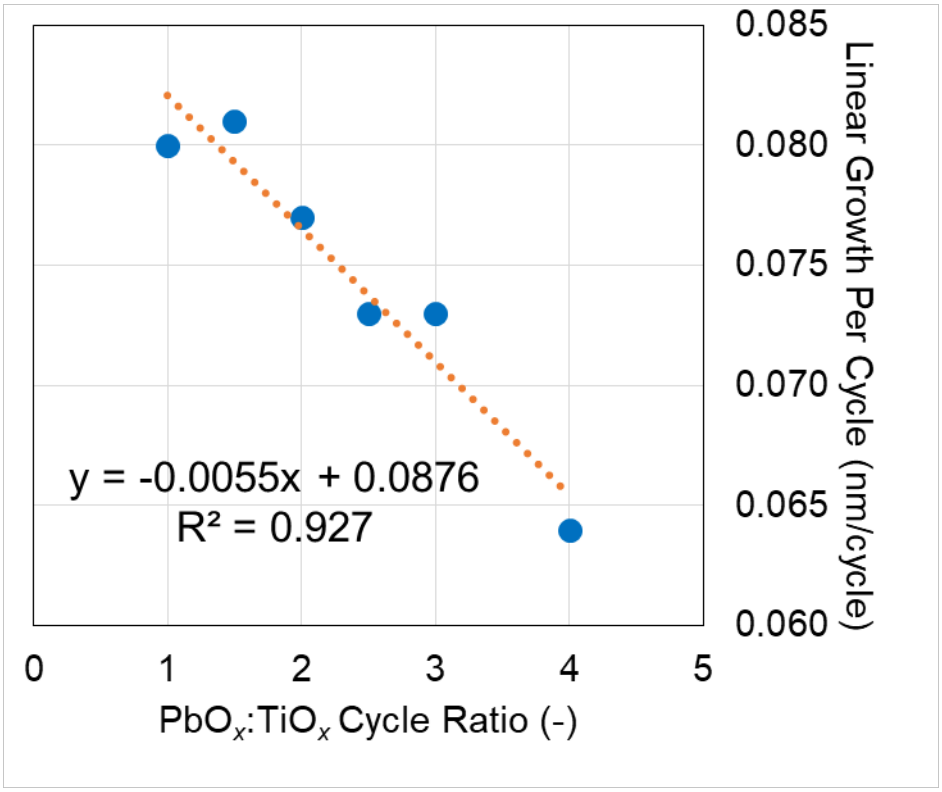

Figure 5.2: GPC of ALD PTO with varied PbO_x:TiO_x Cycle Ratios

As is shown in Fig. 5.2, the GPC tends to decrease with increasing PbO_x cycles. This is unfortunate, since the necessary stoichiometry was obtained at a PbO_x:TiO_x cycle ratio of 4:1. Still, the PTO growth rates reported here fall in between 0.012 to 0.161 nm/cycle, which is the range of growth rates reported in previous attempts to grow Pb-based perovskites grown by ALD. See Table 5.2 below.

Table 5.2: GPC of prior attempts to grow ALD Pb-based perovskites compared to this work (parenthesis indicate the substrate temperature).

Reference	**ALD Perovskite**	**GPC (nm per cycle)**
Harjuoja[2]	PTO	0.025 (250 °C)
Hwang[3]	PTO	0.064 (200 °C)

Watanabe[4]	PTO	0.03 (240 °C)
Lee[5]	PTO	0.161 (200 °C)
Sbrockey[6]	PTO	0.10 (250 °C)
Harjuoja[7]	PZO	0.012 (275 °C)
Watanabe[8]	PZT	Not Reported (240 °C)
Watanabe[9]	PZT	Not Reported (240 °C)
Choi[10]	PZT	0.15 (250 °C)
This Work	PTO	0.064 (250 °C)

In-Situ Thickness Measurement

In-situ thickness measurements were performed using a Films Sense FS-1 multi-wavelength ellipsometer, which was described in Chapter 3. The optical constants used to model the in-situ film growth were obtained from ex-situ spectroscopic ellipsometer analyses of the same films. For simplicity, the roughness was held fixed in the fits for the duration of the ALD growth. PTO films grown with a 3:1 PbO_x;TiO_x ratio were chosen as representative of the range of compositions grown in this work. Figs 5.3-5.5, shown below, detail the in-situ growth kinetics for a 1401 cycle deposition.

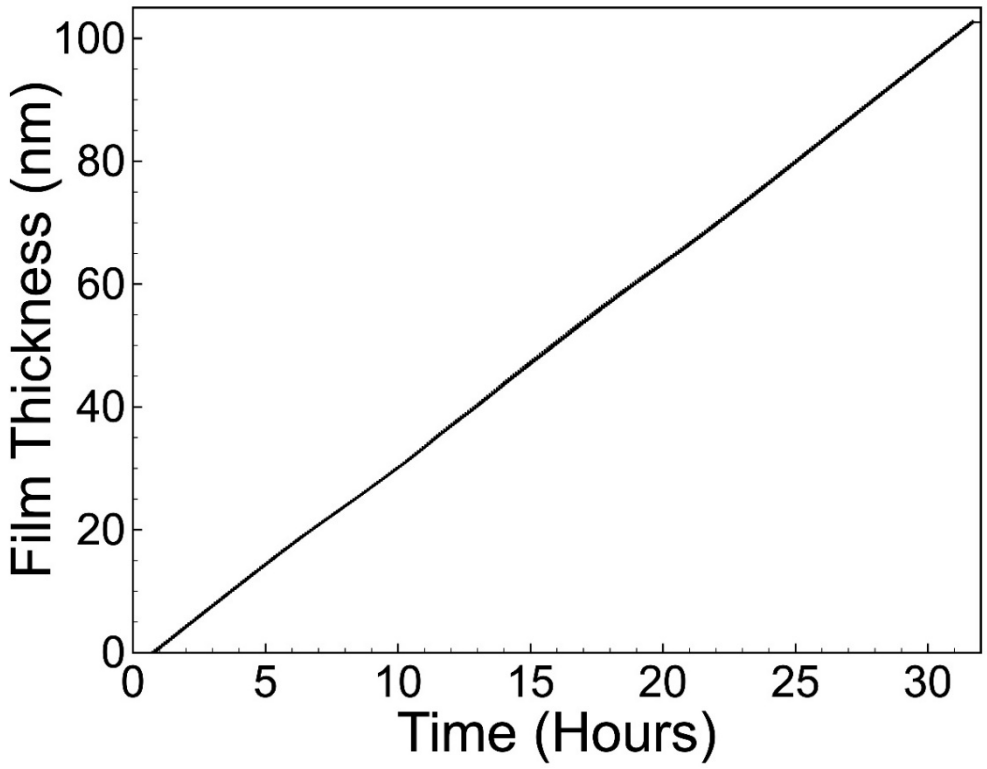

Figure 5.3: ALD PTO (Pb-deficient) thickness versus time for a 3:1 PbO_x;TiO_x ratio covering the entire deposition process.

Fig. 5.3 provides little detail other than to show the high degree of linearity of the thickness versus time. The film thickness trace shown in Fig. 5.3 fit to a line with an R^2 value of 0.999 and a standard deviation of 0.3 nm, which is less than 0.5% of the overall thickness. The thickness trace of the other PbO_x:TiO_x cycle ratios were similarly linear, but the slope varied based on differences in GPC. The consistency of the linear growth is not surprising since the substrate temperature was held constant at 250 °C, which is within the ALD window of both TDMAT and $Pb(DMAMP)_2$. One full TiO_x cycle took about 40-s to complete, while one full PbO_x cycle took about 72-s. The cycle times were dominated by the long oxidation steps and subsequent purge steps that were

left intentionally lengthy to ensure saturated film oxidation or complete evacuation of the chamber, respectively.

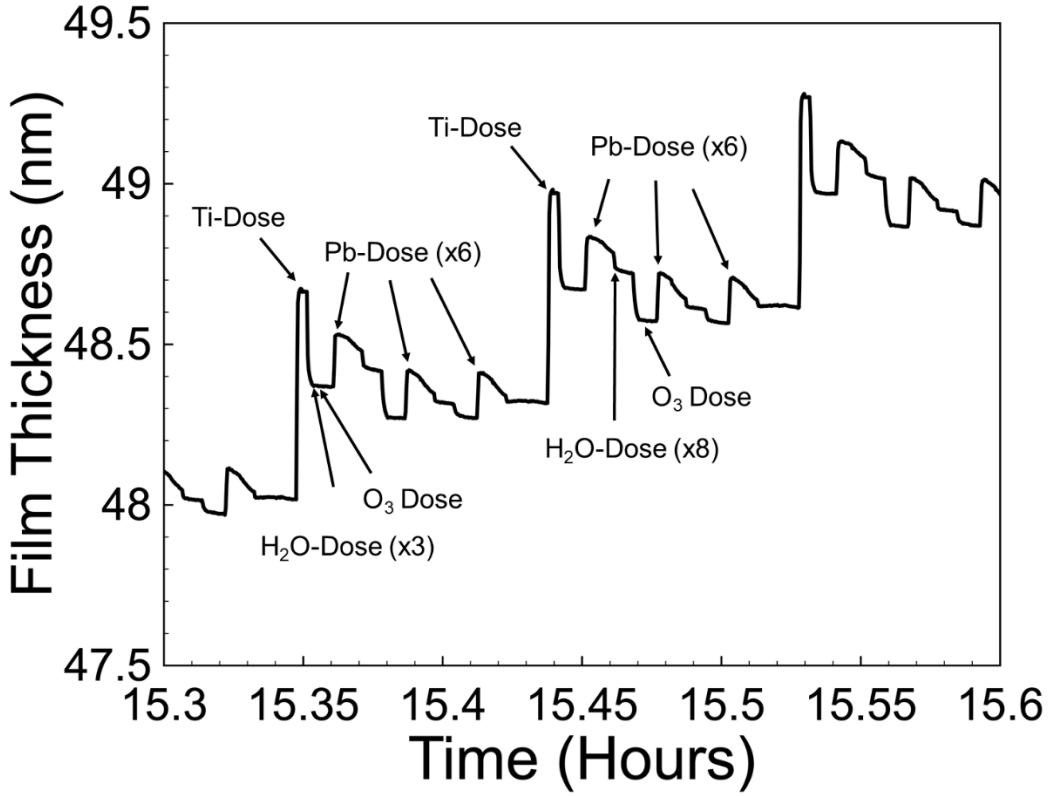

Figure 5.4: Close-up view of the in-situ ALD PTO growth from Figure 5.3 with labelled doses for 3:1 PbO_x;TiO_x ratio.

Fig. 5.4 contains more detail related to the ALD growth kinetics. The cation and oxidizer doses are labelled for clarity. Stepwise growth was observed following each Ti-dose. For a PbO_x:TiO_x cycle ratio of 3:1, the films were determined to be slightly Pb-deficient (see Fig. 5.1), however, based on the thickness increases measured by the in-situ ellipsometer, one might expect a severely Pb-deficient film. It is not clear why the Pb-incorporation is not completely captured by the ellipsometer. The thickness increase following the Ti-dose is consistently around 0.2 nm, which is five times larger than the equilibrium GPC of the TiO_2 binary process based on TDMAT which was

previously determined to be about 0.04 nm/cycle. It seems that the surface-bound PbO_x is not fully accounted for (optically) until the subsequent titanium dose. Growth models are currently being explored to understand this phenomenon (see Chapter 8).

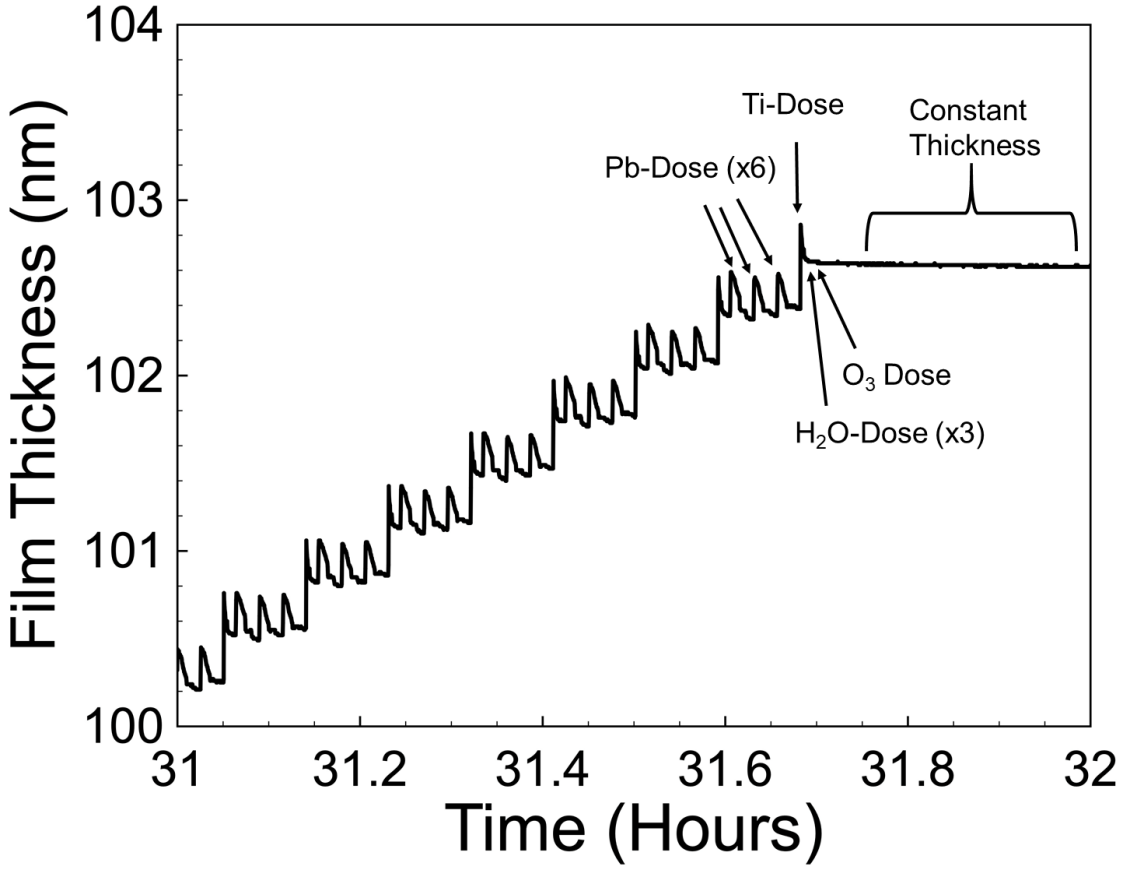

Figure 5.5: Close-up view of the final cycles of the ALD PTO growth from Figure 5.3 with labelled doses for 3:1 PbO_x;TiO_x ratio.

Fig. 5.5 shows the growth kinetics of the final ALD cycles in an (approximately) 100 nm-growth. The apparent thickness increases following the Ti and Pb-pulses are identical to those early on in the growth (Fig. 5.4), indicating that the growth mode is in a steady state during the (long) growth duration. Following the final O_3 oxidation, the final thickness was constant with respect to time, which implies that no deleterious chemical reactions occurred while the sample sat on the heated chuck.

Phase Identification by X-ray Diffraction

XRD of PTO Films Grown at Different Elemental Concentrations

Figures 5.6-5.9 show X-ray diffraction patterns of both annealed and unannealed PTO samples under a variety of conditions. For this chapter, a 700 °C rapid thermal anneal (RTA) with a 60-s hold at a 90 °C/s ramp rate in O_2 was adopted as the standard anneal. The standard anneal was previously shown to crystallize (001)-oriented PTO/PZT deposited using sol-gel.[11] Figure 5.6 shows the variation of θ-2θ X-ray diffraction scans of PTO grown with different PbO_x:TiO_x cycle ratios, and thus different Pb/Ti cation ratios. The experimental conditions for the X-ray diffraction are discussed in Chapter 3.

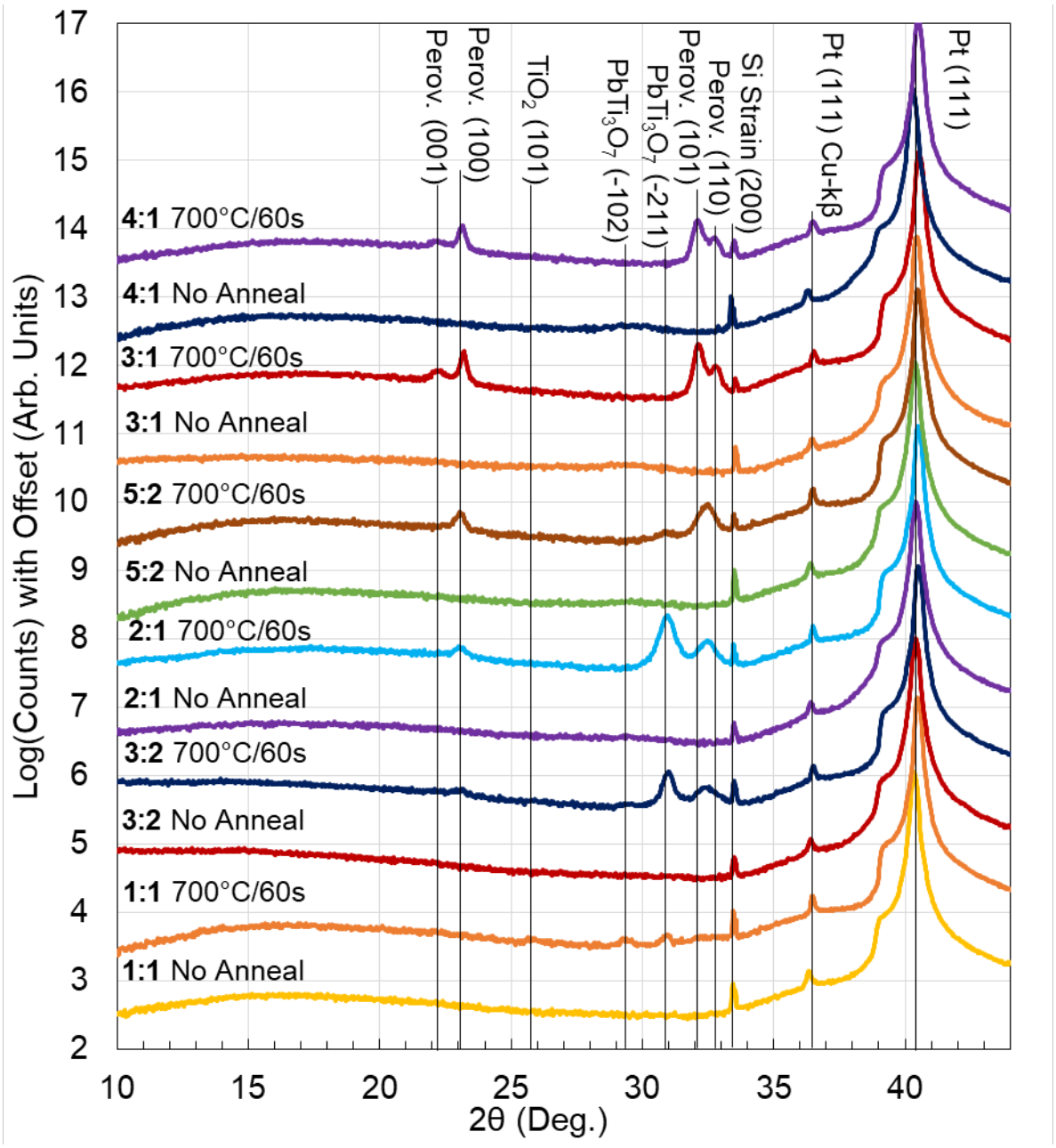

Figure 5.6: X-ray diffraction θ-2θ scans of ALD PTO grown with PbO_x:TiO_x cycle ratios before and after annealing in O_2.

Only three well-defined peaks are present in the unannealed samples regardless of the cation ratio, and they are unrelated to the PTO phase itself. These are the Si (200) strain peak at 33.4°, the Pt (111) Cu-kβ reflection at 36.4°, and the Pt (111) Cu-kα reflection

at 40.5°. The Pt {111} peak is very strong because the film is highly oriented, as is discussed in Chapter 4. A small-intensity hump is observed near 29° on the unannealed samples with PbO_x:TiO_x ratios greater than 2:1. Since the hump appears only at high Pb concentrations, the phase or phases that cause the hump can be assumed to contain Pb. No hump is observed in the annealed samples. Based on Table 5.1 little to no change in chemical composition occurred upon annealing. Therefore we can assume the phase(s) that caused the hump were primarily absorbed into the final perovskite crystal structure. The unidentified phases responsible for the hump may be a Pb-rich lead-titanium-oxygen compound, or lead oxide. If the phase is lead oxide, the stoichiometry should be close to PbO, again leveraging Table 5.1. The PbO Massicot phase (PDF #00-038-1477) has high-intensity peaks at 29.079° for (111) and 30.316° for (020), which nearly matches the 2θ range observed for the hump. A Pb-rich lead-titanium-oxygen compound with stoichiometry $PbTi_{0.8}O_{2.6}$ (PDF# 00-049-0863) has a strong reflection at 29.326° for (101) lattice spacing. Additional analysis techniques are required to determine conclusively which phases caused the hump. Further discussion of the partially crystallized unannealed samples are contained in the "Cross Section STEM Analysis" section later in this chapter.

The XRD plot for the annealed PbO_x:TiO_x 4:1 in Fig. 5.6 from left to right shows perovskite $PbTiO_3$ (PDF# 00-006-0452) (001), (100), (101), and (110) peaks. The PTO (111) peak at 39.187° is seemingly missing, but may have been obfuscated by the Pt (111) peak shoulder. The annealed 4:1 sample did not display any non-perovskite peaks other than those belonging to the substrate. The annealed PbO_x:TiO_x 3:1 scan appears almost identical to the 4:1 scan. The annealed samples in the PbO_x:TiO_x range of 5:2-

3:2 have an additional peak close to 31° which is attributed to (-211) $PbTi_3O_7$ (PDF# 00-045-0533) and is consistent with the measured Pb-deficient compositions. The samples in the same 5:2-3:2 range also displayed lower intensities for the perovskite reflections, which is due to the perovskite phase being suppressed for the Pb-deficient samples. The perovskite (101) and (110) peaks appear to have collapsed into a single peak that is somewhat broadened compared to the same reflections for the 3:1 and 4:1 samples. The reason for the peak collapse is still unclear. The sample grown with a 1:1 cycle ratio was severely Pb-deficient and did not have any peaks attributable to perovskite following annealing. The three peaks that were not attributable to the substrate were (from left to right), anatase (PDF# 00-021-1272) TiO_2 (101), followed by $PbTi_3O_7$ (PDF# 00-045-0533) (-102) and (-211).

XRD of Stoichiometric $PbTiO_3$ Annealed Under Different Conditions

Several different annealing sequences were investigated for PTO samples grown with a 4:1 PbO_x:TiO_x ratio. The effects of a 400 °C pre-anneal with a 5 min. hold were investigated in order to replicate a pyrolysis step frequently implemented for sol-gel PZT growth.[11] The XRD patterns corresponding to the different annealing sequences are shown below in Fig. 5.7. The unannealed samples did not show any features not previously discussed in the preceding paragraphs. The sample that received only the 400 °C pre-anneal with a 5 min. hold had a slightly more defined peak (compared to the hump of the unannealed sample) at about 30.2°, which can be attributed to PbO Massicot (020) which occurs at 30.316°. No clear trends are present in the samples that received a full crystallization anneal. The sample that received a 700 °C anneal with a

1 min. hold and the sample that received the 400 °C pre-anneal before a 600 °C anneal with a 5 min. hold displayed peaks at each of the expected PTO perovskite locations except (111). Future measurements using glancing angle X-ray diffraction (GIXRD) may be able to screen out the Pt (111) for better resolution of the PTO (111) peak. The sample that received the 400 °C pre-anneal before a 700 °C anneal with a 1 min. hold, and the sample that received a 600 °C anneal with a 5 min. hold only displayed the PTO perovskite (100) reflection and the collapsed (101)/(110) peak. Based on the XRD alone, none of the other RTA sequences displayed significantly better peak intensity, preferred orientation, or phase purity than the standard anneal.

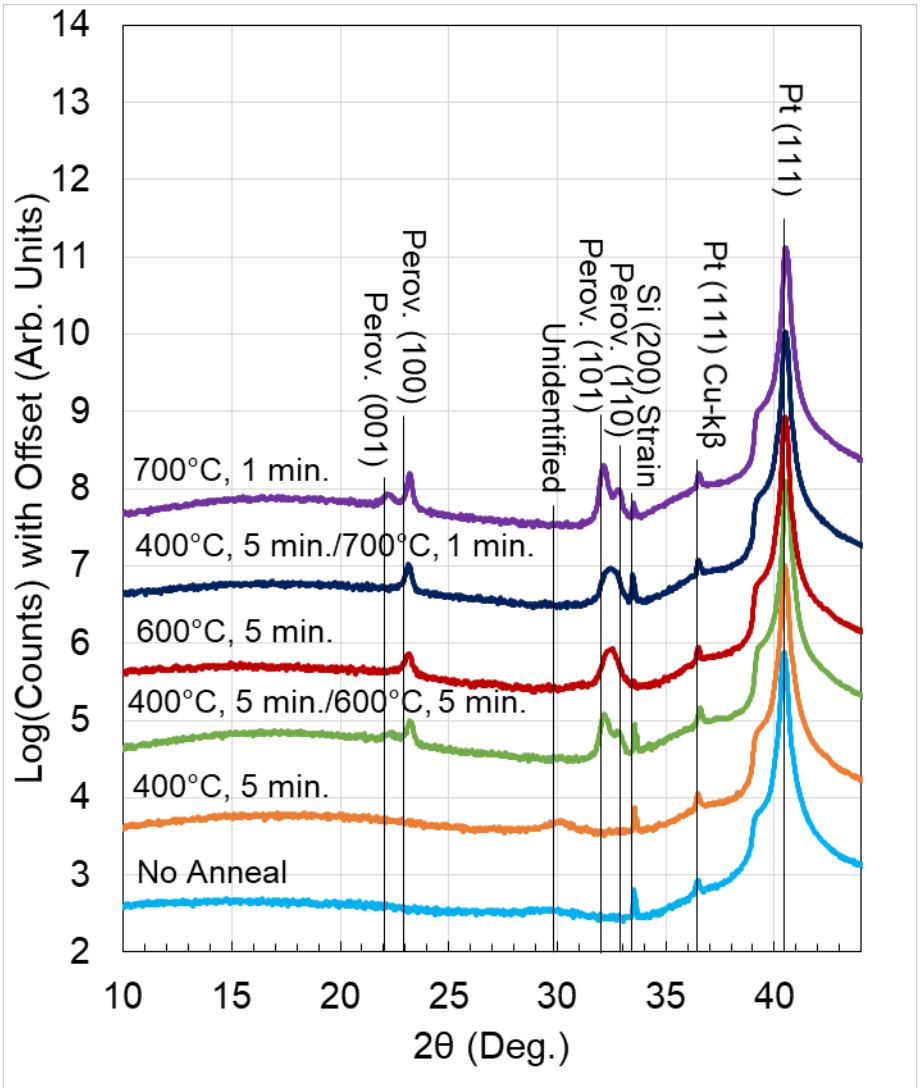

Figure 5.7: X-ray diffraction θ-2θ scans of ALD PTO grown with a PbO_x:TiO_x 4:1 cycle ratio with several different anneal protocols.

The crystallite size of the PbO was estimated using the Scherrer equation for the unannealed sample and for the sample that received a 400 °C pre-anneal with a 5 min. hold. The PbO peak (attributed to Massicot PbO) centered at 29.6° belonging to the unannealed sample was measured to have a full-width at half-maximum of 1.3° (Fig. 5.7). The corresponding crystallite size was calculated to be approximately 6-nm, assuming K (crystallite shape constant) equals 0.9. The PbO peak centered at 30.2°

belonging to the sample that received a 400 °C pre-anneal with a 5 min. hold was measured to have a full-width at half-maximum of 1.0° (Fig. 5.7). Assuming the same K as before (0.9), the crystallite size was calculated to be approximately 8-nm. The calculated crystallite sizes are not expected to be highly accurate since the effect of strain was not considered, but do provide a coarse estimate of the magnitude of the crystallite size.

The effect of the RTA temperature ramp rate was considered as a variable. The ramp rate was varied for samples ranging from 10 °C/s to 200 °C/s but each received the same 700 °C with a 1 min. hold final crystallization. The XRD patterns are shown below in Fig. 5.8. Though each of the samples displayed perovskite peaks, there are slight differences between the slow (10 °C/s and 50 °C/s) and fast (100 °C/s and 200 °C/s) recipes. All four of the annealed samples showed little to no evidence of a (001) perovskite peak, but did show the (100) peak. The samples annealed with the fast ramp displayed (barely) distinguishable perovskite (101) and (110) peaks, whereas the samples annealed with the slow ramp only showed collapsed (101) and (110) peaks.

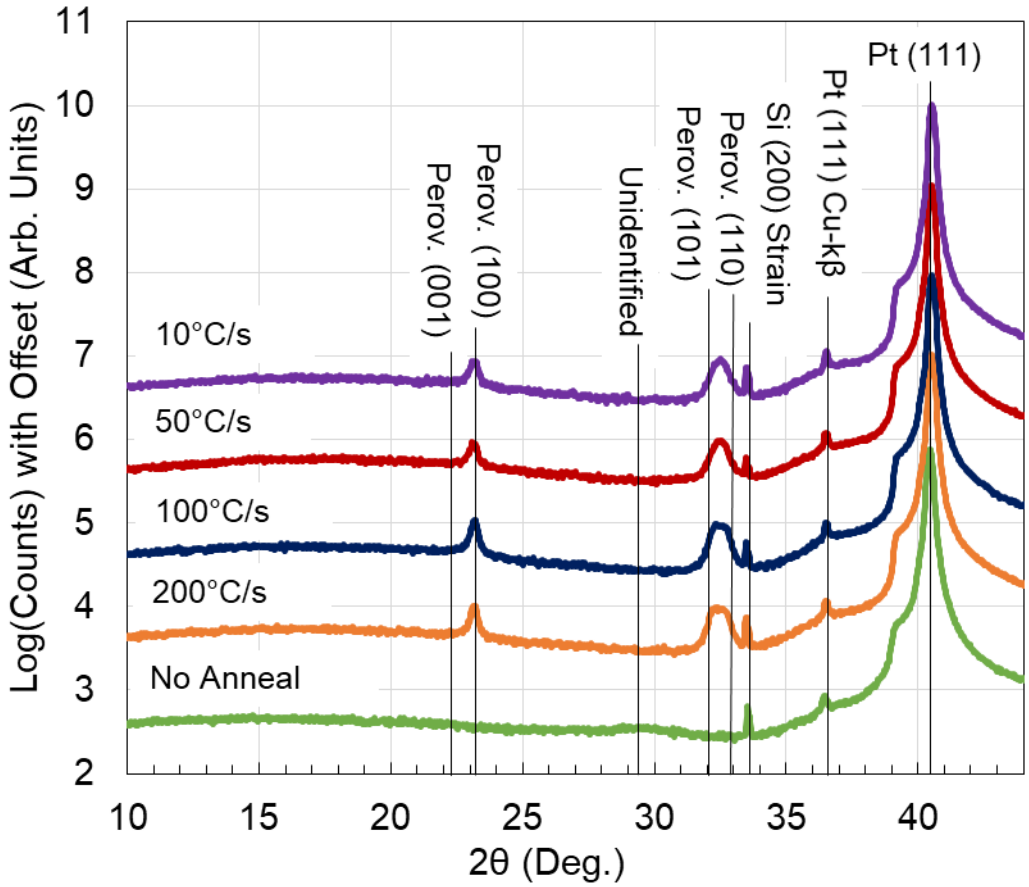

Figure 5.8: X-ray diffraction θ-2θ scans of ALD PTO grown with PbO_x:TiO_x a 4:1 cycle ratio with several different ramp rates to 700 °C with a 1 min hold.

XRD of Pb-deficient $PbTiO_3$ Annealed Under Different Conditions

To determine whether the RTA recipe had any effect on the crystallization on slightly Pb-deficient PTO, several samples were annealed from an ALD PTO wafer grown with a 3:1 PbO_x:TiO_x ratio. The XRD patterns are shown below in Fig. 5.9. The 700 °C anneal with a 1 min. hold was repeated for two different samples to assess the repeatability. The results are strikingly similar to those reported in Fig. 5.7. The

duplicated 700 °C anneals with a 1 min. holds did not exactly match, which suggests that some other variable may be influencing the shape of the perovskite peaks. Chemical composition uniformity mapping has not been performed, so small differences in stoichiometry cannot be ruled out. However, small differences in stoichiometry are not likely responsible for the different crystallization behavior, since we do not see a large difference even between the PbO_x:TiO_x 3:1 and 4:1 samples. Some other variables include: RTA chamber conditioning, temperature overshoot, and position of the piece parts within the RTA. Those effects should be studied in detail in future work.

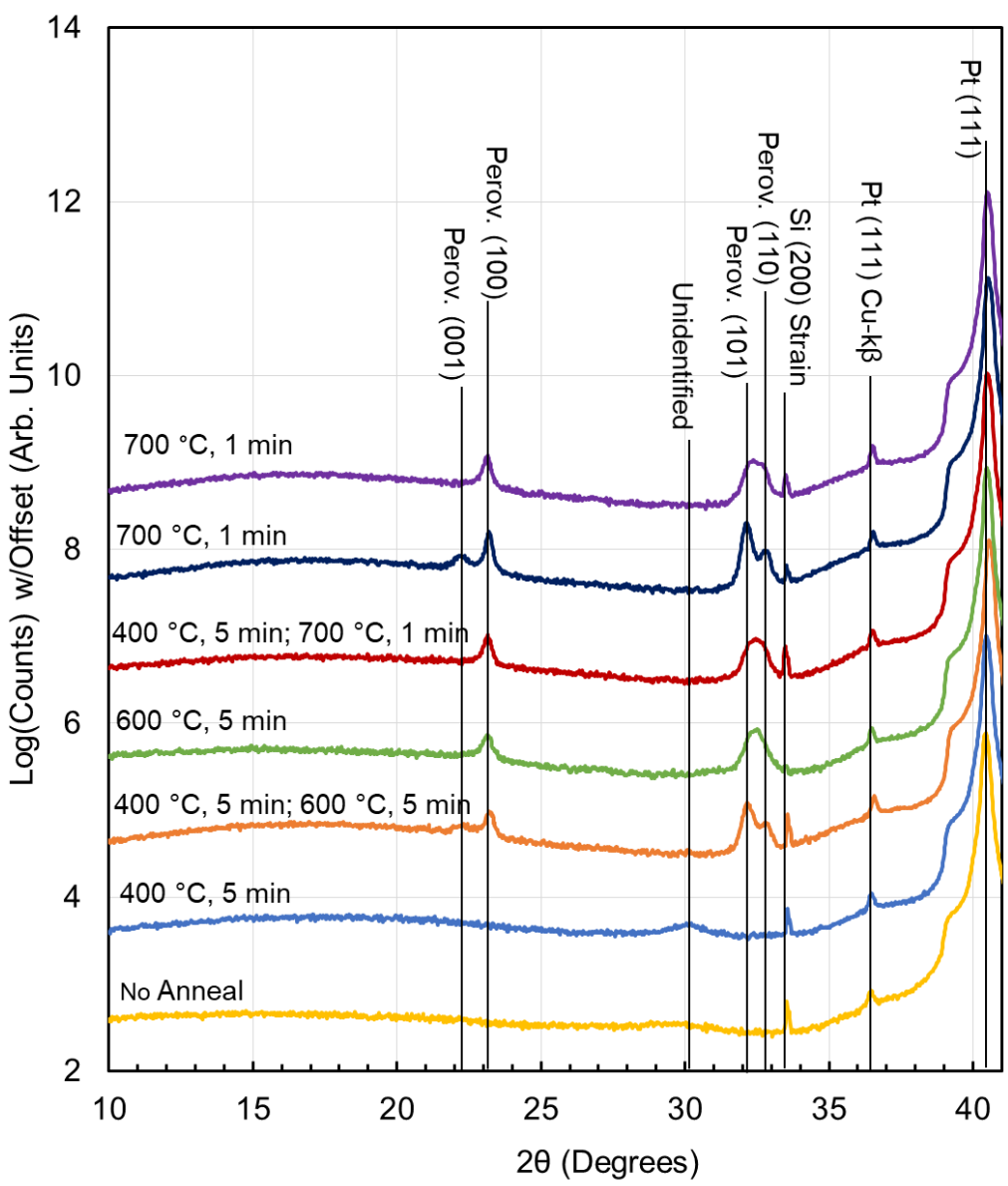

Figure 5.9: X-ray diffraction θ-2θ scans of ALD PTO grown with a PbO_x:TiO_x 3:1 cycle ratio with several different anneal protocols.

Phase Identification of PTO with a PbO_x Seed Layer

To this point, PTO has shown minimal preferred orientation, despite being grown on {111}-oriented Pt. PTO has been shown to grow in a preferred (001) direction if grown

on a PbO-rich 1-10 nm-thick seed layer.[12] (001)-oriented PTO may serve as a growth template for (001)-oriented PZT.[11] The (001) orientation increases the piezoelectric coefficients of PZT.[13] In this section, PTO samples with a 4:1 PbO_x:TiO_x cycle ratio on an ALD-grown PbO_x seed layer in order to produce a (001)-oriented film, following RTA are studied. The seed layers were deposited according to the binary PbO_x process outlined in Chapter 4. The thickness was measured by ex-situ ellipsometery and was found to be 8 nm-thick based on a Cauchy model. Fig. 5.10 shown below details the XRD patterns obtained using the PbO_x seed layer.

The unannealed sample with the PbO_x seed layer and 1401 cycles of ALD PTO displayed two large, unidentified peaks at 38.8° and 43.1°. Both peaks were absent following the 400 °C pre-anneal in O_2. Further investigation is required to conclusively identify the peaks, but a few possibilities are presented here. First, the peaks may be attributed to PbO_x. The 38.8° peak may match massicot (121) at 39.515°, though it is a low-intensity peak and differs from the actual peak location by a little over 0.7°. The 43.1° peak could match (102) litharge (PDF# 00-005-0561) at 42.528°, though it is also a low intensity peak and differs in location by 0.6°. The low intensity peaks cannot be excluded out-of-hand since the Pt is highly oriented and may have induced preferred orientations of the PbO that better match the Pt {111} lattice spacing. Since the 38.8° and 43.1° peaks straddle the large Pt{111} peak, this is a plausible explanation. Application of the Scherrer formula to the 38.8° and 43.1° yields crystallite sizes of 13 and 8-nm, respectively, which are on the order of the film thickness measured by ellipsometry (8-nm using a Cauchy model). Although the crystallite size appears to match quite well to the apparent film thickness measured by ellipsometry, it important

to note a caveat related to the ellipsometer model. The 100 nm-thick Pt substrate fully attenuated the ellipsometer signal, and it was considered to be infinitely thick (by the model). Chemical reactions or inter-diffusion of the PbO_x film with the Pt substrate could appear as a thickness increase in the Cauchy model, so additional characterization methods are required to more accurately determine the deposited film thickness.

A second hypothesis is that the peaks correspond to a Pb_4Pt alloy (PDF# 00-006-0463) where the observed 38.8° and 43.1° peaks match the (220) and (212) peaks at 38.783° and 42.824°, respectively. The peaks are much higher intensity than either of the PbO peaks, and the observed peaks better match the Pb_4Pt pattern than either of the PbO patterns. The Pb_4Pt pattern also contains a (202) peak at 40.414° which overlaps the Pt {111} peak almost exactly. The formation of $PbPt_x$ intermetallics has been reported for PZT grown on Pt by several different deposition techniques. Nittala et al reported an intermediate Pt_3Pb phase that was formed at ~500 °C upon annealing sol-gel PZT that was pyrolyzed at 300 °C.[14] The $PbPt_3$ phase disappeared upon crystallization of the perovskite phase at 650 °C. The behavior of the $PbPt_3$ phase identified by Nittala doesn't match the behavior of the present unidentified phases, which were formed at 250 °C and disappeared at 400 °C in O_2. In addition, the reported 2θ locations of the $PbPt_3$ intermediate phase reflections do not match the present unidentified peaks. Nonetheless, the growth model proposed by Nittala, whereby $PbPt_x$ intermetallics are formed at the Pt/(amorphous PTO or PZT) interface at low temperatures and the Pb is diffuses into the amorphous PTO or PZT at higher temperatures, may apply to the present case. A more direct comparison is found in Otani et al, that showed the presence of a $PbPt_x$ alloy in PZT films deposited by MOCVD on Pt substrates.[15] In that case, the

$PbPt_x$ appeared in the as-deposited films grown at substrate temperatures between 400-550 °C. However, the $PbPt_x$ XRD peak disappeared upon annealing in air at 450 °C and above. Although no PDF number was provided for the $PbPt_x$ reflection and the 2θ location was not reported to a high precision, it appeared to match the unidentified peak at 38.8° in this work. Tentatively, it seems that the present unidentified peaks most likely belong to an intermediate $PbPt_x$ alloy, possibly $PbPt_{0.25}$ (or Pb_4Pt) that disappears at 400 °C in O_2. More analysis is required to conclusively test the nucleation and out-diffusion mechanism behind the intermediate phase, but ultimately its presence did not seem to negatively affect the ability of the PTO film to crystallize into the perovskite phase.

The samples shown in Fig. 5.10 that received a full crystallization RTA are nearly identical to the samples reported in this chapter, with the exception of the sample that received only a 700 °C anneal with a 1 min. hold, which is shown as the purple line. Unlike the other samples, the (111) perovskite is observed. The (001) perovskite peak also appears to be a higher intensity than the rest of the samples in Fig. 5.10. None of the samples exhibited the desired strong (001) orientation. The reason behind the seemingly nearly random grain orientation, with little (001) orientation, is explored in later sections in this chapter.

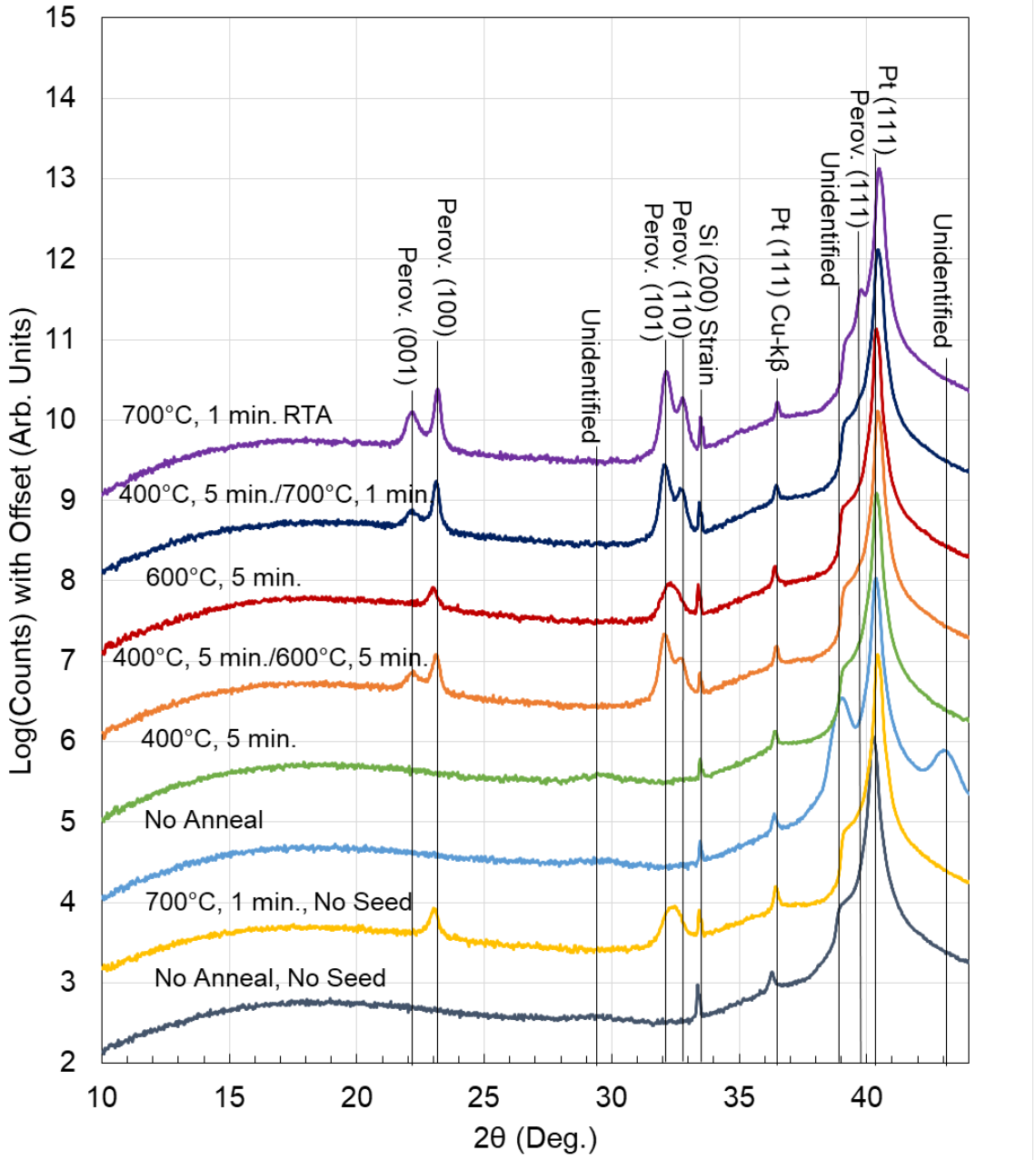

Figure 5.10: X-ray diffraction θ-2θ scans of ALD PTO grown with PbO_x:TiO_x a 4:1 cycle ratio on a 250 ALD cycle PbO_x seed layer with different anneal conditions.

Phase Identification of PTO with a TiO_x Seed Layer

A TiO_x seed layer was implemented as an alternative to a PbO_x seed layer in an effort to induce a (111)-oriented PTO texture. TiO_2 seed layers 1-5 nm-thick have been previously shown to induce a (111)-orientation in PTO.[16] A 1 nm-thick TiO_x seed layer was grown by ALD and annealed in O_2 at 700 °C with a 1 min hold to induce crystallization. Neither the chemical composition nor the crystal structure of the as-deposited or annealed 1 nm-thick TiO_x film was measured due to difficulties in analyzing such a thin film. The thickness was measured by in-situ ellipsometry using tabulated optical constants for TiO_2. The XRD patterns corresponding to the PTO films grown with TiO_x seed layers are shown below in Fig. 5.11. The PTO films were grown using the same sequence (PbO_x:TiO_x cycle ratio of 4:1) and cycles (1401) as each of the previous trials. The results are unremarkable. None of the samples deviated significantly from the control, which is plotted as the turquoise line. All samples that received a crystallization anneal showed peaks corresponding to the perovskite phase and no secondary phases. The perovskite (101) and (110) peaks appear to be collapsed for each of the samples except 700 °C with a 1 min hold, for which the peaks were more easily distinguished. The PTO grain orientation doesn't seem to be strongly influenced by the addition PbO_x or TiO_x seed layers.

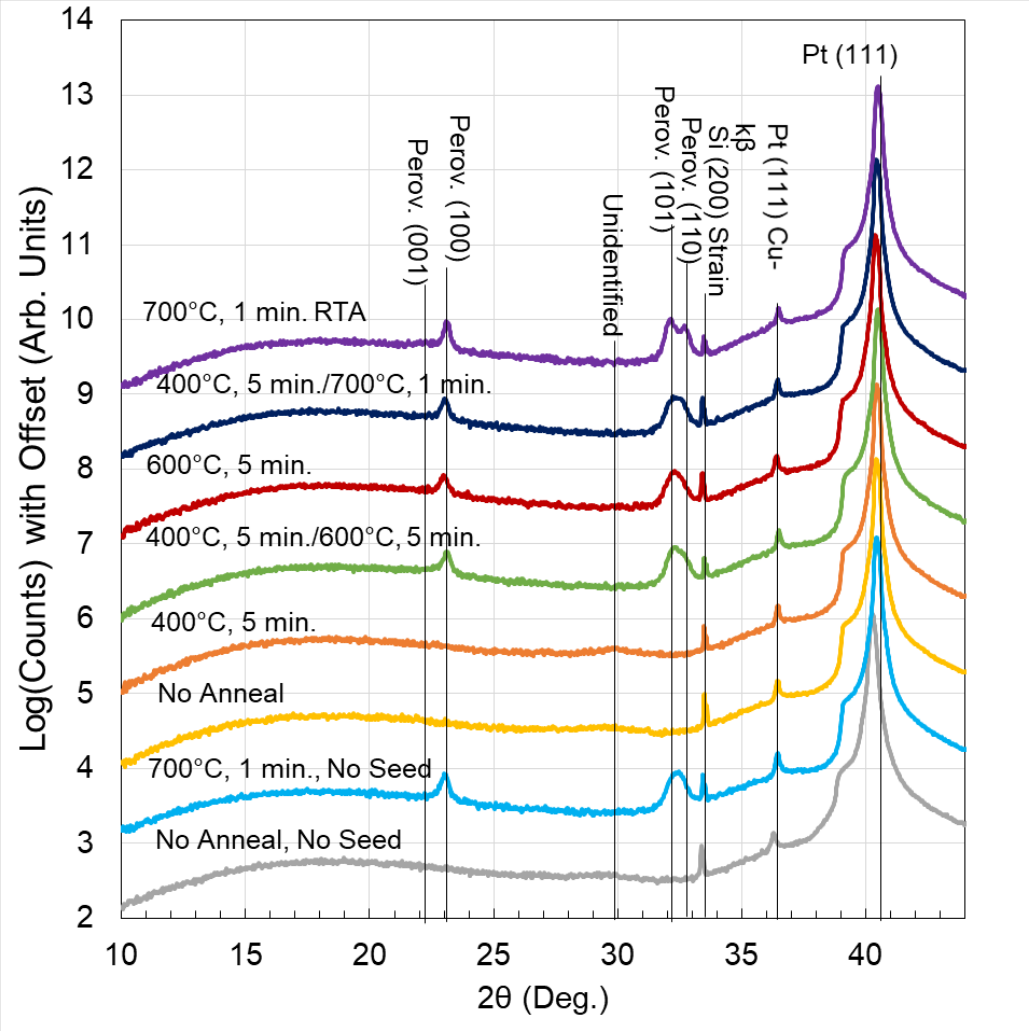

Figure 5.11: X-ray diffraction θ-2θ scans of ALD PTO grown with PbO_x:TiO_x a 4:1 cycle ratio on a 20 ALD cycle TiO_x seed layer with different anneal conditions.

Cross Section STEM Analysis

Unannealed ALD $PbTiO_3$

Cross-section STEM images are shown below for both unannealed (Fig. 5.12) and annealed (Fig. 5.13) PTO samples grown with a 4:1 PbO_x:TiO_x cycle ratio, with 1401

total ALD cycles, and no seed layer. The images presented are high-angle annular dark-field (HAADF) which means that elements with higher Z are lighter (more intense), while those with lower Z are darker (less intense). Figure 5.12 shows the cross-section of an unannealed sample. The image appears to contain small white blotches throughout the PTO layer. The white blotches appear to be embedded in a gray matrix. Most of the white blotches are approximately 2 to 5-nm in diameter, though some appear to be as large as 10-nm in diameter. Since Pb has the highest Z of the elements present in the sample (between Ti, O, and possible residual Ga from the ion beam sample preparation), we conclude that the white blotches contain higher concentrations of Pb. The massicot PbO phase was previously identified in XRD patterns of unannealed samples, which is consistent with the HAADF contrast. The observed crystallite size range from the STEM image agrees with the crystallite size calculated previously using the Scherrer equation that predicted 6 to 8-nm crystallites. Qualitatively, the gray matrix in the PTO layer appears similar in contrast to the TiO_2 underlayer, while the white blotches in the PTO are similar to the Pt protective cap, which has a similar Z compared to Pb. The film appears to contain PbO with nanometer-diameter grains embedded within a TiO_x-matrix that is amorphous according to XRD (see Fig. 5.7). This is similar to the growth mode previously identified for ALD PZT grown with different precursors, which demonstrated PbO_x nanoclusters embedded in an amorphous Ti-Zr-O matrix.[17] Although the growth mode doesn't follow the layer-by-layer ALD archetype, the deposition rate still appeared to be self-limited, which preserves the capability to coat high aspect-ratio structures. ALD

growth models are currently in development to explain the unusual growth behavior (see Chapter 8).

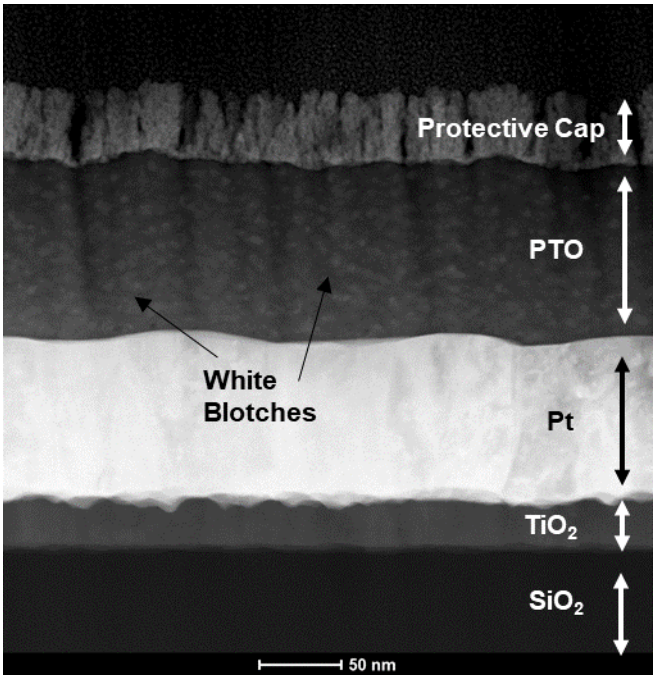

Figure 5.12: STEM cross-section of unannealed PTO sample grown with a 4:1 PbO_x:TiO_x cycle ratio.

Annealed ALD $PbTiO_3$

Figures 5.13 and 5.14, shown below, are STEM cross sections of an annealed sample grown with the same conditions as the unannealed sample shown in Fig. 5.12. The annealed samples didn't display columnar grain boundaries like those observed in sputtered, sol-gel, and MOCVD films. Instead, the grains appeared to nucleate throughout the thickness of the film. The random nucleation, versus heterogeneous nucleation at the growth surface interface, explains why neither the PbO_x nor TiO_x nucleation layers significantly affected the film texture. Another feature present in the annealed samples are small 2-5 nm diameter round patches dark in contrast throughout

the PTO layer. These seem to be pores or Ti-rich nuclei, owing to the HAADF contrast. A small number of larger defects were also observed and are shown in Fig. 5.14. The dark, circular regions that are approximately 5-10 nm in diameter appear to be small voids within the sample. Near the surface, there is a larger dark region that protrudes from the top of the film approximately 20 nm-deep into the film. This is possibly a pinhole, but may also be a result of FIB damage and over-thinning of the sample.

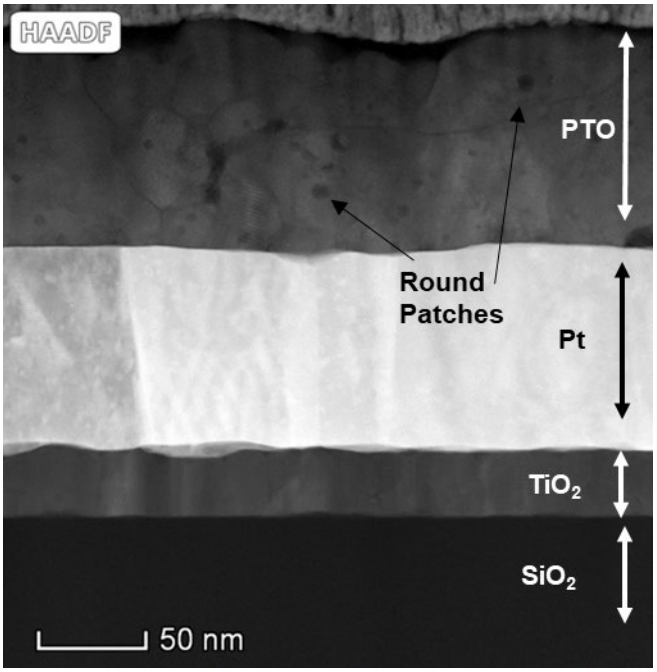

Figure 5.13: STEM cross-section of PTO sample grown with a 4:1 PbO_x:TiO_x cycle ratio and annealed at 700 °C with a 60-s hold, at a 90 °C/s ramp rate, in O_2.

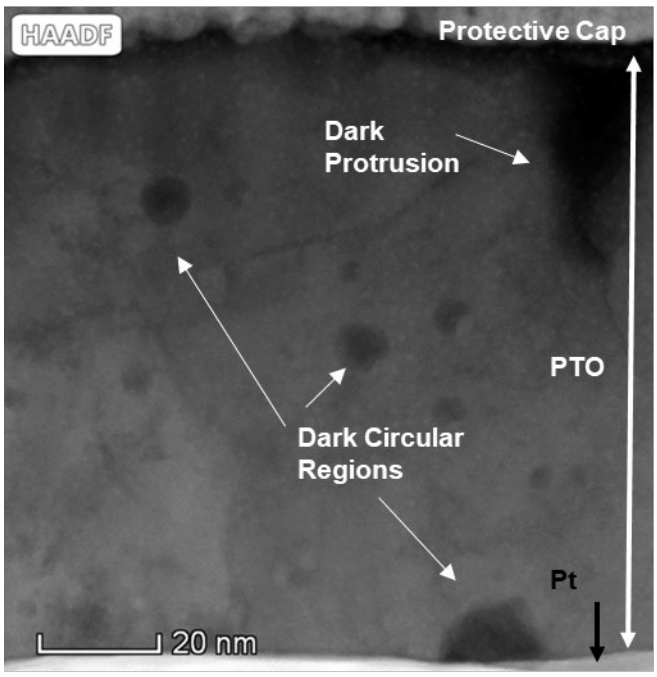

Figure 5.14: High-magnification STEM cross-section of PTO sample grown with a 4:1 PbO_x:TiO_x cycle ratio and annealed at 700 °C with a 60-s hold, at a 90 °C/s ramp rate, in O_2.

The STEM images show that the ALD PTO films were dense and pinhole-free as deposited. Upon annealing, the PTO perovskite grains nucleated randomly throughout the thickness in the films, which was indicated by the large number of grain boundaries in seemingly all directions. The annealed film contained nanometer-sized pores and possibly larger pinholes near the surface of the film.

Ferroelectric Characterization

Polarization/Electric-Field Hystersis

MIM capacitors were fabricated as detailed in Chapter 4 to characterize the ferroelectric properties of the ALD PTO films. Pt was used as both the top and bottom

electrode. The top electrode of the tested circular capacitors was 4.92×10^{-4} cm^2 in area. The PTO was deposited as four separate ALD 1401-cycle ALD growths, each followed by a 700 °C, 1 min anneal. The layers were approximately 100 nm-thick as deposited and shrank 10% after RTA. The final total thickness of 360 nm was determined by ex-situ spectroscopic ellipsometry. The polarization versus electric-field measurement is shown below in Fig. 5.15. The test period was 10-ms. The ferroelectric figures of merit are P_{max} = 48 μC/cm^2, $2P_r$ = 60 μC/cm^2, E_{c-} = -73 kV/cm, and E_{c+} = 125 kV/cm. The sample displayed a large, permanent, and reversible polarization in response to an electric field, which is indicative of ferroelectric films. The as-processed films were initially quite leaky electrically until a final crystallization anneal of 600 °C with a 30 minute hold was performed after all micromachining was performed. It is unclear if the final anneal served only to recover damage (for example, top electrode adhesion) from the micromachining process, or if it served to improve the density of the film.

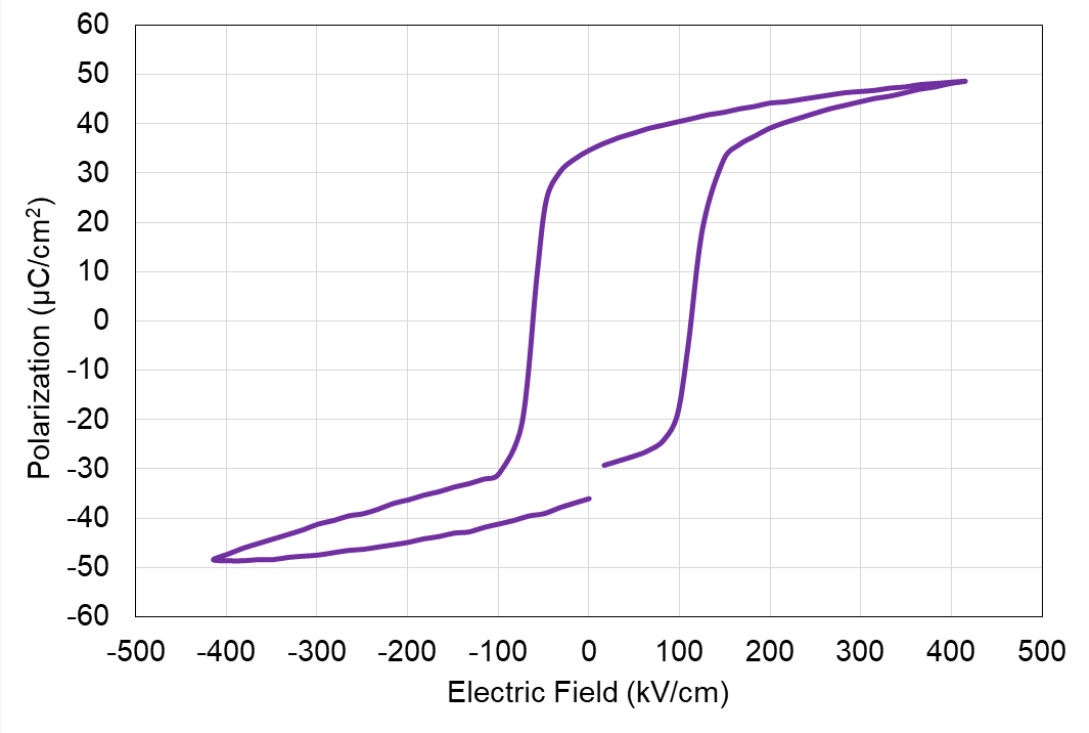

Figure 5.15: Polarization versus electric field measurement of ALD PTO grown with PbO_x:TiO_x a 4:1 cycle ratio with a film thickness of 360 nm.

Relative Permittivity, Loss Tangent, and Leakage Current

Figure 5.16 contains the capacitance-voltage measurement (reported as relative permittivity versus electric field) of the MIM capacitors with 360 nm ALD PTO. The films showed a zero-field dielectric constant of 255 with a tuning range of 196 to 288 for -276 kV/cm < E < 277 kV/cm. Tan δ was simultaneously measured during the capacitance-voltage measurement and is reported in Fig. 5.17. The Tan δ remained lower than 0.035 throughout the range of voltages tested and showed characteristic peaks coinciding with the maximum dielectric constant reported in Fig. 5.16. The Tan δ is skewed up and to the left, which is likely a result of the higher leakage current in the negative test direction. The leakage current density is plotted directly in Fig. 5.18, shown below. As the voltage was stepped in the positive direction, the leakage current density did not exceed 16 $\mu A/cm^2$. However, when the voltage was stepped in the negative direction, the leakage current increased by an order of magnitude to 212 $\mu A/cm^2$.

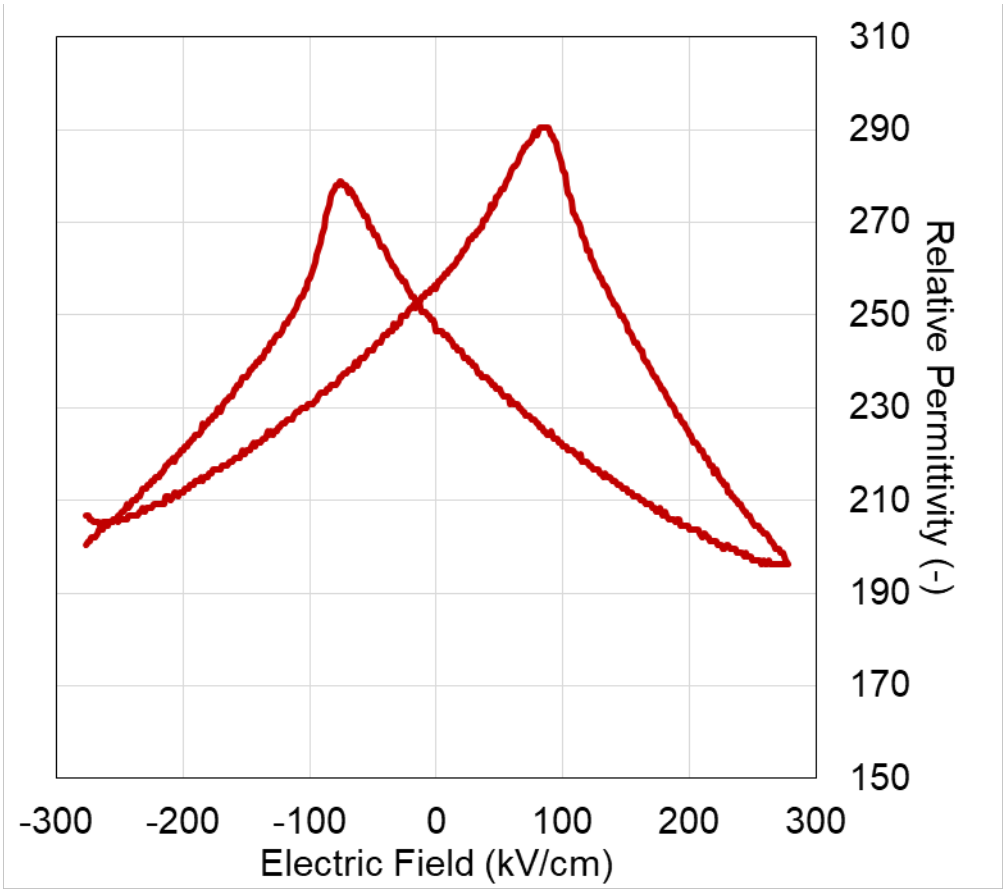

Figure 5.16: Relative permittivity versus electric field measurement of ALD PTO grown with PbO_x:TiO_x a 4:1 cycle ratio with a film thickness of 360 nm.

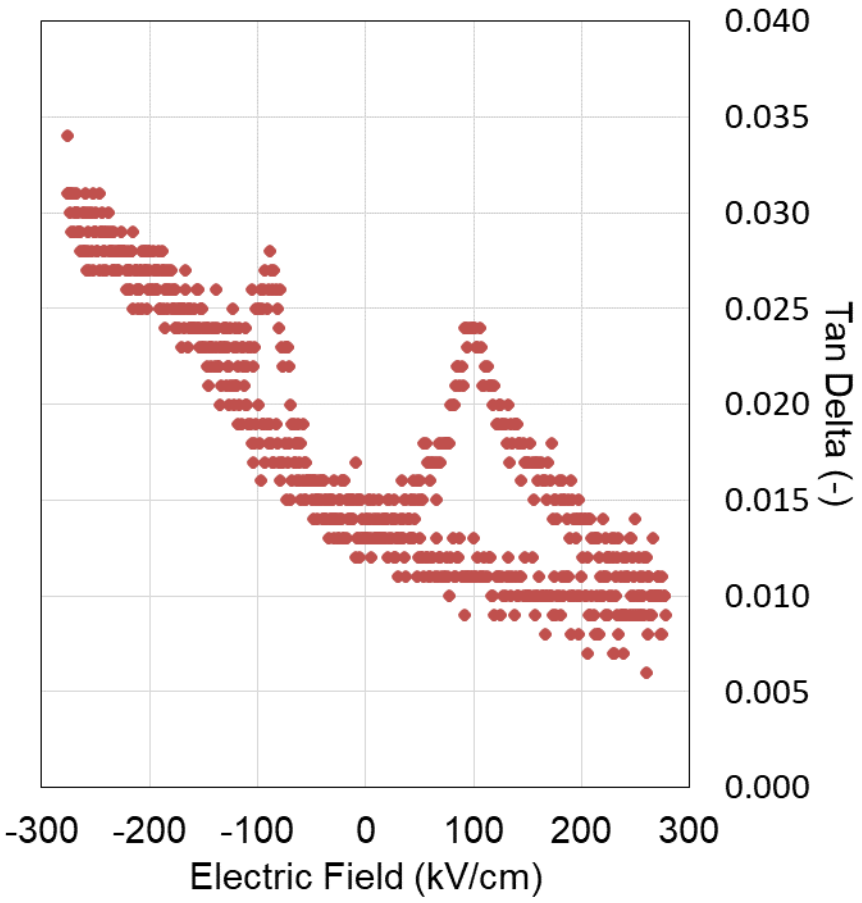

Figure 5.17: Dielectric loss measurement of ALD PTO grown with PbO_x:TiO_x a 4:1 cycle ratio with a film thickness of 360 nm.

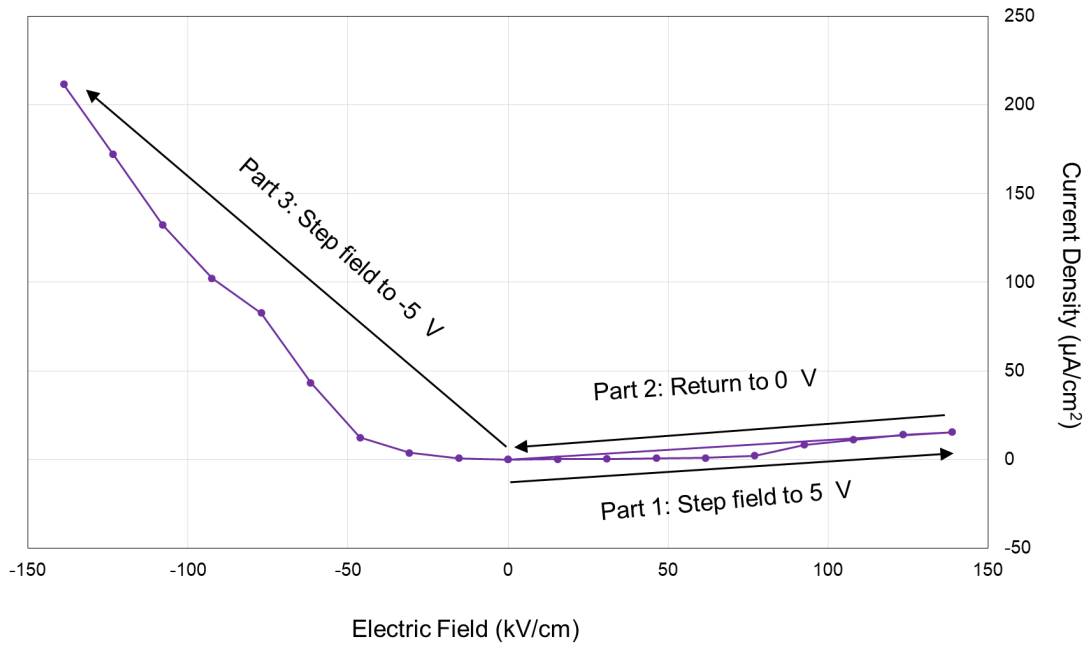

Figure 5.18: Leakage current measurement of ALD PTO grown with PbO_x:TiO_x a 4:1 cycle ratio with a film thickness of 360 nm.

Although the leakage current measurement performed here (Fig. 5.18) is not intended to comprehensively identify leakage current mechanisms, some discussion of the anomalous diode-like conduction behavior is warranted. Note that the bias was applied to the bottom electrode while the top electrode was held at ground potential. The overall conduction of a MIM capacitor (at low electric fields) is limited either by the charge injection from the electrode held at reverse-bias potential into the dielectric, the bulk conduction of the dielectric, or the discharge into forward-biased electrode. The asymmetric leakage current suggests that conduction is not limited by the bulk conduction through the dielectric (otherwise, the leakage would be symmetrical). We can assume that the thermally excited electrons that make it into the PTO should easily be able to cross the Schottky barrier formed at the PTO/forward-biased electrode.

Therefore, the limiting mechanism is the charge injection from the reverse-bias electrode into the PTO. For negative applied fields, the bottom electrode is considered to be reverse-biased while the top electrode is considered to be forward-biased (and vice/versa for positive applied fields). Mojarad et al.[18] investigated leakage current mechanisms for a similar materials system that consisted of MIM capacitors with Pt used as the metal for both electrodes, and ALD $SrTiO_3$ as the insulator. Mojarad identified the low-field electron injection mechanism to be trap-assisted tunneling, with oxygen vacancies serving as the dominant trap species.[18] Applying those findings to the limited data presented in Fig. 5.18 suggests that some trap species, possibly oxygen vacancies, may be more concentrated near the bottom Pt electrode compared to the top Pt electrode. There are two possible explanations for the possible difference in oxygen vacancy concentration. First, the growth characteristics at the start of the growth, where the precursors are exposed to the bare Pt surface, was not thoroughly investigated. Therefore, we cannot rule out that the elemental concentration at the bottom Pt-electrode interface may be different from the bulk. Second, the RTA in O_2 probably reduced the oxygen vacancy concentration at the PTO near the top surface, since the flow of the O_2 gas passed directly over the top surface. More testing is required to prove that oxygen vacancies are the dominant trap species, such as temperature-dependent leakage current measurements, leakage current measurements performed at higher fields, and time-of-flight secondary ion mass spectroscopy (TOF-SIMS).

Ferroelectric Figures of Merit

For convenience, the ferroelectric figures of merit (FOM) are reprinted below in Table 5.3. The values from Table 5.3 will be referenced in Chapter 8, which includes a comparison of the ALD PTO FOM presented here to relevant examples from literature.

Table 5.3: ALD PTO Ferroelectric Figures of Merit

Parameter	**ALD PTO**
Thickness	360 nm
Composition	$Pb_{1.0}Ti_{1.0}O_{3.0}$
GPC	0.064 nm/cycle
P_{max}	48 μC/cm^2 at 415 kV/cm
P_{r+}	34.6 μC/cm^2
P_{r-}	-36 .0 μC/cm^2
E_{c+}	125 kV/cm
E_{c-}	-73 kV/cm
Zero Field ε_r	255
Max ε_r	288 at -67 kV/cm
Min ε_r	196 at -496 kV/cm
Max Tan δ	0.034 at -275 kV/cm
Leakage Current Density +	16 μA/cm^2 at 138 kV/cm
Leakage Current Density -	212 μA/cm^2 at -138 kV/cm

Summary and Conclusions

ALD PTO was successfully grown using a new process with $Pb(DMAMP)_2$ and TDMAT as the cation precursors, and H_2O and O_3 as co-oxidizers. The as-deposited films contained PbO_x nanoclusters, likely PbO massicot, embedded in an amorphous

TiO_x (x close to 2) matrix. The annealed films crystallized into the perovskite phase under a variety of RTA temperatures and hold times in O_2 atmosphere. PbO_x and TiO_x seed layers did not significantly impact the grain orientation of the annealed PTO films because the nucleation seemed to occur randomly, instead of heterogeneously at the Pt-PTO interface. The ferroelectric properties of 360 nm ALD PTO films were measured on MIM capacitor structures with Pt electrodes. These films displayed a P_{max} = 48 $\mu C/cm^2$, $2P_r$ = 60 $\mu C/cm^2$, E_{c-} = -73 kV/cm, and E_{c+} = 125 kV/cm, following a 600 °C recovery anneal with a 30 min hold in O_2. Capacitance-voltage measurements displayed a zero-field dielectric constant of 255 with tuning range 196 to 288 for -276 kV/cm < E < 277 kV/cm and Tan δ less than 0.035 throughout the range of tested voltages. The leakage current density was measured to be 16 $\mu A/cm^2$ in the positive direction and 212 $\mu A/cm^2$ in the negative. The electrical properties presented for the PTO films tested in this work compare favorably to the prior attempts at ALD PTO which were summarized in Chapter 2. A detailed comparison of the electrical properties is presented in Chapter 8.

References

[1] Strnad NA, Potrepka DM, Pulskamp JS, et al. Texture and Phase Variation of ALD $PbTiO_3$ Films Crystallized by Rapid Thermal Anneal. *J Vac Sci Technol A.* 2019;37:020917.

[2] Harjuoja J, Kosola A, Putkonen M, et al. Atomic layer deposition and post-deposition annealing of $PbTiO_3$ thin films. *Thin Solid Films.* 2006;496:346-352.

[3] Hwang GW, Lee HJ, Lee K, et al. Atomic Layer Deposition and Electrical Properties of $PbTiO_3$ Thin Films Using Metallorganic Precursors and H_20. *J Electrochem Soc.* 2007;154:G69-G76.

[4] Watanabe T, Hoffman-Eifert S, Mi S, et al. Growth of ternary PbTiOx films in a combination of binary oxide atomic layer depositions. *J Appl Phys.* 2007;101:014114.
[5] Lee HJ, Park MH, Min Y-S, et al. Unusual Growth Behavior of Atomic Layer Deposition $PbTiO_3$ Thin Films Using Water and Ozone as Oxygen Sources and Their Combination. *J Phys Chem C.* 2010;114:12736-12741.
[6] Sbrockey NM, Tompa GS, Lavelle R, et al. Atomic layer deposition of $PbTiO_3$ and $PbZr_xTi_{1-x}O_3$ films using metal alkyl and alkylamide precursors. *J Vac Sci Technol A.* 2018;36:031509.
[7] Harjuoja J, Vayrynen S, Putkonen M, et al. Atomic layer deposition of $PbZrO_3$ thin films. *Appl Surf Sci.* 2007;253:5228-5232.
[8] Watanabe T, Hoffman-Eifert S, Peter F, et al. Liquid Injection ALD of $Pb(Zr,Ti)O_x$ Thin Films by a combination of Self-Regulating Component Oxide Processes. *J Electrochem Soc.* 2007:154:G262-G269.
[9] Watanabe T, Hoffman-Eifert S, Hwang CS, et al. Growth Behavior of Atomic-Layer-Deposited Pb(Zr,Ti)Ox Thin Films on Planar Substrate and Three-Dimensional Hole Structures. *J Electrochem Soc.* 2008:155:D715-D722.
[10] Choi JH, Zhang F, Perng Y-C, et al. Tailoring the composition of lead zirconate titanate by atomic layer deposition. *J Vac Sci Technol B.* 2013;31:012207.
[11] Sanchez LM, Potrepka DM, Fox GR, et al. Optimization of $PbTiO_3$ seed layers and Pt metallization for PZT-based piezoMEMS actuators. *J Mater Res.* 2013;28:1920-1931.
[12] Hiboux S, Muralt P. Mixed titania-lead oxide seed layers for PZT growth on Pt(111): a study on nucleation, texture and properties. *J Eur Ceram Soc.* 2004;24:1593.
[13] Ledermann N, Muralt P, Baborowski J, et al. {100}-Textured, piezoelectric $Pb(Zr_xTi_{1-x})O_3$ thin films for MEMS: integration, deposition, and properties. *Sens Actuators A.* 2003;105:162.
[14] Nittala K, Mhin S, Dunnigan KM, et al. Phase and texture evolution in solution deposited lead zirconate titanate thin film: Formation and role of the Pt_3Pb intermetallic phase. *J Appl Phys.* 2013;113:244101.

[15] Otani Y, Okamura S, Shiosaki T. Fabrication of Ferroelecctric Pb(Zr,Ti)O3 Thin Films by Liquid Delivery Metalorganic Chemical Vapor Deposition Using a Novel Titanium Source $Ti(OEt)_2(DPM)_2$. *Jpn J Appl Phys.* 2006;45:1752-1756.
[16] Muralt P, Maeder T, Sagalowicz A, et al. Texture control of $PbTiO_3$ and Pb(Zr, Ti)O_3 thin films with TiO_2 seeding. *J Appl Phys.* 1998;83:3835-3841.
[17] Watanabe T, Hoffmann-Eifert S, Hwang CS, et al. Growth Behavior of Atomic-Layer-Deposited Pb(Zr,Ti)O_x Thin Films on Planar Substrate and Three-Dimensional Hole Structures. *J Electrochem Soc.* 2008;55:D715-D722.
[18] Mojarad SA, Kwa KSK, Goss JP, et al. A comprehensive study on the leakage current mechanisms of Pt/$SrTiO_3$/Pt capacitor. J Appl Phys. 2012;111:014503.

Chapter 6: ALD $PbZr_xTi_{1-x}O_3$

Introduction

The following chapter summarizes the development of a new process to grow ALD PZT using $Pb(DMAMP)_2$, TDMAT, and TDMAZ as the Pb, Ti, and Zr precursors, respectively. This process is similar to the PTO process presented in Chapter 5, with TDMAZ substituted for TDMAT in various proportions. Several additional ALD PZT dose sequences were tested and are described in Chapter 4. A shorthand ("Alternate 1" Pb:Ti 4:1-Pb:Zr 6:4, "Alternate 2" Pb:Ti:Zr 8:1:1, "Alternate 3" Pb:Ti:Zr 8:1:3) is used to refer to each of those additional dose sequences.

Chemical Composition and Growth per Cycle

Overall Composition Measurements

RBS was used to measure the concentration of ALD PZT samples grown according to the super-cycle method described in Chapter 4, with varying PZO/(PZO+PTO) cycle ratios. The atomic percent of each element is plotted over a wide range of cycle ratios below in Fig. 6.1. The Pb:Ti ratio was held at 4:1 for each of the cycle ratios plotted in Fig. 6.1 except at 10% PZO/(PZO+PTO) in which the Pb:Ti ratio was 3:1. The margins of error for O, Ti, Zr, and Pb were ±4 at%, ±1 at%, ±1 at% and ±0.3 at%, respectively. Each column of data points in the plot displays measurements taken from a single growth. Multiple points within the same column represent the Zr, Ti, Pb, and O concentrations measured on different wafer pieces cleaved from the same growth

specimen. The PZT super-cycles typically contained 30-110 total cycles depending on the PZO/(PZO+PTO) cycle ratio. The PZT super-cycle was repeated for each growth to reach 1400±50 total cycles. The range of cycles (1350-1450) stems from the fact that the number of super-cycles was always rounded to a whole number. This nominal 1400 total ALD cycle count is defined as the standard PZT deposition. The PZO cycle contained more (6 total) PbO_x cycles per ZrO_x cycle compared to PTO, which (typically) had four PbO_x cycles per TiO_x. One consequence is that as the PZO cycle ratio increased, the relative number of both the PbO_x and ZrO_x cycles per growth increased compared to TiO_x. To clarify this slight ambiguity, the relative $PbO_x/(TiO_x+ZrO_x)$ cycle ratio (plotted as "Rel. Pb") is plotted to the left of each data column in Fig. 6.1.

No clear trends were observed with respect to the oxygen concentration and the PZO/(PZO+PTO) cycle ratio. The oxygen content hovered around 60 at% and mostly fell within the margin of error of ±4 at%. The Pb and Ti atomic concentrations show the expected trends in Fig. 6.1. The Pb at% (red diamonds in Fig. 6.1) increases because the relative number of PbO_x cycles increase, while the Ti at% (blue dashes) decreases because the relative number of TiO_x cycles decrease. The Zr at% (green circles) does not show the expected trend, and appears flat as a function of PZO cycle ratio.

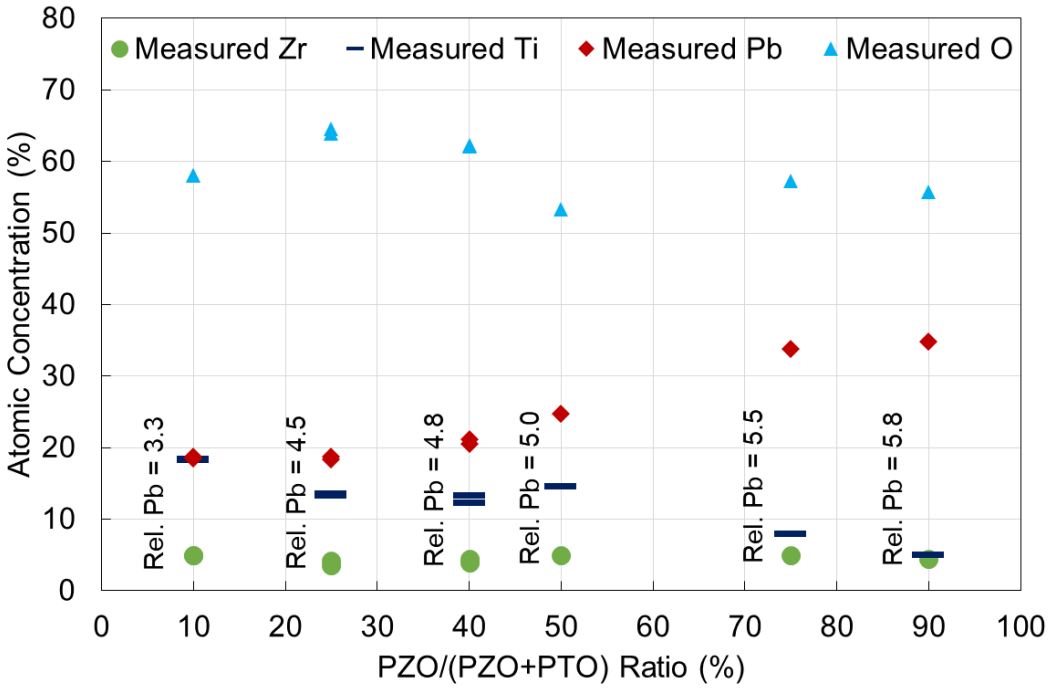

Figure 6.1: Chemical composition variation of ALD PZT films grown with varying PZO/(PZO+PTO) cycle ratios.

The desired PZT composition ($PbZr_{0.52}Ti_{0.48}O_3$) near the morphotropic phase boundary (MPB) theoretically occurs at Pb=20 at%, Ti = 9.6 at%, Zr=10.4 at%, and O=60 at%. The MPB composition was not achieved in the present work because the Zr concentration in this process was limited to 4.4 ±1 at% regardless of the PZO cycle ratio. The strange behavior of the Zr concentration is not yet fully understood, but will be discussed later in this section.

Data Interpolation and Recipe Optimization

Shown below are Figs. 6.2 – 6.5 with simple linear fits of the Ti, Pb, Zr, and film thickness to serve as a model for interpolating the data contained in Fig. 6.1. The purpose is to generate a model that predicts the optimal recipe for the given set of precursors. Simple linear fits were performed (rather than higher order polynomial fits)

to capture the overall expected trends. Although MPB PZT is not possible with this approach, PTO-rich PZT is still useful and may serve as a touchstone for future attempts at MPB PZT.

Figure 6.2 shows the Ti concentration in at% plotted against TiO_x cycle ratio. The data generally followed the expected trend of increasing Ti concentration with increasing cycles. There were no issues incorporating Ti into the film even at relatively low TiO_x cycle ratios. The data fit to the plotted line with an R^2 value of 0.8745. Figure 6.3 shows the Pb at% versus the $PbO_x/(TiO_x+ZrO_x+PbO_x)$cycle ratio for three columns of data near Pb=20 at%. A simple linear fit was performed to estimate the cycle ratio expected to yield Pb=20 at%, while data points with much higher Pb concentrations (higher than 0.83 $PbO_x/(TiO_x+ZrO_x+PbO_x)$, or higher than 50% PZO/(PZO+PTO) cycle ratio) were removed from Fig. 6.3 because they diverged significantly from linearity. Even for the limited range plotted in Fig 6.3, the R^2 value was 0.3144, though it is noteworthy that the number of data points was quite limited (only 6 points).

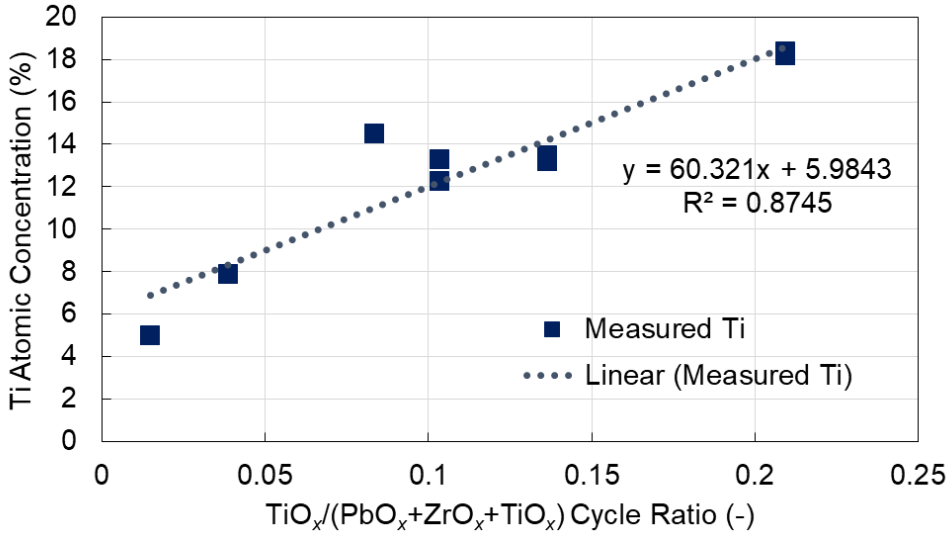

Figure 6.2: Ti atomic concentration versus number of TiO_x cycle ratio.

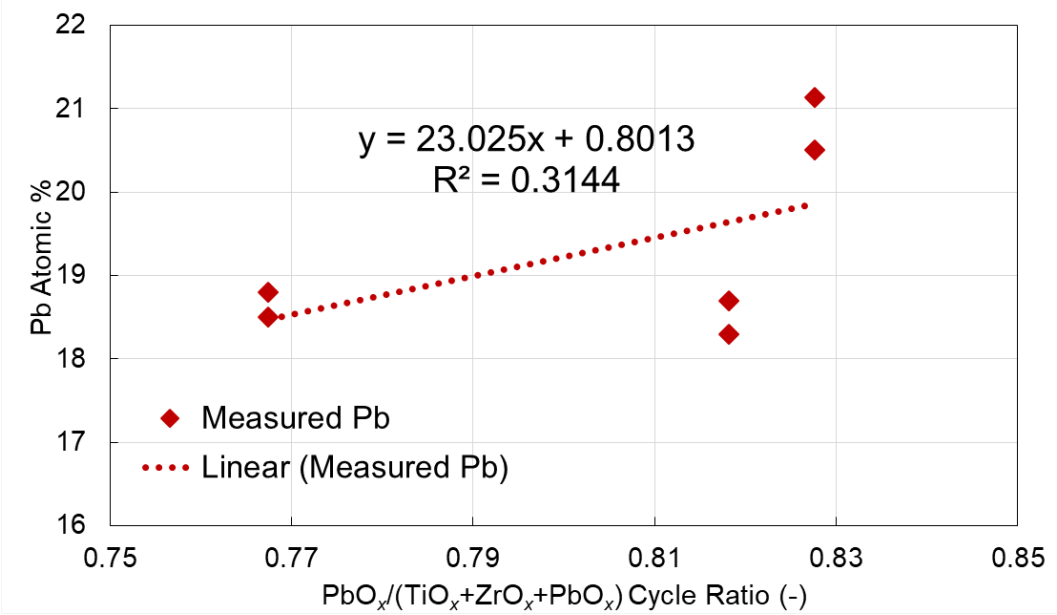

Figure 6.3: Pb atomic concentration versus number of PbO_x cycle ratio.

Figure 6.4 details the Zr composition as a function of number of $ZrO_x/(TiO_x+ZrO_x+PbO_x)$ cycle ratio, with a linear fit plotted alongside the measured RBS data. The fit line is nearly flat, owing to the strange non-incorporation of Zr into the ALD PZT. Each of the data points falls within 4.4 ±1 at%, which is the margin of error of the RBS measurement. The R^2 value (Fig. 6.4) is shown to be 0.01, indicating that points are essentially randomly distributed about the average. Figure 6.5 shows interesting linear growth behavior (R^2 = 0.8525) of the PZT film with respect to the $TiO_x/(TiO_x+ZrO_x+PbO_x)$ cycle ratio. The PZT film thickness was measured by in-situ ellipsometry. The same general model was used for each point which was based on a Tauc-Lorentz parametrized model with a UV pole, the details of which are described in Chapter 3. Although each point varied in stoichiometry, the model was left

unchanged to better enable an in-kind comparison between the growths. The real index *n* was held at 2.76, 2.66, 2.57, and 2.52 at wavelengths of 463, 521, 599 and 640-nm, respectively. The imaginary index k was held at 0.03, 0.04, 0.05, and 0.04 at wavelengths of 463, 521, 599 and 640-nm, respectively. Thus, the thickness is not reported to a high absolute accuracy and should be taken as approximate growth trends.

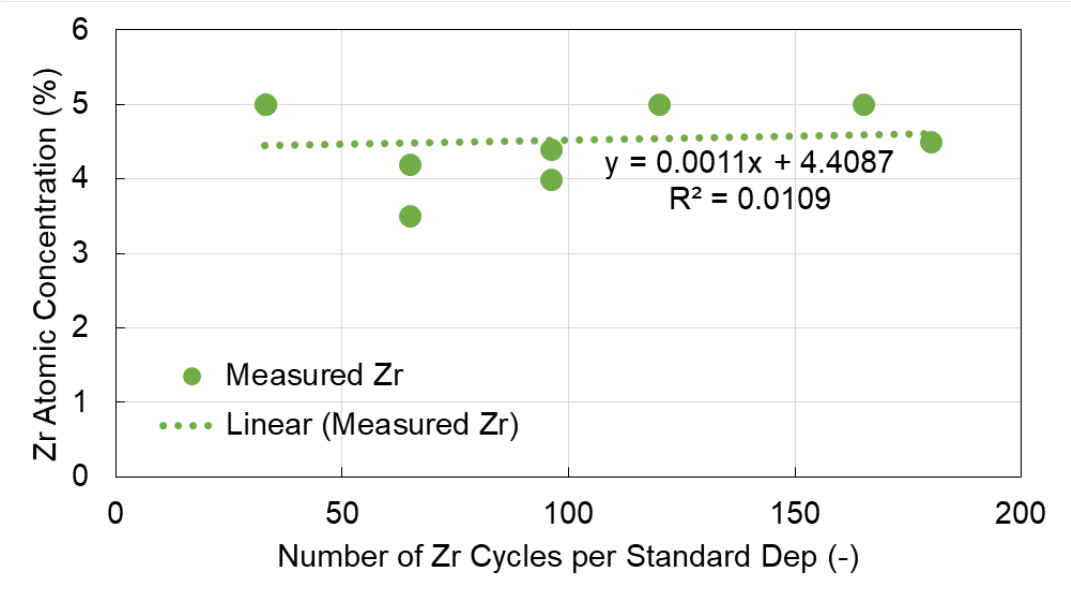

Figure 6.4: Zr atomic concentration versus number of ZrO_x cycle ratio.

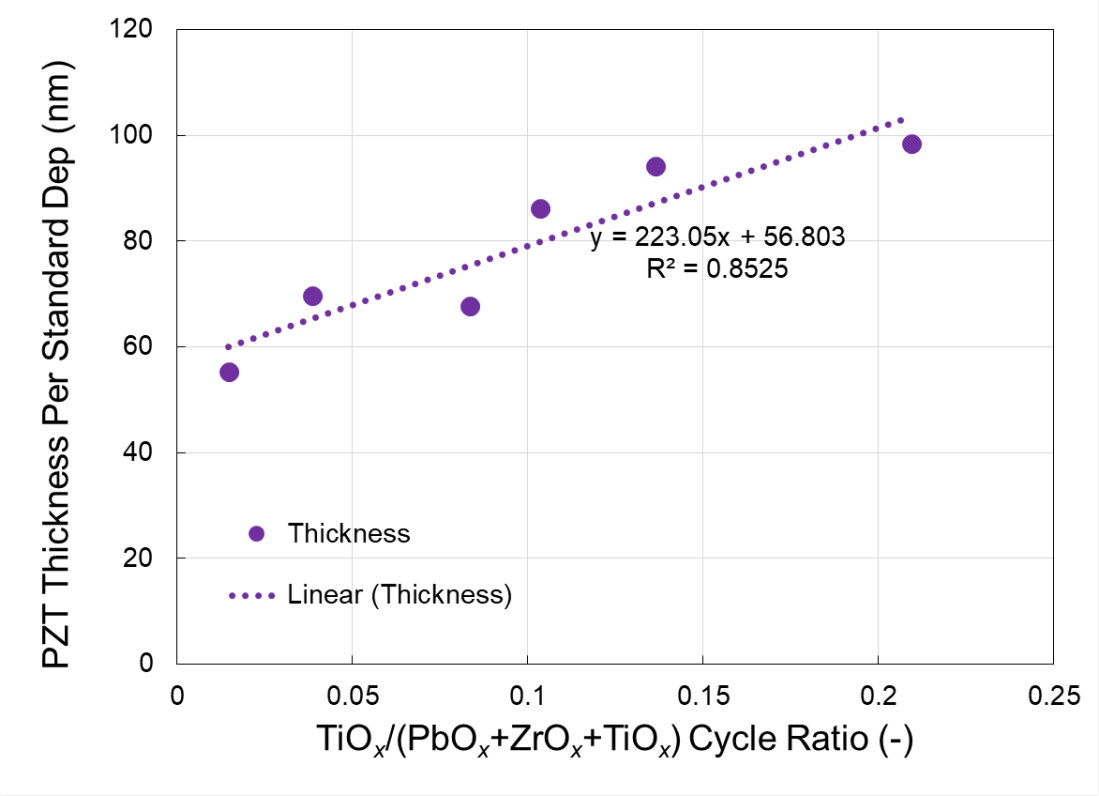

Figure 6.5: PZT thickness versus TiO_x cycle ratio.

The linear fit data is plotted against the measured data in Figs. 6.6 and 6.7. The range of the x-axis in Fig. 6.6, corresponding to PZO/(PTO+PZO) cycle ratio (%), was reduced to $10 \leq x \leq 40$ to correspond to the limited number of points interpolated for the Pb at% estimate (see Fig. 6.3). Qualitatively, each of the elements fit well to the simple linear approximation. The O concentration was not directly modeled, but instead was assumed to be the balance after summation of the cations. The film thickness modeled in Fig. 6.7 is replotted in Fig. 6.5 as a function of PZO/(PZO+PTO) ratio to match the style of Figs. 6.6 and 6.8. Figure 6.8 replots aspects of Fig. 6.6 to show the PZO cycle ratio expected to yield a 1:1 Pb(Ti+Zr) cation ratio. The yellow line corresponds to the calculated Ti+Zr at %, while the red line corresponds to the calculated Pb at %. The lines intersect at 19.2% PZO/(PTO+PZO) cycle ratio for

Pb=Zr+Ti=19.5 at%. Table 6.1 contains a complete description of an optimized recipe expected to yield PTO-rich PZT with stoichiometric Pb content, calculated using fixed Pb:Ti (4:1) and Pb:Zr (6:1) ratios. Column 1 contains the results directly from the modeled data in Fig. 6.8. Column 2 contains modeled results for a feasible recipe with parameters near the optimized recipe. Column 3 contains the measured film properties from the optimized recipe for comparison. For the measured film properties, the thickness was measured by in-situ ellipsometry and the composition was measured by RBS. The fit predicts that a PZO/(PZO+PTO) cycle ratio of 20% will yield $Pb_{1.01}Zr_{0.23}Ti_{0.77}O_{3.15}$ (normalized to Ti+Zr=1).

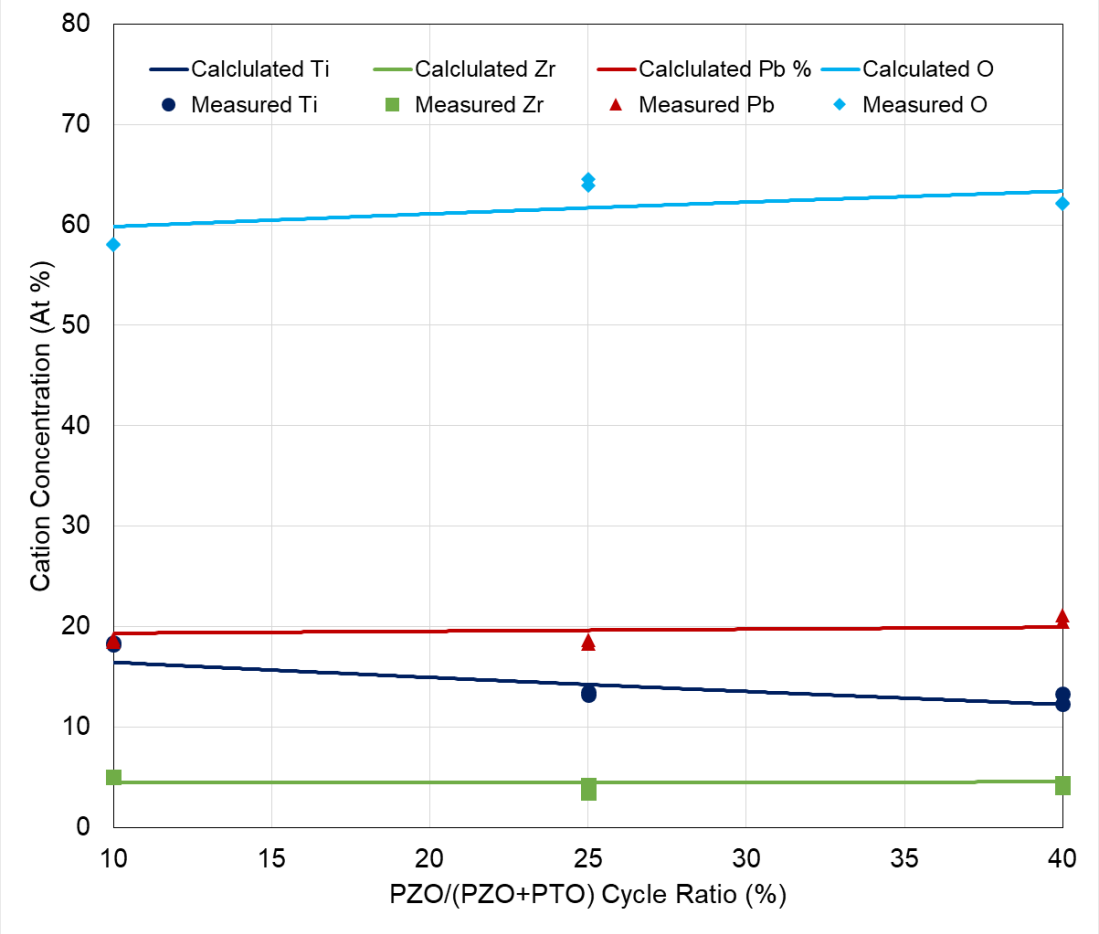

Figure 6.6: Measured RBS concentration versus linear-fit

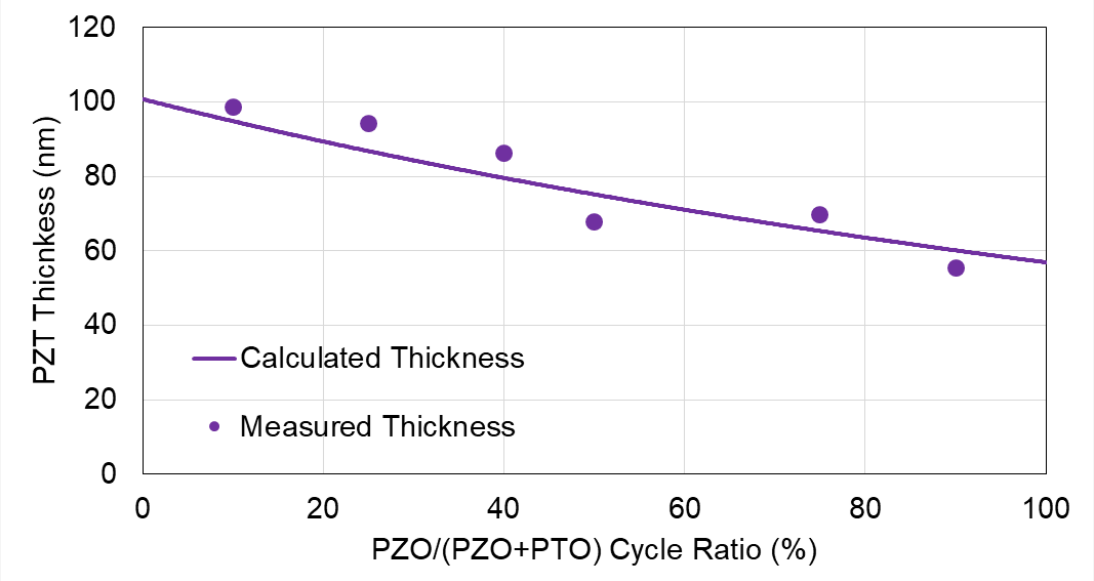

Figure 6.7: Thickness versus PZO/(PTO+PZO) cycle ratio

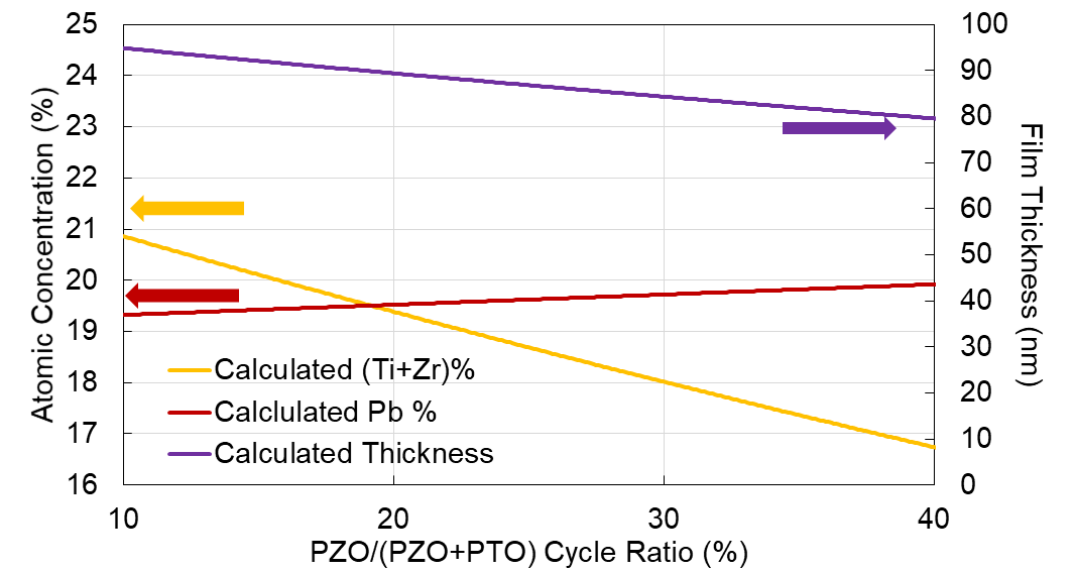

Figure 6.8: Determination of ideal PZO cycle ratio for a fixed Pb:Ti ratio of 4:1.

Table 6.1: Parameters for optimized recipe with PZO:PTO 2:8

Parameter	Calculated Recipe	Actual Recipe
PZO/(PZO+PTO)	19.2%	20.0%
PZO:PTO	N/A	2:8
Pb:Ti	4.0	4.0
Pb:Zr	6.0	6.0
Supercycles	N/A	26
TiO_x Cycles	210	208
ZrO_x Cycles	50	52
PbO_x Cycles	1140	1144
Ti Concentration (±1%)	15.0% (Est.)	14.9% (Est.)
Zr Concentration (±1%)	4.5% (Est.)	4.5% (Est.)
Pb Concentration (±0.3%)	19.5% (Est.)	19.5% (Est.)
O Concentration (±4%)	61.0% (Est.)	61.1% (Est.)
Pb Excess (%)	0% (Est.)	0.1% (Est.)
Pb%/(Ti+Zr%)	1.00 (Est.)	1.01 (Est.)
Thickness	89.8 nm (Est.)	89.5 nm (Est.)

Another way to calculate an optimized recipe that would yield a Pb:Ti+Zr cation ratio of 1:1 is to fix the PZO/(PTO+PZO) cycle ratio and vary the PbO_x:TiO_x cycle ratio. PZO cycle ratios above 10% didn't lead to any measurable increase in Zr content, so fixing the PZO/(PTO+PZO) cycle ratio at 10% can be expected to make more efficient use of the TDMAZ precursor. However, optimizing the recipe this way would require increasing the PbO_x:TiO_x cycle ratio above 4:1, which has not been attempted to this point. Since the growth relationship between the PbO_x and TiO_x is complex and

interrelated (see Chapter 5), extrapolating the simple linear curve fits performed in this section to as-yet-untested PbO_x:TiO_x cycle ratios is less likely to yield accurate calculations. Therefore, this second way of optimizing the PTO-rich PZT recipe is left to future work.

Alternative Dose Sequences

Several alternative PZT dose sequences were used to attempt to increase the Zr concentration. The processes are described in detail in Chapter 4 Subsection F, and a shorthand ("Alternative 1", "Alternative 2", and "Alternative 3") is used at present to define the dose sequences. The concentrations measured by RBS for the three alternative dose strategies are contained below in Table 6.2. Each strategy received the same standard deposition of approximately 1400 total cycles. The Zr concentration for each sample was measured to be 4.5 at%, indicating that none of the different dose sequences effectively raised the Zr content. The atomic concentrations measured for alternative sequences 2 and 3 were identical. The concentrations measured for alternative sequence 1 nearly match the concentrations (within the measurement error) measured for PZO/(PTO+PZO) cycle ratio of 50% (under standard Pb:Ti 4:1 and Pb:Zr 6:1) which yielded Ti, Zr, Pb, and O concentrations of 14.5, 3.5, 24.5, and 57.3 at%, respectively. The Zr (from TDMAZ) only seems to incorporate on PbO_x/TiO_x surfaces at a fixed percentage, and doesn't incorporate on newly-deposited ZrO_x surfaces. Limited Zr incorporation has been reported previously for a different ALD PZT materials system and is explored in some detail below.

Table 6.2: Composition of Alternative PZT Dose Sequences (Measured by RBS)

PZT Dose Sequence	Ti Concentration	Zr Concentration	Pb Concentration	Oxygen Concentration
Alt. 1 PTO:PZO 1:1 Pb:Ti 4:1, Pb:Zr 6:4	14.7	4.5	25.5	55.4
Alt. 2 Pb:Ti:Zr 8:1:1	16.3	4.5	23.9	55.3
Alt. 3 Pb:Ti:Zr 8:1:3	16.3	4.5	23.9	55.3

Discussion

In a previous study by Watanabe, $Pb(DPM)_2$, TTIP, and $Zr(DPM)_4$ [Note: the Zr precursor is alternatively written as $Zr(TMHD)_4$ in other studies] were used as cation precursors, however the Zr concentration could not be increased above (approx.) 4 at%.[1] In a related study, the $Zr(DPM)_4$ precursor was replaced with $Zr(DIBM)_4$, which increased the zirconium content in the PZT film by a factor of 3 and enabled PZT deposition near the MPB.[2] Both $Zr(DPM)_4$ and $Zr(DIBM)_4$ are β-diketonate precursors with octahedral oxygen coordination. Their ligand chemistries are nearly identical, except that two of the methyl groups in $Zr(DPM)_4$ are replaced with hydrogen bonds to form $Zr(DIBM)_4$. The small change in ligand chemistry led to an 8-fold increase in the vaporization rate.[3] In both studies by Watanabe,[1,2] the precursor dose was reported as the total volume of precursor injected into a vaporizer held at 200 °C. That method of reporting may be misleading for certain precursors such as $Zr(DPM)_4$ if the rate of vaporization limits the overall dose instead of the total injected volume. The fact that an increased dose of a nearly identical precursor, $Zr(DIBM)_4$, led to higher Zr incorporation suggests that the initial $Zr(DPM)_4$ dose was not saturated. This is further evidenced by a later study by Choi, who reportedly grew perovskite PZT near the MPB using the same $Zr(DPM)_4$ [reported as $Zr(TMHD)_4$] precursor, presumably using a fully saturated dose.[4] In the present study, the TDMAZ dose did not appear to have

problems with vaporization. Each TDMAZ pulse produced a consistent 3-10 mTorr pressure pulse above the background pressure of approximately 1.8 Torr. The films with a 90% PZO/(PZO+PTO) ratio would have received a factor of eight higher overall TDMAZ dose than those films with a 10% PZO/(PZO+PTO) ratio but did not have a higher Zr at% within the measurement error of RBS. This suggests that unlike the report by Watanabe,[1] the limited Zr incorporation in the present work is not due to limited precursor dose, but rather something fundamental in the surface chemistry. The exact cause of the limited Zr incorporation hasn't yet been determined, but there are some clues from the in-situ thickness trace that help isolate the problem.

In-Situ Thickness Measurement

The example shown below in Fig. 6.9 was selected as a representative general example of the in-situ growth kinetics of the ALD PZT system. The ALD recipe used for the modeled data (Fig. 6.9) consisted of a PbO_x:TiO_x ratio of 4:1, PbO_x:ZrO_x of 5:1, and PZO/(PTO+PZO) of 10%, which resulted in a Pb-deficient PZT film with Zr near 4.5 at%. In-situ thickness measurements were performed by multi-wavelength ellipsometry to show the kinetic growth behavior of the ALD PZT films. The experimental details regarding the in-situ measurements are described in Chapter 3. The ALD PZT was modeled with an n and k model (referenced in the previous section) with starting parameters that were based on a Tauc-Lorentz oscillator with a UV pole ex-situ spectroscopic ellipsometry model. Roughness was not considered for the in-situ model, but was measured to be 1-2 nm using the ex-situ ellipsometry which nearly

matches that of the Pt substrate (as described in Chapter 4). The optical constants were determined from the final thickness measurement. The in-situ data was then re-analyzed with the fixed optical constants while the thickness was allowed to vary. The results of the thickness fit over the full growth are shown below in Fig. 6.9. The thickness was fit to a line with an R^2 value of 0.996 and a standard deviation of 0.9 nm, which is less than 1% of the final determined thickness. The standard deposition took approximately 31 hours to complete.

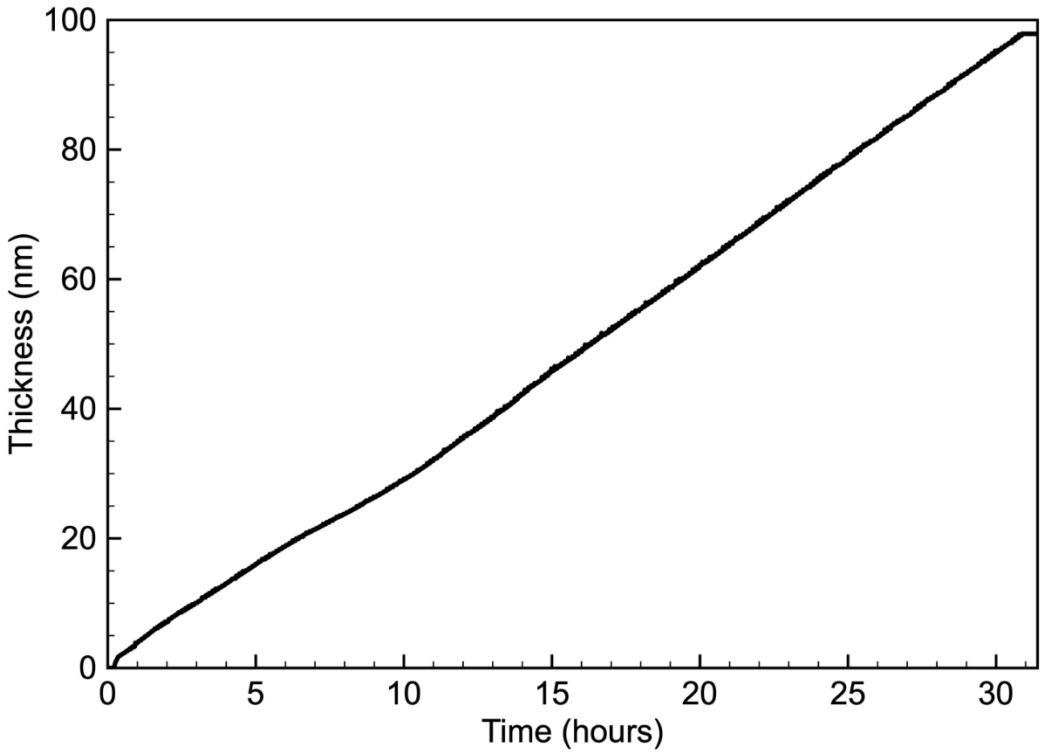

Figure 6.9: ALD PZT thickness trace using in-situ ellipsometry

The thickness during the initial nucleation stages of the growth are shown below in Fig. 6.10. The growth begins as super-linear on the Pt substrate and quickly levels off to linear growth. The composition of the initial 2 nm hasn't been determined. The

thickness at steps of the process (about half-way through the standard deposition) are shown in Fig. 6.11. The chemisorption of each precursor is represented by an apparent thickness increase, followed by an apparent decrease during the oxidation half-cycles. Like the ALD PTO, the apparent thickness increase following the TDMAT pulse (after ligand oxidation) is approximately 3 Å. While the thickness increase of all four PbO_x cycles combined is only 1 Å. The thickness increase following the TDMAZ pulse (after oxidation) is 2 Å, compared to also 1 Å for the PbO_x prior to the TDMAZ dose. The change in thickness following the TDMAT dose plus the TDMAZ dose is approximately 5 Å compared to 2 Å total for PbO_x. The estimated stoichiometry of PZT grown with the stated parameters is $Pb_{0.95}Zr_{0.21}Ti_{0.79}O_{2.90}$, which is a far higher Pb content than is suggested by the in-situ thickness trace. Like the PTO, is isn't known why the PbO_x content isn't fully represented until the subsequent TDMAT or TDMAZ dose. One possibility is that the PbO_x crystallites are only loosely bound to surface until the TDMAT or TDMAZ are pulsed and encapsulate them. That hypothesis is explored in more detail in Chapter 8. Nonetheless, the in-situ thickness trace displays step-wise growth that is indicative of a well-behaved ALD process. Six consecutive doses of $Pb(DMAMP)_2$ were used for *each* PbO_x cycle to ensure precursor saturation. No thickness increase occurs after the first dose, which suggests the growth is truly self-limited. A single TDMAT and TDMAZ dose were sufficient for saturation, which is proven by the low thickness non-uniformity across a 50µm-deep trench structure shown in the "SEM Analysis" section. Multiple (between 3 and 8) H_2O pulses were used to fully oxidize the full 150 mm wafer. The final cycles during the standard deposition are shown in Fig. 6.12, which shows that the stepwise growth continues

throughout the deposition, and that the final thickness is static after final precursor dose of the growth (as is expected for an ALD process).

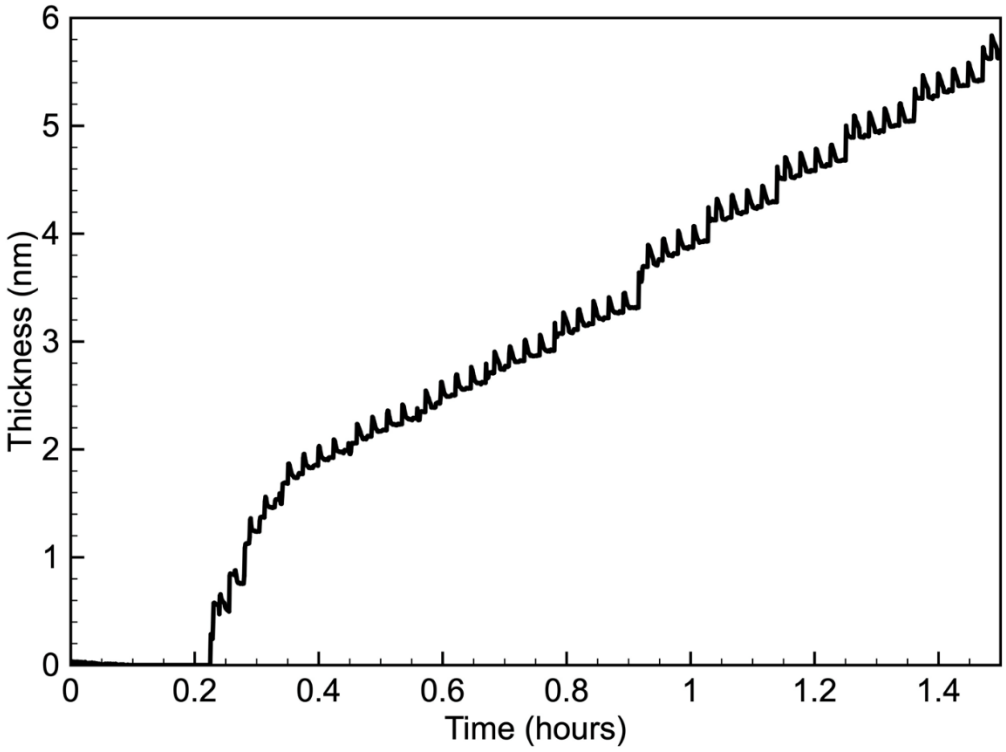

Figure 6.10: Nucleation phase of ALD PZT measured by in-situ ellispometry

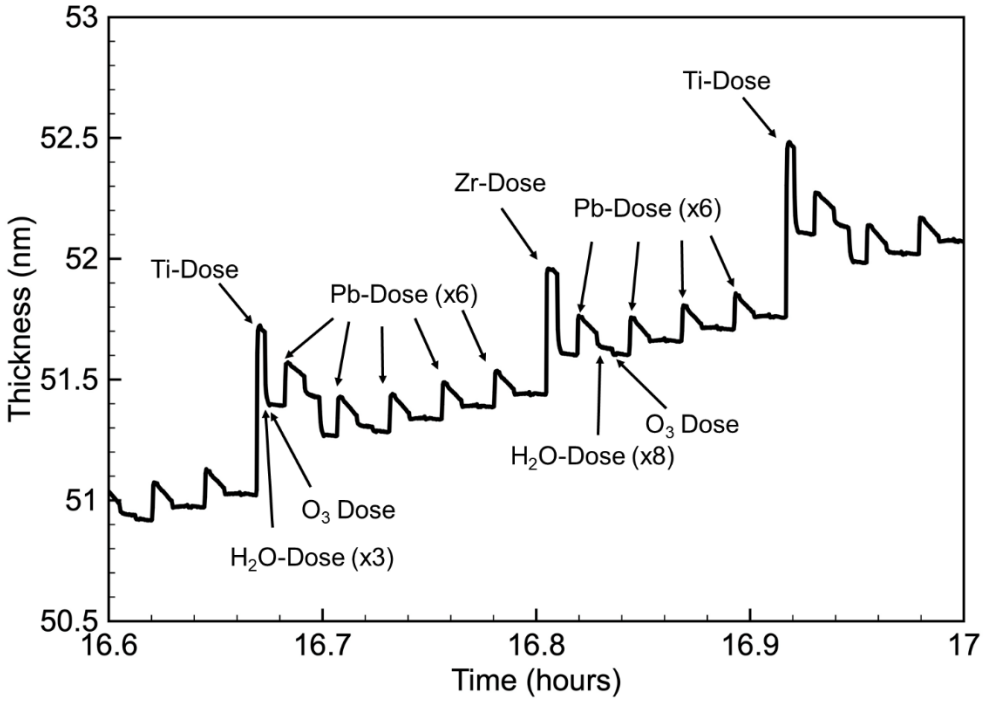

Figure 6.11: Equilibrium growth of ALD PZT measured by in-situ ellispometry for the same material as in Figure 6.10. The multiplier (x3, x6, x8) indicates the number of sequential pulses used during each respective dose cycle.

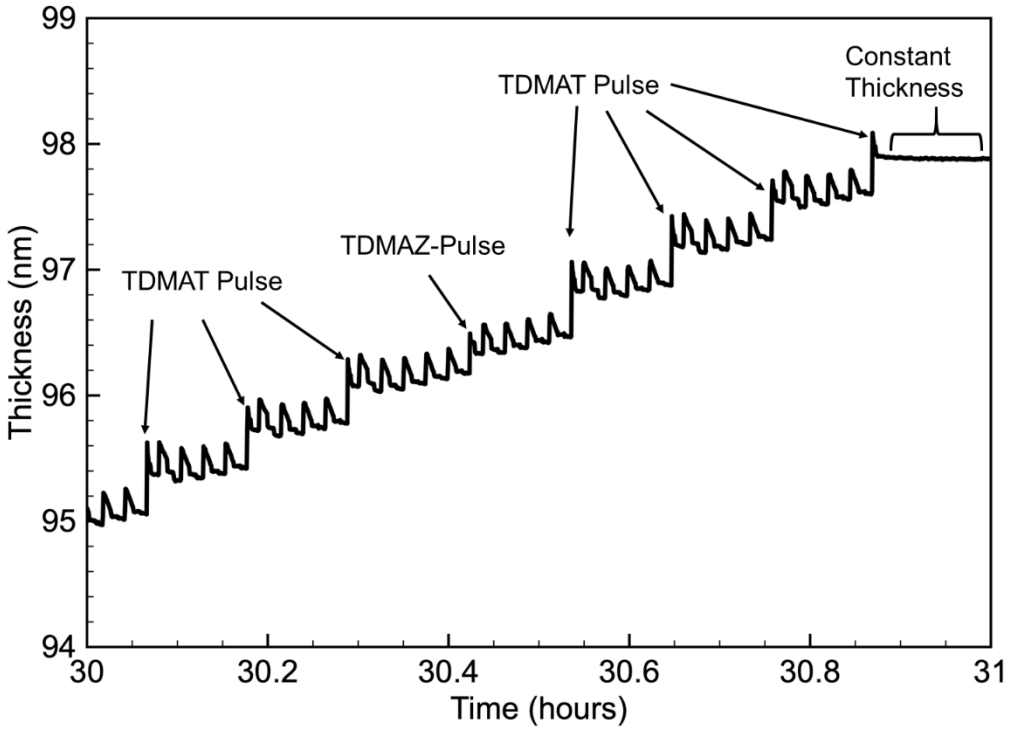

Figure 6.12: Final steps of ALD PZT growth measured by in-situ ellispometry for the film in Figure 6.10.

Some generalities regarding the growth mechanisms of ALD PZT can be inferred by combining the RBS composition data and the in-situ thickness traces. First, it is apparent that the TDMAZ chemisorbs to the surface of freshly deposited PbO_x. The relative magnitude of thickness increase following the TDMAT and TDMAZ pulses suggests that the TDMAT is more readily chemisorbed (thickness increase of 0.8 nm) compared to TDMAZ (thickness increase of 0.5 nm). The difference is observed throughout the deposition (see Figs. 6.11 and 6.12). Towards the end of the deposition in Fig. 6.12, a TDMAZ pulse (preceded by 6 PbO_x cycles) occurs at about 30.45 hours that has a visibly smaller thickness increase compared to the surrounding TDMAT pulses. For the two alternative PZT dose strategies that employed several back-to-back

ZrO_x cycles (Alt. 1 and Alt. 3, see Table 6.3), no apparent chemisorption occurs after the first TDMAZ pulse following the PbO_x or TiO_x cycles (not pictured). That means that the TDMAZ first chemisorbs to a limited number of sites (fewer sites than are available to TDMAT) and poisons the surface for itself. The growth rate of the pure PZO (composition wasn't measured) was quite low (17 nm per 1400 cycles), which implies that the TDMAZ chemisorption sites are not primarily generated from the PbO_x cycle, but rather the TiO_x cycle. The exact cause is still under investigation, but is complicated by the fact that TDMAH seems to chemisorb more like TDMAT than TDMAZ, as will be shown in Chapter 7.

Phase Identification by X-ray Diffraction

XRD of Pb-Poor $Pb_{0.79}Zr_{0.21}Ti_{0.79}O_{2.9}$

XRD θ-2θ scan patterns for ALD PZT grown at compositions ranging from 0.79 to 1.2 lead content, Pb-poor to Pb-rich, are presented in Figs. 6.13-6.15. Each of the perovskite phases were identified according to a pattern for PTO-rich tetragonal PZT (PDF#00-050-0346). Figure 6.13 shows the results of Pb-poor PZT with composition $Pb_{0.79}Zr_{0.21}Ti_{0.79}O_{2.9}$ (measured by RBS) annealed by RTA in O_2 using several different recipes. The unlabeled intensity shoulder at approximately 39° is a result of the Ni-foil filter affecting the Pt (111) peak and appears on all samples with Pt. Both the un-annealed and pre-annealed (400 °C, with 5 min. hold) displayed a broad, low-intensity peak over the range of approximately 29° - 30° which is attributed to PbO Massicot (111) and (020). The PbO crystallites were calculated to be 5 nm for the unannealed

sample and 7 nm for the pre-annealed (400 °C, with 5 min. hold) sample using the Scherrer formula. The PbO Massicot (orthorhombic) phase was previously identified in PTO (discussed in Chapter 5) grown with similar Pb-concentrations and crystallite sizes. No PbO reflections are apparent in the samples that received a final crystallization at 600 °C and above. RBS measurements were performed on several samples both pre and post-anneal which showed no change in composition within the accuracy limits of the tooling. Therefore, it can be inferred that the PbO was primarily absorbed into the PZT film, rather than evaporated during the anneal. The perovskite phase was identified in all samples that received a final crystallization at or above 600 °C. For each of those samples, both the (001)/(100) and (101)/(110) peak pairs are unresolved, in each case appearing as a single, wide peak, similar to the overlap of the (001)/(100) and (101)/(110) pairs observed for ALD PTO. A small hump near 31° is present in the second scan from the top in Fig. 6.13. This is attributed to the (-211) reflection of $PbTi_3O_7$; however, some Zr- doping cannot be ruled out of the identified $PbTi_3O_7$ solid solution since Zr was present in the film composition. The presence of the Pb-poor phase is not surprising since the film was measured to be quite Pb-deficient. The peak corresponding to perovskite PZT (111) isn't present in any of the films shown in Fig. 6.13. Two separate samples cleaved from the same wafer were annealed separately at 700 °C to test the repeatability of the standard anneal, which was defined in Chapter 5 as a 700 °C anneal with a 1 min. hold. Since the phase distribution is slightly different between the two scans, there is some variability in the RTA process that should be carefully considered in future work. The variables affecting the RTA are discussed in Chapter 5.

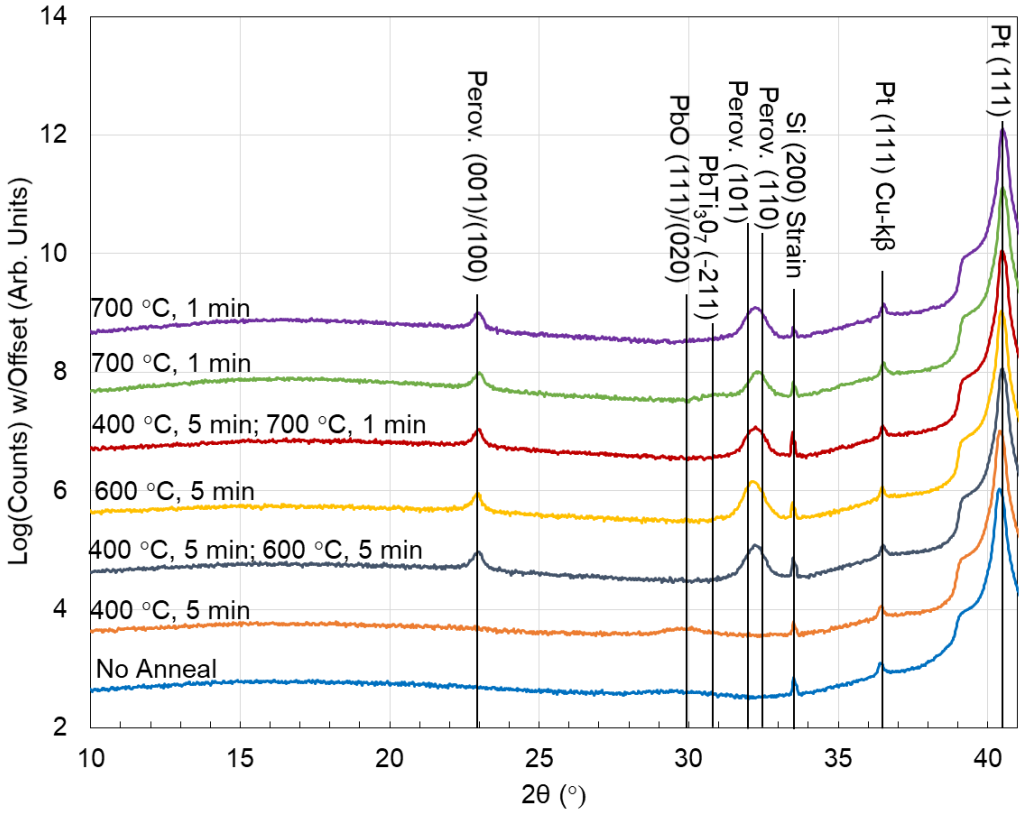

Figure 6.13: XRD Scan of 7 different $Pb_{0.79}Zr_{0.21}Ti_{0.79}O_{2.9}$ samples

XRD of slightly Pb-Rich $Pb_{1.07}Zr_{0.24}Ti_{0.76}O_{3.7}$

Pb-rich ALD PZT samples with lead content 1.07 and 1.2 were investigated by XRD in Figs. 6.14 and 6.15, respectively. Figure 6.14 shows the θ-2θ scan patterns for slightly Pb-rich $Pb_{1.07}Zr_{0.24}Ti_{0.76}O_{3.7}$ composition, determined by RBS. The apparent oxygen content is too high (Subscript O=3.7) for ideal PZT (Subscript O=3.0). However, the relative concentration of each cation was measured to a much higher accuracy (±1 at%) than the oxygen(±4 at%). Since the subscripts were normalized to Sub-Zr + Sub-Ti=1, the relative cation subscripts should be viewed as more accurate than the O subscript. A broadened peak in the region of the (111) and (020) reflection

of the PbO Massicot phase is present in the unannealed sample but absent in the annealed case. The PbO Massicot crystallite size were calculated to be 7 nm for the unannealed sample using the Scherrer formula and matches the Pb-poor sample (Fig. 6.13).

Both of the annealed samples contained the same pairs of perovskite peaks observed in Fig. 6.13 for the Pb-deficient PZT and lacked a (111) perovskite peak. No secondary peaks were present in the annealed samples (Fig. 6.14), although the perovskite pair (101)/(110) is slightly wider and more flat topped in the 700 °C sample versus the 600 °C sample. The perovskite crystallite size was calculated to be 40 and 29 nm for the samples annealed for 700 °C with a 1-min. hold, and 600 °C with a 5-min. hold, respectively.

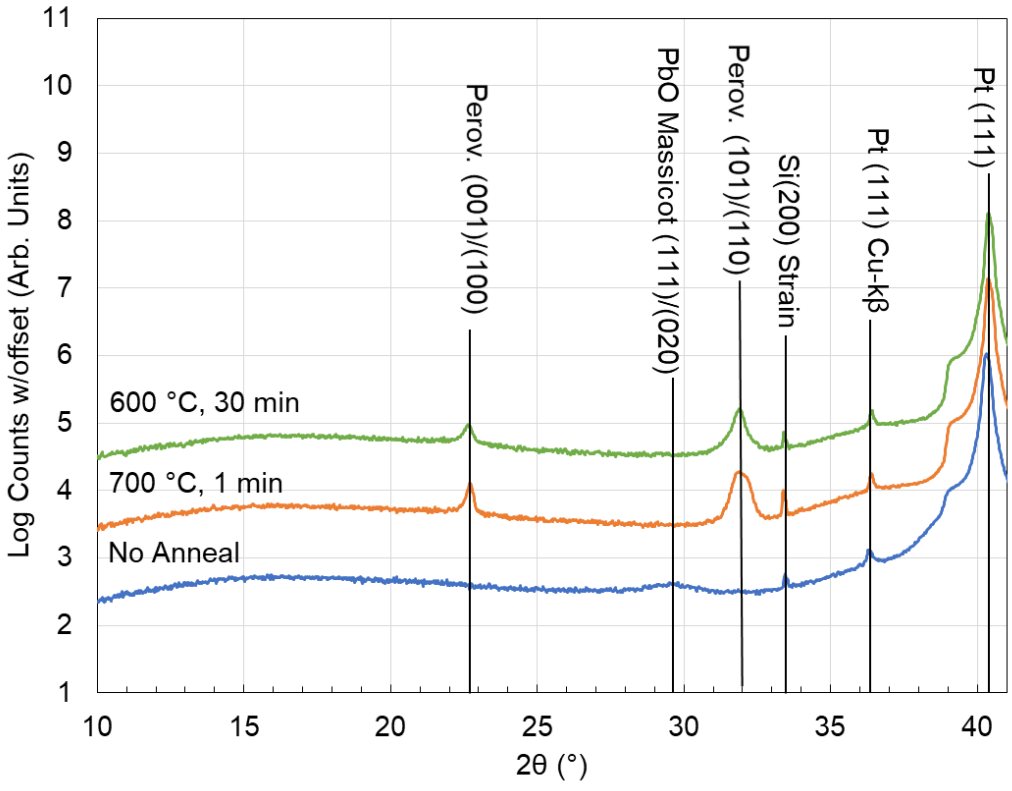

Figure 6.14: XRD Scan of $Pb_{1.07}Zr_{0.24}Ti_{0.76}O_{3.7}$

XRD of Pb-Rich $Pb_{1.2}Zr_{0.23}Ti_{0.77}O_{3.6}$

Figure 6.15, shown below, explores the same anneal conditions used in Fig. 6.14 but the Pb content was increased to 1.2 ($Pb_{1.2}Zr_{0.23}Ti_{0.77}O_{3.6}$ ALD PZT composition). Like the other scans in this section, PbO Massicot reflections for (020) and (111) are present in the unannealed sample. The Massicot PbO crystallites were calculated to be 7 nm, like the other unannealed samples grown at different Pb-concentrations. The perovskite peaks in the annealed samples are similar in character to the peaks observed in Fig. 6.14. The sample annealed at 700 °C (Fig. 6.15) has an observable (001) perovskite peak and a wider (101)/(110) peak compared to the sample annealed at 600 °C. Each of the annealed samples contained secondary phases which are identified as various phases of lead oxide. For the sample annealed at 700 °C (Fig. 6.15), the (010) Massicot PbO reflection is observed just above 15°, with the secondary (020) reflection observed just above 30°. The wide peak at approximately 28° is well-below the range of the other Massicot reflections and attributed to (tetragonal) PbO Litharge (101), which happens to be the highest intensity peak for that pattern. The perovskite crystallite size for the sample annealed at 700 °C was calculated to be 33 nm. The sample annealed at 600 °C (Fig. 6.15) displays fewer secondary phases but has a small peak (more of a hump) at about 27° that cannot be attributed to Massicot or Litharge. Minium (tetragonal) Pb_3O_4 (PDF# 00-041-1493) has a (111) peak at 26.347° and (002) peak at 27.140°, which are fairly close matches, and may help to explain the relatively high oxygen content. However, since there are many PbO_x phases with reflections that partially fit, Minium

is left as a tentative identification. The perovskite crystallite size for the sample annealed at 600 °C with a 30 min. hold was calculated to be 27 nm.

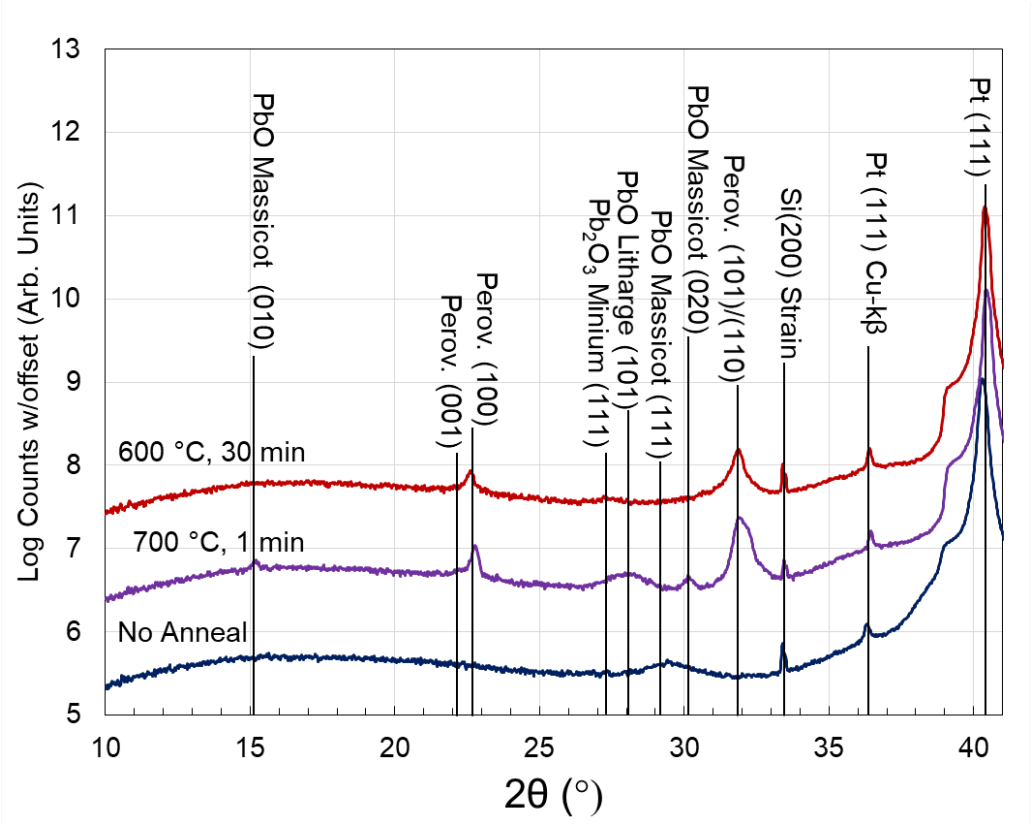

Figure 6.15: XRD Scan of $Pb_{1.2}Zr_{0.23}Ti_{0.77}O_{3.6}$

In this section, samples were grown with compositions ranging from about 20% Pb-poor ($Pb_{0.79}Zr_{0.21}Ti_{0.79}O_{2.9}$) to 20% Pb-rich ($Pb_{1.2}Zr_{0.23}Ti_{0.77}O_{3.6}$). The relative Pb-excess had no effect on the perovskite crystallite orientation, though the Pb-rich samples displayed deleterious PbO_x phases. Overall, the XRD results for the present PZT samples bear some similarity to the XRD results obtained previously for PTO, in that the perovskite peaks did not display a preferred orientation, despite being grown on highly-oriented (111) Pt. For the PTO samples, STEM cross-section images showed that the crystallized grains were not columnar, and appeared to have nucleated

randomly throughout the film thickness. The nucleation of the ALD PZT films appears to be quite similar, and will be discussed in the Cross-section TEM Analysis section.

SEM Analysis

Cross-section of 45 μm-deep Trench Structure

ALD PZT was grown on micro-machined Si trench structures to test the conformal deposition capabilities of the process. The trenches were etched using a Plasmatherm Deep Silicon Etch platform using the Bosch process. Figures 6.16-20 show SEM cross-section images ALD PZT grown on trenches nominally 20 μm wide by 45 μm deep, while Figs. 6.21-22 detail a separate growth on trenches nominally 20 μm by 100 μm deep. The trenches were coated using slightly different ALD PZT recipes, and additionally each received a different number of total cycles.

The 45 μm-deep trench structure was coated with an ALD PZT recipe that consisted of a PbO_x:TiO_x ratio of 4:1, a PbO_x:ZrO_x ratio of 5:1, and a PTO:PZO ratio of 9:1. The PZT recipe was repeated for 27 super-cycles (1378 total cycles including one TiO_x nucleation layer) which was equivalent to one standard deposition. The film stoichiometry for the preceding recipe has not been directly quantified by RBS, but was estimated to be approximately 1.5 at% Pb-deficient based on data interpolation. Figure 6.16 shows a zoomed out view of the full 45 μm-deep trench structure. The PZT film appears white in contrast, while the Si substrate appears gray. The ALD PZT film completely coated the 45 μm-deep trench, as expected for an ALD process. Figure 6.17 shows the top left corner of the center trench that is labelled in Fig. 6.16. As is labelled

in the Fig. 6.17, some particulate debris is present on the top film surface that is a result of the specimen preparation. The sample was cleaved before insertion into the ALD tool and was cleaved again post-ALD to expose the trench cross-section. The sample was also removed from the cleanroom for imaging which resulted in particulate contamination (a cleaner sample is presented in Figs. 6.21-22). A scalloping effect that is characteristic of the Bosch process is also observed in Fig. 6.17. It is noteworthy that the ALD PZT conformally coated the etch scallops. The ALD PZT thickness was measured at the film surface to be approximately 95 nm (+/- 5nm). The uncertainty stems mainly from the debris that partially obfuscated the ALD film. The thickness of the ALD PZT film wasn't measured by ellipsometry in this case because the substrate was Si, not Pt. Inter-diffusion of Si into PZT and oxidation of Si are known to occur,[5] which reduce the accuracy of a thickness measurement by ellipsometry. The thickness of the sidewall wasn't quantified (by SEM) because the scalloping caused too much uncertainty. Figures 6.18 and 6.19 detail the ALD PZT growth on the sidewall and bottom left corner, respectively. Figure 6.20 details the ALD PZT at the bottom of the trench structure that had a measured thickness of 95 nm, which matches the top surface. Thus, the 50 μm-deep trench structure was coated conformally by the ALD PTO-rich PZT process presented here, which strongly suggests that the process window is within an ALD-regime.

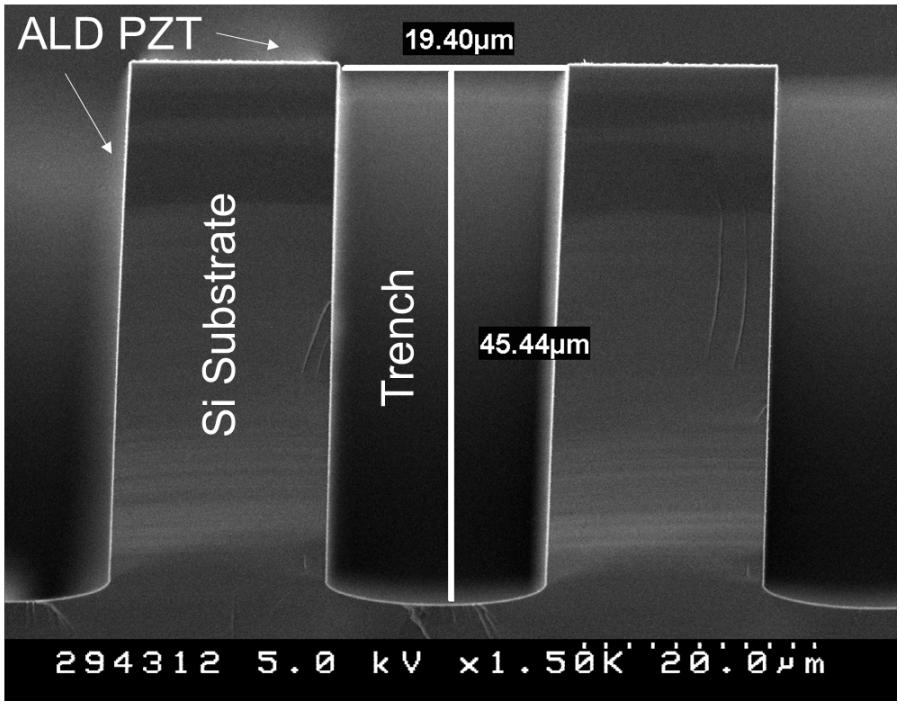

Figure 6.16: SEM cross-section of ALD-coated 45 µm-deep trench etched into silicon. (Estimated to be 1.5% Pb-deficient)

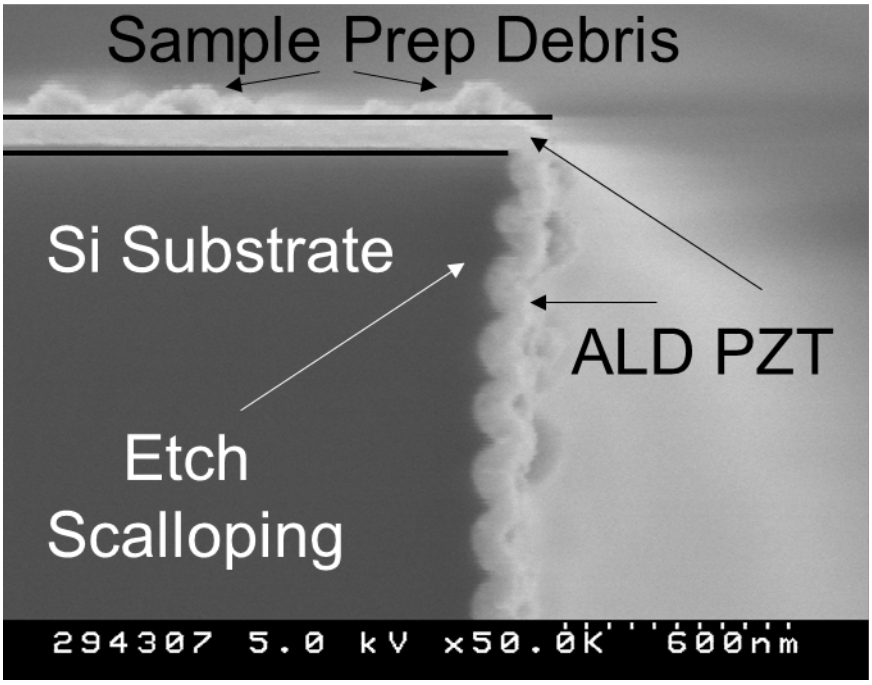

Figure 6.17: Top-left corner of 45 µm-deep trench structure coated with ALD PZT.

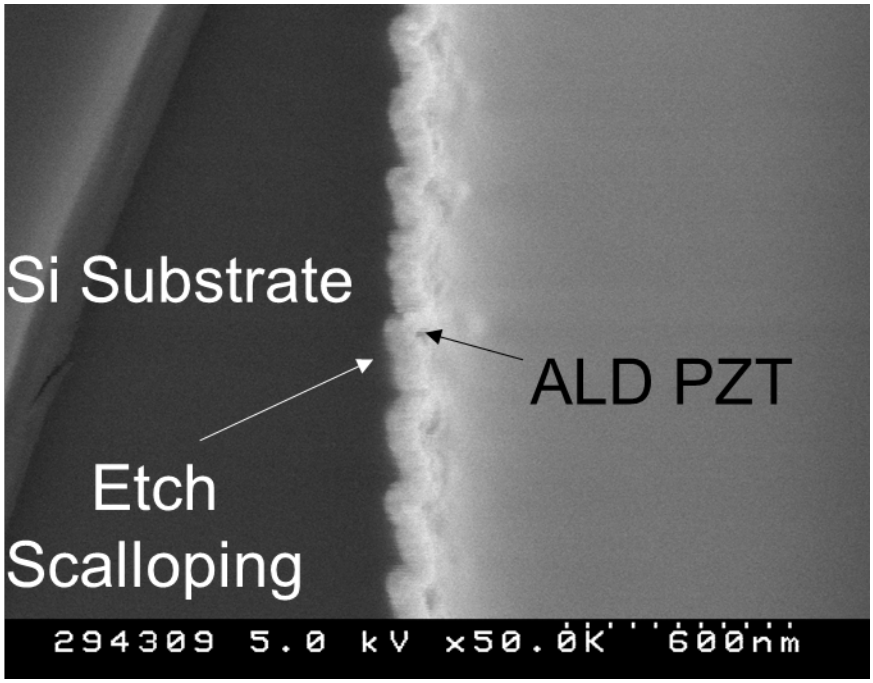

Figure 6.18: Left sidewall of 45 µm-deep trench structure coated with ALD PZT

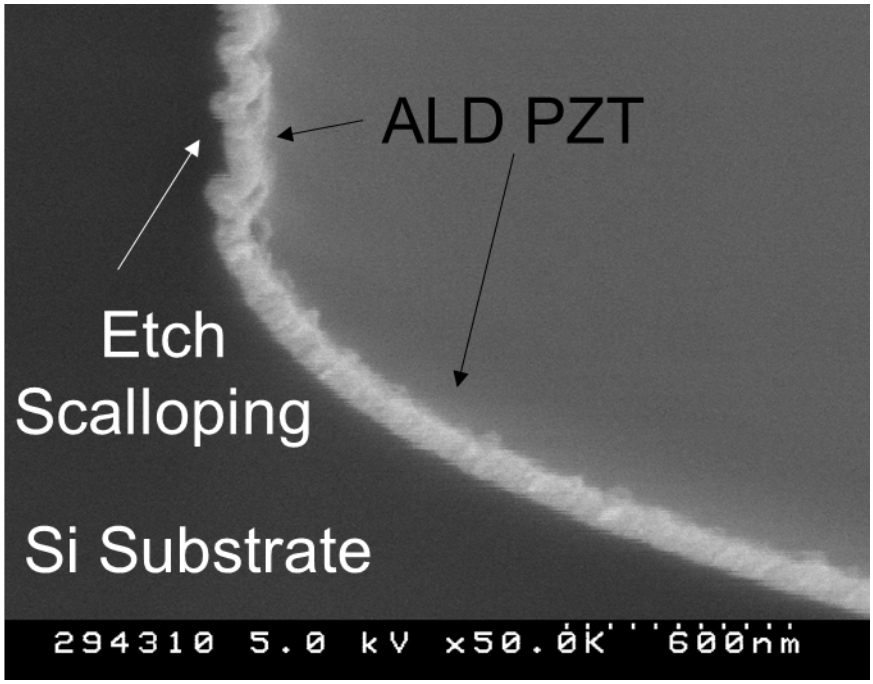

Figure 6.19: Bottom left corner of 45 µm-deep trench structure coated with ALD PZT

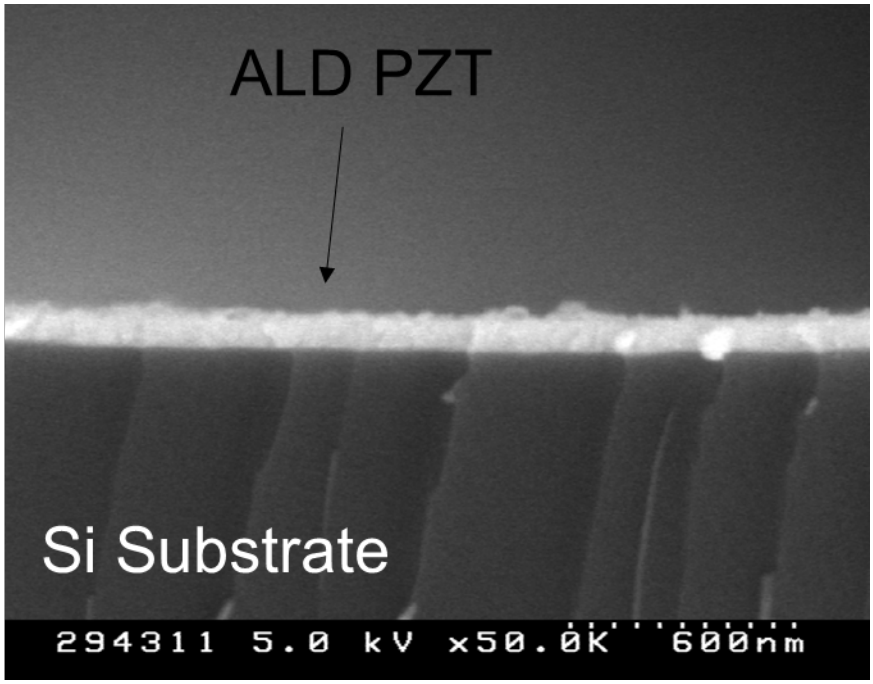

Figure 6.20 Bottom of 45 µm-deep trench structure coated with ALD PZT

Plan View and Cross-section of 100 µm-deep Trench Structure

A separate, 100 µm-deep trench structure was coated with ALD PZT that utilized a PbO_x:TiO_x ratio of 4:1, a PbO_x:ZrO_x ratio of 6:1, and a PTO:PZO ratio of 17:3. The elemental composition of the ALD PZT sample wasn't measured, but was estimated to be 0.2 at% Pb-deficient. The sample received 28 PZT super-cycles (2967 total cycles, including the TiO_x nucleation layer), or a little more than double the standard deposition. The plan view of the film surface with as-grown ALD PZT is shown in Fig. 6.21. Part of a trench is shown as the dark region of the left side of the image. The top surface of the as-grown ALD PZT film is not perfectly smooth. Small features are observed in the plan view SEM that are roughly 10-100 nm in diameter that appear as small hillocks or crystallites. In Chapter 5, unannealed ALD PTO was shown to be

comprised of PbO_x crystallites embedded in an amorphous TiO_x matrix. The observed PbO_x crystallites in PTO were far smaller (2-5 nm diameter), as were the calculated PbO_x crystallites for PZT (5-7nm), than the features observed in Fig. 6.21 (10-100 nm in diameter). One possibility is that the introduction of Zr into ALD PTO causes the PbO_x to grow in sparse, but larger crystallites compared to pure PTO. However, large crystallites on the order of 100 nm were not present in the film cross-section (see Fig. 6.22), which appears to be homogeneous. Not enough information is available to make a strong claim about the surface features, but they are tentatively labelled "crystallites" that may be PbO_x, intermediate phases, or amorphous domains. Figure 6.22 details the SEM cross-section of the 100 μm-deep trench coated with ALD PZT. The film thickness at the top wafer surface was measured to be 161.8 nm, while the thickness at the bottom of the trench was about 19% thinner and measured 131.1 nm. The simplest explanation for the difference in thickness is that the precursor dose wasn't high enough to reach saturation for the deeper, 100 μm trench. Operating the reactor in a static-dose mode, rather than a continuous laminar perpendicular-flow mode, would be better suited to coat high aspect-ratio structures.

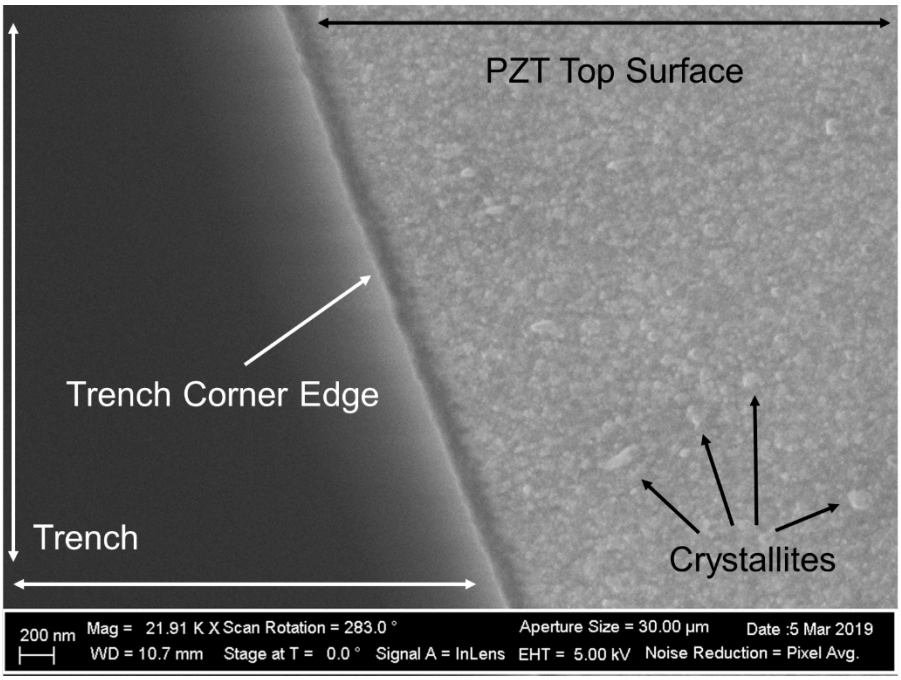

Figure 6.21: Top-down view of ALD PZT coated Si surface (as-grown)

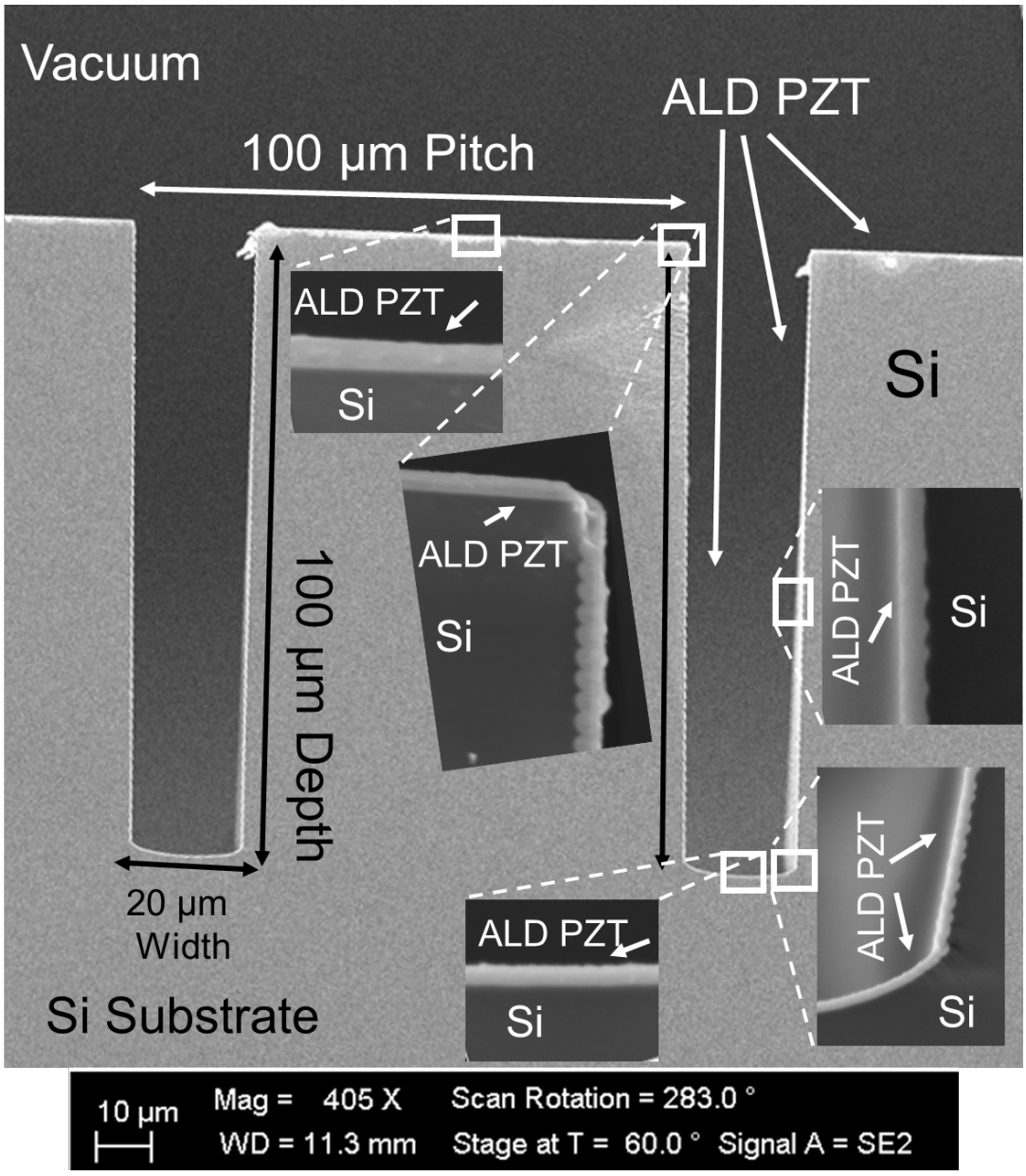

Figure 6.22: SEM cross-section of 100 µm deep trench structures coated by ALD PZT (Note: insets are not to scale).

Cross Section TEM Analysis

TEM cross-section images were collected for an ALD PZT sample with a Pb-rich composition of $Pb_{1.07}Zr_{0.24}Ti_{0.76}O_{3.7}$ that was annealed at 600 °C for 30 min. and are shown below in Figs. 6.23-6.24. It is the same sample that was characterized by XRD shown in Fig. 6.16 (top scan). Figure 6.23 shows a labelled cross-section of the films stack. The 500 nm-thick SiO_2 layer appears amorphous, which is expected from a thermal oxide. The 32 nm-thick TiO_2 layer displays highly columnar grains that serve as a growth template for the Pt lower electrode. The 88 nm-thick Pt layer is too dark to clearly see the entire film, though several columnar grains boundaries are present. One example of each columnar grain boundary is identified in Fig. 6.23. The PZT sample does not appear to be thin enough to observe all of the grain boundaries in the cross section, unlike the PTO sample analyzed in Chapter 5. However, several crystallites (in the PZT layer) are identified in the image that are presumably PZT. Like the PTO sample from Chapter 5, the grains are 10's of nm in diameter. No pinholes or pores were observed in the present ALD PZT sample. It is not clear whether the pinholes and pores observed in the ALD PTO samples were a result of over-thinning of the sample (thus grains simply fell out) or if they were actually present in the as-annealed film. If the pinholes observed for the PTO sample are not a result of sample preparation, it is unclear if the lack of pinholes in the present PZT sample are due to a crystallization property of the PZT, or due to the different annealing conditions (700 °C with a 1 min. hold for PTO, versus 600 °C for 30 min. for the present PZT). More experiments and careful imaging are required to make that distinction.

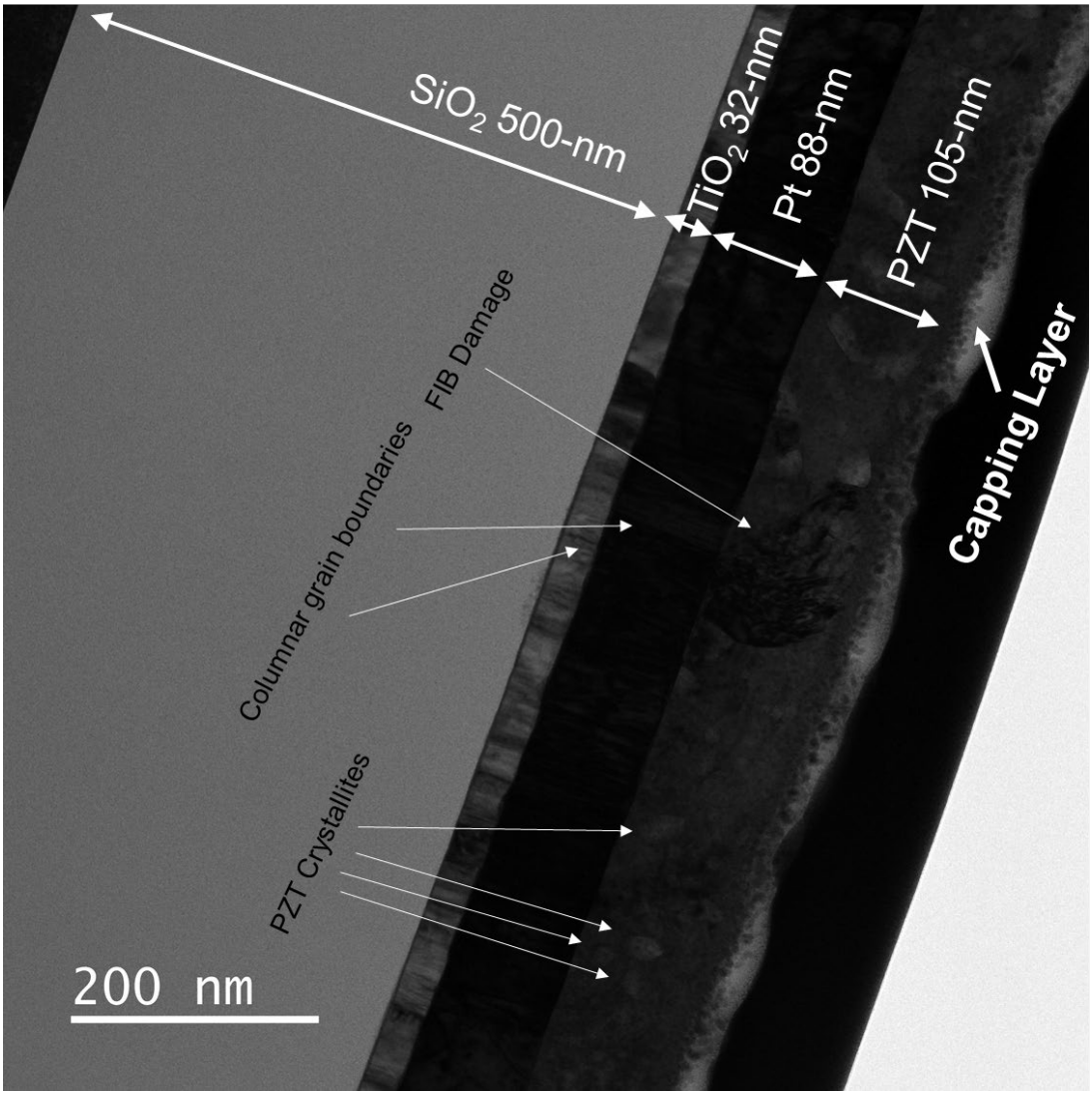

Figure 6.23: TEM Image of annealed ALD $Pb_{1.07}Zr_{0.24}Ti_{0.76}O_{3.7}$

A higher magnification of the ALD PZT sample is shown below in Fig. 6.24. Several grain boundaries are labelled in the center of the film which do not correspond to columnar grains. Like the PTO, the PZT grains appear to have nucleated throughout the film, and that the nucleation was not controlled at the Pt-PZT interface. This explains why, despite being grown on a highly (111)-oriented Pt bottom electrode, that the ALD PZT crystallites showed no preferred orientation. Nonetheless, the

crystallized ALD PZT film appears to be dense and smooth despite the atypical nucleation mode.

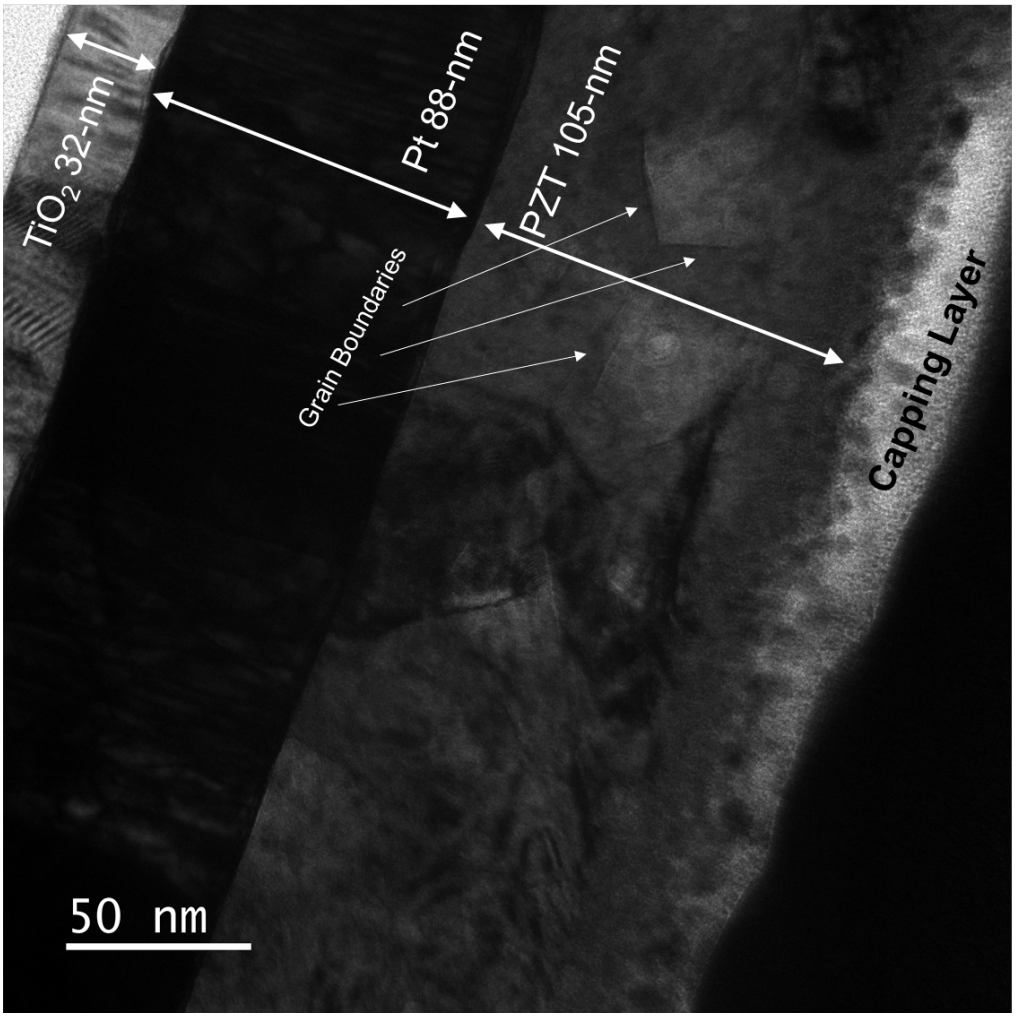

Figure 6.24: Higher magnification TEM Image of annealed ALD $Pb_{1.07}Zr_{0.24}Ti_{0.76}O_{3.7}$

Ferroelectric Characterization

Polarization/Electric-Field Hysteresis Loops

MIM capacitors were fabricated according to the procedure defined in Chapter 4. ALD PZT was grown with a $Pb_{1.07}Zr_{0.24}Ti_{0.76}O_{3.7}$ composition and was measured to be 200

nm-thick by ex-situ spectroscopic ellipsometry following RTA at 700 °C with a 1 min hold. Two separate depositions and anneals were implemented to achieve the stated thickness. Circular top electrodes with 4.92×10^{-4} cm^2 area were used for electrical testing with a probe station connected to a Radiant ferroelectric tester. The common bottom electrode was accessed by scratching through the 200 nm-thick PZT. Polarization/electric-field measurements are shown below in Figs. 6.25-6.27. A combination of bipolar and unipolar polarization measurements are shown in Fig. 6.25. The test procedure was defined so that domain switching and non-switching were superimposed on the same chart. The ferroelectric figures of merit extracted from Fig. 6.25 are as follows: P_{r+} = 26 μC/cm^2, P_{r-} = -27 μC/cm^2, E_{c+} = 170 kV/cm and E_{c-} = -150 kV/cm. Figure 6.26 shows nested loop measurements performed immediately after the measurement shown in Fig. 6.25. The nested loops in Fig. 6.26 were collected from ±1 V to ±15 V in 2 V steps. The nested loops were only tested in the switched, bipolar condition. The test period for the measurements performed in Figs. 6.25 and 6.26 was held constant at 10 ms per loop. Figure 6.27 shows hysteresis loops (±10 V) collected with test periods ranging from 10 ms to 250 ms per loop. Very little change is observed between the 10 ms and 250 ms test period samples, which suggests that the leakage current was low.

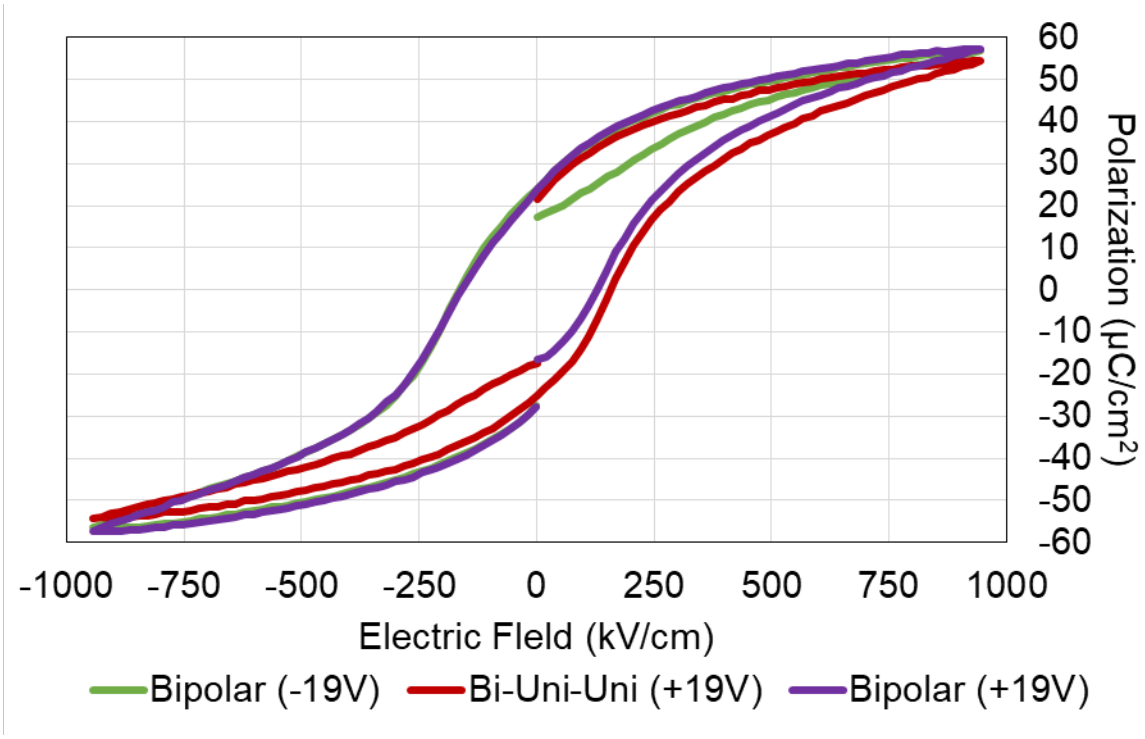

Figure 6.25: Polarization versus Electric Field Plot for ALD $Pb_{1.07}Zr_{0.24}Ti_{0.76}O_{3.7}$

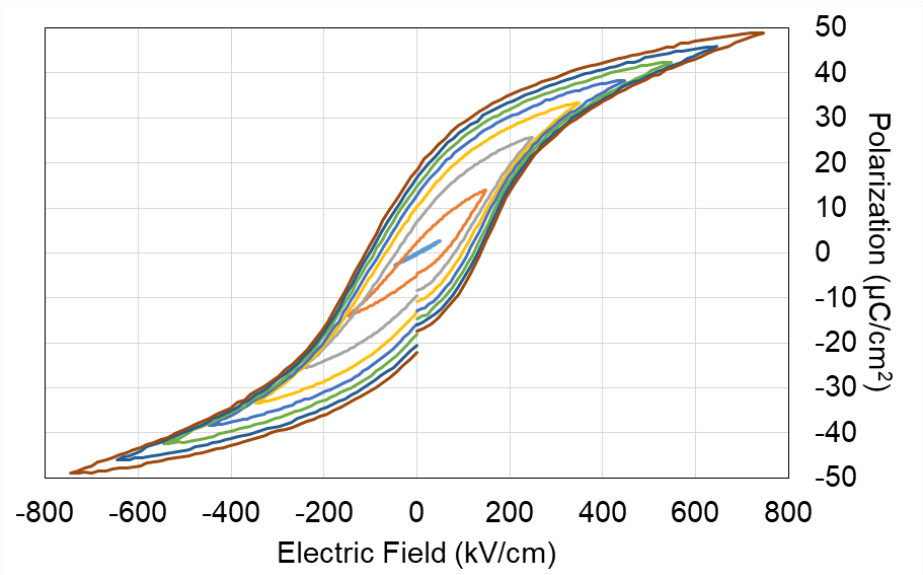

Figure 6.26: Nested Polarization versus Electric Field Plot for ALD

$Pb_{1.07}Zr_{0.24}Ti_{0.76}O_{3.7}$

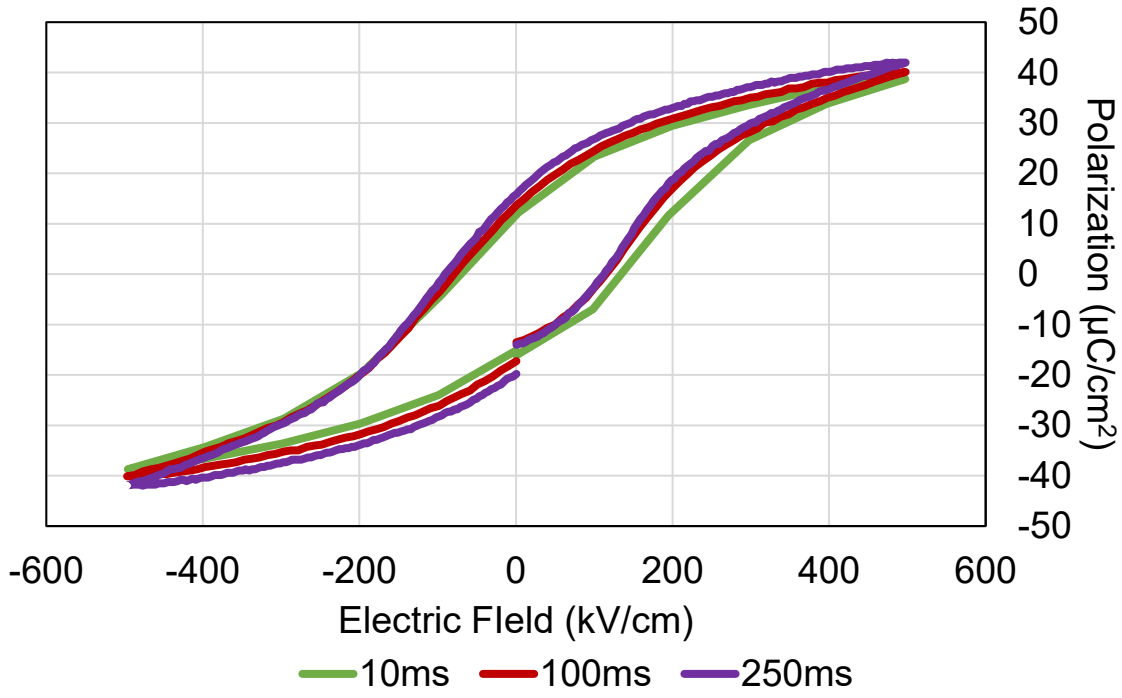

Figure 6.27: Polarization versus Electric Field Plot for ALD $Pb_{1.07}Zr_{0.24}Ti_{0.76}O_{3.7}$ with Different Test Periods

Relative Permittivity, Loss Tangent, and Leakage Current

Capacitance versus electric field measurements were performed on the same capacitor tested above using the same probe station connected to an HP/Agilent signal generator controlled with a LabVIEW interface. The results are plotted below in Fig. 6.28. The dielectric constant, ε_r, was 500 at zero field, and showed a tuning range of 552 at -67 kV/cm, and 219 at -496 kV/cm. The Tan δ was 0.03 or lower (rounded to the nearest hundredth) throughout the test range of ±500 kV/cm and mirrored the shape of the dielectric constant. Leakage current measurements were performed on the same sample and the results are plotted in Fig. 6.29. The leakage current density remained below 0.7

$\mu C/cm^2$ throughout the test range of ±250 kV/cm. The ferroelectric figures of merit are tabulated in Table 6.3 for quick reference.

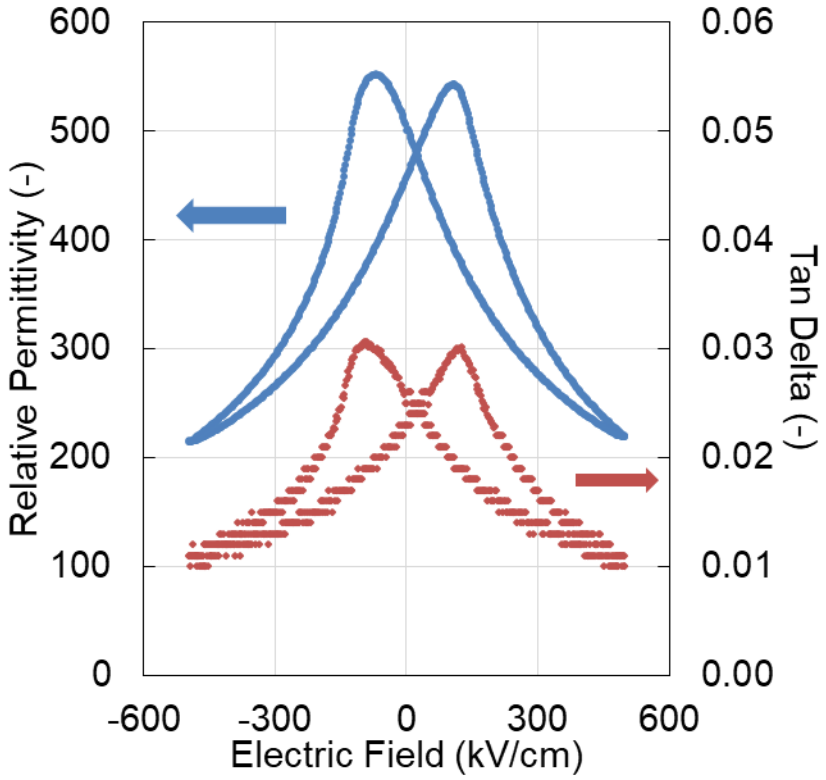

Figure 6.28: Relative permittivity (calculated from capacitance-voltage measurement) and Tan Delta versus electric field.

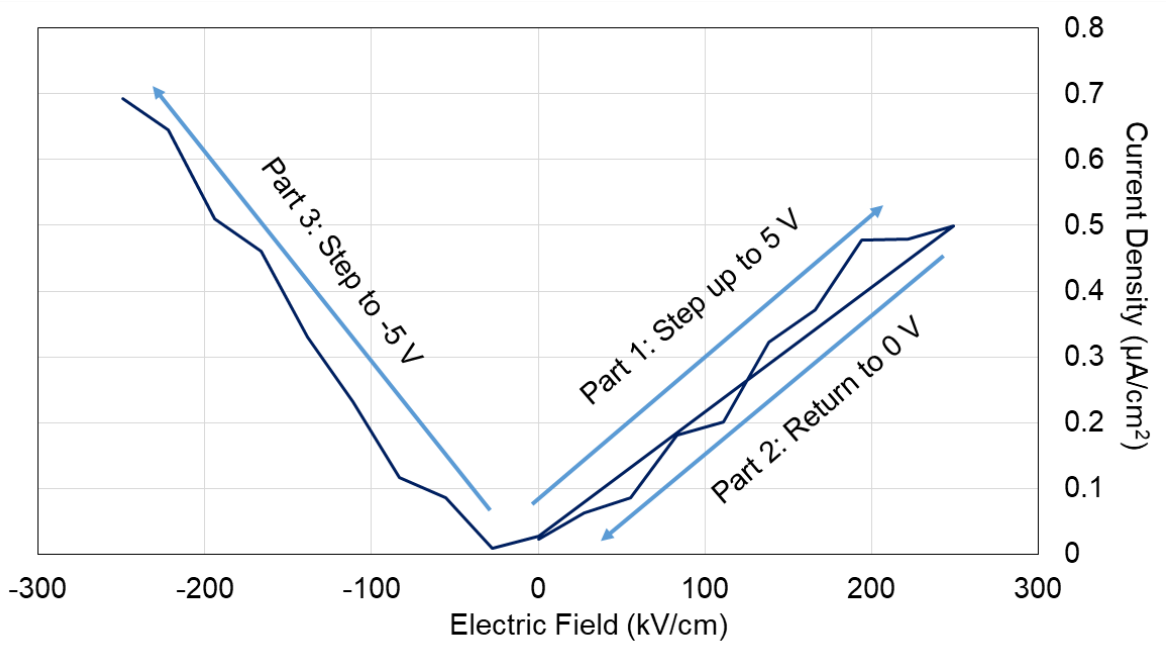

Figure 6.29: Leakage current density plot

Table 6.3: Ferroelectric FOM for ALD PZT

Parameter	**200 nm-thick PZT ($Pb_{1.07}Zr_{0.24}Ti_{0.76}O_{3.7}$)**
P_{r+}	26 μC/cm^2
P_{r-}	-27 μC/cm^2
E_{c+}	170 kV/cm
E_{c-}	-150 kV/cm
Zero Field ε_r	500
Max ε_r	552 at -67 kV/cm
Min ε_r	219 at -496 kV/cm
Max Tan δ	0.03 at -80 kV/cm
Leakage Current Density +	0.5 μA/cm^2 at 250 kV/cm (+5 V)
Leakage Current Density -	0.7 μA/cm^2 at -250 kV/cm (-5 V)

Summary and Conclusions

PTO-rich PZT was grown by ALD using $Pb(DMAMP)_2$, TDMAT, and TDMAZ cation precursors. The Zr-content was limited to approximately 4.5 at% regardless of the relative number of ZrO_x cycles and was not affect by the precursor sequence. The in-situ growth rate measured by multi-wavelength ellipsometry was shown to be linear within a 0.9 nm standard deviation. ALD PZT films deposited near the ideal perovskite composition (Pb at = Ti+Zr at%) crystallized into the perovskite phase upon annealing above 600 °C with no observed secondary phases. Two ideal recipes are suggested from the aggregate data. Micromachined trenches 45 μm deep were coated with uniform thickness using the new ALD PZT process reported here. The annealed films were shown using TEM cross section images to be dense and pinhole free following annealing at 600 °C for 30 min. Ferroelectric hysteresis loops of the ALD PZT measured from MIM capacitors with Pt electrodes displayed high-quality ferroelectric properties (summarized in Table 6.3) and low leakage current. Future work should be focused on substitution or addition of a different Zr-precursor to obtain PZT compositions near the MPB.

References

[1] Watanabe T, Hoffman-Eifert S, Peter F, et al. Liquid Injection ALD of $Pb(Zr,Ti)O_x$ Thin Films by a combination of Self-Regulating Component Oxide Processes. *J Electrochem Soc.* 2007:154:G262-G269.

[2] Watanabe T, Hoffman-Eifert S, Hwang CS, et al. Growth Behavior of Atomic-Layer-Deposited Pb(Zr,Ti)Ox Thin Films on Planar Substrate and Three-Dimensional Hole Structures. *J Electrochem Soc.* 2008:155:D715-D722.

[3] Hwang CS. Atomic Layer Deposition for Semiconductors. Chapter 6 FeRAM, page 163. New York, NY: Springer Science+Business Media:2014
[4] Choi JH, Zhang F, Perng Y-C, et al. Tailoring the composition of lead zirconate titanate by atomic layer deposition. *J Vac Sci Technol B.* 2013;31:012207.
[5] Muralt, P. PZT Thin Films for Microsensors and Actuators: Where Do We Stand?. *IEEE Trans on Ultrason Ferroelectr Freq Control.* 2000;47:903-915

Chapter 7: ALD $PbHfO_3$ and $PbHf_xTi_{1-x}O_3$

Introduction

The following chapter provides an overview of recent efforts to grow antiferroelectric lead hafnate (PHO) and ferroelectric lead hafnate titanate (PHT) by ALD using a process similar to that previously developed for lead titanate (PTO). Tetrakis dimethylamino hafnium (TDMAH) was substituted for TDMAT either entirely (for PHO) or partially (for PHT). ALD PHO displayed remarkably similar growth characteristics to PTO. A solid solution of PTO and PHO yielded PHT (Hf=Ti≈10 at%) near the MPB, unlike the case of PZT which showed that the Zr concentration couldn't be raised about approximately 5 at%.

PHO ($PbHfO_3$) is a lead-based perovskite that is typically considered to be an isomorph of PZO.[1] Comparison of the XRD PDFs corresponding to PHO (PDF# 98-017-4106) and PZO (PDF# 00-049-0011) indicates that both are orthorhombic and belong to the Pbam (#55) space group. The unit cell dimensions for PHO (a,b,c = 5.8400, 11.7050, 8.1700 Å) and PZO (a,b,c = 5.88, 11.787, 8.231 Å) differ by less than 1%. The ionic radius of Hf (85 pm) is only one-pm smaller than Zr (86 pm) in the same coordination. Both Hf and Zr are group 4 transition metals. The largest difference between PHO and PZO is the atomic number of Zr (Z=40) and Hf (Z=72) which results in a 20% larger mass density of PHO (10.32 g/cm^3) compared to PZO (8.06 g/cm^3). Pure PHO and PZO are antiferroelectric and have potential applications in thin-film energy storage.[2]

PHT ($PbHf_xTi_{1-x}O_3$) is a lead-based perovskite that is a solid solution of PHO and PTO. PHT is relatively under-researched compared to PZT, though there are several reports that suggest that PHT is structurally similar to PZT and has comparable ferroelectric and piezoelectric properties. Frantti et al. measured the lattice constants of PHT ($0 \leq x \leq 50$) which indicated the presence of a monoclinic phase transition at x=0.50 which is similar to the MPB transition in PZT that occurs at x=0.52.[3] Fantozzi et al. fabricated PHT (x=0.5) using a powder sintering process that displayed a zero-field dielectric constant of 820 with tan delta of 0.008, and a d_{33} of 140 pC/N.[4] Thin film PHT grown by sol-gel[5] and PLD[6] retained a higher remanent polarization compared to un-doped PZT following fatigue testing, which suggests PHT may exhibit a higher fatigue resistance than PZT.

Chemical Composition and Growth Per Cycle

Lead Hafnate ($PbHfO_3$, PHO)

Thin-film PHO was grown by ALD using the process detailed in Chapter 3 using a PbO_x:HfO_x cycle ratios ranging from 3:1 to 4:1. The chemical composition of the 4:1 PHO was measured by RBS and is reported below in Table 7.1. The error associated with the atomic concentrations is reported in parentheses. The RBS measurement error associated with the cations is higher here than for the previous measurements for PTO and PZT because of the small difference in atomic number between Hf, Pt, and Pb. The combined measurement error of Pb+Hf was reported to be ±2%, which is slightly better than the individual cations. Although the measured composition indicates that the PHO was slighty Pb-rich, the measurement error defines a wide range of possible

compositions between $Pb_{0.80}HfO_{2.5}$ to $Pb_{1.44}HfO_{3.44}$ (normalized to Hf=1.0). Therefore, the composition identification is left as tentative. The PHO film reported in Table 7.1 was approximately 50 nm-thick and was deposited on the standard Pt bottom electrode stack defined in Chapter 4.

Table 7.1: RBS composition measurement of PHO ($Pb_{1.08}HfO_{2.9}$)

PbO_x:HfO_x Cycle Ratio	Pb (at %)	Hf (at %)	O (at %)
4:1	21.5 (±3)	20 (±3)	58.5 (±4)

Subsequent ALD PHO growths were performed with a 3:1 PbO_x:HfO_x cycle ratio to correct for the (possible) Pb oversaturation. In-situ thickness measurements performed by multi-wavelength ellipsometry are reported below in Figs. 7.1 – 7.4 for a 3:1 PbO_x:HfO_x cycle ratio deposition. The film received approximately 700 total cycles of deposition, or half the 'Standard Deposition.' Unlike the PTO and PZT samples, the PHO growth did not start with one cycle of ALD TiO_x. Instead, the PHO growth immediately began with a normal super-cycle (defined in Chapter 4), which starts with PbO_x as the first cycle. Figure 7.1 displays the thickness variation over the entire film growth. The thickness trace fits well to a linear curve with an R^2 value of 0.995 and a standard deviation of 0.17 nm. The first hour of growth is shown in Fig. 7.2, which indicates super-linear deposition for the first two nm, followed by approximately linear growth. The precursor doses are detailed in Fig. 7.3 which contains a thickness snapshot from hour six of the growth. The PHO super-cycle is nearly identical to the PTO super-cycle, except that TDMAH was substituted for TDMAT. Figure 7.4 contains a thickness snapshot from the end of the growth, and indicates that the growth

continued in a stepwise linear-fashion that is characteristic of a well-behaved ALD process. The final thickness was measured to be approximately 53.4 nm over the 700 cycle growth, which indicates an average GPC of 0.075 nm/cycle. The 0.075 nm/cycle growth rate almost exactly matches the GPC of PTO (0.073), grown with the same cycle ratio.

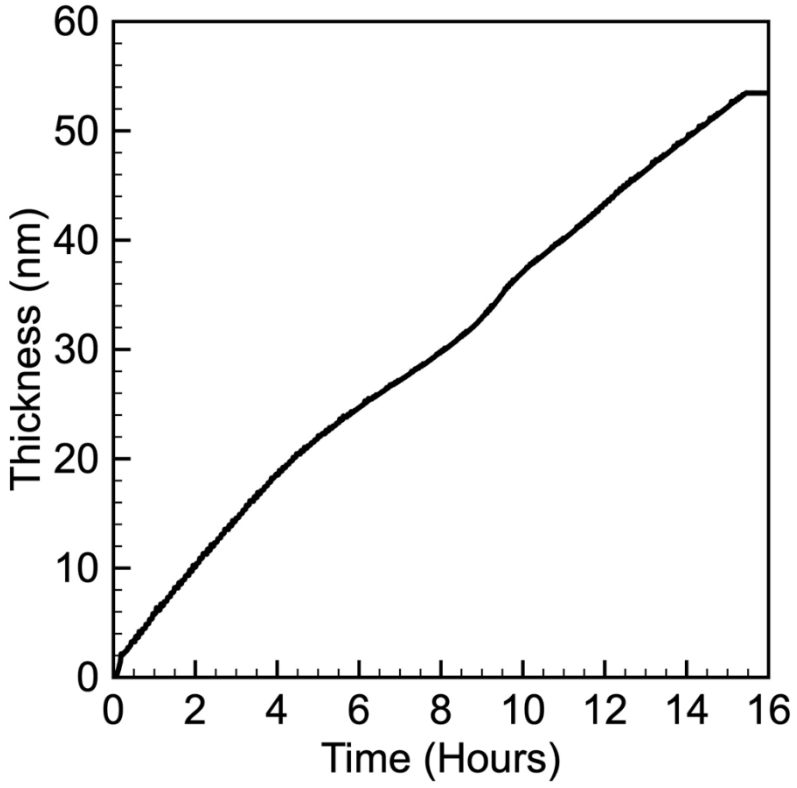

Fig 7.1: In-situ multi-wavelength ellipsometer measurement for the full time range of ALD PHO deposition (PbO_x:HfO_x ratio of 3:1)

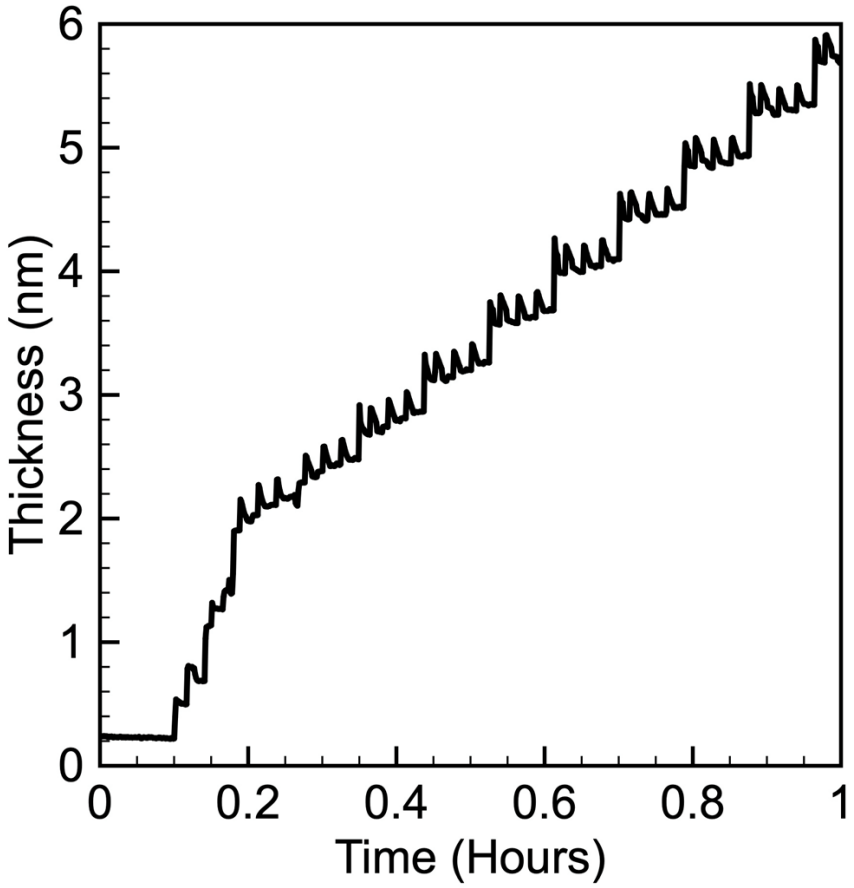

Fig 7.2: Substrate-enhanced growth near the onset of ALD PHO deposition (PbO_x:HfO_x ratio of 3:1) for the same film in Fig. 7.1.

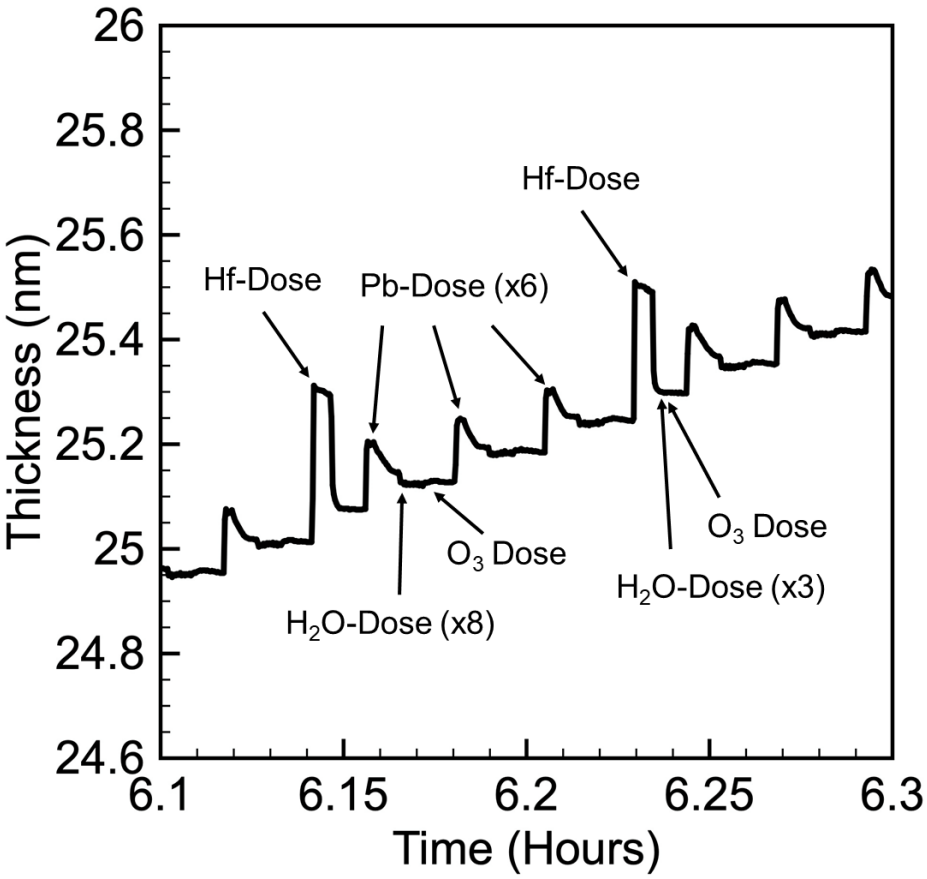

Fig 7.3: Detailed precursor dose steps for ALD PHO near hour six of the film growth illustrated in Fig. 7.1.

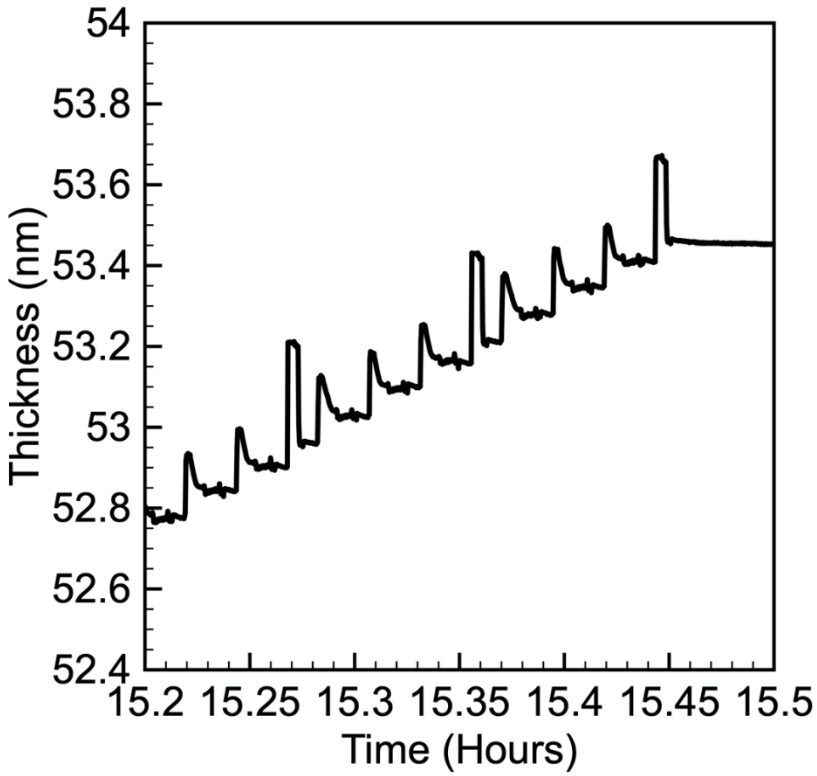

Fig 7.4: Thickness snapshot near the end of the ALD PHO deposition for the same film growth depicted in Fig. 7.1.

Lead Hafnate-Titanate ($PbHf_xTi_{1-x}O_3$, PHO)

PHT was grown by ALD at two different compositions using a combination of PTO and PHO processes. The PHO:PTO cycle ratio was maintained at 1:1, however the relative number of PbO_x cycles was varied between the two samples. The atomic concentration was determined by RBS for each sample, and the results are tabulated below in Table 7.2. The chemical formulae for the PHT are shown in parenthesis, and were normalized to (Hf+Ti)=1. Both of the ALD PHT samples were measured to be

somewhat Pb-deficient, though the Pb subscript (0.91) of the $Pb_{0.91}Hf_{0.47}Ti_{0.53}O_{3.22}$ sample with a 4:1/4:1 PbO_x:HfO_x / PbO_x:TiO_x Cycle Ratio was within the measurement error of the ideal subscript 1.00. The Pb composition relative to the PbO_x/(HfO_x+TiO_x) cycle ratio is plotted in Fig. 7.5 with a linear extrapolation. The extrapolated line crosses y=1 at approximately x=4.45. Interestingly, the PbO_x/(ZrO_x+TiO_x) ratio calculated in Chapter 6 to yield stoichiometric PTO-rich PZT was 4.40, which is very close to 4.45 (with HfO_x substituted for ZrO_x) in the present case. The Hf/(Hf+Ti) cation ratio is plotted versus the relative number of PHO/(PTO+PHO) cycles in Fig. 7.6. Since the only samples measured were grown with a PHO:PTO ratio of 1:1 [PHO/(PTO+PHO) = 0.50], a quadratic interpolation between the endpoints was used to estimate the Hf composition variation. The ideal Hf/(Hf+Ti) cation ratio of 0.5 is estimated to occur in Fig. 7.6 at PHO:PTO ratio of 9:8 [PHO/(PTO+PHO) = 0.53]. Based on these estimates, the recipe expected to yield PHT with the ideal Hf/(Hf+Ti) cation ratio of 0.5 and stoichiometric Pb content is detailed in Table 7.3.

Table 7.2: RBS composition measurements of PHT

PbO_x:HfO_x / PbO_x:TiO_x Cycle Ratio	Pb (at %)	Hf (at %)	Ti (at %)	O (at %)
3:1/4:1 ($Pb_{0.82}Hf_{0.47}Ti_{0.53}O_{2.99}$)	17.0 (±0.5)	9.8 (±1)	11.0 (±1)	62.2 (±4)
4:1/4:1 ($Pb_{0.91}Hf_{0.47}Ti_{0.53}O_{3.22}$)	17.8 (±0.5)	9.2 (±1)	10.3 (±1)	62.7 (±4)

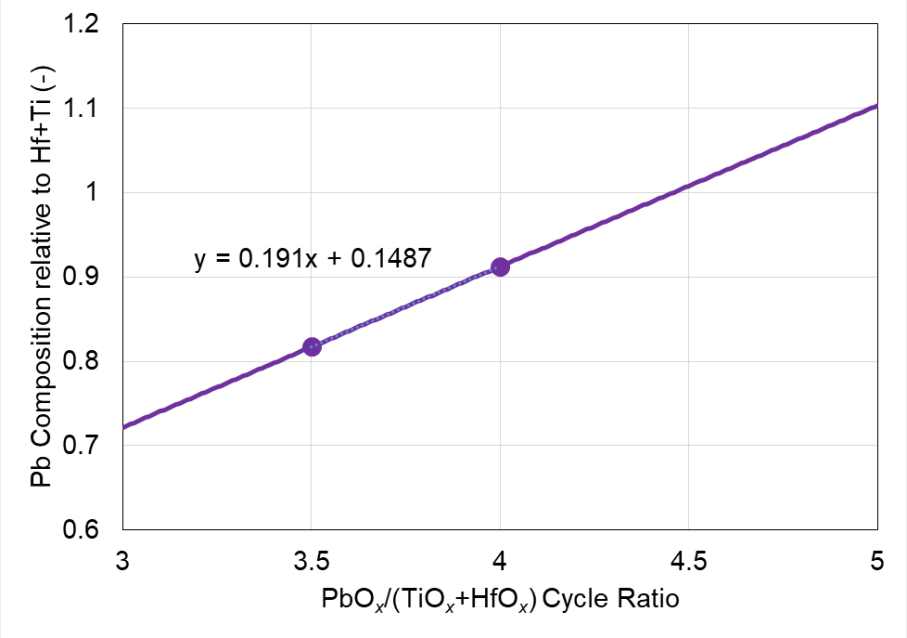

Fig 7.5: Variation of Pb composition with binary oxide cycle ratio

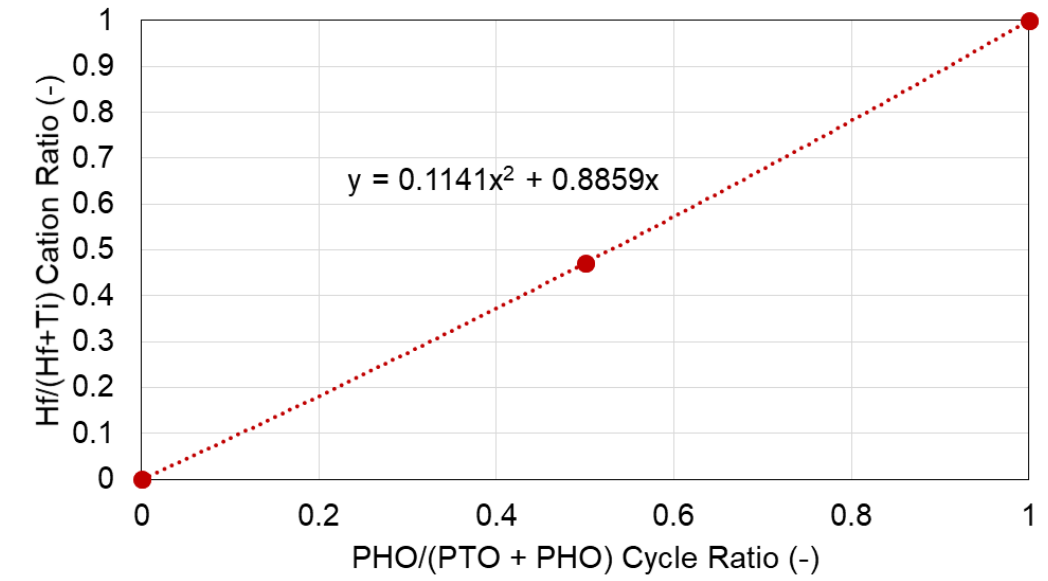

Fig 7.6: Variation of Hf cation ratio with PHO and PTO cycles

Table 7.3. Calculated Optimized near-MPB PHT recipe

Parameter	Recipe (Calculated)
PHO/(PHO+PTO)	0.53
PHO:PTO	9:8
PbO_x:TiO_x	4:1(x5), 5:1(x3)
PbO_x:HfO_x	4:1(x5), 5:1(x4)
Supercycles (Std)	19
TiO_x Cycles	152
HfO_x Cycles	171
PbO_x Cycles	1102
Ti Concentration (at%)	10.0% (estimate)
Hf Concentration (at%)	10.0% (estimate)
Pb Concentration (at%)	20.0% (estimate)
O Concentration (at%)	60.0% (estimate)
Pb Excess (%)	0% (estimate)
Pb%/(Ti+Hf%)	1.00 (estimate)

In-situ thickness measurements were performed on the sample characterized in row two of Table 7.2 and are shown below in Fig. 7.7. The PHT sample received approximately 1400 ALD cycles (equal to the Standard Deposition). The thickness was linear with an R^2 value of 0.998 a standard deviation of 0.4 nm. The first hour of growth is shown below in Fig. 7.8. The PHT sample received an initial TiO_x ALD cycle prior to the PTO or PHO super-cycles. Like the PHO, PTO, and PZT, the initial PHT grown on the Pt substrate was superlinear until about 3 nm of deposition and was subsequently linear. The PHT precursor doses are detailed in Fig. 7.9, which includes a thickness snapshot during hour 15 of growth. The chemisorption kinetics appear to be nearly

identical during both the PTO and PHO cycles. The Ti and Hf precursors, TDMAT and TDMAH, respectively, are both alkyl-amide precursors that contain identical ligands. In addition to having identical ligands, both Ti and Hf cations belong to the same element group, so it is not surprising they react similarly within the PHT materials system. However, in the PZT process reported in Chapter 6, the Zr precursor TDMAZ (which is also an alkyl amide precursor) did not react well in the PZT system. The reasons why TDMAH grows well with $Pb(DMAMP)_2$ while TDMAZ does not are still being investigated. In the meantime, it is convenient that TDMAH works well since it appears to enable the growth of ALD PHT near the MPB (which is critical to obtaining the highest-possible piezoelectric coefficients). Figure 7.10 displays the final cycles of the PHT growth, and indicates that like the PHO, PTO, and PZT, the PHT growth is step-wise throughout the deposition which is a characteristic of ALD processes. The final thickness was measured to be 114.5 nm over the 1396 cycle growth, indicating a GPC of 0.082 nm/cycle.

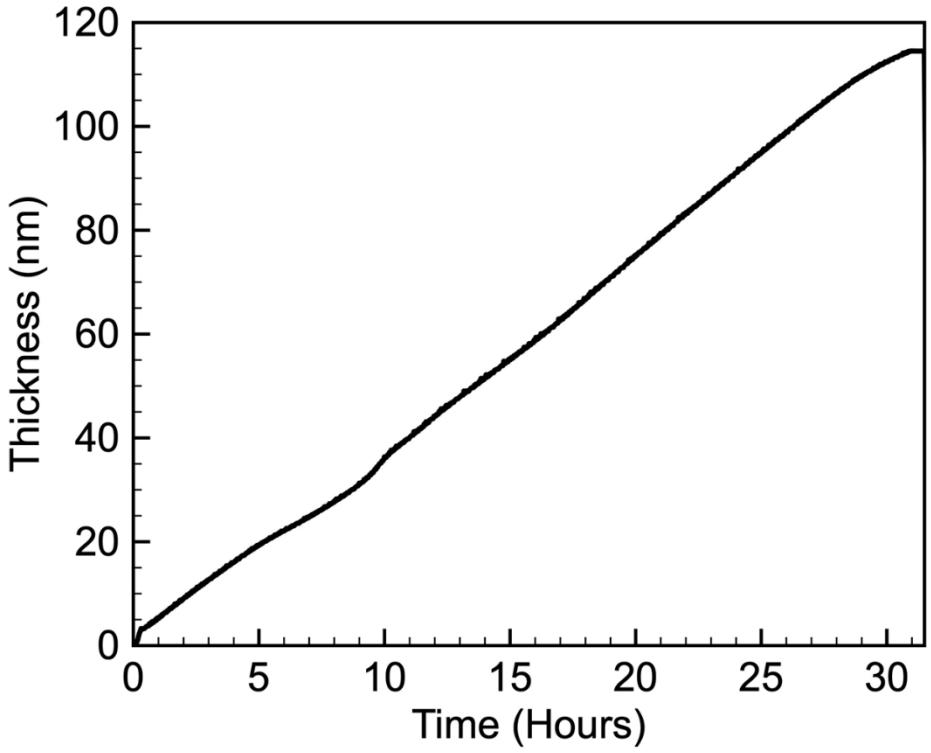

Fig 7.7: In-situ multi-wavelength ellipsometer measurement for $Pb_{0.82}Hf_{0.47}Ti_{0.53}O_{2.99}$

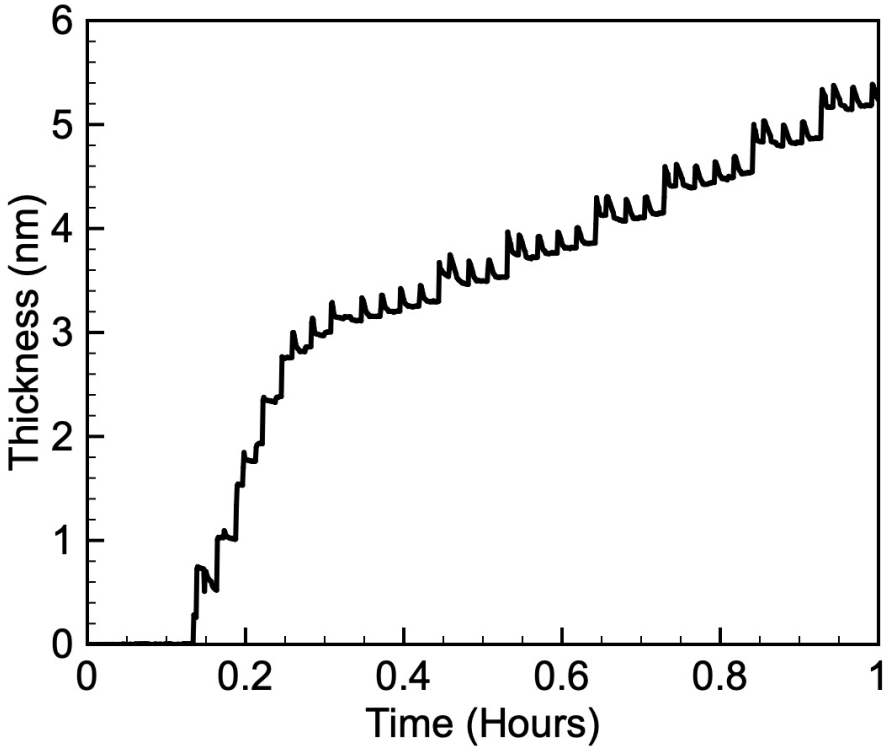

Fig 7.8: Nucleation stage of ALD PHT on Pt substrate for the film growth in Fig. 7.7.

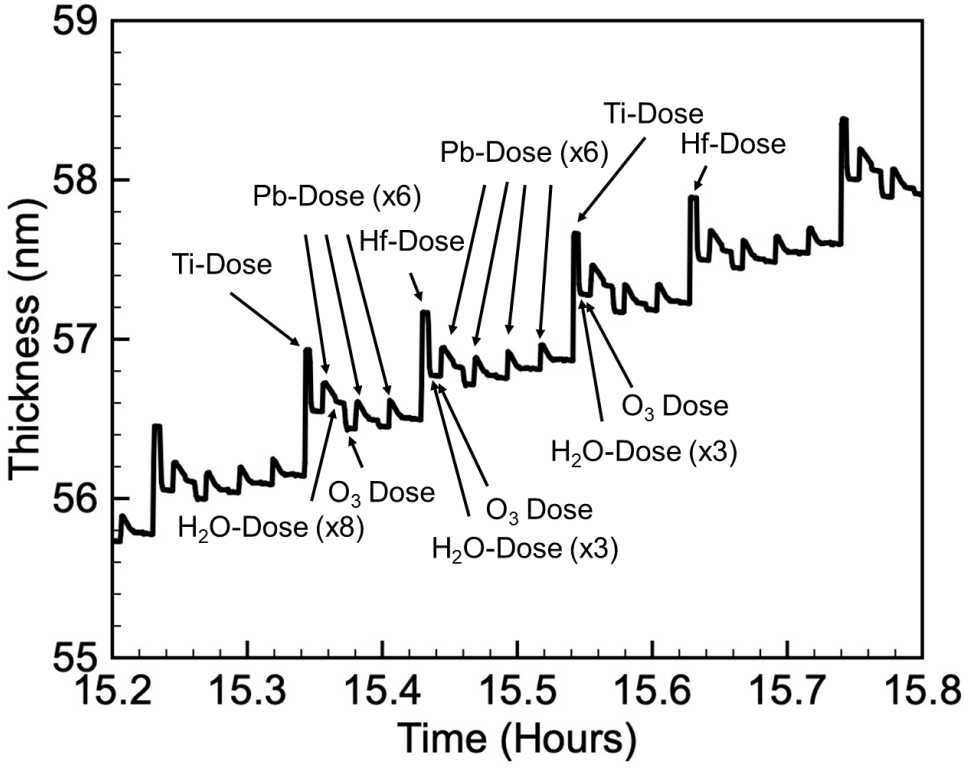

Fig 7.9: Mid-deposition PHT thickness-trace with labelled precursor doses for the film growth in Fig. 7.7.

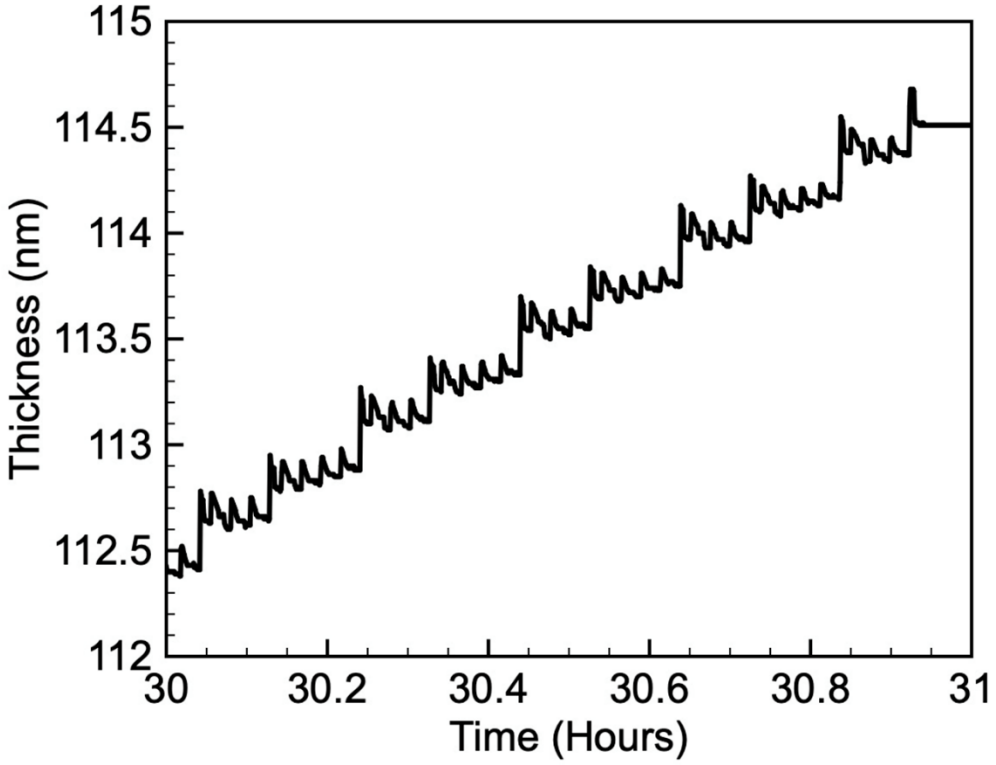

Fig 7.10: In-situ thickness trace of final ALD PHT cycles for the film growth in Fig. 7.7.

Phase Identification by X-ray Diffraction

Lead Hafnate ($PbHfO_3$, PHO)

Grazing incidence X-ray diffraction (GIXRD) was performed on an annealed PHO film that was grown on the standard Pt bottom electrode. The PHO films was grown with a 3:1 PbO_x:TiO_x cycle ratio. The composition of the 3:1 film has not yet been measured, but is assumed to be either stoichiometric or slightly Pb-poor based on the atomic percentages obtained by RBS for the 4:1 sample as discussed in the Chemical

Composition and Growth per Cycle section. The PHO film was measured to be 202 nm-thick by in-situ ellipsometry. The Pt top-electrode was sputtered at room temperature prior to crystallization by RTA at 600 °C with a 30 min. hold in an O_2 background. The GIXRD scan is plotted below in Fig. 7.11. Two peaks are clearly identified. The peak just below 31° is labelled as perovskite (040)/(200)/(122). The PHO XRD reference pattern (PDF# 98-017-4106) lists those three reflections at 30.525°, 30.591°, and 30.746°, respectively. The peak maximum is observed at 30.875°, which is nearest to the PDF's (122) peak location. However, the full-width at half-max (FWHM) is approximately 0.5°, which is broad enough to include each of the identified reflections. Therefore, the observed peak may be a superposition of some or all three of the identified reflections. The Pt (111) reflection is identified near 40° and corresponds to the top Pt electrode. The peaks U1 through U4 are not clearly identified, but may correspond to a combination of reflections listed in the aforementioned PHO PDF. The measured peak maxima are listed in Table 7.4 alongside possible PHO reflections contained within the PDF. PbO Massicot, PbO Litharge or other PbO_x phases have not been ruled-out as the source of the unidentified peaks. Regardless, it appears that the PHO crystallized primarily into the perovskite phase, though a small percentage of secondary phases may be present.

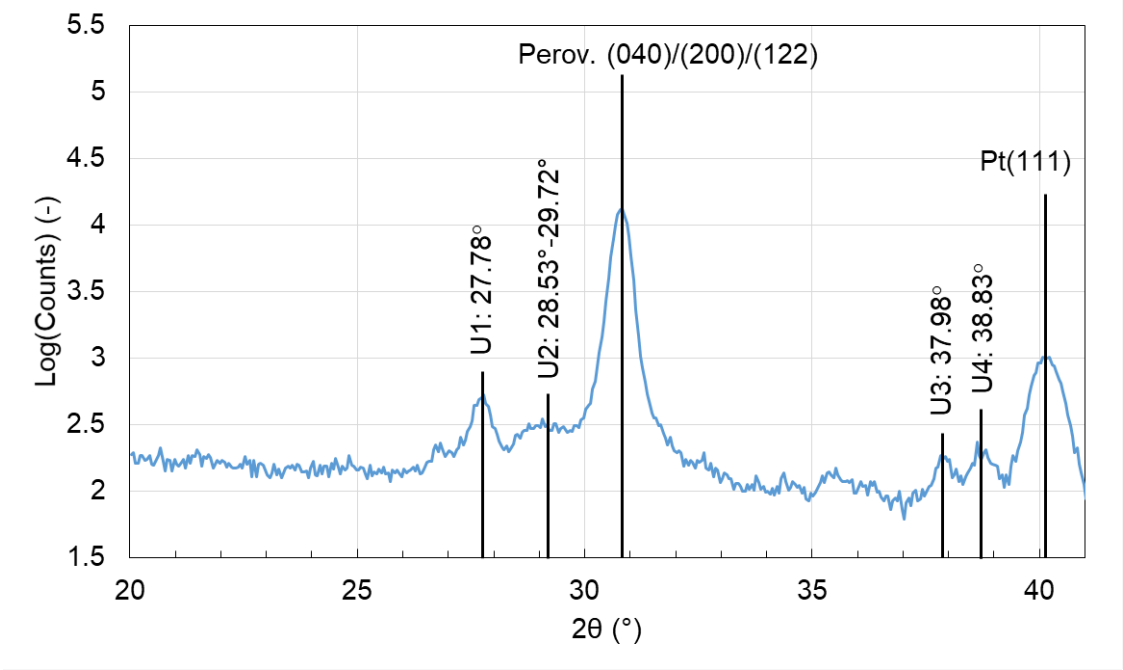

Figure 7.11: Grazing Incidence XRD of PHO (3:1 PbO_x:TiO_x cycle ratio)

Table 7.4: Observed PHO reflections versus PDF# 98-017-4106

Reflection	**d spacing (Å)**		**2θ (°)**	
	Reference	**PHO (This Work)**	**Reference**	**PHO (This Work)**
(130) **U1**	3.224	N/A	27.470	N/A
(112) **U1**	3.218	3.21	27.696	27.78
(131) **U2**	3.015	3.12-3.00	29.603	28.53-29.72
(040)	2.926	N/A	30.525	N/A
(200)	2.920	N/A	30.591	N/A
(122)	2.906	2.89	30.746	30.875
(042) **U3**	2.379	N/A	37.787	N/A
(202) **U3**	2.376	2.37	37.842	37.98
(230) **U4**	2.338	N/A	38.477	N/A
(212) **U4**	2.328	2.32	38.644	38.83

Lead Hafnate-Titanate ($PbHf_xTi_{1-x}O_3$, PHO)

GIXRD was also performed on ALD PHT with a sputtered Pt electrode. Unlike the PHO, the top 50 nm-thick Pt electrode was sputtered at 500 °C after the film was already crystallized by RTA at 600 °C with a 30 min. hold in an O_2 atmosphere. The PHT film was measured to be 225 nm-thick by ex-situ spectroscopic ellispometry using a Tauc-Lorentz oscillator with a UV-pole with a restricted wavelength range of 500-1000 nm (the same model used for PZT) at the X-ray spot. The expected peak locations and lattice spacing are reported below in Table 7.5. The reference values were extracted from Frantti, who characterized the space group and lattice parameters of $PbHf_xTi_{1-x}O_3$ ($0.10 \leq x \leq 0.50$) by neutron diffraction.[3] The observed peaks match the reported tetragonal PHT at $x = 0.40$ quite well, as is shown in Table 7.5. The GIXRD pattern is shown in Fig. 7.12. The largest peaks correspond to the top Pt electrode that covered the PHT. The Pt (111) peak occurs near 40° and is partially cut-off at the edge of the chart. The Pt (111) kβ is the second largest and occurs at 36.6°. The remaining two peaks correspond to perovskite PHT. The peak observed at 31.37° falls in between the (101) and (110) reflections. The peak at 22.11° falls closer to (100) than to (001). Although no secondary phases were observed in the GIXRD scan, the intensity was overall quite low. This is most likely because the beam was aligned towards the Pt layer rather than to the PHT layer. Future GIXRD scans should be performed without the top Pt layer so that the beam can be more easily aligned to the top PHT layer. Despite the low intensity, it is clear the PHT film crystallized into the desired perovskite phase.

Table 7.5: Observed versus calculated PHT reflections

Reflection	d spacing (Å)		2θ (°)	
	Ref.	$Pb_{0.82}Hf_{0.47}Ti_{0.53}O_{2.99}$ (This Work)	Ref.	$Pb_{0.82}Hf_{0.47}Ti_{0.53}O_{2.99}$ (This Work)
(001)	4.116	N/A	21.564	Not Observed
(100)	4.001	4.01	22.192	22.11
(101)	2.869	2.85	31.137	31.37
(110)	2.829	2.85	31.587	31.37
(111)	2.331	N/A	38.569	Not Observed

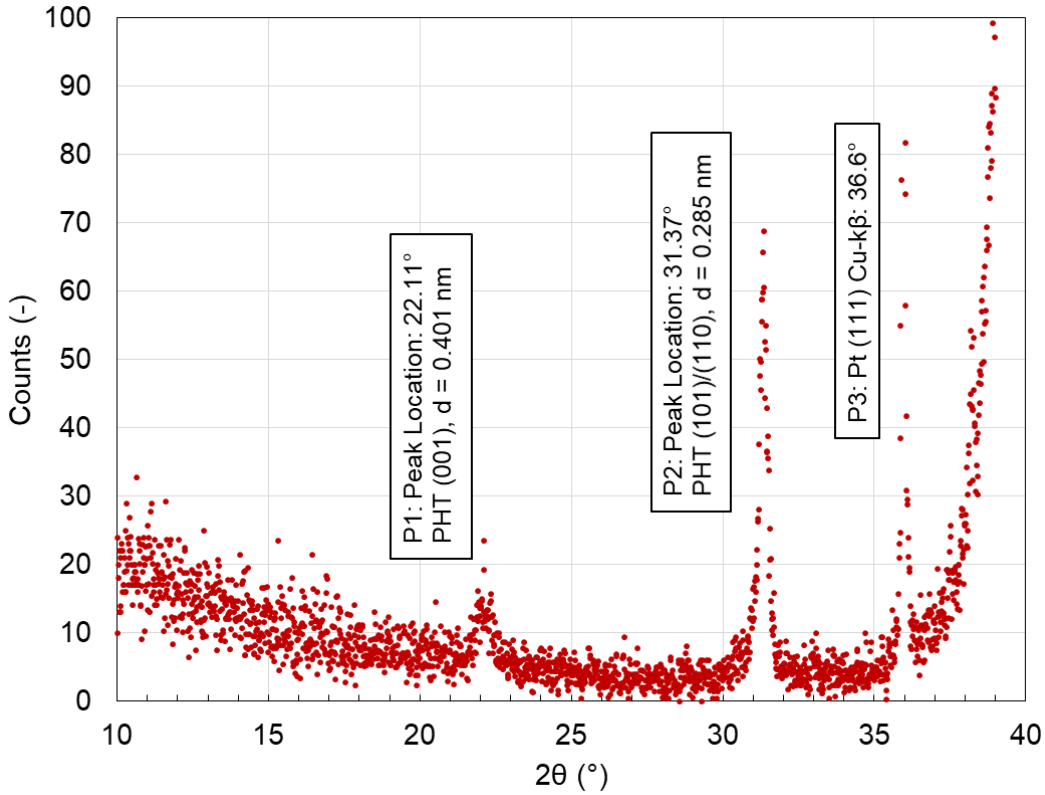

Figure 7.12: Grazing Incidence XRD $Pb_{0.82}Hf_{0.47}Ti_{0.53}O_{2.99}$

Electrical Characterization

Lead Hafnate ($PbHfO_3$, PHO)

Polarization-voltage loops were measured from MIM capacitor structures with 202 nm-thick ALD PHO that was previously measured by GIXRD in Fig. 7.11, and are shown below in Figs. 7.13-14. The sputtered top Pt electrodes were patterned using a lift-off technique. The top electrodes were disk-shaped and were 4.92×10^{-4} cm^2 in area. The antiferroelectric (AFE) figures of merit (FOM) are listed in Table 7.6. P_{max} refers to the maximum polarization magnitude in the + and – bias directions. E_F is the minimum field required to induce the AFE-ferroelectric phase transition. The ferroelectric-AFE phase transition occurs once the voltage magnitude is lowered below E_A. The polarization exhibits hysteresis because energy loss is associated with the phase transition. The discharge energy is defined as the area between the polarization/electric-field curve re-trace and the y-axis (polarization), and is indicated by the red hash marks (see Fig. 7.13).[7] In this case, energy storage capacity was calculated from the polarization-voltage measurement using a rectangular area integral approximation between each data pair and is reported in Table 7.7. Nested loops are reported below in Fig. 7.14. The PHO retains AFE behavior from ±0-6 V. The ferroelectric phase begins to show at ±8 V, which is larger in magnitude than both E_{F+} and E_{F-}.

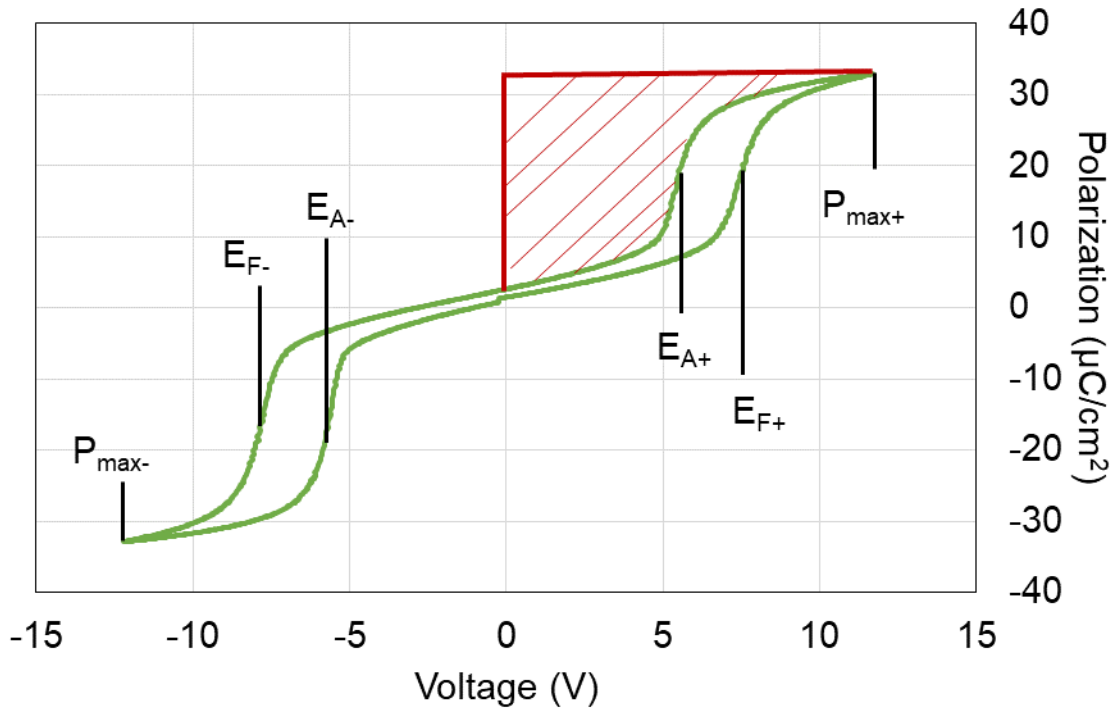

Fig 7.13: P/V ALD PHO (202 nm-thick)

Table 7.6: Measured AFE FOM for ALD PHO

FOM	E_{A-}	E_{F-}	E_{A+}	E_{F+}	P_{max+} (μC/cm^2)	P_{max-} (μC/cm^2)
Value	-5.7 V	-7.8 V	5.5 V	7.5 V	32.9 (at 11.7 V)	-32.9 (at -12.2 V)

Table 7.7: Calculated Energy Storage of 202 nm-thick PHO, 4.92x10^{-4} cm^2 capacitors

FOM	Total Energy Storage	2-D Energy Density	Energy Per Unit Volume
Calculated	8.3x10^{-8} J	1.7x10^{-4} J/cm^2	8.4 J/cm^3

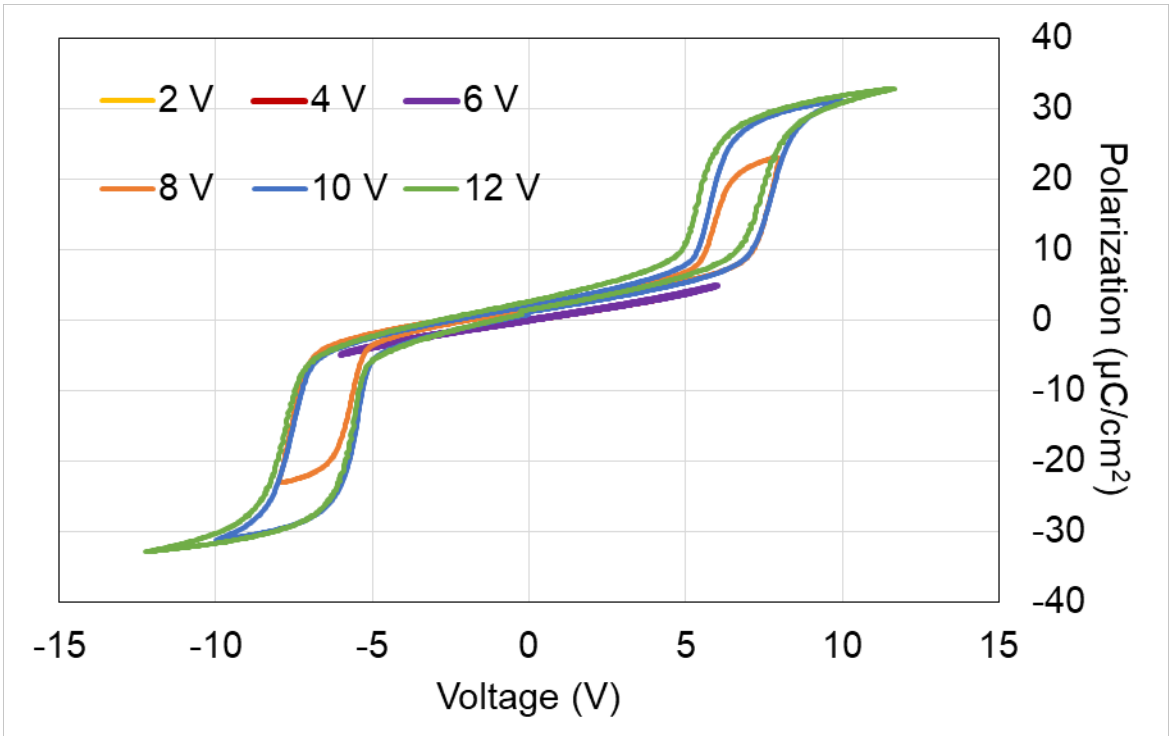

Fig 7.14: P/V ALD PHO with nested loops

Lead Hafnate-Titanate ($PbHf_xTi_{1-x}O_3$, PHO)

MIM capacitors were fabricated using 225 nm-thick ALD PHT in order to test the ferroelectric properties. The ALD PHT samples were grown using the process shown in Fig. 7.9. The top Pt electrodes were deposited and patterned according to the process defined in Chapter 4. The electrical measurements were performed on top electrodes that were 4.92 x 10^{-4} cm^2 in area. Polarization vs electric field loops are shown below in Fig. 7.15. Three bipolar loops are superimposed that display the polarization behavior for both switching and non-switching conditions. The positive remnant polarization (P_{r+}) was measured to be 8.7 $\mu C/cm^2$, while the negative remnant polarization (P_{r-}) was shown to be -7.0 $\mu C/cm^2$. The positive coercive field (E_{c+}) was

shown to be 84 kV/cm while the negative coercive field (E_{c-}) was -100 kV/cm. Nested double-switching bipolar loops are plotted from ±1 V to ±15 V in 2 V increments. Polarization versus electric field loops measured for different test periods ranging from 10 ms to 250 ms at ±440 kV/cm (±10 V) are plotted in Fig. 7.17. The polarization loops are nearly identical for each of the test periods, which suggests that the films exhibit low leakage-current. The leakage current was quantified using a test protocol that included an initial 1-s voltage soak prior to current measurement. The results are plotted in Fig. 7.18, and indicate that the leakage current density was less than 0.7 μA/cm^2 at ±222 kV/cm (±5 V), confirming low current dissipation.

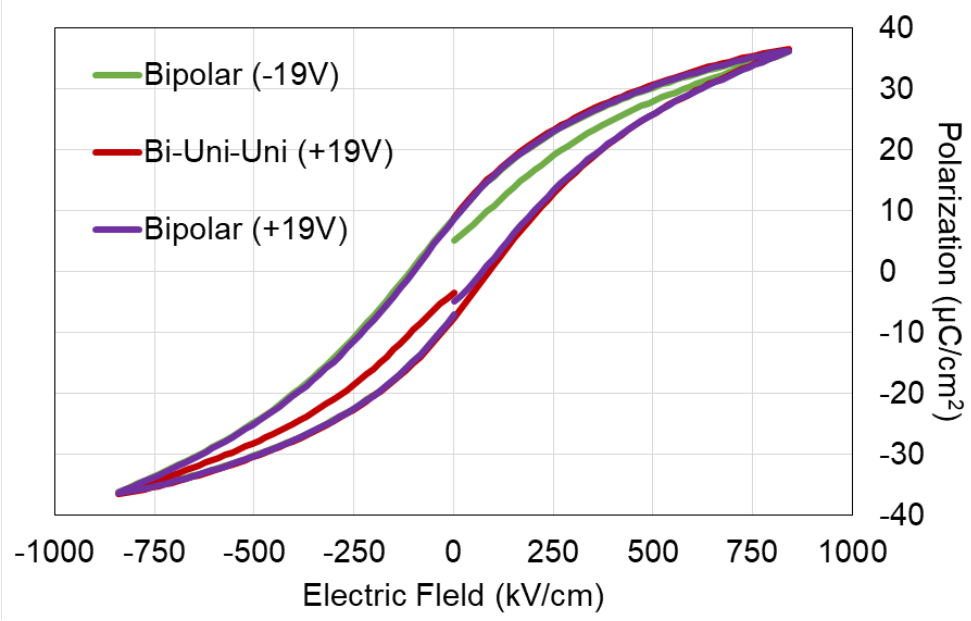

Figure 7.15: P/V bipolar switching loops $Pb_{0.82}Hf_{0.47}Ti_{0.53}O_{2.99}$

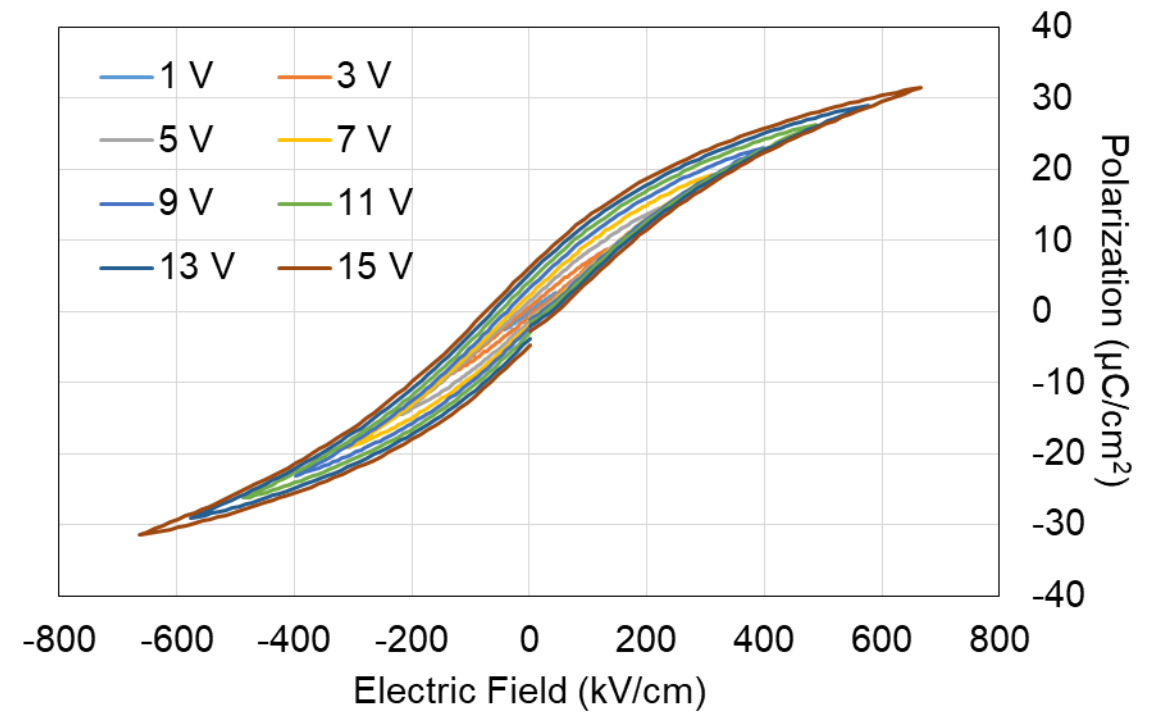

Figure 7.16: Polarization-electric field nested loops of ALD $Pb_{0.82}Hf_{0.47}Ti_{0.53}O_{2.99}$

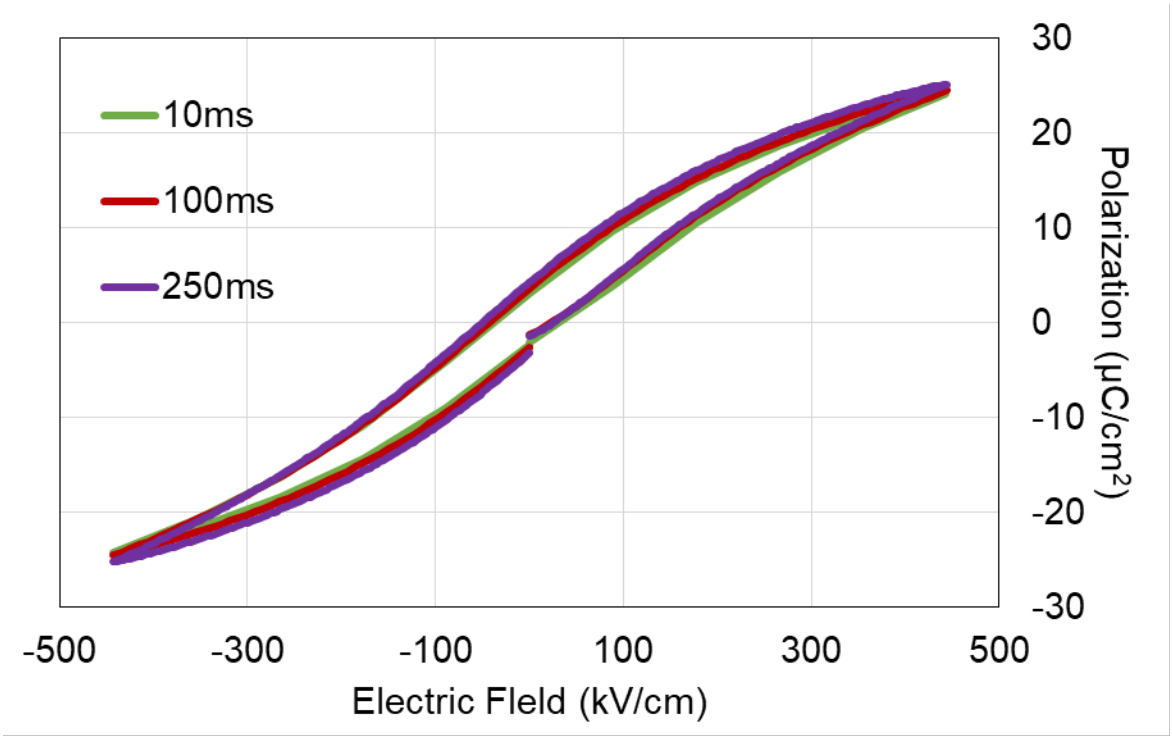

Figure 7.17: Polarization-electric field with varied test period of ALD $Pb_{0.82}Hf_{0.47}Ti_{0.53}O_{2.99}$

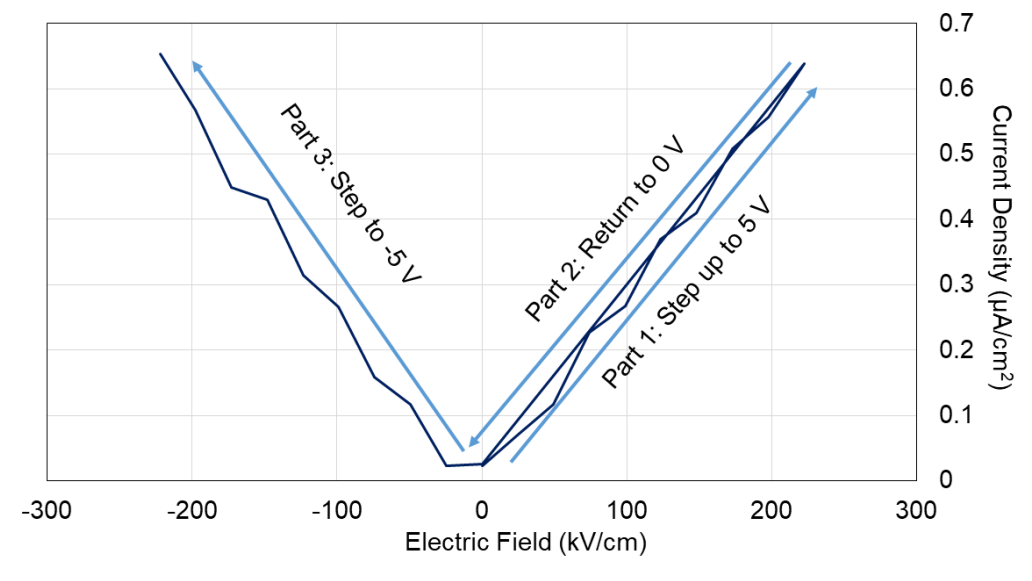

Fig 7.18: Leakage ALD PHT $Pb_{0.82}Hf_{0.47}Ti_{0.53}O_{2.99}$

Capacitance-voltage measurements were performed on the same capacitor characterized in Figs. 7.15-7.18, and the results are plotted below in Fig. 7.19. The ALD PHT exhibited a zero-field dielectric constant (ε_r) of 550 with a tuning range of 580 at 46 kV/cm, to 252 at 444 kV/cm. The loss tangent barely exceeded 0.02 across the entire tested field range of ±444 kV/cm (±10 V). For convenience, the ferroelectric figures-of-merit for 225 nm-thick ALD PHT are tabulated in Table 7.8, shown below.

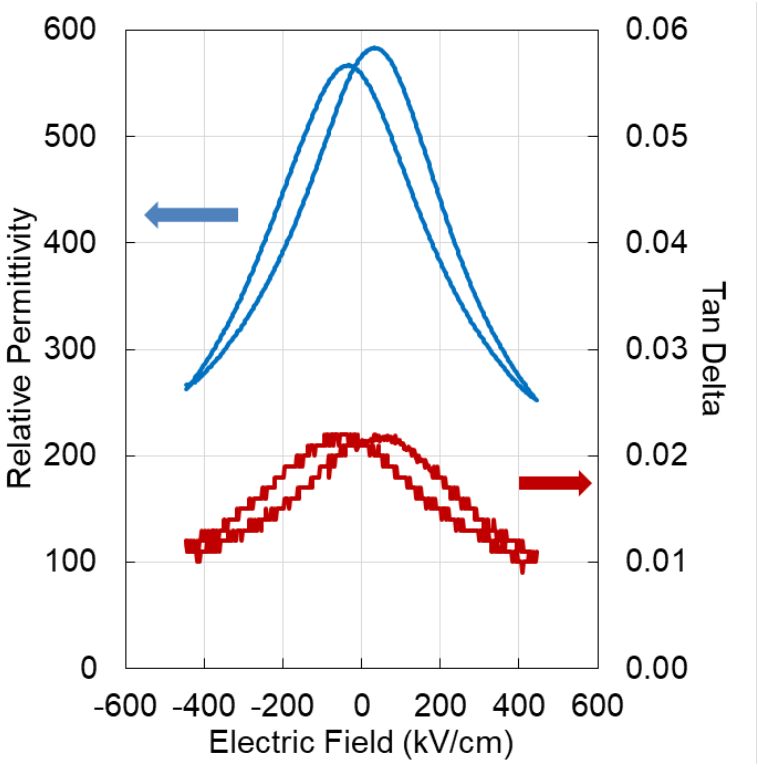

Fig 7.19: C/V ALD PHT $Pb_{0.82}Hf_{0.47}Ti_{0.53}O_{2.99}$

Table 7.8: Ferroelectric and dielectric properties of ALD PHT $Pb_{0.82}Hf_{0.47}Ti_{0.53}O_{2.99}$

Parameter	**225 nm-thick PHT ($Pb_{0.82}Hf_{0.47}Ti_{0.53}O_{2.99}$)**
P_{max}	36 μC/cm^2 at 840 kV/cm
P_{r+}	8.7 μC/cm^2
P_{r-}	-7.0 μC/cm^2
E_{c+}	84 kV/cm
E_{c-}	-100 kV/cm
Zero Field ε_r	550
Max ε_r	580 at 46 kV/cm
Min ε_r	252 at 444 kV/cm
Max Tan δ	0.022 at -40 kV/cm

Leakage Current Density +	0.64 μA/cm^2 at 222 kV/cm (+5 V)
Leakage Current Density -	0.65 μA/cm^2 at -222 kV/cm (-5 V)

Pyroelectric characterization was performed on a capacitor from the same ALD PHT wafer that was electrically characterized above. The pyroelectric coefficient was calculated according to the following relation, from Hanrahan et al.[8]:

$$\Pi = \frac{I_\Pi}{A\frac{dT}{dt}} \qquad \text{Eqn. 7.1}$$

Where Π is the pyroelectric coefficient (C/m^{2}k), I_Π is the pyroelectric current, A is the current collection area (in this case, 4.92 x 10^{-4} cm^2, corresponding to the top Pt electrode), T is the temperature, and t is time. The temperature of the ALD PHT MIM capacitor was varied between 55-62 °C according to (approximately) a sine wave at an average rate of 7.5 °C/s. The pyroelectric coefficient was measured at DC bias voltages which ranged from 0-10 V and is plotted in Fig. 7.20. The AC current was measured as the temperature was varied, which corresponded to the pyroelectric current. The pyroelectric coefficient of the ALD PHT was measured to be comparable to, but not better than sol-gel PZT grown near the MPB (approximately 380 μC/m^{2}K at 250 kV/cm).

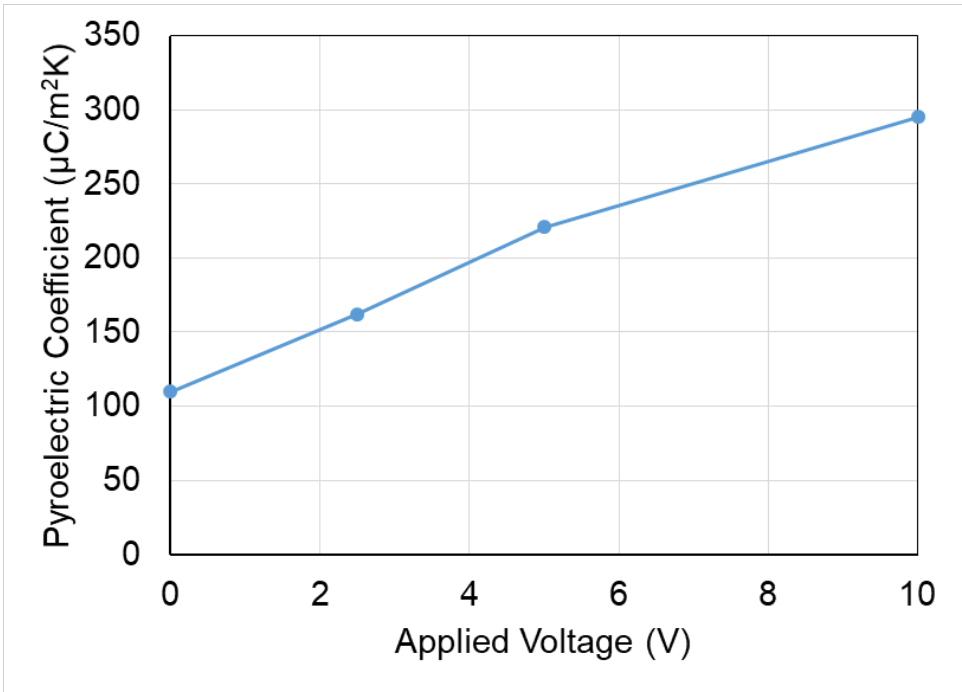

Fig 7.20: Pyroelectric Coefficient Measurement of ALD $Pb_{0.82}Hf_{0.47}Ti_{0.53}O_{2.99}$

Summary and Conclusions

New ALD processes for antiferroelectric PHO and ferroelectric PHT have been successfully demonstrated using a similar methodology as the previously demonstrated PTO. This is unequivocally the first reported instance of either material grown by ALD. The ALD PHO films crystallized by RTA into the perovskite phase displayed polarization hysteresis loops characteristic of an antiferroelectric, with P_{max+} and P_{max-} equal to 32.9 μC/cm^2 and -32.9 μC/cm^2, respectively. The E_{A-}, E_{F-}, E_{A+}, and E_{F+} were equal to -5.7, -7.8, 5.5, and 7.5 V, respectively. The ALD PHO film showed a promising energy storage density of approximately 8.4 J/cm^3. The ALD PHO films may be implemented in future high aspect ratio structures that could enable both high energy storage and power output. Slightly Pb-deficient ALD PHT was successfully

grown near the MPB. ALD PHT with composition $Pb_{0.82}Hf_{0.47}Ti_{0.53}O_{2.99}$ measured by RBS crystallized into the perovskite phase upon annealing. The PHT displayed ferroelectric figures of merit P_{r+}, P_{r-}, E_{c+}, and E_{c-} of 8.7 μC/cm^2, -7.0 μC/cm^2, 84 kV/cm, and -100 kV/cm, respectively. The ALD PHT also exhibited a zero-field dielectric constant of 550 with a tuning range of 252-580, and a loss tangent below 0.03 throughout the tested range of ±10 V. The leakage current density was also small, and was measured to be less than 0.7 μA/cm2 throughout the tested range of ±5 V. The preliminary tests of near-MPB ALD PHT suggest that it may be a viable alternative (pending additional process development and characterization) to near-MPB ALD PZT.

References

[1] Jaffe B, Roth SR, Marzullo S, Properties of Piezoelectric Ceramics in the Solid-Solution Series Lead Titanate-Lead Zirconate-Lead Oxide: Tin Oxide and Lead Titanate-Lead Hafnate. *J Res Natl Bur Stand.* 1955; 55:239-254.

[2] Nguyem MD, Rijnders G, Electric field-induced phase transition and energy storage performance of highly-textured PbZrO3 antiferroelectric films with a depositions temperature dependence. *J Eur Ceram Soc.* 2018;38:4953-4961.

[3] Frantti J, Fujioka Y, Eriksson S, et al. Neutron Powder Diffraction Study of $Pb(Hf_xTi_{1-x})O_3$ Ceramics ($0.10 \leq x \leq 0.50$). *Inorg Chem.* 2005;44:9267-9278.

[4] Fantozzi G, Idrissi H, Favotto C, et al. Lead hafnate titanate (PHT) ceramics: processing and proeprties. *J Eur Ceram Soc.* 2000;20:1671-1676.

[5] Schorn PJ, Schneller T, Bottger U, et al. Characterization of Chemical Solution Deposition-Derived Lead Hafnate Titanate Thin Films. *J Am Ceram Soc.* 2005;88:1312-1314.

[6] Wu Z, Zhu J, Liu X. Improved fatigue property of hafnium substitute lead zirconate titanate deposited by pulsed laser deposition. *J Mater Sci Mater Electron.* 2017;28:1819-1823.
[7] Jaffe B. Antiferroelecric Ceramics with Field-Enforced Transitions: A New Nonlinear Circuit Element*. *Proc IRE*. 1961;1264-1267.
[8] Hanrahan B, Espinal Y, Neville C, et al. Accounting for the various contributions to pyroelectricity in lead zirconate titanate thin films. *J Appl Phys.* 2018;183:124104.

Chapter 8: Summary, Preliminary Results, and Future Work

Electrical Characterization in Context

ALD $PbTiO_3$ Summary

The best example of ALD PTO to use as a comparison to the present work[1] was reported by Hwang,[2] who reported the first use of the $Pb(DMAMP)_2$ lead precursor. The $Pb(DMAMP)_2$ precursor is the same one used in the present work, but Hwang used $Ti(O\textit{t}\text{-}Bu)_4$ as the Ti cation precursor instead of TDMAT.[2] One interesting note is that the GPC reported by Hwang for near-stoichiometric PTO is the same as reported for this work, 0.064 nm/cycle. Despite the similarity, the growth temperature was quite different; Hwang utilized a substrate temperature of 200 °C, while 250 °C was used in the present work. The relative number of PbO_x:TiO_x cycles was also quite different. For Hwang, a PbO_x:TiO_x cycle ratio of 3:4 yielded stoichiometric PTO, while 4:1 yielded stoichiometric PTO in the present work. Therefore, the similarity in GPC does not suggest that growth proceeded in identical fashion for each process, and that the precise agreement is most likely a coincidence. However it is likely that the steric hindrance of the $Pb(DMAMP)_2$ ligand contributed to the general similarity in GPC, limiting the growth rate. Steric hindrance is a chemisorption suppression effect that results from the limited areal packing density of precursor ligands, which are often larger than the cation species being deposited.

The ferroelectric figures of merit (FOM) for both process are summarized below in Table 8.1. Although a 1-to-1 comparison is not possible since the thicknesses differ

between the two studies, the FOM have been normalized to the applied electric field to improve the analysis. Generally, the FOM from the two studies were quite similar. The P_{max}, P_{r+}, and P_{r-} are all slightly higher in the present study compared to Hwang. The E_{c+} and E_{c-} are equivalent between the two studies to within ±10 kV/cm. The maximum measured ε_r was slightly higher in the present study (288) compared to Hwang (280) measured over a similar electric field range. By far the largest difference comes in the reported Tan δ and leakage current density, where the present work is remarkably better. The max Tan δ in the present work is reported to be 0.034 at -275 kV/cm, which was at the end of the tested electric field range (±275 kV/cm) for the capacitance-voltage testing. At a similar but somewhat smaller electric field, Hwang reported a Tan δ nearly three-times higher of 0.1. The asterisk denotes that the Tan δ reported by Hwang rose by an order of magnitude to 1.2 at ±384 kV/cm. In addition, the leakage current density reported by Hwang ($3x10^5$ μA/cm^2 at ±128 kV/cm) is 3-4 orders-of-magnitude higher than in the present work (16-212 μA/cm^2 at ±138 kV/cm).

Table 8.1: ALD PTO Ferroelectric FOM comparison (see above text for explanation of *)

Parameter	**This Work (Ch. 5)**[1]	**Hwang**[2]
Thickness	360 nm	78 nm
Composition	$Pb_{1.0}Ti_{1.0}O_{3.0}$	$Pb_{1.0}Ti_{1.0}O_{3.0}$
GPC	0.064 nm/cycle	0.064 nm/cycle
P_{max}	48 μC/cm^2 at 415 kV/cm	38 μC/cm^2 at 512 kV/cm
P_{r+}	34.6 μC/cm^2	30 μC/cm^2
P_{r-}	-36 .0 μC/cm^2	-25 μC/cm^2
E_{c+}	125 kV/cm	128 kV/cm
E_{c-}	-73 kV/cm	-92 kV/cm
Zero Field ε_r	255	270
Max ε_r	288 at -67 kV/cm	280 at 128 kV/cm
Min ε_r	196 at -496 kV/cm	190 at -385 kV/cm
Max Tan δ	0.034 at -275 kV/cm	0.1 at ±256 kV/cm*
Leakage Current Density +	16 μA/cm^2 at 138 kV/cm	3x10^5 μA/cm^2 at 128 kV/cm
Leakage Current Density -	212 μA/cm^2 at -138 kV/cm	3x10^5 μA/cm^2 at -128 kV/cm

There are a few possible explanations as to why the leakage current reported by Hwang is much higher than the present work. Other than the difference in thickness, the most notable difference between the two processes are the number of separate sets of ALD, followed by RTA. In the present work, four discrete sets of ALD and RTA were used to grow the 360 nm-thick PTO films. Hwang deposited the 78 nm-thick film in a single deposition, followed by RTA post-treatment. Local electrical conduction atomic force microscopy (LCAFM) scans of annealed ALD PTO reported by Hwang show that the film contained a large number of leakage sites that appeared to be randomly distributed

across the film, including a few sparsely dispersed leaky perovskite grains. Multiple sets of ALD followed by RTA likely create a circuitous leakage pathway, assuming the leakage sites are randomly distributed in each layer of the film (which we have not yet conclusively proven). In that scenario, the leakage pathway would not have the shunting effect that appears to be present in the PTO films grown by Hwang. Another large difference between the two studies is the ligand oxidation step. Hwang oxidized the ALD PTO films using H_2O as the oxidizer for each precursor, whereas the present work utilized both H_2O and ozone as co-oxidizers. Although it has been speculated that the ozone acts as an in-situ carbon-clean,[1] that appears to not be a primary differentiating factor between the two processes, since Hwang reported the carbon content to be less than 1 at% using H_2O alone, as measured by auger electron spectroscopy (AES).

Very few publications have been published for un-doped PTO with electrical properties over the past two decades. Most work has focused on doped variants of ALD PTO, or PTO-rich PZT for applications where tetragonal Pb-based ferroelectrics are attractive. Nonetheless, one example by Khan et al. of pure PTO grown by PLD is presented below for comparison.[3] The work by Khan, though not heavily cited, appeared to have comparable polarization properties and was grown at a thickness (530 nm) in a similar regime to the present ALD PTO. The PLD PTO films prepared by Khan had a substrate temperature of 530 °C. The films were annealed between 400-600 °C in O_2 for one-hour following the deposition. Cross-section SEM images indicated that the growth produced a dense, columnar grain structure. The perovskite phase was confirmed by XRD, and the film composition was quantified by energy dispersive X-ray

microanalysis (EDX). Ferroelectric properties obtained for PLD PTO were measured from a fabricated MIM capacitor (gold top electrode, Pt bottom electrode) and are summarized below in Table 8.2.

Table 8.2: ALD and PLD PTO Ferroelectric FOM comparison

Parameter	**This Work (Ch. 5)**[1]	**Khan**[3]
Thickness	360 nm	530 nm
Composition	$Pb_{1.0}Ti_{1.0}O_{3.0}$	$Pb_{1.0}Ti_{1.0}O_{3.0}$
P_{max}	48 μC/cm^2 at 415 kV/cm	60 μC/cm^2 at 250 kV/cm
P_{r+}	34.6 μC/cm^2	40 μC/cm^2
P_{r-}	-36 .0 μC/cm^2	-40 μC/cm^2
E_{c+}	125 kV/cm	100 kV/cm
E_{c-}	-73 kV/cm	-105 kV/cm
Zero Field ε_r	255	310
Max ε_r	288 at -67 kV/cm	Not Reported
Min ε_r	196 at -496 kV/cm	Not Reported
Max Tan δ	0.03 at -80 kV/cm	Not Reported
Leakage Current Density +	16 μA/cm^2 at 138 kV/cm	1.3x10^5 μA/cm^2 at 138 kV/cm (tested at 85 °C)
Leakage Current Density -	212 μA/cm^2 at -138 kV/cm	Not Reported

The P_{max} reported by Khan (60 μC/cm^2 at 250 kV/cm) is a bit higher than the P_{max} reported in the present work (48 μC/cm^2 at 415 kV/cm). However, the P_{max} reported by Khan may be distorted by an unusually high leakage current, which will be evaluated in the next paragraph. The remanent polarizations, P_{r+} and P_{r-}, reported by Khan are 5.6 and 4.0 μC/cm^2, respectively, higher than the present work. Both of the coercive fields, E_{c+} and E_{c-}, reported by Khan fall within ±20 kV/cm of the present work. The reported

zero-field dielectric constant, ε_r, of 310 was slightly higher than that reported here (255). The dielectric constant tuning range wasn't reported, and thus neither was the variation of Tan δ with electric field. The Tan δ was not reported directly most likely because it was extremely high due to excessive leakage. Khan notes that the "leakage current was substantial above 10 kHz", with respect to the polarization/electric-field loops. That is troubling, because the polarization/electric-field ALD PTO films in the present work were performed at 100 Hz, and leakage current is typically more pronounced at lower frequencies. Furthermore, the reported leakage current density of $1.3x10^5$ $\mu A/cm^2$ at 138 kV/cm is three orders of magnitude higher than the present work. Even taking into account the fact that the leakage current reported by Khan was for films heated to 85 °C, it is still far too high. The author acknowledges that, "the conductivity contributes to the high value of permittivity at room temperature." The conductivity also manifests in the P/E loops, which is why the reported P_{max}, P_{r+}, and P_{r-} skew to slightly larger values compared to the ALD PTO presented here. Nested P/E loops tested over a wide range of frequencies would have helped to untangle the polarization contributions from ferroelectricity and resistive leakage. It is noteworthy that the leakage current density reported by Khan[3] more closely matches the leakage current density reported by Hwang[2] than the current work.

The current work does not represent the first instance of PTO grown by ALD, nor does it represent the first use of the $Pb(DMAMP)_2$ precursor. However, (after a thorough search of the literature) the current work represents the largest remanent polarization for PTO grown by ALD to date, and marks a big step forward towards the drastic reduction of the leakage current and Tan δ. The mechanism of improvement is

speculated to be primarily due to the multiple coats/anneal method. More work is required to determine if the multiple coats/anneal method would work to reduce the leakage current for thinner films on the order of 50-100 nm, which could be desirable for FRAM applications.

ALD $PbZr_xTi_{1-x}O_3$ Summary

To date, only one report of PZT grown by ALD has been demonstrated to have ferroelectric FOM comparable to the present work. Watanabe previously reported PZT grown by ALD using the β-diketonate precursors $Pb(TMHD)_2$ and $Zr(DIBM)_4$ as the Pb and Ti cation precursors, respectively, and TTIP (an alkoxide) as the Ti precursor.[4] The films were deposited at a substrate temperature of 240 °C and were annealed by RTA at 400 °C for 30 min., followed by 700 °C for 10 min. in O_2 to crystallize them into the perovskite phase. The films characterized by Watanabe[4] do not provide a 1:1 comparison to the present work for a couple of reasons. First, the films grown by Watanabe were more Zr-rich and had a Zr:(Zr+Ti) ratio of 47:53, which is close-to but not exactly at the MPB. Second, the film was 70 nm-thick, which is thinner than the film reported in the present work (which is 200 nm-thick). With these differences in mind, the ferroelectric FOM are reported below in Table 8.3.

Table 8.3: ALD PZT Ferroelectric FOM comparison (* reported as $2P_r$ or $2E_c$)

Parameter	**This Work (Ch. 6)**	**Watanabe[4]**
Thickness	200 nm	70 nm
Composition	$Pb_{1.07}Zr_{0.24}Ti_{0.76}O_{3.7}$	$Pb_{1.20}Zr_{0.47}Ti_{0.53}O_x$
GPC	0.071 nm/cycle	Not directly reported
P_{max}	57 μC/cm^2 at 944 kV/cm	50 μC/cm^2 at 857 kV/cm
P_{r+}	26 μC/cm^2	12 μC/cm^2*
P_{r-}	-27 μC/cm^2	12 μC/cm^2*
E_{c+}	170 kV/cm	100 kV/cm *
E_{c-}	-150 kV/cm	100 kV/cm*
Zero Field ε_r	500	Not Reported
Max ε_r	552 at -67 kV/cm	Not Reported
Min ε_r	219 at -496 kV/cm	Not Reported
Max Tan δ	0.03 at -80 kV/cm	Not Reported
Leakage Current Density +	0.5 μA/cm^2 at 250 kV/cm	Not Reported
Leakage Current Density -	0.7 μA/cm^2 at -250 kV/cm	Not Reported

Unfortunately, the dielectric constant, Tan δ, and leakage current weren't reported. One mention of leakage current arises in the following discussion from Watanabe[4] of the polarization/electric-field loops, "clear hysteresis loops were not observed for other PZT films, which were prepared by (Pb–O)–2(Zr–O)–(Ti–O) or (Pb–O)–(Zr–O)–(Ti–O) sequences and have a lower Zr/(Zr + Ti) ratio due to larger leakage currents", which qualitatively indicates that the majority of films were too leaky to measure. The P_{max} reported by Watanabe of 50 μC/cm^2 is 7 μC/cm^2 lower than the present work, though it should be noted that P_{max} is not a reliable ferroelectric FOM if the leakage current is high. The remanent polarization reported by Watanabe (±12 μC/cm^2) matches that of

comparable sol-gel films grown with a similar composition[5,6] more closely than those measured in the present work (see Table 8.4 below). The reported E_{c+} and E_{c-} match the present work to within ±35 kV/cm, but overall the coercive field matches better to prior reports of ALD PTO.[1,2] The differences in films composition (MPB versus PTO-rich) and thickness (70 nm versus 200 nm) limit the usefulness of the head-to head comparison presented here. In addition, the lack of quantitative leakage current measurements and Tan δ make it especially difficult to compare the overall electrical quality of the films.

Table 8.4: ALD PZT Ferroelectric FOM comparison to sol-gel (*Different Samples, **Esimate from bar graph[6])

Parameter	**This Work (Ch. 6)**	**Sanchez[5,6]**
Thickness	200 nm	500 nm (approx.)
Composition	$Pb_{1.07}Zr_{0.24}Ti_{0.76}O_{3.7}$	$Pb_xZr_{0.52}Ti_{0.48}O_y$
P_{max}	57 μC/cm^2 at 944 kV/cm	50 μC/cm^2 at 857 kV/cm
P_{r+}	26 μC/cm^2	12.2 to 15.9 μC/cm^2
P_{r-}	-27 μC/cm^2	-12.2 to -15.9 μC/cm^2
E_{c+}	170 kV/cm	10 to 60 kV/cm
E_{c-}	-150 kV/cm	-10 to -60 kV/cm
Zero Field ε_r	500	988 to 1354
Max ε_r	552 at -67 kV/cm	1354* (Zero-Field)
Min ε_r	219 at -496 kV/cm	425* (Unknown Field)
Max Tan δ	0.03 at -80 kV/cm	0.03 at -30 kV/cm*
Leakage Current Density +	0.5 μA/cm^2 at 250 kV/cm	0.1 to 4 μA/cm^2 at 200** kV/cm
Leakage Current Density -	0.7 μA/cm^2 at -250 kV/cm	Not Reported

Given the overall dearth of reports in the literature of comparable electrical properties for ALD PZT, it is useful to make comparison to well-known technologically useful PZT grown by other methods. Two such examples have been selected. First, Table 8.4 presents a head-to-head comparison of ALD PTO-Rich PZT to sol-gel PZT deposited near the MPB.[5,6] Sol-gel PZT provides a useful comparison because of the previously demonstrated application to MEMS,[5,6] and provides the additional comparative bonus of having been grown in the same facility (Specialty Electronic Materials and Sensors Cleanroom, U.S. Army Research Laboratory, Adelphi, MD, USA) using similar process technology. In addition, the sol-gel films, like the ALD films, are not crystallized into the perovskite phase until post-deposition annealing. However, though the difference in composition and thickness limit a 1:1 comparison, it is useful to judge the relative film quality by comparing Tan δ and leakage current density. Note that the values presented for sol-gel PZT were not obtained from a single sample, but rather a collection of samples analyzed in Refs. [5] and [6]. As presented in Table 8.4, the max Tan δ of 0.03 for the ALD PZT in this work is identical with that in the sol-gel study. Both were tested at the same frequency (10 kHz) but the electric field for the sol gel measurements was about one third that for the ALD PZT measurements. The leakage current density reported in the present work (0.5-0.7 $\mu A/cm^2$) is at the low end of the range reported for similar electric fields in the sol-gel PZT work, and an order of magnitude below the sol-gel PZT measurements' upper bound of 4 $\mu A/cm^2$. Perhaps surprisingly, the ALD PZT performs well electrically compared to the sol-gel PZT, given the relatively minimal process optimization compared to the latter.

Finally, a direct comparison between PTO-Rich PZT grown by ALD and PTO-Rich PZT grown by MOCVD is presented in Table 8.5. The MOCVD FOM are from PZT that is used in the TI commercial FRAM process.[7,8] A near 1:1 comparison can be made, because other than the deposition technique the only substantial difference between the two films is the thickness which differs by a little less than a factor of three. First, it is noted that the films have nearly identical Zr:Ti cation ratios. Second, although the P_{max} reported in the present work (57 $\mu C/cm^2$) is much higher than that reported by Rodriguez (38 $\mu C/cm^2$),[8] the test range of the electric field (±215 kV/cm) was much lower than the present work (±944 kV/cm). The polarization obtained in the present work at the same electric field (215 kV/cm) yields 41 $\mu C/cm^2$, which is only 3 $\mu C/cm^2$ higher than that reported by Rodriguez, [8] and provides a more accurate comparison. The P_{r+} (26 $\mu C/cm^2$) and P_{r-} (-27 $\mu C/cm^2$) reported in the present work compares favorably to that reported by Rodriguez (±20 $\mu C/cm^2$).[8] However, the coercive field is much larger for the ALD PZT presented in the current work compared to the MOCVD PZT. Low coercive field values lead to lower operating voltages for FRAM devices, so in this case large values are comparatively worse. The large difference in coercive field may be explained by grain size differences. It has been previously shown that the coercive field increases as grain size decreases for ferroelectric $BiFeO_3$ films with nanocrystalline grains.[9] The reason is reportedly due to the fact that the grain boundary density increases as the grain size decreases, and the grain boundaries provide an energy barrier for domain wall motion. [9] A similar effect may be present in the current work. Although the PZT grown by MOCVD appeared to have columnar grains,[7] the ALD PZT did not. Although a clear picture of the grain

structure wasn't obtained for ALD PZT, the grain structure of ALD PTO showed that the annealed films exhibited a range of grain sizes from 10-50 nm in diameter, which is significantly smaller than the MOCVD PZT grains. Residual carbon cannot be ruled out as a contributor to domain wall impingement for the ALD PZT films, and may also partly explain the difference in coercive field. The leakage current density reported by Aggarwal[7] appears to fall within the range of 0.1 to 10 μA/cm^2 at 215 kV/cm. For obvious reasons, the exact process conditions (thus the exact leakage current) for the production line wasn't disclosed in the report,[7] however a range of representative values was reproduced in Table 8.5 for comparison. Even at the low end of the leakage current reported by Aggarwal,[7] the ALD PZT falls within the same order of magnitude. This is extremely promising since the MOCVD PZT is known to be of exceptionally high-quality and is used in a commercial Fab-line. It is important to note that this favorable comparison only covers some, but not all ferroelectric properties of interest. The fatigue properties of the ALD PZT were not tested, nor was the breakdown strength. Further testing is naturally required to fully evaluate the capabilities of ALD PZT.

Table 8.5: ALD PZT Comparison to MOCVD

Parameter	**This Work (Ch. 6)**	**Aggarwal,[7] Rodriguez[8]**
Thickness	200 nm	70 nm
Composition	$Pb_{1.07}Zr_{0.24}Ti_{0.76}O_{3.7}$	$Pb_xZr_{0.25}Ti_{0.75}O_y$
P_{max}	57 μC/cm^2 at 944 kV/cm 41 μC/cm^2 at 215 kV/cm	38 μC/cm^2 at 215 kV/cm
P_{r+}	26 μC/cm^2	20 μC/cm^2
P_{r-}	-27 μC/cm^2	-20 μC/cm^2
E_{c+}	170 kV/cm	70 kV/cm

E_{c-}	-150 kV/cm	-70 kV/cm
Zero Field ε_r	500	Not Reported
Max ε_r	552 at -67 kV/cm	Not Reported
Min ε_r	219 at -496 kV/cm	Not Reported
Max Tan δ	0.03 at -80 kV/cm	Not Reported
Leakage Current Density +	0.5 $\mu A/cm^2$ at 250 kV/cm	0.1 to 10 $\mu A/cm^2$ at 215 kV/cm
Leakage Current Density -	0.7 $\mu A/cm^2$ at -250 kV/cm	Not Reported

In summary, the ALD PZT presented in this work compare favorably to PZT deposited by alternative ALD processing and other methods such as sol-gel and MOCVD. The electrical characterization of the ALD PZT films presented here is far more comprehensive than that reported previously by Watanabe.[4] In addition, the ALD PZT process presented in this work represents the clearest case of self-limited growth behavior to date. The non-saturating behavior of the $Pb(TMHD)_2$ precursor demonstrated by Watanabe[4,10] alongside the non-saturating behavior of the TTIP precursor,[10] raise questions regarding the thermal stability of the combination of β-diketonate and Ti-alkoxide precursors. The other reports utilizing $Pb(TMHD)_2$ as the Pb-precursor did not contain precursor-dose uptake curves, nor was uniform deposition demonstrated on 3D-features.[11,12] In the present case, 20 μm-wide by 45 μm-deep trenches were coated with a uniform PZT coating with minimal process optimization.

ALD $PbHfO_3$ Summary

There does not appear to be a prior report of a pure lead hafnate thin-film deposited by any technique. Accordingly, no materials are available for a 1:1 comparison. On the

other hand, lead zirconate is more widely studied and exhibits many similar properties to lead hafnate, though the number of overall reports is still small compared to PZT. Unfortunately, the only other prior report of lead zirconate grown by ALD contained no electrical characterization.[13] A prior report by Zhai nicely details the ferroelectric switching behavior of antiferroelectric (AFE) PZO grown by sol-gel at various thicknesses, and will be used as the first comparison.[14] Table 8.6, shown below, details the differences between the ALD-grown PHO compared to PZO grown by sol-gel. Although some material properties were reported for 200 nm-thick films, the 900 nm-thick films were more comprehensively analyzed. The reason the 200 nm-thick film wasn't analyzed in detail is because the PZO at that thickness displayed an unusually high E_F of 790 kV/cm, which is denoted in Table 8.6.

Table 8.6: ALD PHO Comparison to sol-gel

Parameter	**This Work (Ch. 7)**	**Zhai[14]**
Thickness	202 nm	900 nm
Composition	$Pb_{1.08}HfO_{2.9}$	PZO (not measured)
P_{max}	32.9 at 579 kV/cm	23 μC/cm^2 at 550 kV/cm
E_A-	-282 kV/cm	-280 kV/cm
E_F-	-386 kV/cm	-500 kV/cm
E_{A+}	272 kV/cm	280 kV/cm
E_{F+}	371 kV/cm	500 kV/cm
		(790 kV/cm for 200 nm-thick film)
Total Energy Storage	8.3e-8 J	Not Reported
2-D Energy Density	.00017 J/cm^2	Not Reported
Energy Per Unit Volume	8.4 J/cm^3	Not Reported

There is surprising agreement (a difference of 8 kV/cm) in E_A (the ferroelectric back-to antiferroelectric phase transition) between the 900 nm-thick films PZO characterized by Zhai and the 202 nm-thick PHO films characterized in the present work. The PZO films switched from antiferroelectric to ferroelectric at more than 100 kV/cm higher electric-field magnitude than the PHO reported in the present work. From an energy storage (dielectric, capacitive) standpoint, an antiferroelectric material that exhibits a field-induced ferroelectric phase-transition like PZO and PHO will have greater energy loss the greater the difference between E_F (the field onset of the phase transition to ferroelectric) and E_A. Therefore, the PHO tested in the present work can be expected to have lower energy loss than the referenced PZO.[14] The maximum polarization of the PHO is also approximately 10 $\mu C/cm^2$ higher than the referenced PZO at a similar electric field, which indicates that a greater energy storage capacity is expected per unit electric field. Although the energy storage density was not directly reported, the reported antiferroelectric FOM indicates that the ALD-grown PHO can be expected to have a greater energy storage capacity per unit electric-field and lower energy loss than the reference PZO grown by sol-gel. It should be noted that one key figure of merit for capacitive energy storage is the dielectric breakdown strength, which was not reported for PHO (this work) nor PZO.[14]

Much attention has been given to both ferroelectric and antiferroelectric $Hf_xZr_{1-x}O_2$ (HZO) and doped variants grown by ALD in recent years.[15] Depending on the Hf:Zr ratio and the dopant/concentration, the HZO films may adopt a ferroelectric or antiferroelectric structure. One such example of antiferroelectric $Hf_{0.2}Zr_{0.8}O_2$ that exhibits a field induced ferroelectric phase transition is presented by Park et al.[15] The

9.2 nm-thick $Hf_{0.2}Zr_{0.8}O_2$ films were grown by ALD and sandwiched between two ~10 nm-thick TiN electrodes that were deposited by DC reactive sputtering. The stack was then annealed by RTA at 500 °C for 30-s in an N_2 environment. The antiferroelectric figures of merit were adapted from polarization hysteresis loops published by Park, and are tabulated below in Table 8.7.[15]

Table 8.7: ALD PHO Comparison to ALD $Hf_{0.2}Zr_{0.8}O_2$

Parameter	**This Work (Ch. 6)**	**Park [15]**
Thickness	202 nm	9.2 nm
Composition	$Pb_{1.08}HfO_{2.9}$	$Hf_{0.2}Zr_{0.8}O_2$
P_{max}	32.9 at 579 kV/cm	25 μC/cm^2 at 3 MV/cm
E_A-	-282 kV/cm	-0.5 MV/cm
E_F-	-386 kV/cm	-2.5 kV/cm
E_{A+}	272 kV/cm	0.5 MV/cm
E_{F+}	371 kV/cm	2.5 MV/cm
Total Energy Storage	8.3e-8 J	Not Reported
2-D Energy Density	.00017 J/cm^2	Not Reported
Energy Per Unit Volume	8.4 J/cm^3 at 579 kV/cm	35 J/cm^3 at 4 MV/cm 1 J/cm^3 at 500 kV/cm

It is immediately of note that Park's $Hf_{0.2}Zr_{0.8}O_2$ films were far thinner than the PHO films presented in the present work. One consequence of that is that larger electric fields were applied to the $Hf_{0.2}Zr_{0.8}O_2$ films at lower voltages. The P_{max} reported for PHO is 7.9 μC/cm^2 higher than that reported by Park for $Hf_{0.2}Zr_{0.8}O_2$ and was obtained at a far lower applied field (579 kV/cm versus 3 MV/cm). The reported E_A and E_F values of the $Hf_{0.2}Zr_{0.8}O_2$ are much larger than those reported for the present PHO, possibly due to substrate clamping effects. The difference between E_A and E_F for the PHO is much

less (100 kV/cm) than the difference for $Hf_{0.2}Zr_{0.8}O_2$ (2 MV/cm), which implies the unrecoverable energy due to polarization switching is much smaller for PHO compared to $Hf_{0.2}Zr_{0.8}O_2$. At similar electric fields, the recoverable energy storage density of the PHO is 8.4 J/cm^3 at 579 kV/cm, which is a factor of 8 higher than $Hf_{0.2}Zr_{0.8}O_2$, which is 1 J/cm^{3}at 500 kV/cm. However, the overall energy storage of the $Hf_{0.2}Zr_{0.8}O_2$ (35 J/cm^3) was larger by a factor of 4 because much larger fields (4 MV/cm compared to 579 kV/cm) were more readily applied to the 9.2 nm-thick $Hf_{0.2}Zr_{0.8}O_2$ film. Overall, the films grown by Park displayed better energy storage characteristics compared to the PHO in the present work. One outstanding question is whether the PHO can be grown thinner and still maintain the large P_{max} and relatively lower E_A and E_F. The comparably larger P_{max} indicates that the ALD PHO has the potential for greater energy storage compared to $Hf_{0.2}Zr_{0.8}O_2$ if the breakdown strength is maintained at similar (~10 nm) thicknesses.

ALD $PbHf_xTi_{1-x}O_3$ Summary

To date, few studies of lead hafnate-titanate (PHT) exist in the literature, and there are no prior reports of PHT grown by ALD. Two useful literature comparisons are presented here of PHT grown by other methods. It may also be useful to compare the ALD (near-MPB) PHT to the near MPB PZT sol-gel films (Table 8.4) or near MPB ALD PZT films (Table 8.3), but for this section the discussion is limited to PHT. Fantozzi fabricated bulk-like PHT samples (near the MPB) using a sintering method. The ferroelectric characterization did not include polarization hysteresis loops, but did contain piezoelectric characterization, dielectric constant, and Tan δ measurements. The FOM are summarized below in Table 8.8.

Table 8.8: ALD PHT Comparison to bulk sintered ceramic

Parameter	**This Work (Ch. 7)**	**Fantozzi[16]**
Thickness	225 nm	1 mm (bulk ceramic)
Composition	$Pb_{0.82}Hf_{0.47}Ti_{0.53}O_{2.99}$	$PbHf_{0.5}Ti_{0.5}O_3$
P_{max}	36 μC/cm^2 at 840 kV/cm	Not Reported
P_{r+}	8.7 μC/cm^2	Not Reported
P_{r-}	-7.0 μC/cm^2	Not Reported
E_{c+}	84 kV/cm	Not Reported
E_{c-}	-100 kV/cm	Not Reported
Zero Field ε_r	550	820
Max ε_r	580 at 46 kV/cm	Not Reported
Min ε_r	252 at 444 kV/cm	Not Reported
Max Tan δ	0.022 at -40 kV/cm	0.008 at Low Field
d_{33}	Not Reported	140 pC/N
Leakage Current Density +	0.64 μA/cm^2 at 222 kV/cm	Not Reported
Leakage Current Density -	0.65 μA/cm^2 at -222 kV/cm	Not Reported

The low zero (or low-field) ε_r of the ALD PHT is lower (550) than that reported in the bulk sample (820). This may be a result of the Pb-deficiency reported in the ALD PHT sample (Pb subscript = 0.82), but at this point that is a speculative claim. Although not reported for the ALD PHT film presented in the current work, the d_{33} reported for the bulk PHT was reported by Fantozzi to be 140 pC/N, which puts it in the range of PZT grown near the MPB.[16] The high d_{33} demonstrates that PHT may be promising for piezoelectric applications. The Tan δ reported for the ALD PHT (0.022) was three times higher than the Tan δ reported for the bulk PHT (0.008), but each of those values

are extremely low overall, and compare favorably to the other perovskites reviewed in this chapter.

Schorn et al. demonstrated a sol-gel process for thin-film PTO-rich PHT with FRAM application in mind.[17] Although the dielectric constant, Tan δ, and leakage current were not reported, polarization hysteresis loops were presented, and the FOM are presented below in Table 8.9. The difference in composition prevents a 1:1 comparison. However, the thickness similarity provides a useful benchmark. The sol-gel PTO-rich PHT displayed higher P_{max} and remanent polarization than the ALD near-MPB PHT, though the coercive fields were identical to within ± 10 kV/cm. The PTO-rich PHT properties appeared to be more closely aligned with the ALD PTO properties reported in Table 8.1 than to the MPB-PHT properties reported in Table 8.9. This implies that the composition is a strong driving factor behind the ferroelectric properties of PHT.

Table 8.9: ALD PHT Comparison to sol-gel

Parameter	**This Work (Ch. 7)**	**Schorn[17]**
Thickness	225 nm	140 nm
Composition	$Pb_{0.82}Hf_{0.47}Ti_{0.53}O_{2.99}$	$PbHf_{0.3}Ti_{0.7}O_3$
P_{max}	36 $\mu C/cm^2$ at 840 kV/cm	45 $\mu C/cm^2$ at 350 kV/cm
P_{r+}	8.7 $\mu C/cm^2$	31.2 $\mu C/cm^2$
P_{r-}	-7.0 $\mu C/cm^2$	-31.2 $\mu C/cm^2$
E_{c+}	84 kV/cm	70 kV/cm
E_{c-}	-100 kV/cm	-105 kV/cm
Zero Field ε_r	550	Not Reported
Max ε_r	580 at 46 kV/cm	Not Reported
Min ε_r	252 at 444 kV/cm	Not Reported
Max Tan δ	0.022 at -40 kV/cm	Not Reported
Leakage Current Density +	0.64 $\mu A/cm^2$ at 222 kV/cm	Not Reported
Leakage Current Density -	0.65 $\mu A/cm^2$ at -222 kV/cm	Not Reported

ALD Growth Models

This subsection provides tentative growth models for the ALD-grown PTO, PZT, PHO and PZT. Each of these processes may be considered part of the same family, consisting of the 4+ cation (Ti, Zr, Hf) alkyl-amide precursors paired with the $Pb(DMAMP)_2$ precursor, and co-oxidized by H_2O and ozone. The growth models presented here are deduced primarily from TEM images, GPC correlations, and chemical composition data. In the future, an effort will be made to calculate the exact reaction mechanisms,

free-energy differences, and activation energies corresponding to each step, but that is beyond the scope of this work.

ALD $PbTiO_3$ Model

Figure 8.1 (A-I) shown below contains a graphical representation of the ALD PTO process during the middle of a typical growth. For simplicity, the PTO nucleation on the Pt substrate is omitted from the discussion at this time. The growth proceeds according to the labeled blocks in alphabetical order. Block A (Fig. 8.1) displays a freshly deposited TiO_x surface (labelled as Ti-O). The two protruding aspherical caps are due to underlying PbO_x nuclei from the prior supercycle buried beneath the current TiO_x layer. The $Pb(DMAMP)_2$ dose proceeds in block B, where the Pb-precursor readily chemisorbs on the TiO_x surface. The ease of chemisorption is evidenced by the fact that the growth rate of stoichiometric PTO (0.064 nm/cycle) is higher than the growth rate of either component oxide (0.02 nm/cycle for PbO_x,[2] 0.04 nm/cycle for TiO_x[18]) and that the in-situ ellipsometry showed no nucleation delay for the PbO_x cycle during the PTO super-cycle. Following ligand oxidation, the PbO_x species are shown on the TiO_x surface in block C. In this model, PbO does not wet TiO_x, leading to a growth mode similar to Volmer-Weber.[19] Indeed, based upon the balance of surface and interface tensions, if TiO_x wets PbO, at least in equilibrium.[20]

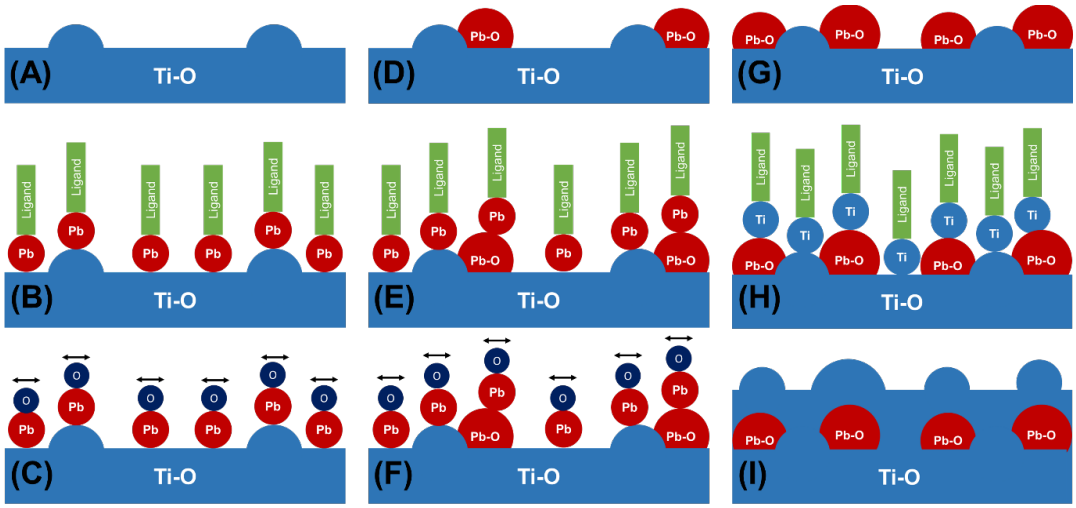

Figure 8.1: Growth Model for ALD PTO

The black arrows (Fig. 8.1 block C) are to indicate that the PbO_x species are free to diffuse along the surface of the TiO_x at a growth temperature of 250 °C. A previous study by Buhlmann et al. provides the activation energy of PbO diffusion across a TiO_2 surface (E_D=800 meV) as well as the hopping vibration frequency of PbO (υ=10^{12} Hz).[21] For the purposes of the following simple treatment, the PbO_x species is assumed to belong to Massicot PbO as suggested by XRD, and which was previously identified in Chapter 5 as the dominant PbO_x species in the as-grown films. The successful hopping rate for the lead oxide molecule to go from an occupied site and other (available) sites may then be given by the following relation (adapted from reference [22]):

$$\Gamma = \upsilon e^{\frac{-E_D}{k_B T}} \qquad \text{Equation 8.1}$$

where k_B is Boltzmann's constant, and T is the temperature. The root-mean-squared displacement is given by:

$$Displacement\ (RMS) = a * \sqrt{\Gamma t} \qquad \text{Equation 8.2}$$

where *a* is the hopping distance, and *t* is time. In this case, *a* is not precisely known but can be assumed to be in the range of 3-5 Å. The variation of RMS displacement with hopping distance and time is plotted below in Fig. 8.2.

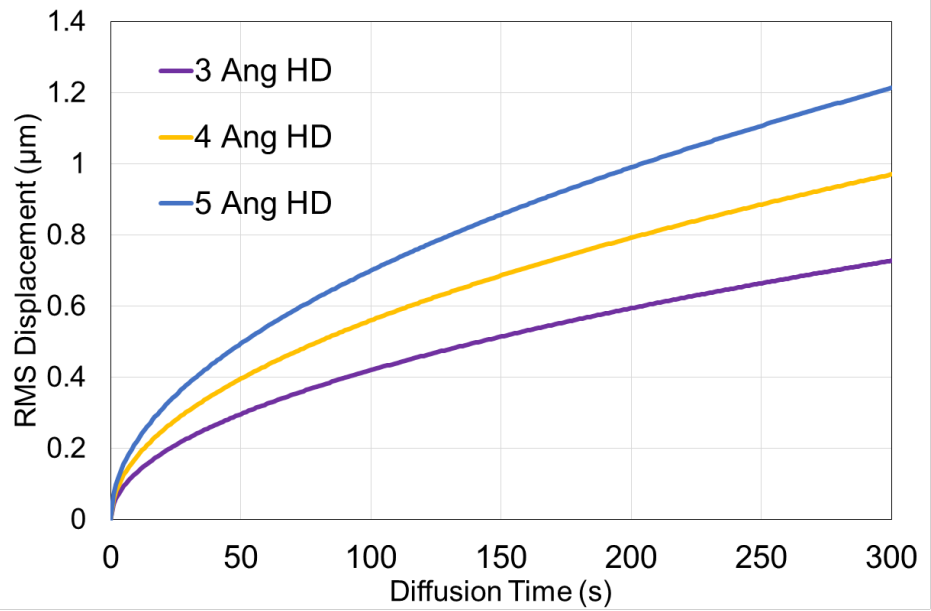

Figure 8.2: RMS displacement of surface-bound PbO at hopping distances (HD) of 3, 4, and 5 Å, respectively.

For reference, the unit cell length of PTO and PZT is approximately 4.0 Å. The RMS displacement is plotted as a function of unit time up to 300-s at the deposition temperature T = 250 °C (Fig. 8.2). In this work, one complete Pb-O ALD cycle was performed in 72-s. For a typical PTO super-cycle, four Pb-O cycles are repeated sequentially which add up to 288-s total. This simple model illustrates the high surface mobility of surface-bound PbO species (approximately 0.5-2 µm RMS displacement for a diffusion time of 72-s) within the time scale of the four sequential Pb-O cycles. The total distance traveled is much larger, as is depicted in Fig. 8.3 below. In reality, it is not likely the PbO species travel that far since the PbO is expected to form a stable cluster that moves more slowly. The diffusion may also be influenced by other factors.

First, the chemical potential of the TiO_x surface is not expected to be invariant due to expected differences in TiO_x bond energy in close proximity to (or on top of) PbO_x domains. Second, surface roughness and chemical defects (C, N, OH) can be expected to serve at heterogeneous nucleation sites for the PbO crystallites.[23] The STEM images presented in Chapter 5 indicated that the PbO nuclei were 2-5 nm in diameter. The Scherrer formula provided an estimate of the PbO_x crystallite sizes, which were calculated to be between 5-8 nm (in reasonable agreement with the STEM Image). The 3D PbO nuclei are depicted in Fig. 8.1 D. We postulate that the domains might nucleate near protrusions which mark buried PbO crystallites, either due to coordination at protrusion edges, or possibly due to strain fields, an effect known to cause diffusional bias of adatoms to surface strain minima.[24]

Taking the total thickness deposited per PbO_x cycle (0.032 nm, assumed to be half of the GPC of PTO), the number of PbO molecules deposited per unit area (per PbO_x cycle) may be estimated. As a first-order estimate, the PbO molecules are assumed to be spherical for the purposes of calculating the surface area coverage. Taking the diffusion length shown in Fig. 8.3 times the PbO molecule size yields the total area traversed by a single PbO molecule. The number of PbO molecules intercepted by a single diffusing PbO molecule can be estimated by taking the total area traversed by a single PbO molecule times the area density of deposited PbO molecules. The estimated number of PbO molecules intercepted in the diffusion path is shown in Fig. 8.4, which approximates the first PbO_x ALD cycle on a freshly deposited TiO_x layer. Taking a hopping distance of 4 Å leads to at least one PbO molecule interaction over the duration (72-s) of a single PbO_x cycle (Fig. 8.4). The number of PbO molecules (or clusters)

intercepted is expected to increase with each subsequent PbO_x cycle since the amount of surface-bound PbO increases as well as the overall diffusion time. In summary, the preceding simple treatment shows that the PbO molecules will travel an RMS distance of approximately 0.5 µm across the TiO_x surface and are likely to intercept at least one PbO molecule or cluster along the diffusion path in the timeframe of one PbO_x ALD cycle.

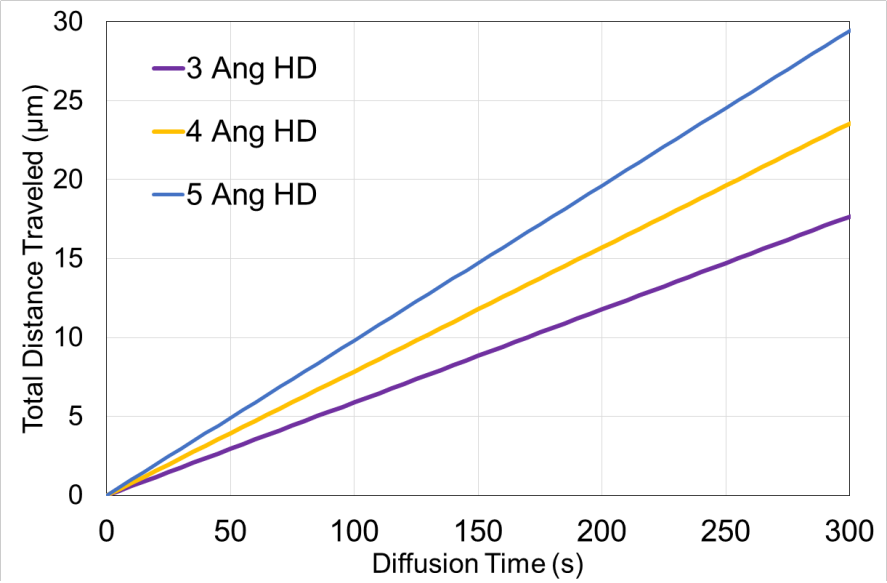

Figure 8.3: Total distance traveled by surface-bound PbO molecules at hopping distances (HD) of 3, 4, and 5 Å, respectively.

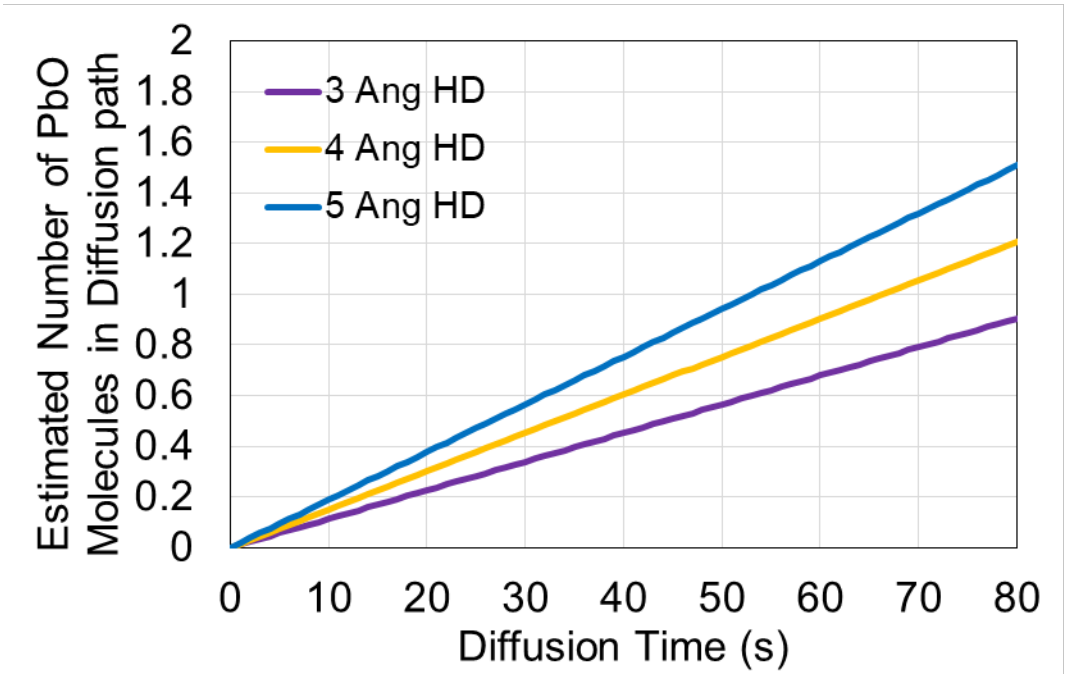

Figure 8.4: Estimated number of molecules intercepted along PbO diffusion path.

An alternative growth model that might be used to explain the presence of nm-scale PbO_x nuclei in the as-deposited PTO films is a defect-initiated nucleation of islands, followed by film coalescence, similar to that observed for ALD Pt.[25] However, this mode of growth does not match the observed behavior for PbO_x. The growth of Pt films proceeds by an initial nucleation of islands, followed by coalesce of the islands into a continuous film. Prior to coalescence, the film growth rate increases with each sequential cycle because it scales with the crystallite size. For PTO growth, the overall growth rate goes down as the relative number of PbO_x cycles increases (0.080 nm/cycle for 1:1 and 0.064 nm/cycle for 4:1, respectively). This implies that a significant portion of the $Pb(DMAMP)_2$ chemisorption occurs on the TiO_x underlayer, rather than on the PbO_x crystallites, which is reflected in Fig. 8.1 E. Thus, the 2D island nucleation and growth mode is ruled out for ALD PTO. Figure 8.1 blocks F and G display that

additional PbO cycles cause new PbO nuclei to form, as well as grow additional nuclei. Figure 8.1 blocks H and I show that the Ti-precursor (TDMAT) sticks to both the TiO_x underlayer and the PbO nuclei, and ultimately encapsulate PbO nuclei. The film surface is now restored to a similar chemistry as Fig. 8.1 block A (which is a requirement for ALD), and Fig. 8.1 block I generally reflects the STEM image of as-deposited ALD PTO.

ALD $PbZr_xTi_{1-x}O_3$ Model

The ALD PZT process is similar to the ALD PTO process, with the addition of the Zr precursor, TDMAZ. The major difference between the two processes is that the TDMAZ precursor is inherently limited to about 4.5 at.% incorporation. The ALD PZT process is detailed in Fig. 8.5 shown below. Figure 8.5 blocks A-G proceed identically to the PTO process (Fig. 8.1). Figure 8.5 block H indicates that the TDMAZ precursor sticks to available TiO_x chemisorption sites and does not stick to PbO nuclei sites. This is informed primarily due to the much lower deposition rate of the PZO super-cycle (0.011 nm/cycle) compared to either the binary process for PbO (0.02 nm/cycle)[2] or ZrO_2 (0.093 nm/cycle),[26] and because the TDMAZ chemisorption shows a lower apparent thickness increase on the in-situ ellipsometer (2 nm) than TDMAT (3 nm). It is not currently known whether the TDMAZ does not stick to the PbO nuclei outright, or if the growth is significantly suppressed. For simplicity, it is shown as not sticking. Figure 8.5 block I shows that the ZrO_x covers the available TiO_x sites. The TDMAZ poisons the surface for itself, but not for PbO_x as is detailed in Chapter 7 by the chemical composition data of several alternative dose sequences. Figure 8.5 block J indicates that the $Pb(DMAMP)_2$ chemisportion proceeds uninhibited by the ZrO_x layer, which is

indicated by the thickness increase shown by the in-situ ellipsometer following a Zr-O cycle. Figure 8.5 blocks K and L show that the PbO is expected to nucleate in a similar manner to that on the PTO, although the activation energy of diffusion is expected to be slightly different. Nonetheless, the presence of PbO_x nuclei was confirmed by Watanabe et al.[4] in a prior attempt to grow PZT by ALD, so the PbO growth mechanism is not expected to be grossly different on ZrO_x compared to TiO_x. Finally, blocks M and N (Fig. 8.5) show that the TDMAT sticks to the ZrO_x and the PbO nuclei, encapsulating both species. This is indicated by the similarity in apparent thickness increase due to the TDMAT chemisorption following either PTO or PZO cycle. The growth surface shown by blocks A and N (Fig. 8.5) are quite similar, which is expected for an ALD process.

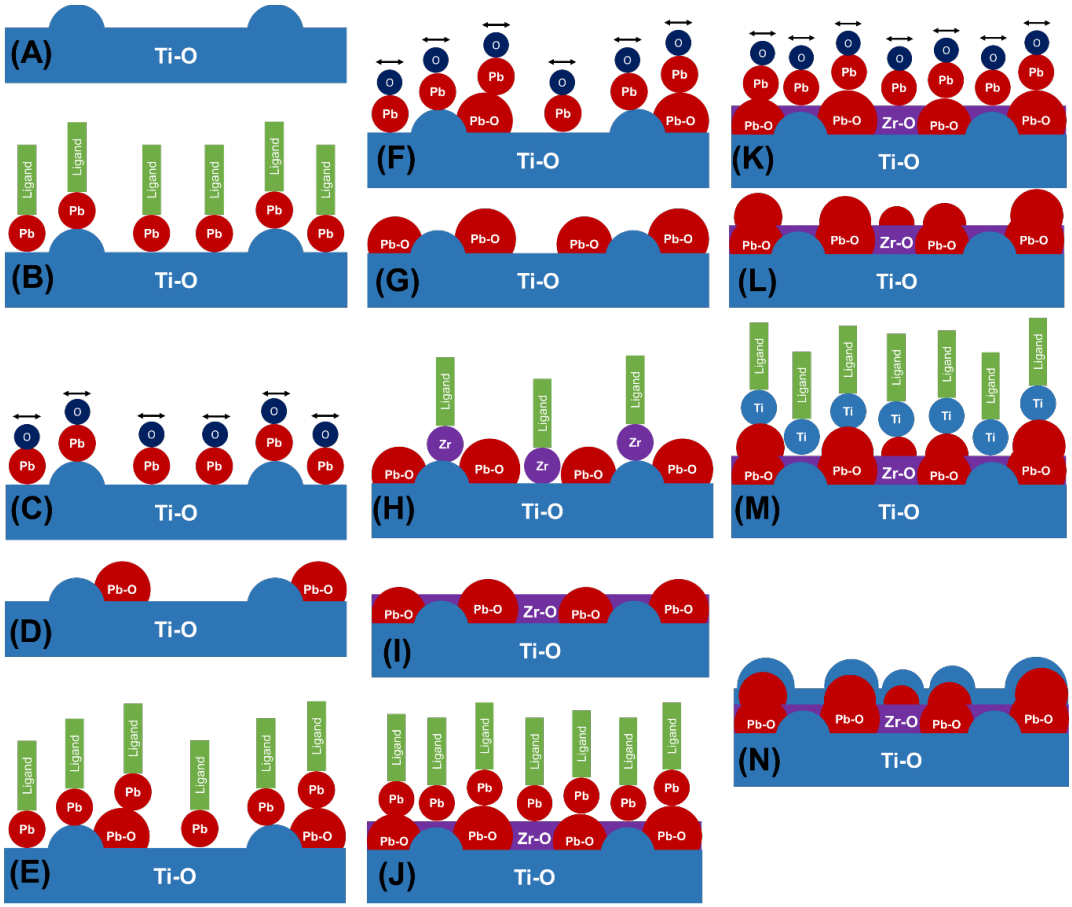

Figure 8.5: Growth Model for ALD PZT

ALD $PbHfO_3$ Model

Although no TEM cross-section images are available for PHO, the growth mechanism can be inferred from the RBS composition data and the thickness (thus the GPC) obtained from ellipsometry. For both PTO and PHO, a PbO_x:(Ti or Hf)O_x cycle ratio of 4:1 yielded approximately stoichiometric PTO or PHO, respectively. In addition, the equilibrium GPC is very similar between PTO (0.073 nm/cycle) and PHO (0.075 nm/cycle) grown with a 3:1 (slightly Pb-poor) PbO_x:(Ti or Hf)O_x cycle ratio. The in-situ thickness traces of PTO and PHO are qualitatively nearly identical. Thus, it can be concluded that the PTO and PHO growth proceed in the same manner. Figure 8.6,

shown below, details the growth model of ALD PHO, which proceeds identically to PTO, but Hf is substituted for Ti.

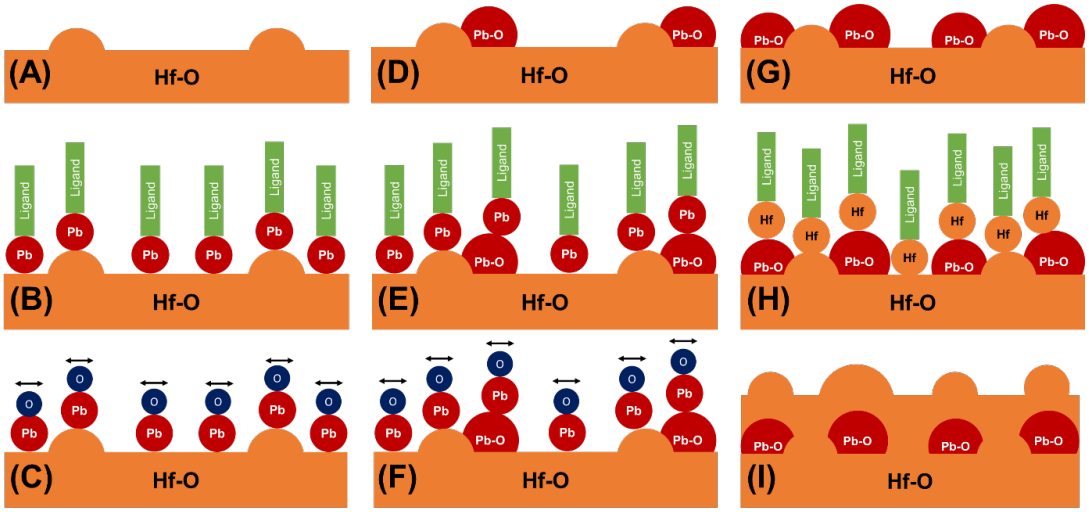

Figure 8.6: Growth Model for ALD PHO

ALD $PbHf_xTi_{1-x}O_3$ Model

In contrast to the growth model for PZT, there seemed to be no issue mixing the PTO and PHO processes to form ALD PHT. The only significant difference between the growth of PHT and the constituent ternary oxides is that the PbO_x:(Ti or Hf)O_x ratio expected to yield stoichiometric PHT increased from 4:1 for PTO and PHO to approximately 4.5:1 for PHT, indicating that the mixing of cations slightly depressed the Pb-incorporation. Interestingly, PbO_x:(Ti or Zr)O_x ratio expected to yield stoichiometric PTO-rich PZT is also close to 4.5:1, implying a similar Pb-suppression mechanism. The PHT growth model is shown below in Fig. 8.7 and ends with a final TiO_x layer encapsulating the underlying HfO_x and PbO nuclei. The full super-cycle proceeds with the blocks A-G repeated (Fig. 8.7), then with the Ti precursor (TDMAT)

and Ti-O shown in blocks H and I replaced with the Hf precursor (TDMAH) and Hf-O, respectively.

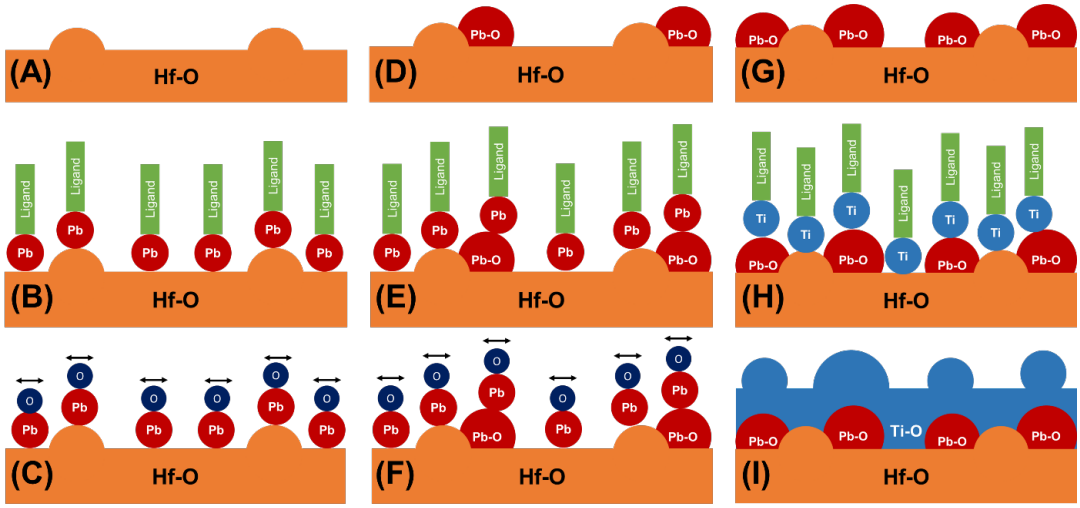

Figure 8.7: Growth Model for ALD PHT

Although the model presented in this section shows that the growth does not fit the typical layer-by-layer ALD archetype, it is important to note that although the layers of the film form unconventionally, the amount of film deposited per cycle is self-limited. The mobility of the PbO molecules should be kept in mind for growth on complex 3-D structures. Complex structures that contain aggressive features may contain “sinks” for the highly mobile PbO species. For example, features that contain conventional heterogeneous nucleation areas (high roughness, cracks) may be expected to be Pb-rich while depleting the surround film of Pb. This is left as a speculative claim, as a more through treatment is required to understand the exact nucleation properties of the PbO molecules.

Preliminary Results: A Path Toward PZT near the MPB

Zirconium tert-butoxide [$Zr(O\textit{t}\text{-}Bu)_4$] was identified in Chapter 2 as a viable alternative Zr-precursor and was substituted for TDMAZ to attempt to improve the Zr-incorporation. The results presented in this section are preliminary. Neither the dose, nor the thermal stability of the $Zr(O\textit{t}\text{-}Bu)_4$ have been thoroughly evaluated. Nonetheless, preliminary results are promising. Figure 8.8, shown below, shows the in-situ thickness trace of one complete super-cycle of a new ALD PZT process. The process is a combination of the PTO cycle evaluated in Chapter 5, and a PZO process consisting of a combination of $Pb(DMAMP)_2$ and $Zr(O\textit{t}\text{-}Bu)_4$ precursors. The cation dose steps are labelled explicitly in the figure. Each cation dose was followed by the same oxidizer strategy of H_2O first, followed by ozone. Only one example of the oxidation step is shown for each cation precursor, though each cation dose received an equivalent oxidation. A zoomed-in view of just the PZO cycle is shown is Fig. 8.9. The PbO_x:ZrO_x cycle ratio that appeared to yield the same thickness increase is shown to be 1:4 for each of the subcycles in Fig. 8.8. This is the reverse of the PbO_x:TiO_x cycle ratio, which is 4:1. The growth rate of the PZO (0.02 nm/cycle) appears to be suppressed compared to the PTO (0.064 nm/cycle). The lower growth rate is significant and is the reason that more PZO cycles are required to reach the MPB than PTO cycles. The PZO:PTO ratio was selected to be 4:1 in this example to yield slightly Zr-rich PZT (PTO equivalent thickness=0.32 nm/super-cycle, PZO equivalent thickness=0.4/super-cycle). Since this deposition trial was preliminary, it was not definitively proved whether or not the $Zr(O\textit{t}\text{-}Bu)_4$ was saturating. Since the growth rate of the binary ZrO_2 oxide has been previously shown to be above 0.1 nm/cycle, there is reason to be

optimistic that the growth rate could be greatly increased upon proper dose optimization. Nonetheless, the growth rate of ZrO_x appears to be a linear function of the number of Zr-O cycles (Fig. 8.9), and grows equally well on a freshly deposited PbO_x layer as it does on itself. The growth rate of the PTO cycle appears to be uninhibited by increased Zr-content of the films (Fig. 8.8). Therefore, it can be reasoned that achieving compositions near the MPB is simply a matter of balancing the relative number of PTO and PZO cycles using the new combination of precursors. The process parameters of the new process are detailed in Table 8.10. The composition values presented in Table 8.10 were measured using a combination of RBS and X-ray fluorescence. The composition of the PZT using the $Zr(O\textit{t}\text{-}Bu)_4$ is shown to be slightly Pb-deficient, PZO-rich PZT ($Pb_{0.78}Zr_{0.59}Ti_{0.41}O_{3.09}$). It is important to note that unlike the PTO-rich PZT process using TDMAZ and TDMAT, the new process using requires far more (non-optimized) ZrO_x (16) cycles compared to PbO_x (8) or TiO_x (1) per super-cycle. Thus, there seems to be plenty of process latitude to optimize the cycle ratio by decreasing the relative number of ZrO_x cycles (to slightly decrease the Zr content) and increasing the relative number of PbO_x cycles (to slightly boost the Pb content) to reach the desired composition of $PbZr_{0.52}Ti_{0.48}O_3$.

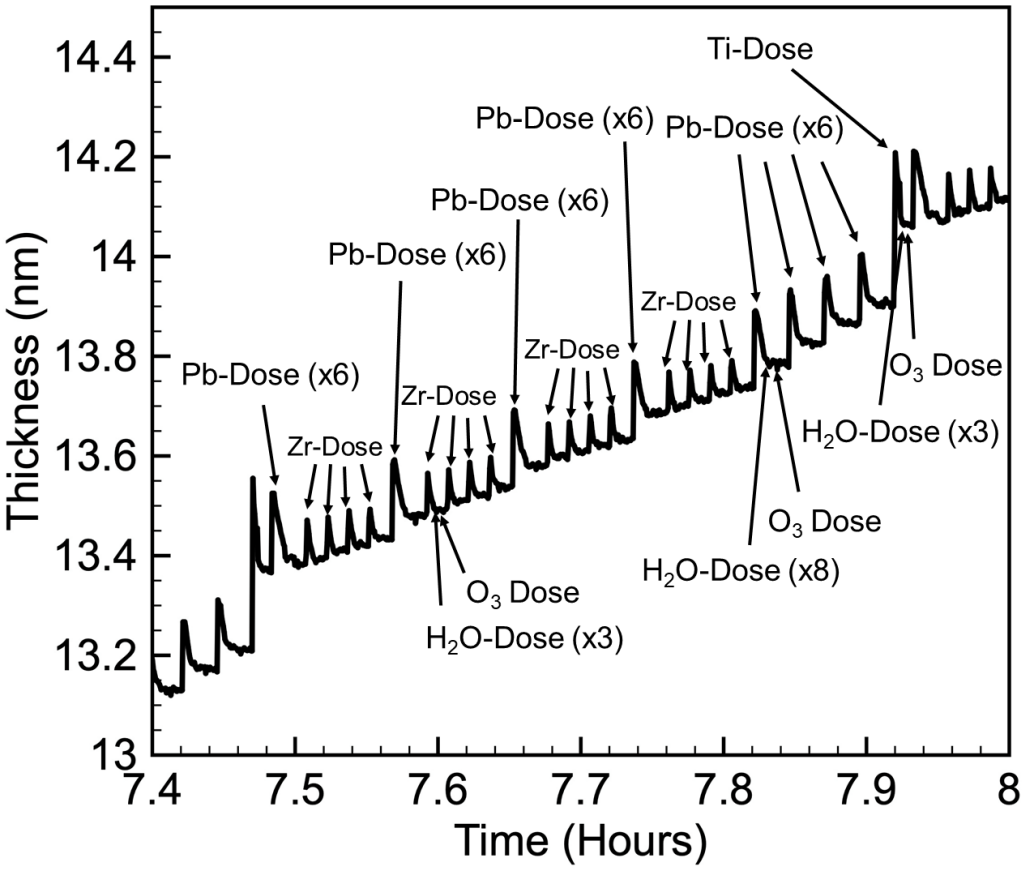

Figure 8.8: In-situ thickness trace of ALD PZT with $Zr(O\textit{t}\text{-}Bu)_4$.

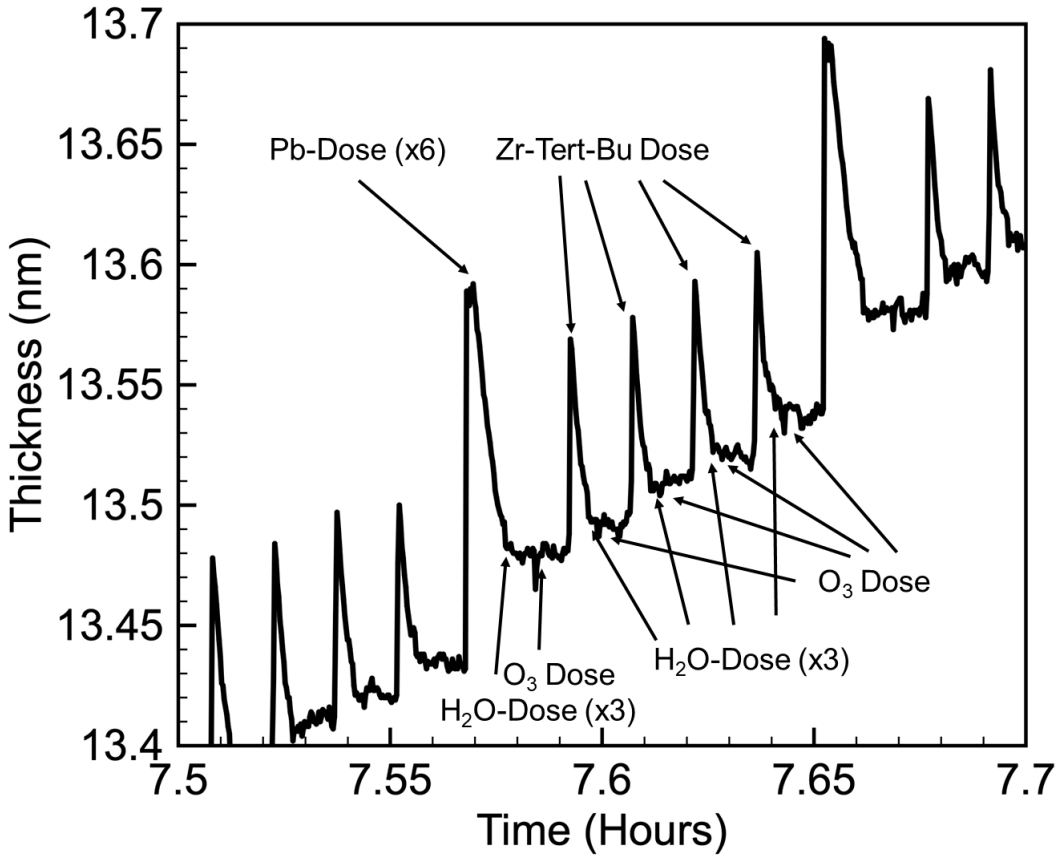

Figure 8.9: Close-up view of the in-situ thickness trace of the new PZO cycle.

Table 8.10: ALD PZT ($Pb_{0.78}Zr_{0.59}Ti_{0.41}O_{3.09}$) Properties grown with Zr(O*t*-Bu)$_4$

Parameter	PZT with Zr Tert-butoxide
PZO/(PZO+PTO)	20.0%
PZO:PTO	4:1
Pb:Ti	4:1
Pb:Zr	1:4
Supercycles	168 (3x Standard Dose)
TiO_x Cycles	168
ZrO_x Cycles	2688
PbO_x Cycles	1344
Ti Concentration (±1%)	8.4 at%
Zr Concentration (±1%)	12.1 at%
Pb Concentration (±0.3%)	16.1 at%
O Concentration (±4%)	63.4 at%
Pb Excess (%)	-4.5 at%
Pb%/(Ti+Zr%)	0.78
GPC	0.03 nm/cycle
Thickness	126.1 nm

Future Work

Process Optimization

Thus far, the ALD cycle ratios have not been optimized to a fine degree. This is partly due to the limited precision of RBS, which was used as the dominant composition measurement technique. Further process optimization is required to evaluate the repeatability and overall precision of the thickness and cation composition. Going forward, the chemical composition of the films should be measured using a

combination of techniques (such as time-of-flight secondary ion mass spectroscopy [TOF-SIMS], XRF, and/or RBS) to avoid over-reliance on a single technique (RBS) and to improve the measurement precision. In addition, composition gradients through the deposited film thickness should be investigated (for example, with TOF-SIMS). Whole-wafer characterization techniques should be employed, such as multi-point XRD and RBS with wafer-mapping to evaluate possible composition variance across the 150-mm Si substrates. The ALD PZT process with the new Zr precursor $Zr(O\textit{t}\text{-}Bu)_4$ will continue to be investigated and optimized. The rapid thermal anneal (RTA) step has proven to be critical in the crystallization of the films into the desired perovskite structure. Thus, the RTA process should be carefully optimized for each materials system, and the RTA itself should be investigated for cross-wafer variances in temperature and gas flow. The RTA process optimization should be accompanied by TEM measurements and electrical testing (in addition to XRD, RBS, etc.) to observe the relationship between the ferroelectric FOM and the microstructure. Quantification of trace impurities such as carbon, nitrogen, and hydrogen has thus far not been performed, but it critical to the understanding of possible leakage current and degradation mechanisms. The early-stage growth effects of the Pb-based perovskites on the Pt substrate should be investigated to determine the chemical and structural composition at the interface.

Electrical Testing

Electrical testing should continue to be performed in the manner outlined in this thesis, with the addition of dielectric breakdown strength and fatigue testing. Piezoelectric

testing should be performed, especially for ALD PZT and PHT on 2D cantilever structures to quantitatively evaluate the piezoelectric coefficients.

3D Actuator Development and Testing

3D device development will continue with the goal of achieving sidewall actuator structures, which requires the implementation of several other ALD processes, such as SiO_2, Al_2O_3, and Pt (or other electrode material). Other potential 3D devices of interest would be simple MIM capacitors grown on trench/pore structures, targeting large polarizations per unit area. Ferroelectric testing of 3D MIM capacitors could help us to infer piezoelectric properties of films grown on similar (trench) structures.

Doped Variants

Dopants such as Al (precursor: trimethylaluminum) or La (precursor: Lanthanum isopropoxide), just to name two possibilities, may be easily embedded into the processes presented in this thesis. The ease with which a small number of dopant cycles could be incorporated presents an opportunity to investigate the effect of different dopants at various concentrations.

Scientific Exploration and Modeling

The phase or phases of the as-deposited PbO_x crystallites should be conclusively determined (perhaps by TEM). The ALD growth models could be improved by performing monte-carlo simulations of the nucleation kinetics of the PbO_x crystallites.

In addition, a model for the crystallization of the perovskites should be developed to better understand the relationship between the anneal temperature and the microstructure. There may also be other applications for the PbO_x nanocrystallites, (for example, photocatalysis[27]) that could be exploited.

References

[1] Strnad NA, Potrepka DM, Pulskamp JS, et al. Texture and Phase Variation of ALD $PbTiO_3$ Films Crystallized by Rapid Thermal Anneal. *J Vac Sci Technol A*. 2019;37:020917.

[2] Hwang GW, Lee HJ, Lee K, et al. Atomic Layer Deposition and Electrical Properties of $PbTiO_3$ Thin Films Using Metallorganic Precursors and H_20. *J Electrochem Soc.* 2007;154:G69-G76.

[3] Khan MA, Comyn TP, Bell AJ. Deposition of PbTiO3 films on Pt/Si substrates using pulsed laser deposition. *J Eur Ceram Soc*. 2008;28:591-597.

[4] Watanabe T, Hoffman-Eifert S, Hwang CS, et al. Growth Behavior of Atomic-Layer-Deposited Pb(Zr,Ti)Ox Thin Films on Planar Substrate and Three-Dimensional Hole Structures. *J Electrochem Soc.* 2008:155:D715-D722.

[5] Sanchez LM, Potrepka DM, Fox GR, et al. Optimization of PbTiO3 seed layers and Pt metallization for PZT-based piezoMEMS actuators. J Mater Res. 2013;28:1920-1931.

[6] Sanchez LM. Optimization of Pb(Zr52Yi38)O3 through improved platinum metallization, use of a PbTiO3 seed layer, and fine tuning of annealing conditions for applications in multilayer actuator MEMS technology. PhD Dissertation*; The University of Maryland*; 2014.

[7] Aggarwal S, Udayakumar KR, Rodriguez JA. Stoichiometry and phase purity of Pb(Zr, Ti)O_3 thin films deposited by metal organic chemical vapor deposition *J Appl Phys.* 2006;100:064103.

[8] Rodriguez J, Remack K, Boku KR, et al. Reliability Properties of Low Voltage PZT Ferroelectric Capacitors and Arrays. *International Reliability Physics Symposium.* Feb 16, 2004; Pheonix, AZ, USA.
[9] Tang X, Zhu X, Dai J, et al. Self-limited grain growth, dielectric, leakage and ferroelectric properties of nanoscrystalline BiFeO3 thin films by chemical solution deposition. *Acta Mater.* 2013;61:17391747.
[10] Watanabe T, Hoffman-Eifert S, Peter F, et al. Liquid Injection ALD of $Pb(Zr,Ti)O_x$ Thin Films by a combination of Self-Regulating Component Oxide Processes. *J Electrochem Soc.* 2007:154:G262-G269.
[11] Zhang F, Perng Y-C, Choi JH, Wu T, et al. Atomic layer deposition of Pb(Zr, Ti)Ox on 4H-SiC for metal-ferroelectric-insulator-semiconductor diodes. *J Appl Phys.* 2011;109:124109.
[12] Choi JH, Zhang F, Perng Y-C, et al. Tailoring the composition of lead zirconate titanate by atomic layer deposition. *J Vac Sci Technol B.* 2013;31:012207.
[13] Harjuoja J, Vayrynen S, Putkonen M, et al. Atomic layer deposition of $PbZrO_3$ thin films. *Appl Surf Sci.* 2007;253:5228-5232.
[14] Zhai J, Chen H. Direct current field and temperature dependent behaviors of antiferroelectric to ferroelectric switching in highly (100)-oriented PbZrO3 thin films. *Appl Phys Lett.* 2003;82:2673-2675.
[15] Park MH, Lee YH, Kim HJ, et al. Ferroelectricity and Antiferroelectricity of Doped Thin HfO_2-Based Films. *Adv Mater.* 2015;27:1811-1831.
[16] Fantozzi G, Idrissi H, Favotto C, et al. Lead hafnate titanate (PHT) ceramics: processing and proeprties. *J Eur Ceram Soc.* 2000;20:1671-1676.
[17] Schorn PJ, Schneller T, Bottger U, et al. Characterization of Chemical Solution Deposition-Derived Lead Hafnate Titanate Thin Films. *J Am Ceram Soc.* 2005;88:1312-1314.
[18] Strnad NA, Johs B, Phaneuf RJ, et al. Investigation of Bare Silicon and Sputtered Platinum Surface Effects on ALD Growth of TiO_x and ZrO_x by In-Situ Ellipsometry. *Presented at the 15th international conference on atomic layer deposition*; 2015; Portland, OR.
[19] Vollmer M, Weber A. *Z Phys Chem.* 1926;119:227.

[20] Bauer E. *Z Kristollagr.* 1958;110:372.
[21] Buhlmann S, Muralt P, Allmen SV. Lithography-modulated self-assembly of small ferroelectric Pb(Zr,Ti)O_3 single crystals. *Appl Phys Lett.* 2004;84:2614-2616.
[22] Brune H. Growth Modes in Encyclopedia of Materials: Science and Technology. 2001. 3683-3693.
[23] Thurmer K, Williams E, Reutt-Robey J. Autocatalytic Oxidation of Lead Crystallite Surfaces. *Science.* 2002;297:2033-2035.
[24] Springholz G, Pinczolits M, Mayer P, et al. Tuning of Vertica; and Lateral Correlations in Self-Organized PbSe/$Pb_{1-x}Eu_xTe$ Quantum Dot Superlattices. Phys Rev Lett. 2000;84:4669-4672.
[25] Elam JW, Zinovev AV, Pellin MJ, et al. Nucleation and Growth of Noble Metals on Oxide Surfaces Using Atomic Layer Deposition. *ECS Trans*. 2007;3:271-278.
[26] Hausmann DM, Kim E, Becker J, et al. Atomic Layer Deposition of Hafnium and Zirconium Oxides Using Metal Amide Precursors. *Chem Mater.* 2002:14:4350-4358
[27] Momeni MM, Nazari Z. Preparation of TiO2 and WO3-TiO2 nanotubes decorated with PbO nanoparticles by chemical bath deposition process: A stable and efficient photo catalyst. Ceram Int. 2016;42:8691-8697.

Bibliography

Chapter 1

[1] Ott AW, Klaus JW, Johnson JM, George SM. Al3O3 thin film growth on Si(100) using binary reaction sequence chemistry. *Thin Solid Films.* 1997;292:135-144.

[2] Elam JW, Routkevitch D, Mardilovich P, George SM. Conformal Coating of Ultrahigh-Aspect-Ratio Nanopores of Anodic Alumina by Atomic Layer Deposition. *Chem Mater.* 2003;15:3507:3517.

[3] Jaffe B, Roth RS, Marzullo S. Piezoelectric Properties of Lead Zirconate- Lead Titanate Solid Solution Ceramics. *J Appl Phys.* 1954;25:809-810.

[4] Hwang GW, Lee HJ, Lee K, et al. Atomic Layer Deposition and Electrical Properties of $PbTiO_3$ Thin Films Using Metallorganic Precursors and H_20. *J Electrochem Soc.* 2007;154:G69-G76.

[5] Tan X, Ma C, Frederick J, et al. The Antiferroelectric – Ferroelectric Phase Transition in Lead-Containing and Lead-Free Perovskite Ceramics. *J Am Ceram Soc.* 2011;94:4091-4107.

[6] Wei J, Yang T, Want H. Excellent Energy Storage and Charge-discharge Performances in PbHfO3 Antiferroelecctric Ceramics. J Eur Ceram Soc. 2019;39:624-630.

[7] Nguyem MD, Rijnders G, Electric field-induced phase transition and energy storage performance of highly-textured PbZrO3 antiferroelectric films with a depositions temperature dependence. *J Eur Ceram Soc.* 2018;38:4953-4961.

[8] Noheda B, Cox DE, Shirane G, et al. A monoclinic ferroelectric phase in the $Pb(Zr_{1-x}Ti_x)O_3$ solid solution. *Appl Phys Lett.* 1999;74:2059-2061.

[9] Frantti J, Fujioka Y, Eriksson S, et al. Neutron Powder Diffraction Study of $Pb(Hf_xTi_{1-x})O_3$ Ceramics ($0.10 \leq x \leq 0.50$). *Inorg Chem.* 2005;44:9267-9278.

[10] Jaffe B, Roth SR, Marzullo S, Properties of Piezoelectric Ceramics in the Solid-Solution Series Lead Titanate-Lead Zirconate-Lead Oxide: Tin Oxide and Lead Titanate-Lead Hafnate. *J Res Natl Bur Stand.* 1955; 55:239-254.

[11] Pulskamp JS, Polcawich RG.Three dimensional piezoelectric MEMS, US8966993 B2. 2012

[12] Oldham KR, Pulskamp JS, Polcawich RG, et al. Thin-Film PZT Actuators With Extended Stroke. *J Microelectromech S.* 2008;17:890-899.
[13] Gasser W, Uchida Y, Matsumura M. Quasi-monolayer deposition of silicon dioxide. *Thin Solid Films.* 1994;250:213-218.
[14] Lee J-H, Kim U-J, Han C-H, et al. Investigation of Silicon Oxide Thin Films Prepared by Atomic Layer Deposition Using SiH_2Cl_2 and O_3 as the Precursors. *Jpn J Appl Phys.* 2004;43:L328-L330.
[15] Lakomaa EL, Haukka S, Suntola T. Atomic layer growth of TiO_2 on silica. *Appl Surf Sci.* 1992;60/61:742-748.
[16] Kim SK, Hoffmann-Eifert S, Reiners M, et al. Relation Between Enhancement in Growth and Thickness-Dependent Crystallization in ALD TiO2 Thin Films. *J Electrochem Soc.* 2011;158:D6-D9.
[17] Aaltonen T, Ritala M, Sajavaara T, et al. Atomic Layer Deposition of Platinum Thin Films. *Chem Mater.* 2003;15:1924-1928.
[18] Potrepka DM, Sanchez LM, Polcawich RG, et al. Atomic layer deposition of Pt growth template for orienting $PbZr_xTi_{1-x}O_3$ thin films. *J Vac Sci Technol A.* 2012;30:01A129.
[19] Harjuoja J, Kosola A, Putkonen M, et al. Atomic layer deposition and post-deposition annealing of $PbTiO_3$ thin films. *Thin Solid Films.* 2006;496:346-352.
[20] Harjuoja J, Putkonen M, Niinisto L. Exploiting volatile lead compounds as precursors for the atomic layer deposition of lead dioxide thin films. *Thin Solid Films.* 2006:497:77-82.
[21] Watanabe T, Hoffmann-Eifert S, Hwang CS, et al. Liquid-Injection Atomic Layer Deposition of TiO_x and Pb-Ti-O Films. *J Electrochem Soc.* 2006:153:F199-F204.
[22] Watanabe T, Hoffman-Eifert S, Mi S, et al. Growth of ternary PbTiOx films in a combination of binary oxide atomic layer depositions. *J Appl Phys.* 2007;101:014114.
[23] Lee HJ, Park MH, Min Y-S, et al. Unusual Growth Behavior of Atomic Layer Deposition $PbTiO_3$ Thin Films Using Water and Ozone as Oxygen Sources and Their Combination. *J Phys Chem C.* 2010;114:12736-12741.

[24] Sbrockey NM, Tompa GS, Lavelle R, et al. Atomic layer deposition of $PbTiO_3$ and $PbZr_xTi_{1-x}O_3$ films using metal alkyl and alkylamide precursors. *J Vac Sci Technol A.* 2018;36:031509.
[25] Harjuoja J, Vayrynen S, Putkonen M, et al. Atomic layer deposition of $PbZrO_3$ thin films. *Appl Surf Sci.* 2007;253:5228-5232.
[26] Watanabe T, Hoffman-Eifert S, Peter F, et al. Liquid Injection ALD of $Pb(Zr,Ti)O_x$ Thin Films by a combination of Self-Regulating Component Oxide Processes. *J Electrochem Soc.* 2007:154:G262-G269.
[27] Watanabe T, Hoffman-Eifert S, Hwang CS, et al. Growth Behavior of Atomic-Layer-Deposited Pb(Zr,Ti)Ox Thin Films on Planar Substrate and Three-Dimensional Hole Structures. *J Electrochem Soc.* 2008:155:D715-D722.
[28] Zhang F, Perng Y-C, Choi JH, Wu T, et al. Atomic layer deposition of Pb(Zr, Ti)Ox on 4H-SiC for metal-ferroelectric-insulator-semiconductor diodes. *J Appl Phys.* 2011;109:124109.
[29] Choi JH, Zhang F, Perng Y-C, et al. Tailoring the composition of lead zirconate titanate by atomic layer deposition. *J Vac Sci Technol B.* 2013;31:012207.
[30] Strnad NA, Johs B, Phaneuf RJ, et al. Investigation of Bare Silicon and Sputtered Platinum Surface Effects on ALD Growth of TiO_x and ZrO_x by In-Situ Ellipsometry. *Presented at the 15th international conference on atomic layer deposition*; 2015; Portland, OR.
[31] Xie Q, Musschoot J, Deduytsche D, et al. Growth Kinetics and Crystallization behavior of TiO_2 Films Prepared by Plasma Enhanced Atomic Layer Deposition. *J Electrochem Soc.* 2008;155:H688-H692.
[32] Hendrix BC, Cameron TM, Hunks W, et al. Precursor Screening for TiO_2 ALD for Semiconductor Applications. *Presented at the 14th international conference on atomic layer deposition*; 2014; Kyoto, Japan.
[33] Putkonen M, Niinisto L. Zirconia thin films by atomic layer epitaxy. A comparative study on the use of novel precursors with ozone. *J Mater Chem.* 2001;11:3141-3147.
[34] Hwang CS. Atomic Layer Deposition for Semiconductors. Chapter 6 FeRAM, page 163. New York, NY: Springer Science+Business Media:2014

[35] Hausmann DM, Kim E, Becker J, et al. Atomic Layer Deposition of Hafnium and Zirconium Oxides Using Metal Amide Precursors. *Chem Mater.* 2002:14:4350-4358.
[36] Joeng D, Lee J, Kim J. Effects of Various Oxidizers on the ZrO2 Thin Films Deposited by Atomic Layer Deposition. *Integr Ferroelectr.* 2004:67:41-48.

Chapter 2

[1] Jacobsen SC, Wood JE. Micro Electro-Mechanical Systems (MEMS). Presented at The Center for Engineering Design; July 15, 1986; University of Utah, Salt Lake City, UT.
[2] Smith CS. Piezoresistance Effect in Germanium and Silicon. *Phys Rev.* 1954;94:42-49.
[3] Sanchez JC. Semiconductor Strain Gauge. U.S. Patent 3084300. 1963.
[4] Yadzi N, Ayazi F, Najafi K. Micromachined Intertial Sensors. *Proceedings of the IEEE*. 1998;86:1640-1659.
[5] Mastrangleo CH, Muller RS. Fabrication and performance of a fully integrated μ-pirani pressure gauge with digitial readout. *Presented at 6th Int. Conf. on Solid-State Sensors and Actuators (Transducers '91)*; 1991; San Francisco CA. Technical Digest. 245-248.
[6] Eaton WP, Smith JH. Micromachined pressure sensors: review and recent developments. *Smart Mater Struct.* 1997;6:530-539.
[7] Legtenberg R, Groeneveld AW, Elwenspoek M. Comb-drive actuators for large displacements. *J Micromech Microeng.* 1996;**6**:320-329.
[8] Ahn CH, Allen MG. A Fully Integrated Surface Micromachined Magnetic Microactuator with a Multilevel Meander Magnetic Core. *J Microelectromech S.* 1993;2:15-22.
[9] Wright JA, Tai YC, Chang SC. A Large-Force, Fully-Integrated MEMS Magnetic Actuator. *Presented at 1997 Int. Conf. on Solid-State Sensors and Actuators (Transducers '97)*; 1997; Chicago IL. Technical Digest. 793-796.
[10] Huang QA, Lee NKS. Analysis and design of polysilicon thermal flexure actuator. *J Micromech Microeng.* 1999;9:64-70.

[11] Comtois JH, Bright VM. Applications for surface-micromachined polysilicon thermal actuators and arrays. *Sens Actuators, A.* 1997;58:19-25.
[12] Lee WS, Lee SS. Piezoelectric microphone built on circular diaphragm. *Sens Actuators, A.* 2008;144:367-373
[13] Mina IG, Kim H, Kim I, et al. High Frequency Piezoelectric MEMS Ultrasound Transducers. *IEEE Trans on Ultrason Ferroelectr Freq Control.* 2007;54:2422-2430.
[14] Jose KA, Suh WD, Xavier PB, et al. Surface acoustic wave MEMS gyroscope. *Wave Motion.* 2002;36:367-381.
[15] Nemirovsky Y, Nemirovsky A, Muralt P, et al. Design of a novel thin-film piezoelectric accelerometer. *Sens Actuators, A.* 1996;56:239-249.
[16] Harris NR, Hill M, Torah R, et al. A multilayer thick-film PZT actuator for MEMS applications. *Sens Actuators, A.* 2006;132:311-316.
[17] Chakraborty I, Tang WC, Bame DP, et al. MEMS micro-valve for space applications. *Sens Actuators.* 2000;83:188-193**.**
[18] Pulskamp JS, Bedair SS, Polcawich RG, et al. Electrode-Shaping for the Excitation and Detection of Permitted Arbitrary Modes in Arbitrary Geometries in Piezoelectric Resonators. *IEEE Trans on Ultrason Ferroelectr Freq Control.* 2012;59:1043-1060
[19] Piazza G, Stephanou PJ, Pisano AP. Piezoelectric Aluminum Nitride Vibrating Contour-Mode MEMS Resonators. *J Microelectromech S.* 2006;15:1406-1418
[20] Yi SH, Kim ES. Piezoelectric Microspeaker with Compressive Nitride Diaphragm. *The fifteenth IEEE International Conference on Micro Electro Mechanical Systems*; 2002.
[21] Kim HJ, Koo K, Lee SQ, et al. High Performance Piezoelectric Microspeakers and Thin Speaker Array System. *ETRI J.* 2009;31:680-687.
[22] [Internet] [Cited 2019 Feb 11] Available from: http://www.xaar.com/en/products/xaar-printheads/
[23] [Internet] [Cited 2019 Feb 11] Available from: http://www.fujifilmusa.com/shared/bin/PDS00015%20(3).pdf
[24] [Internet] [Cited 2019 Feb 11] Available from: https://global.epson.com/innovation/core_technology/pdf/precisioncore.pdf

[25] [Internet] [Cited 2019 Feb 11] Available from: https://industrial.panasonic.com/cdbs/www-data/pdf/ARC0000/ARC0000CE13.pdf
[26] [Internet] [Cited 2019 Feb 11] Available from: microsound piezo-MEMS earphone/headphone startup http://www.usound.com/technology.html#microsound
[27] Trolier-Mckinstry S. Improved Thin Film Piezoelectrics for Actuator Applications. U.S. Army Research Laboratory Sensors and Electron Devices Directorate *Technical Report. 2008.*
[28] Sanchez LM, Polcawich RG. Optimization of PbTiO3 Seed Layers for PZT MEMS Actuators. U.S. Army Research Laboratory Sensors and Electron Devices Directorate *Technical Report.* 2008.
[29] Sanchez LM, Potrepka DM, Fox GR, et al. Improving PZT Thin Film Texture Through Pt Metallization and Seed Layers. *MRS Proceedings.* 2011.
[30] Sanchez LM, Grobicki AD, Smith GL, et al. Texture Control in lead Zirconate Titanate Multilayer Thin Films. *IEEE Trans on Ultrason Ferroelectr Freq Control.* 2014;61:654-661
[31] Oldham KR, Pulskamp JS, Polcawich RG. Thin-Film Piezoelectric Actuators for Bio-Inspired Micro-Robotic Applications. *Integr Ferroelectr.* 2007;95:54-65.
[32] Oldham KR, Pulskamp JS, Polcawich RG, et al. Thin-Film PZT Actuators With Extended Stroke. *J Microelectromech S.* 2008;17:890-899.
[33] Smith GL, Bedair SS, Schuster BE, et al. Biologically inspired, haltere, angular-rate sensors for micro-autonomous systems. *Proceedings of SPIE 8373 Micro- and Nanotechnology Sensors, Systems, and Applications IV;* May 3, 2012; Baltimore, MD.
[34] Smith GL, Rudy RQ, Polcawich RG, et al. Integrated Thin Film Piezoelectric Traveling Wave Ultrasonic Motor. *Sens Actuators.* 2012;188:305-311.
[35] Polcawich RG. Design, fabrication, test and evaluation of RF MEMS series switches using lead zirconate titanate (PZT) thin film actuators. PhD Dissertation*; The Pennsylvania State University*; 2007.
[36] Proie RM, Polcawich RG, Pulskamp JS, et al. Development of a PZT MEMS Switch Architecture for Low-Power Digital Applications. *J Microelectromech S.* 2011;20:1032-1042.

[37] Pulskamp JS, Bedair SS, Polcawich RG, et al. Ferroelectric PZT RF MEMS Resonators. *2011 Joint Conference of the IEEE International Frequency Control and the European Frequency and Time Forum (FCS)*; May 2-5, 2011; San Francisco, CA.
[38] Pulskamp JS, Judy DC, Polcawich RG, et al. Monolithically Integrated Piezomems SP2T Switch and Contour-Mode Filters. *International Conference on Micro Electro Mechanical Systems;* Jan 25-29, 2009; Sorrento, Italy.
[39] Ballato A. Piezoelectricity: Old Effect, New Thrusts. *IEEE Trans on Ultrason Ferroelectr Freq Control* 1995;42:916-926.
[40] Muralt P, Kholkin A, Kohli M, et al. Piezoelectric actuation of PZT thin-film diaphragms at static and resonant conditions. *Sens Actuators, A.* 1996;53:398-404.
[41] Scott JF, Paz de Araujo CA. Ferroelectric Memories. *Science.* 1989;246:1400-1405.
[42] Jaffe B. Antiferroelecric Ceramics with Field-Enforced Transitions: A New Nonlinear Circuit Element*. *Proc IRE*. 1961;1264-1267.
[43] Lynch AC. Relationship between permittivity and loss tangent. Proc IEEE. 1971;118:244-246.
[44] Jaffe B, Cook WR, Jaffe H. Piezoelectric Ceramics. London, UK: London Academic Publishing:1971:136.
[45] Kasap SO. Principles of Electronic Materials and Devices. 3rded. New York, NY: PUBLISHER;2006:648.
[46] Jaffe B, Cook WR, Jaffe H. Piezoelectric Ceramics. London, UK: London Academic Publishing:1971:117.
[47] B Jaffe B, Cook WR, Jaffe H. Piezoelectric Ceramics. London, UK: London Academic Publishing:1971:125.
[48] Noheda B, Cox DE, Shirane G, et al. A monoclinic ferroelectric phase in the $Pb(Zr_{1-x}Ti_x)O_3$ solid solution. *Appl Phys Lett.* 1999;74:2059-2061.
[49] B Jaffe B, Cook WR, Jaffe H. Chapter 7 in Piezoelectric Ceramics. London, UK: London Academic Publishing:1971.
[50] Noheda B. “Structure and high-piezoelectricity in lead oxide solid solutions”, *Curr Opin Solid St M.* 2002;6:27-34.

[51] Budd KD, et al. Sol-gel Processing of PbTiO3, PbZrO3, PZT, and PLZT Thin Films. *Br Ceram Proc.* 1985;36:107-121.
[52] Dey SK, Budd KD, Payne DA. Thin Film Ferroelectrics of PZT by Sol-Gel Procesing. *IEEE Trans on Ultrason Ferroelectr Freq Control.* 1988;35:80-81
[53] [Internet] [Cited 2019 Feb 10] Available from: https://www.prnewswire.com/news-releases/complete-teardown-report-of-xaars-1201-gs2p5-pzt-printhead-overview-physical-analysis-manufacturing-process-cost-analysis--price-analysis-300744632.html
[54] YOLE development. [Internet] [Cited 2019 Feb 10] Available from: http://www.yole.fr/iso_upload/Samples/Yole_thin_film_PZT_applications_sample.pdf
[55] Maas R, Koch M, Harris NR, et al. Thick-film printing of PZT onto silicon. *Mater Lett.* 1997;31:109-112.
[56] [Internet] [Cited 2019 Feb 12] Available from: http://electroscience.com/400
[57] [Internet] [Cited 2019 Feb 12] Available from: http://www.innovationlab.eastman.com/materials/eastman-texanol
[58] Barrow DA, Petroff TE, Sayer M. Thick ceramic coatings using a sol gel based ceramic-ceramic 0-3 composite. *Surf Coat Technol.* 1995;76-77:113-118.
[59] Jeon Y, Chung J, No K. Fabrication of PZT Thick Films on Silicon Substrates for Piezoelectric Actuator. *J Electroceram.* 2000;4:195-199.
[60] Beeby SP, Blackburn A, White NM. Processing of PZT piezoelectric thick films on silicon for microelectromechanical systems. *J Micromech Microeng*. 1999;9:218-229.
[61] Corker DL, Whatmore RW, Ringgaard E, et al. Liquid-phase sintering of PZT ceramics. *J Euro Ceram Soc.* 2000;20:2039-2045
[62] Wu D, Zhou Q, Kirk K, et al. Dielectric and Piezoelectric Properties of PZT Composite Thick Films with Variable Solution to Powder Ratios. *J Am Ceram Soc.* 2009;92:1276-1279.
[63] [Internet] Meggitt A/S. TF2100 all-round hard PZT. [Cited 2019 Feb 12] Available from: https://www.meggittferroperm.com/wp-content/uploads/2017/10/201708_MSSDK_TF2100_Datasheet-TF2100-1.pdf

[64] Tseng TF, Liu KS, Lin I-N, et al. Growth Behavior of pulsed-laser-deposited PLZTO thin films. *J Ceram Proc.* 1997;43:2857-2864.
[65] Verardi P, Dinescu M, Craciun F. Pulsed laser deposition and characterization of PZT thin films. *Appl Surf Sci.* 2000;154-155:514-518.
[66] Verardi P, Craciun F, Mirenghi L, et al. An XPS and XRD study of physical and chemical homogeneity of $Pb(Zr,Ti)O_3$ thin films obtained by pulsed laser deposition. *Appl Surf Sci.* 1999;138-139:552-556.
[67] Pham MTN, Boukamp BA, Bouwmeester HJM, et al. Microstructural and electrical properties of nanocomposite PZT/Pt thin films made by pulsed laser deposition. *Ceram Int.* 2004;30:1499-1503.
[68] Rajashekhar A, Fox A, Bharadwaja SSN, et al. In situ laser annealing during growth of $Pb(Zr_{0.52}Ti_{0.48})O_3$ thin films. *Appl Phys Lett.* 2013;103:032908.
[69] Rajashekhar A, Zhang HR, Srowthi B, et al. Microstructure Evolution of In Situ Pulsed-Laser Crystallized Pb(ZrTi)O3 Thin Films. *J Am Ceram Soc.* 2016;99:43-50.
[70] Fedder GK, Howe RT, Liu T-J K, et al. Technologies for Cofabricating MEMS and Electronics. *Proc IEEE.* 2008;96:306-322
[71] [Internet] [Cited 2019 Feb 12] Available from: https://www.solmates.nl/40/publications.html
[72] Blank DHA, Dekkers M, Rijnders G. Pulsed laser deposition in Twente: from research tool towards industrial deposition. *J Phys D: Appl Phys.* 2014;47:034006.
[73] Summerfelt SR, Moise TS, Xing G, et al. Demonstration of scaled ($\geq$0.12 μm^2) $Pb(Zr,Ti)O_3$ capacitors on W plugs with Al interconnect. *Appl Phys Lett.* 2001;79:4004-4006.
[74] Gilbert SR, Hunter S, Ritchey D, et al. Preparation of $Pb(Zr,Ti)O_3$ thin films by metalorganic chemical vapor deposition for low voltage ferroelectric memory. *J Appl Phys.* 2003;93:1713-1717.
[75] Aggarwal S, Udayakumar KR, Rodriguez JA. Stoichiometry and phase purity of $Pb(Zr, Ti)O_3$ thin films deposited by metal organic chemical vapor deposition *J Appl Phys.* 2006;100:064103.
[76] Kumar VC, Underdahl B. *Texas Instruments Fram MCUs for Dummies.* Hoboken, New Jersey. John Wiley and Sons, Inc. 2012.

[77] Bilodeau SM, Johnston ST, Russell MW, et al. Voltage scaling of ferroelectric thin films deposited by CVD. *Integr Ferroelectr.* 1999;26:119-135.
[78] [Internet] Silicon Sensing PZT Piezoelectric Sputtering Service. [Cited 2019 Mar 12] Available from: https://www.siliconsensing.com/services/foundry-services/pzt
[79] [Internet] Fugifilm Dimatix Industrial Inkjet Printheads. [Cited 2019 Mar 12] Available from: https://www.fujifilmusa.com/products/industrial_inkjet_printheads/print-products/printheads/index.html
[80] Chu F, Fox GR, Davenport T, et al. The Control of Pb Loss for PZT Based FRAM. *Integr Ferroelectr.* 2002;48:161-169.
[81] Suu K, Tani N, Chu F, et al. Process stability of ferroelectric PLZT thin film sputtering for FRAM ® production. *Integr Ferroelectr*. 1999;26:9-19.
[82] Chu F, Hickert G, Hadnagy TD, et al. Ferroelectric properties of PLZT thin films prepared using ULVAC ZX-1000 sputtering system. *Integr Ferroelectr.* 1999;26:47-55.

Chapter 3

[1] Chipman RA. Handbook of Optics, Vol. II (Devices, Measurements and Properties). 2nded. New York, NY: McGraw Hill, Inc.:1994;22.
[2] [Internet] [Cited 2019 Jan 19] Johs B. http://www.film-sense.com/technology/ellipsometry/
[3] Cauchy MAL. Me'moire sur la Dispersion de la Lumie`re. Calve, Prague. 1836
[4] Azzam RMA. Division-of-amplitude photopolarimeter based on conical diffraction from a metallic grating. *Appl Opt.* 1992;31.
[5] Azzam RMA. Division-of-Amplitude Photopolarimeter (DOAP) for the simultaneous measurement of All Four Stokes Parameters of Light. *Opt Acta.* 1982;29:685-689.
[6] [Internet] [Cited 2019 March 4] Lodewijks K. http://www.kristoflodewijks.be/research/theoretical-background/6-spectroscopic-ellipsometry/

[7] J.A. Woollam Co., Inc. Guide to Using WVASE® Spectroscopic Ellipsometry Data Acquisition and Analysis Software. Version 3.690.: 2008
[8] Garcia-Caudrel E, De Martino A, Gaston JP, et al. Application of Spectroscopic Ellipsometry and Mueller Ellipsometry to Optical Characterization. *Appl Spectrosc.* 2013;67.
[9] J.A. Woollam Co., Inc. M-2000F Spectroscopic Ellipsometer Hardware Manual. Version M2FHB200RT: 2001.
[10] Jellison GE, Modine FA. Parametrization of the optical functions of amorphous materials in the interband region. Appl Phys Lett. 1996;69:371-373.
[11] Kittel C. Introduction to Solid State Physics. 8thed. John Wiley and Sons, Inc.: 2005
[12] Deutsch M, Holzer G, Hartwig J, et al. Kα and Kβ x-ray emission spectra of copper. *Phys Rev A.* Vol.:1995;51.
[13] Chu WK, Mayer JW, Nicolet MA, et al. Principles and Applications of Ion Beam Techniques for the Analysis of Solids and Thin Films. *Thin Solid Films.* 1973;17:1-41.
[14] Perriere J. Rutherford backscattering spectrometry. *Vacuum.* 1987;37:429-432**.**

Chapter 4

[1] Fox GR, Potrepka DM, Polcawich RG. Dependence of {111}-textured Pt electrode properties on TiO_2 seed layers formed by thermal oxidation. *J Mater Sci - Mater Electron.* 2018;29:412-426.
[2] Muralt P. PZT Thin Films for Microsensors and Actuators: Where Do We Stand?. *IEEE Trans Ultrason Ferroelectr Freq Control.* 2000;47:903-915.
[3] Sanchez LM, Potrepka DM, Fox GR, et al. Improving PZT Thin Film Texture Through Pt Metallization and Seed Layers. *MRS Proceedings.* 2011;*1299*.
[4] Potrepka DM, et al. Atomic layer deposition of Pt growth template for orienting $PbZr_xTi_{1-x}O_3$ thin films. *J Vac Sci Technol A*. 2012;30:01A129.

Chapter 5

[1] Strnad NA, Potrepka DM, Pulskamp JS, et al. Texture and Phase Variation of ALD $PbTiO_3$ Films Crystallized by Rapid Thermal Anneal. *J Vac Sci Technol A.* 2019;37:020917.

[2] Harjuoja J, Kosola A, Putkonen M, et al. Atomic layer deposition and post-deposition annealing of $PbTiO_3$ thin films. *Thin Solid Films.* 2006;496:346-352.

[3] Hwang GW, Lee HJ, Lee K, et al. Atomic Layer Deposition and Electrical Properties of $PbTiO_3$ Thin Films Using Metallorganic Precursors and H_20. *J Electrochem Soc.* 2007;154:G69-G76.

[4] Watanabe T, Hoffman-Eifert S, Mi S, et al. Growth of ternary PbTiOx films in a combination of binary oxide atomic layer depositions. *J Appl Phys.* 2007;101:014114.

[5] Lee HJ, Park MH, Min Y-S, et al. Unusual Growth Behavior of Atomic Layer Deposition $PbTiO_3$ Thin Films Using Water and Ozone as Oxygen Sources and Their Combination. *J Phys Chem C.* 2010;114:12736-12741.

[6] Sbrockey NM, Tompa GS, Lavelle R, et al. Atomic layer deposition of $PbTiO_3$ and $PbZr_xTi_{1-x}O_3$ films using metal alkyl and alkylamide precursors. *J Vac Sci Technol A.* 2018;36:031509.

[7] Harjuoja J, Vayrynen S, Putkonen M, et al. Atomic layer deposition of $PbZrO_3$ thin films. *Appl Surf Sci.* 2007;253:5228-5232.

[8] Watanabe T, Hoffman-Eifert S, Peter F, et al. Liquid Injection ALD of $Pb(Zr,Ti)O_x$ Thin Films by a combination of Self-Regulating Component Oxide Processes. *J Electrochem Soc.* 2007:154:G262-G269.

[9] Watanabe T, Hoffman-Eifert S, Hwang CS, et al. Growth Behavior of Atomic-Layer-Deposited Pb(Zr,Ti)Ox Thin Films on Planar Substrate and Three-Dimensional Hole Structures. *J Electrochem Soc.* 2008:155:D715-D722.

[10] Choi JH, Zhang F, Perng Y-C, et al. Tailoring the composition of lead zirconate titanate by atomic layer deposition. *J Vac Sci Technol B.* 2013;31:012207.

[11] Sanchez LM, Potrepka DM, Fox GR, et al. Optimization of $PbTiO_3$ seed layers and Pt metallization for PZT-based piezoMEMS actuators. *J Mater Res.* 2013;28:1920-1931.

[12] Hiboux S, Muralt P. Mixed titania-lead oxide seed layers for PZT growth on Pt(111): a study on nucleation, texture and properties. *J Eur Ceram Soc.* 2004;24:1593.
[13] Ledermann N, Muralt P, Baborowski J, et al. {100}-Textured, piezoelectric $Pb(Zr_xTi_{1-x})O_3$ thin films for MEMS: integration, deposition, and properties. *Sens Actuators A.* 2003;105:162.
[14] Nittala K, Mhin S, Dunnigan KM, et al. Phase and texture evolution in solution deposited lead zirconate titanate thin film: Formation and role of the Pt_3Pb intermetallic phase. *J Appl Phys.* 2013;113:244101.
[15] Otani Y, Okamura S, Shiosaki T. Fabrication of Ferroelecctric Pb(Zr,Ti)O3 Thin Films by Liquid Delivery Metalorganic Chemical Vapor Deposition Using a Novel Titanium Source $Ti(OEt)_2(DPM)_2$. *Jpn J Appl Phys.* 2006;45:1752-1756.
[16] Muralt P, Maeder T, Sagalowicz A, et al. Texture control of $PbTiO_3$ and Pb(Zr, Ti)O_3 thin films with TiO_2 seeding. *J Appl Phys.* 1998;83:3835-3841.
[17] Watanabe T, Hoffmann-Eifert S, Hwang CS, et al. Growth Behavior of Atomic-Layer-Deposited $Pb(Zr,Ti)O_x$ Thin Films on Planar Substrate and Three-Dimensional Hole Structures. *J Electrochem Soc.* 2008;55:D715-D722.
[18] Mojarad SA, Kwa KSK, Goss JP, et al. A comprehensive study on the leakage current mechanisms of Pt/$SrTiO_3$/Pt capacitor. J Appl Phys. 2012;111:014503.

Chapter 6

[1] Watanabe T, Hoffman-Eifert S, Peter F, et al. Liquid Injection ALD of $Pb(Zr,Ti)O_x$ Thin Films by a combination of Self-Regulating Component Oxide Processes. *J Electrochem Soc.* 2007:154:G262-G269.
[2] Watanabe T, Hoffman-Eifert S, Hwang CS, et al. Growth Behavior of Atomic-Layer-Deposited Pb(Zr,Ti)Ox Thin Films on Planar Substrate and Three-Dimensional Hole Structures. *J Electrochem Soc.* 2008:155:D715-D722.
[3] Hwang CS. Atomic Layer Deposition for Semiconductors. Chapter 6 FeRAM, page 163. New York, NY: Springer Science+Business Media:2014
[4] Choi JH, Zhang F, Perng Y-C, et al. Tailoring the composition of lead zirconate titanate by atomic layer deposition. *J Vac Sci Technol B.* 2013;31:012207.

[5] Muralt, P. PZT Thin Films for Microsensors and Actuators: Where Do We Stand?. *IEEE Trans on Ultrason Ferroelectr Freq Control.* 2000;47:903-915

Chapter 7

[1] Jaffe B, Roth SR, Marzullo S, Properties of Piezoelectric Ceramics in the Solid-Solution Series Lead Titanate-Lead Zirconate-Lead Oxide: Tin Oxide and Lead Titanate-Lead Hafnate. *J Res Natl Bur Stand.* 1955; 55:239-254.

[2] Nguyem MD, Rijnders G, Electric field-induced phase transition and energy storage performance of highly-textured PbZrO3 antiferroelectric films with a depositions temperature dependence. *J Eur Ceram Soc.* 2018;38:4953-4961.

[3] Frantti J, Fujioka Y, Eriksson S, et al. Neutron Powder Diffraction Study of $Pb(Hf_xTi_{1-x})O_3$ Ceramics ($0.10 \leq x \leq 0.50$). *Inorg Chem.* 2005;44:9267-9278.

[4] Fantozzi G, Idrissi H, Favotto C, et al. Lead hafnate titanate (PHT) ceramics: processing and proeprties. *J Eur Ceram Soc.* 2000;20:1671-1676.

[5] Schorn PJ, Schneller T, Bottger U, et al. Characterization of Chemical Solution Deposition-Derived Lead Hafnate Titanate Thin Films. *J Am Ceram Soc.* 2005;88:1312-1314.

[6] Wu Z, Zhu J, Liu X. Improved fatigue property of hafnium substitute lead zirconate titanate deposited by pulsed laser deposition. *J Mater Sci Mater Electron.* 2017;28:1819-1823.

[7] Jaffe B. Antiferroelecric Ceramics with Field-Enforced Transitions: A New Nonlinear Circuit Element*. *Proc IRE*. 1961;1264-1267.

[8] Hanrahan B, Espinal Y, Neville C, et al. Accounting for the various contributions to pyroelectricity in lead zirconate titanate thin films. *J Appl Phys.* 2018;183:124104.

Chapter 8

[1] Strnad NA, Potrepka DM, Pulskamp JS, et al. Texture and Phase Variation of ALD $PbTiO_3$ Films Crystallized by Rapid Thermal Anneal. *J Vac Sci Technol A.* 2019;37:020917.

[2] Hwang GW, Lee HJ, Lee K, et al. Atomic Layer Deposition and Electrical Properties of $PbTiO_3$ Thin Films Using Metallorganic Precursors and H_20. *J Electrochem Soc.* 2007;154:G69-G76.
[3] Khan MA, Comyn TP, Bell AJ. Deposition of PbTiO3 films on Pt/Si substrates using pulsed laser deposition. *J Eur Ceram Soc*. 2008;28:591-597.
[4] Watanabe T, Hoffman-Eifert S, Hwang CS, et al. Growth Behavior of Atomic-Layer-Deposited Pb(Zr,Ti)Ox Thin Films on Planar Substrate and Three-Dimensional Hole Structures. *J Electrochem Soc.* 2008:155:D715-D722.
[5] Sanchez LM, Potrepka DM, Fox GR, et al. Optimization of PbTiO3 seed layers and Pt metallization for PZT-based piezoMEMS actuators. J Mater Res. 2013;28:1920-1931.
[6] Sanchez LM. Optimization of Pb(Zr52Yi38)O3 through improved platinum metallization, use of a PbTiO3 seed layer, and fine tuning of annealing conditions for applications in multilayer actuator MEMS technology. PhD Dissertation*; The University of Maryland*; 2014.
[7] Aggarwal S, Udayakumar KR, Rodriguez JA. Stoichiometry and phase purity of Pb(Zr, Ti)O_3 thin films deposited by metal organic chemical vapor deposition *J Appl Phys.* 2006;100:064103.
[8] Rodriguez J, Remack K, Boku KR, et al. Reliability Properties of Low Voltage PZT Ferroelectric Capacitors and Arrays. *International Reliability Physics Symposium.* Feb 16, 2004; Pheonix, AZ, USA.
[9] Tang X, Zhu X, Dai J, et al. Self-limited grain growth, dielectric, leakage and ferroelectric properties of nanoscrystalline BiFeO3 thin films by chemical solution deposition. *Acta Mater.* 2013;61:17391747.
[10] Watanabe T, Hoffman-Eifert S, Peter F, et al. Liquid Injection ALD of Pb(Zr,Ti)O_x Thin Films by a combination of Self-Regulating Component Oxide Processes. *J Electrochem Soc.* 2007:154:G262-G269.
[11] Zhang F, Perng Y-C, Choi JH, Wu T, et al. Atomic layer deposition of Pb(Zr, Ti)Ox on 4H-SiC for metal-ferroelectric-insulator-semiconductor diodes. *J Appl Phys.* 2011;109:124109.

[12] Choi JH, Zhang F, Perng Y-C, et al. Tailoring the composition of lead zirconate titanate by atomic layer deposition. *J Vac Sci Technol B.* 2013;31:012207.
[13] Harjuoja J, Vayrynen S, Putkonen M, et al. Atomic layer deposition of $PbZrO_3$ thin films. *Appl Surf Sci.* 2007;253:5228-5232.
[14] Zhai J, Chen H. Direct current field and temperature dependent behaviors of antiferroelectric to ferroelectric switching in highly (100)-oriented PbZrO3 thin films. *Appl Phys Lett.* 2003;82:2673-2675.
[15] Park MH, Lee YH, Kim HJ, et al. Ferroelectricity and Antiferroelectricity of Doped Thin HfO_2-Based Films. *Adv Mater.* 2015;27:1811-1831.
[16] Fantozzi G, Idrissi H, Favotto C, et al. Lead hafnate titanate (PHT) ceramics: processing and proeprties. *J Eur Ceram Soc.* 2000;20:1671-1676.
[17] Schorn PJ, Schneller T, Bottger U, et al. Characterization of Chemical Solution Deposition-Derived Lead Hafnate Titanate Thin Films. *J Am Ceram Soc.* 2005;88:1312-1314.
[18] Strnad NA, Johs B, Phaneuf RJ, et al. Investigation of Bare Silicon and Sputtered Platinum Surface Effects on ALD Growth of TiO_x and ZrO_x by In-Situ Ellipsometry. *Presented at the 15th international conference on atomic layer deposition*; 2015; Portland, OR.
[19] Vollmer M, Weber A. *Z Phys Chem.* 1926;119:227.
[20] Bauer E. *Z Kristollagr.* 1958;110:372.
[21] Buhlmann S, Muralt P, Allmen SV. Lithography-modulated self-assembly of small ferroelectric $Pb(Zr,Ti)O_3$ single crystals. *Appl Phys Lett.* 2004;84:2614-2616.
[22] Brune H. Growth Modes in Encyclopedia of Materials: Science and Technology. 2001. 3683-3693.
[23] Thurmer K, Williams E, Reutt-Robey J. Autocatalytic Oxidation of Lead Crystallite Surfaces. *Science.* 2002;297:2033-2035.
[24] Springholz G, Pinczolits M, Mayer P, et al. Tuning of Vertica; and Lateral Correlations in Self-Organized $PbSe/Pb_{1-x}Eu_xTe$ Quantum Dot Superlattices. Phys Rev Lett. 2000;84:4669-4672.
[25] Elam JW, Zinovev AV, Pellin MJ, et al. Nucleation and Growth of Noble Metals on Oxide Surfaces Using Atomic Layer Deposition. *ECS Trans*. 2007;3:271-278.

[26] Hausmann DM, Kim E, Becker J, et al. Atomic Layer Deposition of Hafnium and Zirconium Oxides Using Metal Amide Precursors. *Chem Mater.* 2002:14:4350-4358

[27] Momeni MM, Nazari Z. Preparation of TiO2 and WO3-TiO2 nanotubes decorated with PbO nanoparticles by chemical bath deposition process: A stable and efficient photo catalyst. Ceram Int. 2016;42:8691-8697.